Topological Phenomena in Two-Dimensional Electron Systems

Dissertation advisor: Professor Amir Yacoby Michael S. Kosowsky

Topological Phenomena in Two-Dimensional Electron Systems

Abstract

The search for fault-tolerant quantum computing is a major thrust in modern physics. Majorana zero modes are quasiparticles with non-abelian exchange statistics that can be used as a basis for topological quantum computing, which is much more robust against disorder than standard quantum computing. Two-dimensional semiconductor systems with strong Rashba spin-orbit coupling and induced superconductivity, in the presence of in-plane magnetic fields, are predicted to host Majorana zero modes.

In this thesis, we describe several experiments centered around induced superconductivity in two types of semiconductor systems, HgTe and InAs. The first two experiments describe our measurements on HgTe. By measuring Fraunhofer interference in a Josephson junction as a magnetic field is applied parallel to the quantum well, we find that Cooper pairs acquire a tunable momentum that increases with the applied in-plane field, leading to the appearance of superconductivity with triplet-pairing. Our analysis leads to a method for studying the spin-orbit coupling and Fermi surface properties of two-dimensional materials. These experimental observations inspired a theoretical proposal to construct Majorana bound states on the edge of a two-dimensional induced superconductor with spin-orbit coupling. We investigate this theoretical proposal by measuring the local tunneling density of states on the edges of a Josephson junction. We observe a continuum of Andreev levels which

disperse coherently with the phase difference. At high values of applied in-plane magnetic field, we observe an enhanced zero-energy conductance extending over a range of phase difference which range grows with the magnitude of the in-plane field, in accordance with the theoretical prediction.

We then describe our experiments on InAs systems. The first InAs quantum well we study is a surface well with epitaxial aluminum grown on it in the molecular beam epitaxy chamber, which leads to a very strong induced superconducting gap. We discuss our attempts to repeat our HgTe experiments on this system, as well as our investigation of a recent theoretical prediction for ungapped superconducting states at high values of in-plane field. The second InAs experiment discusses a system with a deeper InAs quantum well, which yields mobilities much higher than in the surface case. We show our initial measurements on this system, as well as our initial attempt at measuring a zigzag junction, which is predicted to display a much larger topological gap than that of a planar junction.

Contents

Listing of figures

To my wife Tova, and my children Shani and Koby.

Acknowledgments

In my opinion, the several paragraphs that follow this sentence are the most important ones in my entire dissertation. The research described in this thesis would not be possible without the contributions of the many people who have been incredibly important to my Ph.D. studies over the past six years.

I would like to begin my thanking my advisor, Amir Yacoby. During the beginning of my time in graduate school, before I had joined a research group, I heard Amir give a talk on topological quantum systems, and was immediately enthralled by his passion for the subject. Throughout my time in his lab, he has been a constant source of ideas, and always knows when and how to pivot a project. What impresses me most about Amir is that his passion extends to many areas of physics, and how he manages to run a lab that studies many disparate research areas.

I would also like to thank the other members of my committee, Bertrand Halperin and Philip Kim. Both Bert and Philip were there for me when I hit crossroads in my studies, and gave me very helpful advice with how to proceed. In addition, Bert's brilliant theory work was instrumental in helping us with the publications of our experiments in HgTe. The biweekly meetings with Philip and members of his group provided very useful advice as we progressed with our InAs experiments.

I next would like to thank those who worked with me on Team Topology over the past six years. First and foremost, Sean Hart and Hechen Ren, who were the senior members of the team when I

joined Amir's lab and taught me much about topological physics, as well as how to fabricate and measure devices. Sean's style of teaching was instrumental to my growth as a physicist. I also enjoyed our Beer O'Clock meals, cookouts, and tennis tournament watching. Hechen mentored me on my first project, and was always a great friend to talk with.

One year after my arrival in Amir's lab, I was joined on Team Topology by Andrew Pierce. Although I initially helped train Andrew, I will say that by the end of my time at Harvard, Andrew has taught me as least as much as I have taught him. He is always a great person to discuss physics with, and has had many helpful suggestions that have guided my experiments. Andrew has been one of my closest friends at Harvard, and I will greatly miss his sense of humor and our daily coffee runs.

Andrew Saydjari joined Team Topology in my penultimate year, and immediately showcasted his passion and excitement for our experiments. He has been a helpful member of the team and has done a great job furthering our work.

I also want to acknowledge the contributions to Team Topology of Fokko de Vries, a visiting student in our lab during the beginning of my time in graduate school who helped train me in fabrication, as well as those of Nixia Chen and Sunil Lamichhane, two undergraduate summer students who helped with our research.

During my Ph.D., I was lucky to collaborate with an amazing assortment of brilliant scientists.

Our collaborators at Universität Würzburg made our HgTe work possible. Laurens Molenkamp, Ewelina Hankiewicz, Benedikt Scharf, Christoph Brüne, Hartmut Buhmann, Mathias Mühlbauer, Philipp Leubner and Martin Stehno were essential to these projects, and it was a great pleasure flying to Germany to meet them as well as hosting them at Harvard.

A newer collaboration with Werner Wegscheider's group in ETH Zurich has yielded some promising results, and I have enjoyed working with his students Rüdiger Schott and Erik Cheah. Unfortunately, the end of my time with the collaboration was cut short by the COVID-19 outbreak and forced cancelation of all fabrication, but I am very excited to see what happens on this project in the future when labs reopen.

Some of our InAs work was in collaboration with Javad Shabani's group at NYU. I learned a number of important lessons from Javad, and it was very nice to work with his students Kaushini Wickramasinghe, Billy Mayer, and Joe Yuan.

I would also like to acknowledge Chris Palmstrøm and his student Bo Shojaei for sending me the InAs/GaSb material that I worked on for my first project in Amir's lab.

Falko Pientka is a fantastic theorist whose work was essential to our HgTe papers. I also would like to thank the many other physicists with whom I consulted during my time at Havard. Anton Akhmerov, Eugene Demler, Liang Fu, Ady Stern, and Andrei Bernevig all gave important ideas and comments on our experiments at various times. Claudia Felser both gave important insight as well as provided several samples that were fun to experiment with for short periods of time.

There are many members of the Yacoby Lab who contributed significantly to my Ph.D., although I did not directly work with them. In particular, Shannon Harvey helped me enormously throughout my first five years. She taught me much about cryostats, measurements, and fabrication, and was always one of my first resources when I had questions. She and Charlotte Bøttcher were always there to help maintain the MX400 when needed, and they made my experiments possible by lending me their MX50 fridge when MX400 was down for two years.

Didi Wei, Seung Hwan Lee, Lucas Orona, and Yuliya Dovzhenko were incredibly supportive of me during the rough stretches of my Ph.D., and I will greatly miss hanging out with them.

Pat Gumann is a wealth of knowledge about cryogenic systems, and helped train me initially. Mikey Shulman and John Nichol were also great resources. I'd also like to thank Yinyu Liu, Uri Vool, Francesco Casola, Tony Zhou, Andrei Levin, Assaf Hamo, Loren Alegria, Ziwei Qiu, and Ruolan Xue for interesting discussions.

I'd also like to acknowledge members of the Kim group who helped me, in particular Yuval Ronen and Onder Gul who contributed much insight to my InAs projects, as well as Katie Huang, Andy Joe, Gil-Ho Lee, Jonah Waissman, and Frank Zhao.

The Harvard cleanroom was where I spent most of the past six years, and I would like to thank the staff members who helped me along the way and maintained the tools that I needed. Ameha Gebrey-ohannes, Adam Graham, Yuan Lu, and Jason Tresback all helped me and were more like friends than colleagues. I also want to thank the other CNS staff whose tools I used, namely Jules Gardener, Mac Hathaway, Kenlin Huang, Ed Macomber, Steve Paolini, John Tsakirgis, Malcolm Tse, and Guixiong Zhong.

While technically not a formal staff member of CNS, Arthur Safira was a very helpful resource for fabrication as well during his time in the Lukin lab, and trained me on many cleanroom tools.

Our lab administrator, Hannah Belcher, was an amazing resource during my time at Harvard. She seamlessly handled any administrative issues I had, and was a great friend to talk to. I spent much time in her office talking about the lab and life in general, and will definitely miss these conversations. Hannah's predecessor, Carolyn Moore, was very helpful as well during my first year at Harvard.

Two members of the physics administration helped me throughout my Ph.D. Both Jacob Barandes and Lisa Cacciabaudo were always there to talk to, and I am grateful for everything they did for me and for all of the advice they gave.

Outside of Harvard, I would like to thank Nick Dent from Oxford Instruments, who is probably happy that I am graduating and will no longer be blowing up his phone and email with constant questions and maintainence issues on the MX400. Nick is a cryogenic systems guru, and is the best person to call if there are any fridge issues.

Steve Harvell from Hartech, Mike Golarz from Sharon Vaccuum, and Chris Griffith from KRI were all important resources when I fixed and maintained the Yacoby Lab's thermal evaporator.

I would not have made it through graduate school without the support of my family and friends. Avi Geller and Josh Yarmush, my best friends since childhood, were there for me every step of the way. I am very grateful that they were in Boston with me throughout my time at Harvard. Leslie Black, Harry Chiel, and Leah Naghi were also frequent recipients of my phone calls, and I greatly appreciate their friendship, along with that of Brad Baskir, Michael Kahnowitz, David Lehmann, Aaron Schacht, Yoey Schacht, and Shani Weiner.

The Maimo '09 Fantasy Football and Madden leagues provided great ways to let off steam. My only complaint is that the chats were too active at points, but this is due to the great people in these leagues, all of whom participated in great discussions and debates about anything and everything.

Yakov and Jen Salzberg, Joe Itkis and Abby Phillips, Adir Feifel and Adi Goldberg, and Asher Lindenbaum and Miriam Seidman were great friends in Brighton, along with the entire New Ashkenaz Minyan community. Rabbi Aharon Benmergui was a constant source of guidance and support.

My undergraduate advisor Dave Roberts was always there for me with good advice, as was Katie Weil, with whom I spent many hours working in undergrad and many hours discussing our Ph.D.s while we were in graduate school. I'd also like to thank Amanda Chen and Matt Lim, friends and resources during the job search process, as well as Andy Joe, Aaron Kabcenell, and Doug Mendoza, who were G1s with me and friends throughout graduate school.

No acknowledgement would be complete without including my wonderful wife Tova, who encouraged and supported me throughout the entire process. We went through thick and thin together, and I am excited to begin the next stage of life with her.

I enetered graduate school as a newlywed, and now leave with two amazing children, Shani and Koby, who give me something to look forward to every day when I get home. I love and cherish every second that I get to spend with them.

I am sincerely grateful to my parents for always being there for me when I needed advice or just an outlet to vent. My parents and in-laws made graduate school possible by watching my children several days a week. The value of living near family is something that cannot be overstated. I especially am thankful to my mom, who always was willing to help on a moment's notice.

My sisters were always there to support me throughout my time in graduate school. My sisters and my siblings-in-law were also always willing to help out with childcare support whenever possible, and definitely helped make graduate school possible.

My cousins were always there for me as well. While many of them moved to various parts of the country throughout the past six years, I am happy to have kept in touch with all 12 of them. In particular, Dahlia Gruen, Sam Michaelson, and Jonathan Michaelson were almost daily contacts.

My grandparents were constant sources of inspiration for me. Although I sadly lost three grandparents in my first few years in graduate school, I was lucky to have them in my life for as long as I did. I also am grateful to have lived just minutes from my paternal grandmother for my entire time at Harvard.

Lastly, I would like to thank the National Science Foundation for awarding me their graduate research fellowship that funded my first few years of research.

1

Introduction

1.1 The search for Majorana Zero Modes

1.1.1 Problems with standard quantum computing

A quantum computer is one that performs computations using quantum mechanical principles. For example, a quantum bit, or "qubit," is able to be in a superposition of states instead of a definitive 0 or 1 state like a bit in a classical computer, and two (or more) qubits are able to be quantum mechanically

entangled.

Many classically difficult computing problems become easier to solve using a quantum computer. One of the most famous examples is RSA encryption, which is used by almost all modern computers to encrypt and decrypt information. RSA encryption relies on the fact that prime factorization of very large numbers is almost impossibly hard, even for a powerful computer. However, in 1994, Peter Shor showed that a quantum computer would be able to factor numbers in polynomial time, instead of the exponential time required by classical computers, and thus be able to break modern encryption[66]. Other classically hard problems that quantum computers can solve include many optimization and modeling problems.

The major issues with implementing a quantum computer lie in the physical design, not the theoretical model. Decoherence is a big problem, in which quantum entanglement is lost over time due to environmental entanglement with the system. A second issue is systematic errors, in which a quantum gate operation applies a slightly different operation than designed. For example, a 90.01° rotation instead of a 90° one. While there are methods for fault-tolerant quantum computing, they still require the imperfect systems to be close to ideal ones[67].

1.1.2 Braiding

Alexei Kitaev demonstrated that a two-dimensional system with non-abelian anyonic excitations would intrinsically be fault-tolerant[35]. Standard anyons are particles that, when exchanged with one

another, their overall wavefunction changes by an arbitrary phase (hence "any"-on):

$$\psi(\mathbf{r}_1, \mathbf{r}_2) \to e^{i\varphi}\psi(\mathbf{r}_1, \mathbf{r}_2) \tag{1.1}$$

The two-dimensional nature of the interchange is necessary as a winding of one particle around the other is only well-defined in two dimensions. The most well-known types of anyons are those with the phase $\theta = \pi$ and $\theta = 0$, respectively known as fermions and bosons. In these special cases, interchanging the particles twice returns the original state.

If we expand to some number N indistinguishable particles, we find that the topological classes of trajectories in which the N particles start at some initial position order, wind around each other, and then end up in some final position order, correspond to the elements of the braid group $\mathcal{B}_N$. We can physically draw a representation of braiding operations, as shown in Figure 1.1 [53]. Particle trajectories are represented as worldlines, with time moving vertically on the page. When two particles interchange, we draw their strands passing over each other. Whether the left or right particle in the interchange is the one passing over the other specifies the direction of the exchange, clockwise or counter-clockwise.

These braiding operations cause non-trivial rotations in the degenerate Hilbert space of the particles. At low energies, the only non-trivial unitary operations in the Hilbert space are the braiding operations, protecting the system from errors caused by environmental entanglement [53].

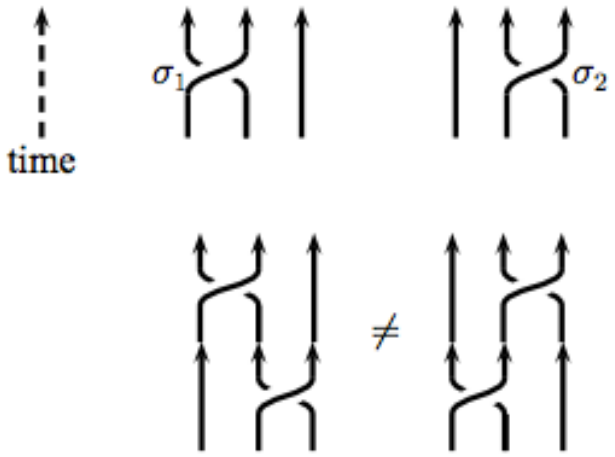

Figure 1.1: Schematic of braiding operations, from [53]. Worldlines of three particles are shown. In the top of the figure, the σ_1 and σ_2 operations are shown respectively on the left and right. σ_1 interchanges particles 1 and 2, when counting from the left, and σ_2 interchanges particles 2 and 3. In the bottom of the figure, we see the non-abelian property of the braid, that $\sigma_1\sigma_2 \neq \sigma_2\sigma_1$.

1.1.3 The Majorana fermion

Almost 100 years ago, Paul Dirac published his relativistic wave equation that described spin-$\frac{1}{2}$ particles [18]. Just under a decade later, Ettore Majorana demonstrated that it was possible for spin-$\frac{1}{2}$ particles to be their own antiparticles [45]. These particles that satisfied Majorana's solution to the Dirac equation gained the name Majorana fermions. Importantly, Majorana fermions possess the non-abelian braiding statistics that would allow for intrinsic fault-tolerant quantum computing.

Using second quantization notation, a Dirac fermion can be described by operator c_i, which satisfies the fermionic relations:

$$c_i c_j + c_j c_i = c_i^\dagger c_j^\dagger + c_j^\dagger c_i^\dagger = 0, \qquad c_i c_j^\dagger + c_j^\dagger c_i = \delta_{ij} \tag{1.2}$$

Majorana fermions can be described by the operator γ_i. Due to the condition that they are their own antiparticle, $\gamma_i = \gamma_i^\dagger$. It is possible to write a Majorana operator in terms of the annihilation and creation operators of a standard Dirac fermion:

$$\gamma_{2j-1} = c_j + c_j^\dagger, \qquad \gamma_{2j} = \frac{c_j - c_j^\dagger}{i} \tag{1.3}$$

We can also write a Dirac operator now in terms of Majorana operators:

$$c_j = \frac{1}{2}(\gamma_j - i\bar{\gamma}_j) \tag{1.4}$$

1.1.4 Kitaev's Model

In another important paper, the aforementioned Alexei Kitaev discussed a toy model for realizing Majorana fermions[34]*.

Kitaev discussed a fermion chain consisting of some large number L sites, each occupied by an electron or empty. The Hamiltonian for such a system can be written as

$$H = \sum_j \left[-w(c_j^\dagger c_{j+1} + c_{j+1}^\dagger c_j - \mu\left(c_j^\dagger c_j - \frac{1}{2}\right) + \Delta c_j c_{j+1} + \Delta^* c_{j+1}^\dagger c_j^\dagger \right] \tag{1.5}$$

where w is a hopping amplitude from site to site, μ a chemical potential, and $\Delta = |\Delta|e^{i\theta}$ the induced

*The careful reader may notice that this paper actually preceded his other paper mentioned above in Section 1.1.2. The 2003 paper actually was posted to arXiv in 1997, before the 2001 paper was posted, but was published after.

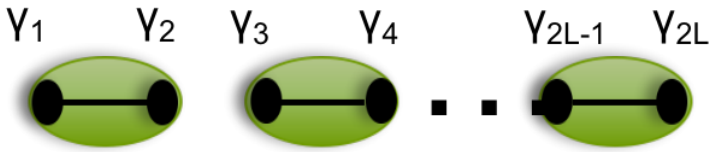

Figure 1.2: Kitaev chain, first configuration. We show the Kitaev chain in the configuration described by Equation 1.8. The green ovals are electron sites, and the black filled circles the Majoranas. Solid black lines connect two Majoranas that are paired.

superconducting gap. Absorbing the phase factors into the Majorana operators,

$$\gamma_{2j-1} = e^{i\theta/2}c_j + e^{-i\theta/2}c_j^\dagger, \qquad \gamma_{2j} = -ie^{i\theta/2}c_j + ie^{-i\theta/2}c_j^\dagger, \tag{1.6}$$

we can rewrite the Hamiltonian as

$$H = \frac{i}{2}\sum_j \left[-\mu\gamma_{2j-1}\gamma_{2j} + (w+|\Delta|)\gamma_{2j}\gamma_{2j+1} + (-w+|\Delta|)\gamma_{2j-1}\gamma_{2j+2}\right]. \tag{1.7}$$

If we take the case of $|\Delta| = w = 0$, and $\mu < 0$, we see that the Hamiltonian is written as

$$H = \frac{-\mu i}{2}\sum_j \gamma_{2j-1}\gamma_{2j}, \tag{1.8}$$

which means the Majorana operators from the same electron site j are paired together, as we see in Figure 1.2.

However, if we take a different special case, in which $|\Delta| = w > 0$ and $\mu = 0$, we see that the

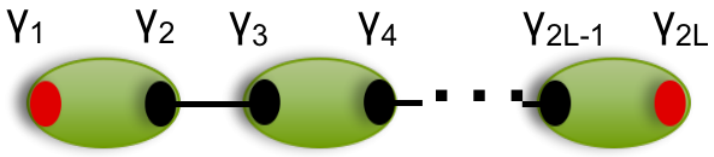

Figure 1.3: Kitaev chain, second configuration. We show the Kitaev chain in the configuration described by Equation 1.9. The green ovals are electron sites, and the black filled circles the Majoranas. Solid black lines connect two Majoranas that are paired. We see the two Majoranas at the edges, colored in red, are unpaired with a neighboring Majorana.

Hamiltonian can be written as

$$H = iw \sum_j \gamma_{2j} \gamma_{2j+1} \tag{1.9}$$

In which now Majorana operators from different sites are paired together. While both cases have the same bulk properties, they have very different boundary properties: in the second case, there exist unpaired Majorana fermions at both ends of the chain, as we see in Figure 1.3. If the Majoranas are sufficiently spatially separated by a distance larger than the superconducting coherence length, they support non-local entanglement.

As the Majoranas are their own antiparticles and have zero energy, they are frequently referred to as Majorana zero modes in this context.

These two special cases in Kitaev's chain are two degenerate ground states of the system, with different parity. Assuming the Hamiltonian conserves parity, this degeneracy is very difficult to break. If we took a linear superposition of the two ground states and subjected them to the Hamiltonian of the system, the phase difference of the wave function would precess over a very large amount of time, due to the negligible energy difference between the two parity states. Moreover, a single Majorana operator

does not conserve fermion parity, so it would not appear as a term in a reasonable Hamiltonian. We thus see that an individual isolated Majorana site should be entirely immune to error[34].

Kitaev's model represents a spinless 1D p-wave superconductor, or a $p + ip$ superconductor in 2D, neither of which is an easily realizable physical state. Theory has shown that Kitaev's model is realizable in a system with induced superconductivity and strong Rashba spin-orbit coupling, in the presence of magnetic fields[43 55].

The search for Majorana zero modes has been a major focus in condensed matter physics for over a decade, and is the motivation for the work that follows in this thesis, where we attempt to find Majoranas in several systems.

1.2 Outline of this thesis

Chapter 2[†] describes experiments on Josephson junctions based on HgTe quantum wells with the chemical potential tuned into the conduction band. We show that applying a magnetic field in the plane of the two dimensional junctions causes surprising changes to the measured interference patterns. We find that Cooper pairs in the quantum well acquire a tunable finite momentum that grows with the magnetic field strength, which leads to triplet pairing of electrons at certain locations within the junction. The details of the interference behavior provide a means to probe the nature of spin-orbit coupling within the quantum well, as well as a measure of geometric properties of the junction. The density dependence of our measurements also allows us to extract the value of $\tilde{g}/v_F$, where $\tilde{g}$ is the effective g-factor and v_F is the Fermi velocity.

[†] Chapter 2 is adapted from reference[31]

Chapter 3[‡] details an experimental pursuit based on a theoretical proposal for Majorana zero modes in a planar Josephson junction. We fabricate local tunnel probes on the edge of planar Josephson junctions made with HgTe quantum wells and perform local tunneling spectroscopy by measuring the differential conductance to measure the local density of states. We control the phase difference across the junction using a perpendicular magnetic field to generate flux in a loop geometry, and apply an in-plane magnetic field to control the strength of the Zeeman effect. We observe a differential conductance profile associated with a continuum of sub-gap states, which oscillate coherently with the phase difference. At high Zeeman fields, we find that the differential conductance develops a zero-bias peak over a range of the phase difference, which grows with the Zeeman field, consistent with the aforementioned theoretical proposal describing the emergence of Majorana modes at the edges of Josephson junction in a topological superconductor phase.

Chapter 4 discusses our attempt to repeat the measurements from Chapter 2 on a new system, InAs quantum wells with epitaxial aluminum. We discuss our fabrication and measurements on devices, which had much stronger induced superconductivity in our quantum wells than in HgTe but much lower mobility. Ultimately, this mobility issue prevented us from seeing the interference patterns from Chapter 2 at high in-plane fields. We also present designs and measurements on gate-defined quantum point contacts, and our initial attempts to pursue a novel theoretical proposal that would lead to gapless superconducting states with partial Fermi surfaces.

Chapter 5 describes our recent attempt to repeat the measurements from Chapter 2 on a different InAs system, one with high-mobility buried quantum wells. We successfully induce superconduc-

[‡] Chapter 3 is adapted from reference [60]

tivity with a strong induced gap in these systems, something that has been a major struggle for many researchers. Unfortunately, our initial measurements also fail to replicate the results from Chapters 2. We also show a first attempt to increase the topological gap of the system by following the procedure of a recent theoretical proposal.

2

Controlled finite momentum pairing and spatially varying order parameter in HgTe quantum wells

Conventional s-wave superconductivity is understood to arise from singlet pairing of electrons with opposite Fermi momenta, forming Cooper pairs whose net momentum is zero [5]. Several recent studies have focused on structures where such conventional s-wave superconductors are coupled to systems with an unusual configuration of electronic spin and momentum at the Fermi surface. Under these conditions, the nature of the paired state can be modified and the system may even undergo a topological phase transition [25,63]. Here we present measurements and theoretical calculations of several HgTe quantum wells coupled to either aluminum or niobium superconductors and subject to a magnetic field in the plane of the quantum well. By studying the oscillatory response of Josephson interference to the magnitude of the in-plane magnetic field, we find that the induced pairing within the quantum well is spatially varying. Cooper pairs acquire a tunable momentum that grows with magnetic field strength, directly reflecting the response of the spin-dependent Fermi surfaces to the in-

plane magnetic field. In addition, in the regime of high electron density, nodes in the induced superconductivity evolve with the electron density in agreement with our model based on the Hamiltonian of Bernevig, Hughes, and Zhang[8]. This agreement allows us to quantitatively extract the value of $\tilde{g}/v_F$, where $\tilde{g}$ is the effective g-factor and v_F is the Fermi velocity. However, at low density, our measurements do not agree with our model in detail. Our new understanding of the interplay between spin physics and superconductivity introduces a way to spatially engineer the order parameter, as well as a general framework within which to investigate electronic spin texture at the Fermi surface of materials.

2.1 Introduction

Below a critical temperature and magnetic field, certain materials undergo a phase transition to the superconducting state. Macroscopically identified through effects such as zero resistivity and the Meissner effect[48], superconductors may further be understood microscopically as arising due to pairing of electrons occupying opposite points on the Fermi surface and having opposite spin. Within a conventional setting this interaction results in Cooper pairs with zero net momentum. However, in certain materials the presence of both magnetic order and superconductivity can lead to intrinsically nonzero pairing momentum as the system enters the Fulde-Ferrell-Larkin-Ovchinnikov (FFLO) state[26,41]. Studies of both $CeCoIn_5$ and κ-$(BEDT\text{-}TTF)_2Cu(NCS)_2$ under large external magnetic fields found evidence for coupled magnetic order and superconductivity, although in each material the field strength needed was in excess of 10 T[33,46].

Exotic superconductivity has recently come under additional investigation through the goal of

combining s-wave superconductors with materials whose properties are rarely found among the conventional superconductors. For example, inducing the singlet pairing of an s-wave superconductor into a material with strong spin-orbit coupling and reduced dimensionality has been recently considered as a viable platform within which to achieve triplet pairing [58] and topological superconductivity [24,63], or to engineer a Josephson φ_0-junction [72,19]. Moreover, when a ferromagnetic layer is sandwiched by two superconductors, pairs traversing the junction acquire momentum due to the exchange field within the ferromagnet [10,16]. Measurements of critical current oscillations in such superconductor-ferromagnet-superconductor (SFS) junctions have provided evidence for this nonzero pairing momentum [39,64,23], although the magnitude of the momentum was effectively untunable due to the typically large exchange fields.

Here we report on coupling between superconducting leads and a two-dimensional electron system realized within HgTe/HgCdTe heterostructures in the inverted regime. Due to the interplay between superconductivity, band structure, and the applied magnetic field, we find that the order parameter has an oscillatory component derived from the finite momentum of paired electrons, and that this momentum can be continuously tuned between conventional and unconventional regimes. Our use of only relatively small external magnetic fields ($\leq$ 4 T overall and $\leq$ 1.8 T for aluminum junctions) and micron-scale device dimensions introduces a new regime in the exploration of the interplay between superconductivity and spin physics.

2.2 Interference Measurements With a Finite Parallel Magnetic Field B_x

To study the effect of magnetic field and band structure on electron pairing, we place two superconducting leads on opposite boundaries of a rectangular section of quantum well. Devices were fabricated at varying angles with respect to the cleavage edges of the crystal (the [110] and [1$\bar{1}$0] axes). The angular alignment corresponds to a rotation angle θ with respect to the principal crystal axis [100], with θ defined modulo $\pi/2$ (Figure 2.1A, see Section 2.6.1). The width W between the two leads is 800 nm and the length L of the resulting Josephson junction is 4 μm. We study the influence of either niobium or aluminum superconductors by applying a small AC current bias between the two leads while measuring the resultant AC voltage[54]. The aluminum thickness is 15 nm in order to sustain superconductivity in moderate parallel magnetic fields (Section 2.6.2)[49], while the niobium thickness is 130 nm. Josephson interference is generated by application of small (up to $\sim$ 10 mT) magnetic fields in the z-direction[50]. Throughout this chapter, the in-plane coordinate axes are referred to as x and y, respectively oriented perpendicular and parallel to the supercurrent flow between leads. The addition of a normal metal top gate allows us to tune the electron density within the junction, thereby providing a means to study superconductivity from the quantum spin Hall regime[38,31] into the electron-doped regime. In the regime of high electron density and with no parallel magnetic field, our junctions display Josephson interference consistent with uniform supercurrent transport through the bulk of the quantum well, shown in 2.1B for a device with aluminum leads.

We primarily study differential resistance with zero applied DC current, due to the efficiency of such measurements in illuminating the structure of the interference pattern. Lower resistance relative

to the normal device resistance typically corresponds to elevated critical current (Section 2.7.1). In an aluminum-based junction, in the electron-doped regime and with angle $\theta = \pi/4$, increasing the magnetic field in the x direction strongly modulates the Josephson interference (Figure 2.1C). Two distinct regions of decreased resistance are separated by a nodal field of approximately $B_x = 1.1$ T, corresponding to the suppression of induced superconductivity. At each value of the parallel field, we extract the minimum junction resistance as a measure of the strength of superconductivity at that particular field. Plotting these minimum junction resistances highlights the oscillatory effect of parallel field on superconductivity, with the nodal field marked by an arrow (Figure 2.1D). The suppression of superconductivity at the nodal field directly results from the finite momentum of induced Cooper pairs.

In an aluminum-based junction oriented with $\theta = \pi/2$, a similar modulation of superconductivity occurs as the parallel field B_x grows (Figure 2.1E, see Sections 2.7.2 and 2.7.3). Although the aluminum leads can sustain superconductivity up to 1.75 T, we only measure this device up to $B_x = 1$ T due to constraints on the range of our vector magnet (see Section 2.6.1).

The resistance of a device with niobium leads and $\theta = \pi/4$ is similarly modulated upon application of a parallel field, with multiple nodes visible as B_x increases to 4 T (Figure 2.1F). A more detailed measurement highlights the presence of three distinct regions of decreased resistance, separated by bands of high resistance occurring near $B_x = 0.9$ T and $B_x = 2.7$ T (Figure 2.1G). We again extract the minimum junction resistance at each particular parallel field value, demonstrating the oscillatory effect of the parallel field on superconductivity (Figure 2.1H). Nodes of the oscillation, marked by arrows, correspond to local maxima in the overall junction resistance.

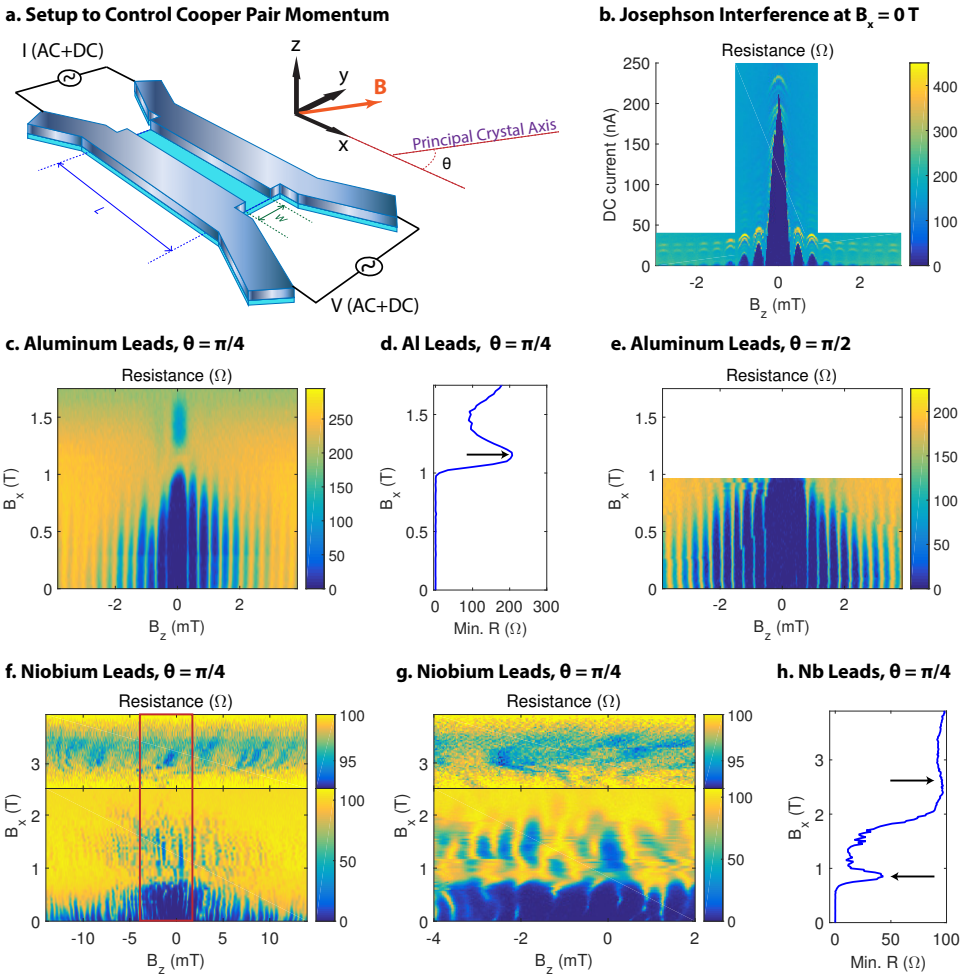

Figure 2.1: Experimental control of the order parameter and of pairing momentum. (A) Two superconducting leads, composed of either aluminum or niobium, couple to a rectangular section of HgTe quantum well to form a Josephson junction. The width W separating the leads is always 800 nm, while the length L of the junction is always 4 μm. The resistance of the junction is monitored by applying a small AC current bias (typically $\sim$ 1 nA) and concurrently measuring the resulting AC voltage. Further sourcing DC current allows measurement of critical currents and normal device resistance. The external magnetic field $\vec{B}$ contains a small z component to generate Josephson interference, while here the larger x component couples significantly to the spin-degree of freedom. Junctions may be oriented at an angle θ with respect to the [100] principal crystal axis, modulo π/2. (B) In the electron-doped regime, the devices show Josephson interference consistent with transport through a doped bulk. In all subsequent measurements, zero DC current is applied. (C) The differential resistance of a junction with aluminum leads oscillates due to Josephson interference as the perpendicular field varies. Increasing the parallel field modulates the strength of induced superconductivity. (D) Plotting the minimum resistance at each value of B_x demonstrates the presence of a nodal resistance maximum near B_x = 1.1 T. (E) In an aluminum-based device oriented with $\theta = \pi/2$, increasing the parallel field similarly modifies the resistance. (F) In a junction with niobium leads, a similar modulation of the resistance occurs. (G) A more detailed study of the space outlined in red in (F) highlights three regions of decreased resistance separated by bands of high resistance near B_x = 0.9 T and B_x = 2.7 T. In both (F) and (G), the decreased resistance above 2.5 T is highlighted via a stretched color scale. (H) The minimum resistance at each value of B_x further shows the oscillatory nature of the superconductivity as the parallel field increases. Successively higher nodes (marked by arrows) occupy broader regions of parallel field, while superconductivity also weakens as the parallel field increases.

Despite the differences in the fabrication of our devices, the nodal structure is both robust and occurs at nearly the same parallel field magnitudes. These observations suggest that the induced pairing momentum originates in the heterostructures and not the bulk superconductors, and is insensitive to details of the crystal orientation. Since superconductivity arises from the pairing of electrons with opposing spins and momenta, it is therefore necessary to examine the nature of both Zeeman coupling and spin-orbit coupling within the quantum well.

2.3 Theoretical Model of the Induced Superconductivity

We model our devices by considering first the quantum well region in the absence of the superconductors, for which a four-band theoretical Hamiltonian H_1 was proposed as a way to describe the topology of the band structure [8]. We adopt a version of this model to include both the external magnetic field and possible contributions from spin-orbit coupling [62,70,37]. The key prediction of the band structure modeling is that the Zeeman coupling from the external field B_x modifies the Fermi surfaces in a manner which depends on the nature of the spin-orbit coupling (See Section 2.8.1). As a consequence, the induced superconducting order parameter is expected to oscillate in space, due to a pairing momentum shift with a magnitude of order $\hbar\Delta k \approx \tilde{g}\mu_B B_x/v_F$, whose orientation also depends on the spin-orbit coupling. Here $\tilde{g}$ is the in-plane g-factor, and v_F is the Fermi velocity.

To theoretically investigate the proximity effect in our quantum wells, we consider a geometry in which the two-dimensional electron gas (2DEG), assumed to have uniform electron density, is contacted by a pair of superconducting leads with a controlled phase difference between them, and we

seek to calculate the maximum supercurrent that can be carried between the strips (Figure 2.3A, see Sections 2.8.2-2.8.5). We assume a Hamiltonian $H = H_1 + H_2$, where H_2 is the coupling between the superconductors and the 2DEG, described by a pairing Hamiltonian of the form

$$H_2 = -\int dxdy \left[\Delta(x,y)\Psi^\dagger(x,y) + \Delta^*(x,y)\Psi(x,y)\right]. \tag{2.1}$$

Here $\Psi(x,y) \equiv \psi_\uparrow(x,y)\psi_\downarrow(x,y)$ is an operator which annihilates a singlet pair of electrons in the 2DEG at the point (x,y), while the pair potential $\Delta(x,y)$ is a complex number that depends on the phase of the superconductor and the tunneling amplitude at that point.

We assume that the contacts between the 2DEG and the superconductors occur at the edges of the superconductors, located at $y = 0$ and $y = W$, so that we may write

$$\Delta(x,y) = \lambda_1(x)\delta(y) + \lambda_2(x)\delta(y-W) \equiv \Delta_1(x,y) + \Delta_2(x,y), \tag{2.2}$$

with $-L/2 < x < L/2$. We assume that the magnitude of the coupling is constant along each lead, but the phase will vary if there is a perpendicular magnetic field $B_z \neq 0$. We choose a gauge where the vector potential points in the x direction, with $A_x = -B_z(y - W/2)$, so that the vector potential vanishes along the midline of the 2DEG. If the superconducting strips have identical widths W_{SC}, then the couplings λ_j will have the form

$$\lambda_j(x) = \left|\lambda_j\right| e^{2\pi i \varphi_j(x)}, \tag{2.3}$$

$$\varphi_j(x) = \varphi_j(0) + \frac{(-1)^{j-1} x B_z (W + W_{sc})}{2\Phi_0}, \tag{2.4}$$

with $j = 1, 2$.

To lowest order in the pairing Hamiltonian H_2, the portion of the total energy that depends on the phase difference between the two superconducting leads can be written in the form:

$$E = -\int dx_2 \left[\lambda_2^*(x_2) \left\langle \Psi(x_2, W) \right\rangle_1 + c.c.\right], \tag{2.5}$$

where $\left\langle \Psi(x,y) \right\rangle_1$ is the order parameter at point (x,y) induced by the superconductor $j = 1$. In turn, this may be written in the form:

$$\left\langle \Psi(x,y) \right\rangle_1 = \int dx_1 \lambda_1(x_1) F(x, x_1, y), \tag{2.6}$$

where F is the propagator from point $(x_1, 0)$ to point (x,y) for an induced Cooper pair. Depending upon the relative magnitudes of spin-orbit coupling and the Zeeman coupling, the propagator F may take various forms (see Section 2.8.4). In the limit where either structural inversion asymmetry (SIA) or bulk inversion asymmetry (BIA) is strong compared to the Zeeman coupling, the pair momentum shift orientation is independent of position on the Fermi surface. The shift occurs along an angle a with respect to the x axis, and the propagator is

$$F(x, x_1, y) = \frac{k_F}{8\pi^2 v_F} \cdot \frac{e^{i\gamma} + e^{-i\gamma}}{(x - x_1)^2 + y^2}, \gamma = \Delta k \left(\sin(a) y + \cos(a)(x - x_1)\right). \tag{2.7}$$

When SIA dominates the spin-orbit coupling, a magnetic field B_x induces pairing momentum in the y direction, and the order parameter also oscillates in the y direction (Figure 2.2A). When $\Delta kW = \pi/2$, the first node of the oscillation coincides with the line $y = W$ corresponding to the width of the junction. Increasing the parallel field so that $\Delta kW = 3\pi/2$ leads to coincidence of the second node and the junction width (Figure 2.2B).

If BIA instead dominates the spin-orbit coupling, when $\theta = 0$ the parallel magnetic field induces order parameter oscillations in the x direction (Figure 2.2C). These oscillations arise due to the finite length of the Josephson junction, with amplitudes that are largest near the ends of the mesa. In contrast to the limit of large SIA, with dominant BIA the nodes of the order parameter never coincide with the junction width. Oscillations in the order parameter instead occur with greater frequency along the x direction as the magnetic field increases.

Finally, when the Zeeman coupling dominates the spin-orbit coupling, the pair momentum shift magnitude is isotropic in-plane, but the orientation lies parallel to the direction of Cooper pair propagation. In this limit the propagator is

$$F(x, x_1, y) = \frac{k_F}{8\pi^2 v_F} \cdot \frac{e^{i\gamma} + e^{-i\gamma}}{(x - x_1)^2 + y^2}, \gamma = \Delta k \sqrt{(x - x_1)^2 + y^2}. \tag{2.8}$$

Here the induced order parameter oscillates along both the x and y directions (Figure 2.2D). Although the shape of the order parameter resembles the limit of strong SIA, the possibility to oscillate in all in-plane directions prevents a node from forming along a line of constant y.

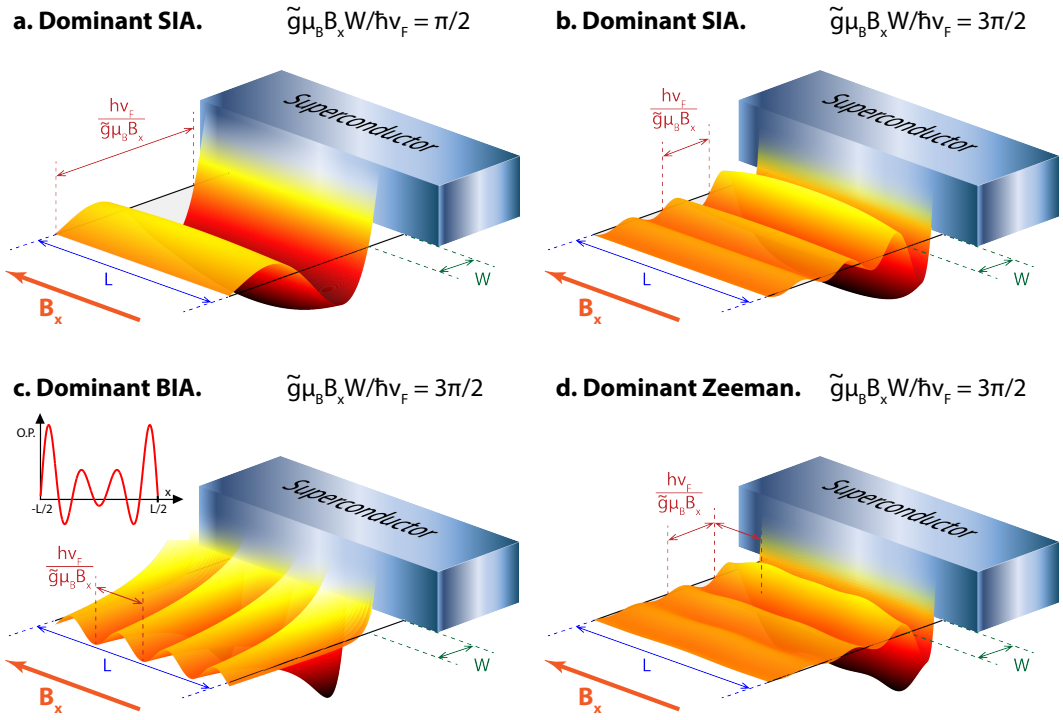

Figure 2.2: Theoretical prediction for the spatially varying order parameter $\langle \Psi(x,y)_1 \rangle$ near a single superconducting lead, with $B_z = 0$. (A) With dominant SIA, application of an in-plane magnetic field B_x induces oscillations of the order parameter in the y direction, with wavelength $hv_F/\tilde{g}\mu_B B_x$. When $\tilde{g}\mu_B B_x W/\hbar v_F = \pi/2$, the first node of the order parameter occurs a distance W from the superconductor. (B) As the magnitude of magnetic field increases, the wavelength of order parameter oscillations decreases. When $\tilde{g}\mu_B B_x W/\hbar v_F = 3\pi/2$, the second order parameter node lies a distance W from the superconductor. (C) If instead BIA dominates, the order parameter oscillations occur in the x direction. As the magnetic field increases, the frequency of oscillations increases. In the inset, a linecut of the order parameter a distance W from the superconductor demonstrates that oscillations are an end effect, with amplitudes which decay into the bulk of the 2DEG. (D) With weak spin-orbit coupling, the parallel field B_x introduces order parameter oscillations in both directions.

2.4 Modeling Interference Patterns

We can link the order parameter oscillations to the Josephson energy E by integrating over the second superconducting lead at position $y = W$, as in equation (2.5). By then differentiating with respect to the phase difference $\varphi_2(0) - \varphi_1(0)$ we find the current-phase relation of the junction, which is then maximized with respect to the phase difference to obtain the critical current.

When SIA dominates the spin-orbit coupling, the critical current periodically disappears when the nodal condition $\Delta kW = (2n + 1)\pi/2$ is satisfied (Figure 2.3B). This suppression of the critical current arises when singlet pairs injected at one lead evolve to become triplet pairs at the location of the second lead. The conversion to triplet pairing corresponds to nodes of the induced singlet order parameter; when these nodes coincide with the positions of the leads, the supercurrent is completely suppressed. Microscopically, these oscillations of the order parameter correspond to finite momentum pairing of electrons, as diagrammed in the inset of Figure 2.3B. In the limit of strong SIA, the Fermi surfaces oppositely shift in the y direction, so that Cooper pairs form internally to each surface with finite wavevector $\Delta k\hat{y}$. Furthermore, as the parallel magnetic field B_x increases beyond the nodal field $B_{node} = \frac{\pi}{2}\frac{\hbar v_F}{g\mu BW}$, we observe evidence that the junction transitions into a π-junction (Section 2.9).

The predicted interference with strong SIA resembles the nodal pattern we observe experimentally. However, in niobium-based devices, we also observe that superconductivity weakens and that nodes occur over an increasingly large range of parallel field strengths as the parallel field increases. To model this behavior, we consider the effect of structural imperfections in the interface between the supercon-

ducting leads and the quantum well. These would introduce random fluctuations in the direction of the in-plane magnetic field at each interface, leading to a random component of the pairing momentum in the x direction that grows linearly with the in-plane field. Hence, we introduce a random phase $\chi \propto (R_1(x_1) - R_2(x_2))\, B_x$, where the random variables $R_1(x_1)$ and $R_2(x_2)$ correspond to fluctuations in the direction of the parallel field at each interface (see Section 2.8.6 for details). With this randomness, the calculated critical currents diminish in magnitude as the in-plane field increases, and nodes occur over a larger range of in-plane field, in agreement with our experimental observation (Figure 2.3C).

Considering, instead, BIA as the dominant source of spin-orbit coupling, when the junction is aligned to the [100] or [010] crystal direction, the order parameter oscillates in the x direction. This oscillation corresponds to shifting of the Fermi surfaces oppositely along x, so that Cooper pairs form internally to each surface with wavevector $\Delta k\hat{x}$ (Figure 2.3D). Since the real-space supercurrent density and the Josephson critical current can be regarded as Fourier conjugates[20], this pairing momentum results in the finite weight of the interference at a particular magnitude of B_z that grows linearly with the parallel field, forming a 'V' shape.

In our measurements of the device oriented with $\theta = \pi/2$, this splitting would be seen in the limit of strong BIA but is not observed experimentally (Figure 2.3E, see Section 2.7.3). Additionally, when junctions are fabricated at an angle $\theta = \pi/4$, with strong BIA the behavior is expected to shift from that shown in Figure 2.3D to the nodal structure in Figure 2.3B. Since we instead observe behavior that does not depend on the crystal orientation, we conclude that BIA in our heterostructure is relatively weak. This conclusion agrees with a previous measurement of Shubnikov-de Haas oscillations in

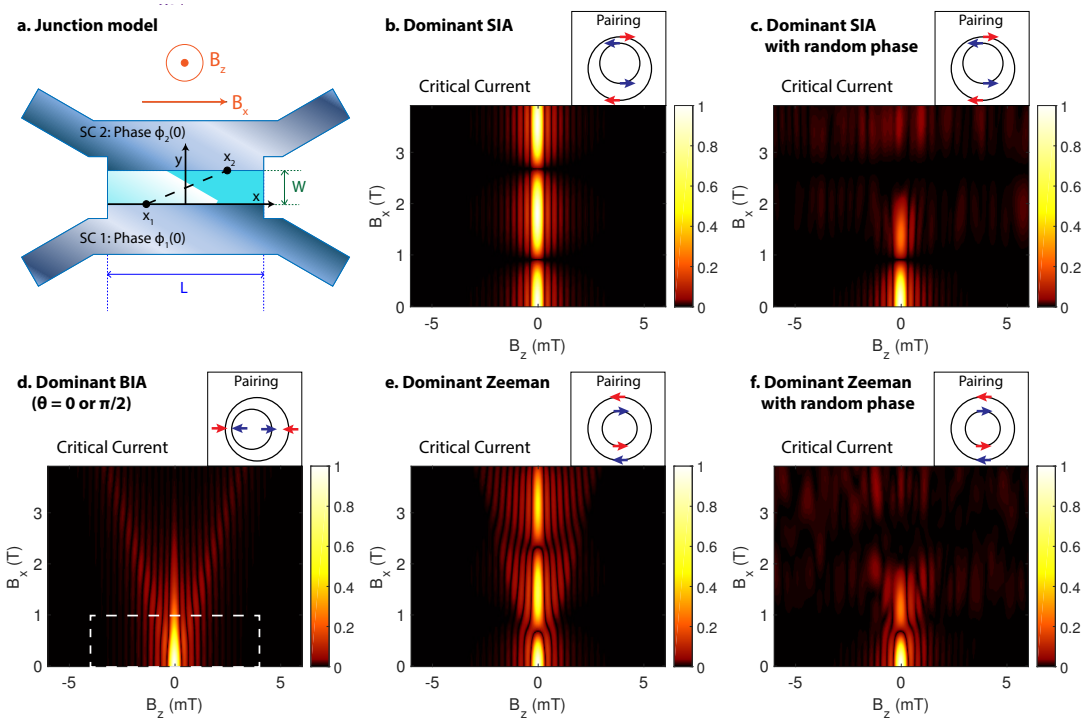

Figure 2.3: Modeling Josephson interference between two superconducting leads. (A) With two leads, paired electrons may traverse the junction beginning at a point x_1 in the lower superconducting lead (SC 1). The pairing amplitude at the point x_2 in the upper lead (SC 2) takes account of the phase accumulated due to finite pairing momentum within the HgTe quantum well. (B) With SIA dominant, the external magnetic field B_x increases the pairing wavevector Δk only in the y direction. At certain values $\Delta k = (2n+1)\pi/(2W)$, where n is an integer, the superconducting interference disappears. A diagram schematically depicts the expected Fermi surfaces and Cooper pairing, where arrows denote spin direction and pairs are each colored blue or red. Similar diagrams throughout this figure indicate the expectation for pairing and Fermi surfaces as the model parameters change. (C) Randomness at the interface between the quantum well and superconductors may arise due to structural imperfections. The random phase causes superconductivity to weaken as the parallel field increases. (D) For junctions aligned to a principal crystal axis, dominant BIA leads to a pairing wavevector Δk that grows in the x direction as B_x increases. The critical current maxima then occur at increasingly large values of $|B_z|$ as B_x grows. Fabricating devices at varying angles with respect to the crystal is expected to modify the interference when BIA dominates. The region outlined in dashed white corresponds to the measured region in Figure 2.1E. (E) With dominant Zeeman coupling, the pairing magnitude is isotropic in-plane and the interference grows as a hybrid of the SIA and BIA cases. Characteristically, interference fringes repeatedly combine to form the central fringe at each successive node in the parallel field. Additionally, with zero perpendicular field, superconductivity disappears at values of the parallel field that are smaller than the nodal magnetic field in the case with dominant SIA. (F) Including randomness leads to a similar picture to (C), while retaining the combining of fringes characteristic of dominant Zeeman coupling.

a HgTe quantum well, which was found to be consistent with strong SIA and weak BIA[28].

In the limit of overall weak spin-orbit coupling, the order parameter oscillates in both in-plane directions. Zeeman coupling at finite values of B_x leads to two concentric Fermi surfaces with opposite spin polarization so that pairing occurs between surfaces with momentum in all in-plane directions (Figure 2.3E). Increasing the parallel magnetic field causes the interference to both spread in B_z and periodically oscillate, a hybrid of the two above cases. Characteristically, at each node the two interference fringes adjacent to the central fringe combine to form the subsequent central fringe, a direct result of the inability to form nodes in the order parameter along lines of constant y. Although it is possible that this behavior is present in the device with niobium leads, the nodal pattern is more consistent with strong SIA with aluminum leads at high density. In the limit of overall weak spin-orbit coupling, with the random phase χ the modeled interference successfully reproduces many aspects of the behavior observed in the niobium device but is still inconsistent with the aluminum devices (Figure 2.3F).

2.5 Dependence on Carrier Density

As an additional study into the nature of electron pairing momentum, we explore the evolution of the minimum junction resistance at different parallel field B_x values, while energizing the global top gate to modify the bulk electron density. Devices used for these measurements were aligned such that $\theta = \pi/4$, corresponding to the devices of Figure 2.1C,D,F-H. At the most positive gate voltage, as the magnetic field is increased the niobium device displays the narrow node of increased resistance near

$B_x = 0.9$ T (Figure 2.4A). As before, an additional wider node is present near $B_x = 2.7$ T. When the top gate voltage is lowered to -5 V, the field magnitude of the lower node increases, first slowly and then more rapidly. In the device with aluminum leads, a similar nodal structure is observed, with the magnitude of the node weakly increasing as the top gate voltage is lowered from 0.5 V to 0 V (Figure 2.4B).

The dependence of the node magnitude on density can be calculated within the framework of our model based on BHZ theory, here assuming the presence of SIA due to a perpendicular electric field equal to 10 mV/nm (see Section 2.8.1). Since the magnitude of the induced Cooper pair momentum is approximately $\hbar\Delta k \approx \tilde{g}\mu_B B_x/v_F$, the dependence of both $\tilde{g}$ and v_F on the electron density will directly influence the magnitude of the parallel field needed to satisfy the nodal condition $\Delta kW = (2n+1)\pi/2$. Due to the inverted nature of the bands, the g-factors in the conduction bands are expected to evolve from -20.5 toward zero as the Fermi wavevector decreases[37], while the expected magnitudes of the Fermi velocities first decrease slightly and then more rapidly fall to zero (Figure 2.4C, D). With these considerations, we expect the magnitudes of the induced pairing wavevectors at 1 T to fall to zero from values near 1.2/ μm as the Fermi wavevector decreases (Figure 2.4E). As a result, the magnetic field needed to satisfy the nodal condition increases as the electron density decreases, finally diverging at zero electron density (calculated in black dotted lines in Figure 2.4A-B). Although the overall evolution agrees well with the expectation from BHZ theory, we find that our measurements on niobium and aluminum devices respectively yield values of $\tilde{g}/v_F$ that are approximately 1.9 and 1.4 times greater than those expected theoretically (see Section 2.8.1).

Several aspects of the density-dependent data do not fall into the modeling framework discussed

above and are interesting for further consideration. First, we expect that the position of the node associated with induced Cooper pair momentum should occur at higher parallel magnetic fields as the density is reduced, a behavior that we observe only at high density. As the density is further reduced, the magnitude of the nodal field eventually begins to decrease, an element of our model that is not present and remains to be understood but could possibly be explained by a finite g-factor at zero density. Second, in the aluminum device, the region of reduced resistance occurring above the first node appears to be strongest near top gate voltages equal to -0.9 V and 0.5 V. We observe that these two regions of reduced resistance are connected by a region in which the resistance is more weakly reduced, but we have no reason to expect that the reduction in resistance above the first node should vary as the density decreases.

Our measurements demonstrate that a parallel magnetic field can be used both to tune the momentum of Cooper pairs in a material and to clarify the nature of spin-orbit coupling in that material. A major current goal of condensed matter physics is to understand the nature of the superconductivity that results when electron pairing is combined with materials possessing exotic spin textures. Therefore, our new understanding that the superconducting order parameter can be engineered in space may be utilized to investigate spin physics within a broad range of materials including InAs-based quantum wells or the surfaces of three-dimensional topological insulators[65]. Our method to tune the Josephson energy could find additional application in the field of quantum information processing, where direct control of the energy levels in a single superconducting qubit could provide a powerful tool for the investigation and optimization of qubit coherence.

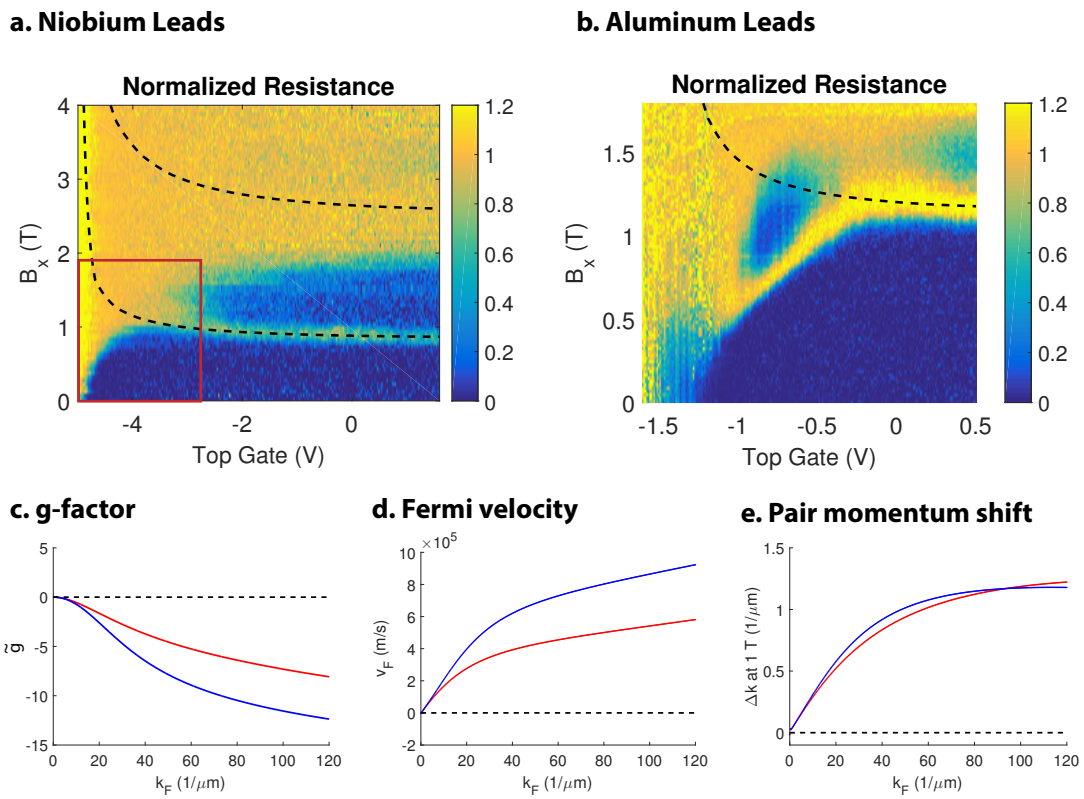

Figure 2.4: The evolution of minimum differential resistance as density and parallel magnetic field B_x vary. Differential resistance measurements are normalized at each point by the normal junction resistance. (A) At the highest gate voltage in the niobium junction, increasing the magnetic field leads to periodic high-resistance nodes separating regions of decreased resistance. As the gate voltage is decreased, the magnetic field at the first node rises to larger values of B_x. (B) The aluminum junction behaves similarly to the niobium junction, although the measurement is limited to a smaller region outlined in red in (A). At low density, the magnitude of the nodal magnetic field begins to decrease as the density is lowered, a feature which remains to be understood. (C) The values of B_x at which we expect nodes to appear are sensitive to the density dependence of both the in-plane g-factors and the Fermi velocities, calculated here assuming that SIA is due to an electric field of 10 mV/nm. Blue and red curves correspond to the inner and outer Fermi surfaces, respectively. As the magnitude of the Fermi wavevector k_F decreases, the in-plane g-factors shift from -20.5 toward zero. (D) Meanwhile, the magnitudes of the Fermi velocities decrease to zero. (E) The pairing momenta induced at 1 T consequently decrease to zero from approximately $1.2/\mu m$. Since there can be no induced momentum at zero density, the nodal magnetic field diverges as the density is lowered. The nodal magnetic field averaged over the two Fermi surfaces is calculated using BHZ theory and plotted as dashed black lines in (A) and (B).

2.6 Device Characteristics and Measurement Details

2.6.1 Wafer characteristics and general measurements

Junctions were fabricated using HgTe/HgCdTe heterostructures grown in the [001] crystal direction (the z direction), composed as shown in Figure 2.5. Wafer I contained an 8 nm quantum well with an electron density of $13.5 \times 10^{11}/\text{cm}^2$ and a mobility of $390,000\ \text{cm}^2/\text{Vs}$. Wafer II contained a 7.8 nm quantum well with an electron density of $2.9 \times 10^{11}/\text{cm}^2$ and a mobility of $790,000\ \text{cm}^2/\text{Vs}$. Josephson junctions fabricated on these wafers were aligned at varying angles with respect to the [110] and $[1\bar{1}0]$ cleavage edges of the crystal, but we do not know which is which in our samples. Therefore, we can only specify that the angular alignment corresponds to a rotation angle θ with respect to the [100] crystal axis, modulo $\pi/2$. Although we do not know which principal axis θ is referenced to experimentally, our model predicts the same results when θ is referenced to either. The x and y-axes always lie respectively perpendicular and parallel to the direction of current flow in devices (see Figure 2.5).

Throughout the remainder of this chapter, devices are referred to in the following manner. Device A was fabricated by depositing aluminum leads onto a mesa etched into Wafer I, and was oriented at an angle $\theta = \pi/4$. Devices B, C, and D were concurrently fabricated by depositing aluminum leads on Wafer II, and were respectively oriented at different angles $\theta = 0, \pi/2$, and $\pi/4$. Device E was fabricated using Wafer I, contained niobium leads, and was oriented at $\theta = \pi/4$. Device F was fabricated using Wafer I, contained aluminum leads, and was oriented at $\theta = \pi/4$.

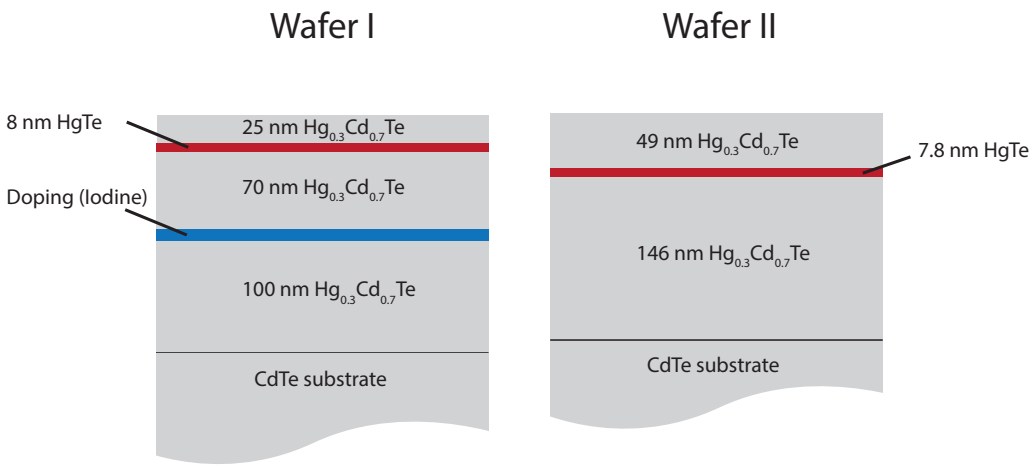

Figure 2.5: Composition of the heterostructures used in the experiment, labeled Wafer I and Wafer II. Both wafers consist of a HgTe quantum well surrounded by barriers of $Hg_{0.3}Cd_{0.7}Te$. In Wafer I, a layer containing iodine dopants lies 70 nm below the quantum well. Both wafers were grown on CdTe substrates, in the [001] crystal direction

Devices were processed as follows. To define the ends of the junctions, mesas 100 nm in height were etched using an argon ion source. To fabricate superconducting contacts, the contact area was etched enough to expose the quantum well using argon milling. Without breaking vacuum, the contact material was then deposited. For devices A-D and F, 5 nm of titanium was deposited by thermal evaporation, followed by thermal evaporation of 15 nm of aluminum. For device E, 10 nm of titanium was deposited by e-beam evaporation, followed by 130 nm of niobium deposited by DC magnetron sputtering. Next, a 50 nm layer of aluminum oxide was grown using atomic layer deposition, to isolate the final top gate layer (10 nm of titanium and 250 nm of gold) from the underlying junctions.

Measurements were performed primarily in a dilution refrigerator outfitted with a 6-1-1 vector magnet capable of applying up to 6 T in one direction, and 1 T in the two remaining directions. Experiments were carried out at the mixing chamber base temperature of 50 mK. Unless otherwise men-

tioned, all measurements occurred in this system. One measurement was performed in a separate dilution refrigerator with a base temperature of 10 mK.

As either the external magnetic field or the top gate voltage was varied, the differential four-terminal resistance of junctions was monitored using standard lock-in techniques. To determine critical currents or to provide bias sufficient to measure the normal resistance of the junctions, sometimes a DC current bias was applied to the junctions. Otherwise, all measurements occurred with no DC current bias.

2.6.2 Characterization of thin aluminum leads

The resistance of thin aluminum leads was characterized as a function of magnetic field in both the x direction and the y direction (Figure 2.6). In each plot, red and blue color coding corresponds to the two leads of a single junction. Different junctions were used in the two plots, demonstrating the consistency of the fabrication process. The critical parallel field of the 15 nm aluminum films was consistently above 1.5 T, in agreement with a previous study of thin aluminum [49]. The data presented in Figure 2.6B was collected at a temperature of 10 mK in the system discussed previously.

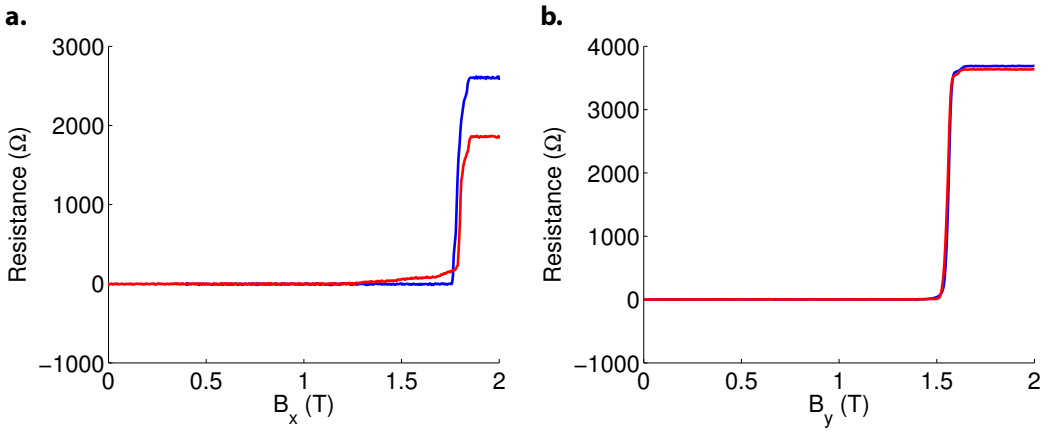

Figure 2.6: Resistances of junction leads as the parallel magnetic field is increased in the x and y directions, for junctions with aluminum leads. The critical field in the plane of the leads is consistently above 1.5 T.

2.7 Further Analysis of the Critical Current

2.7.1 Critical current of a Josephson junction under an external parallel magnetic field

Here we present measurements of the critical current in device D, for different values of the external magnetic field. When compared to corresponding measurements of differential resistance without any applied DC current (Figure 2.8E and Figure 2.2E), it is apparent that both measurement modes reveal the same basic behaviors.

In the measurements of critical current presented here, increasing the external field in either the x or y direction results in a decrease of the maximum critical current (Figure 2.7A, B). This decrease occurs more rapidly for B_y, where the critical current becomes too small to reliably measure when B_y exceeds 0.44 T. B_x, however, must exceed 1.1 T before critical currents become immeasurably small.

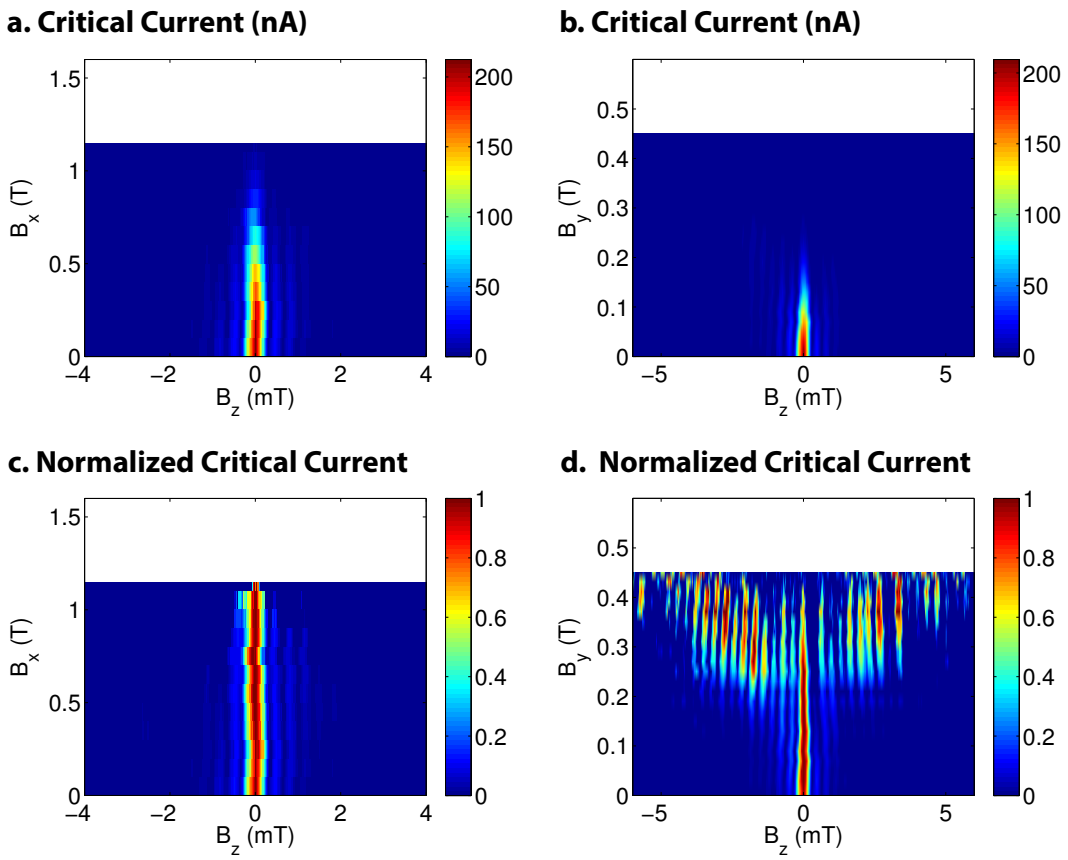

Figure 2.7: The critical current as a function of perpendicular magnetic field B_z, as parallel components of the magnetic field are varied. The data presented here were taken using the device with aluminum leads presented earlier in the chapter (device D). (A, B) As the parallel magnetic field in either the x or y direction is increased, the magnitude of the maximum critical current decreases. This decrease occurs more rapidly in y direction than in the x direction. (C) Normalizing the Fraunhofer interference at each value of B_x shows that the shape of the interference pattern remains essentially unaffected until it becomes immeasurably small. (D) In the B_y direction, normalization reveals a dramatically different behavior of the Fraunhofer interference, where critical current maxima occur at higher values of B_z as B_y is increased. Concurrently, the weight of the critical current at $B_z = 0$ mT decreases to 0. These observations match those deduced through measurements of the differential resistance as the parallel magnetic field varies in either the x or y direction. Therefore, both differential resistance and critical current measurements reflect the same basic phenomenon.

Upon normalization of the interference pattern at each separate value of the parallel field, the asymmetry between the two directions becomes more pronounced (Figure 2.7C, D). At all values of B_x, the shape of the Josephson interference remains essentially unaffected. By contrast, as B_y increases the critical current splits into two separate maxima which occur at larger values of $|B_z|$. In Section 2.8.6, we model the effect of the in-plane field B_y, which we expect to induce a finite x component of the pairing wavevector that grows linearly with B_y. In junctions with finite length and with $B_z = 0$, this pairing momentum in the x direction leads to oscillations in the order parameter which are most pronounced near the ends of the junction. As a consequence, we expect that as B_y increases, the maximum critical currents in our junctions will occur at values of $|B_z|$ that grow linearly with B_y. With only the parallel field B_x present, however, the induced pair momentum is expected to lie along the y direction. In this case, no such wavevector in the x direction is observed.

2.7.2 Josephson Junctions Rotated with Respect to the Crystal

Measurements of the differential resistance were performed on junctions oriented at different angles with respect to the crystal lattice, in order to determine whether bulk inversion asymmetry (BIA) plays a significant role in the momentum acquired by Cooper pairs. As previously mentioned, these devices A-E have orientation $\theta = \pi/4, 0, \pi/2, \pi/4$, and $\pi/4$ respectively. Devices A-D use aluminum leads, while device E uses niobium leads. For each set of the devices, we explored behaviors resulting from a parallel magnetic field applied in the x direction or in the y direction, which in the previous section were shown for device D to differ.

Even as the angle θ varies among devices, the manner in which superconductivity evolves due to

the applied field B_x remains qualitatively unchanged at high density (Figure 2.8). Devices B-D, fabricated on a single piece of wafer, show quantitative agreement in the value of B_x at which a superconducting node appears. Devices A and E were separately fabricated on Wafer I, and show slight quantitative differences but nevertheless the same shape. The appearance of these nodes in the interference evolution, with no dependence on the crystal orientation, signals that structural inversion asymmetry (SIA) dominates the behavior of our quantum wells in the electron-doped regime (see Sections 2.8.1-2.8.4).

With the parallel field applied in the y direction and at high density, the interference pattern splits, forming a 'V' shape as B_y increases that is qualitatively identical for all values of θ (Figure 2.9). The slope of the two arms of the 'V' varies among devices, but it is similar among devices B-D which were fabricated concurrently. The most dramatic effect is seen for device E with 130 nm thick niobium leads, in which the slope is approximately 7 times smaller than the other devices.

From the above measurements, one can conclude that the basic differences in interference as B_x or B_y is increased have little to do with the orientation of the crystal lattice. The most striking difference is found among the data with the magnetic field oriented along the y direction, in which the thickness of the leads correlates to the slope of the interference splitting. This behavior, which results from magnetic flux penetrating the area dL formed by the length L of the junction and the height difference d between the center of the quantum well and the center of the leads, is modeled in Section 2.8.6.

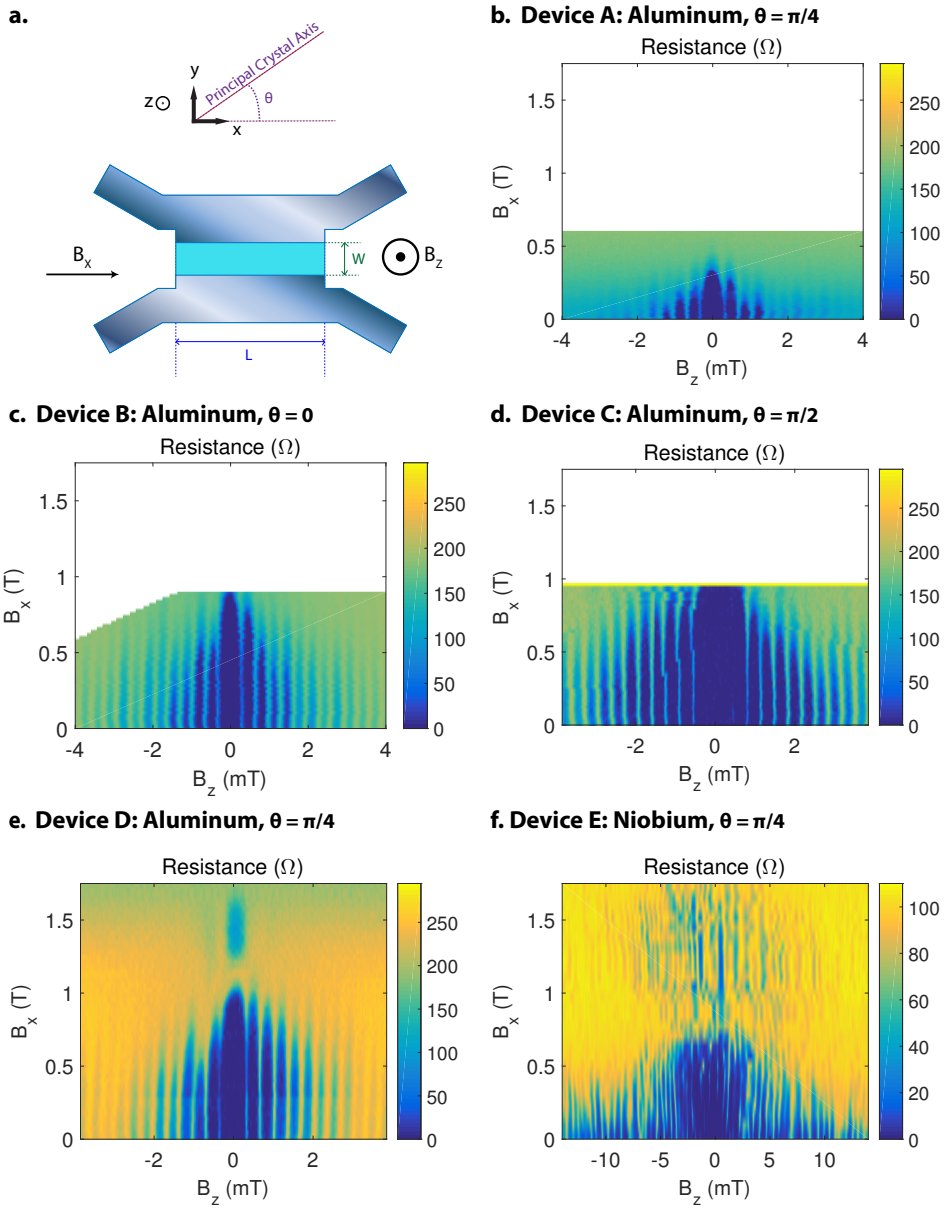

Figure 2.8: Josephson interference as the magnetic field B_x is increased. (A) Junctions were oriented at an angle θ, modulo $\pi/2$, with respect to the [100] axis of the crystal. Devices generating data in (C-E) were concurrently fabricated with respect to the same crystal cleavage edge. Devices in (B) and (F) were separately fabricated. All junctions had aluminum leads except for in (F), where niobium leads were used. (B) For a junction oriented at $\theta = \pi/4$ with respect to the crystal, the differential resistance is monitored as both the perpendicular field B_z and the parallel field Bx is altered. As B_x increases, the position of nodes in the interference pattern does not change, but the interference gradually disappears. (C) A junction oriented at $\theta =$ o and (D) a junction oriented at $\theta = \pi/2$ with respect to the crystal shows qualitatively identical behavior. (E) A further junction aligned at $\theta = \pi/4$ shows the same behavior, as previously presented. (F) The junction with niobium leads is oriented with $\theta = \pi/4$ and shows interference which remains strongly weighted at $B_z =$ o T. The observations on aluminum devices are all consistent with dominant SIA in the quantum well.

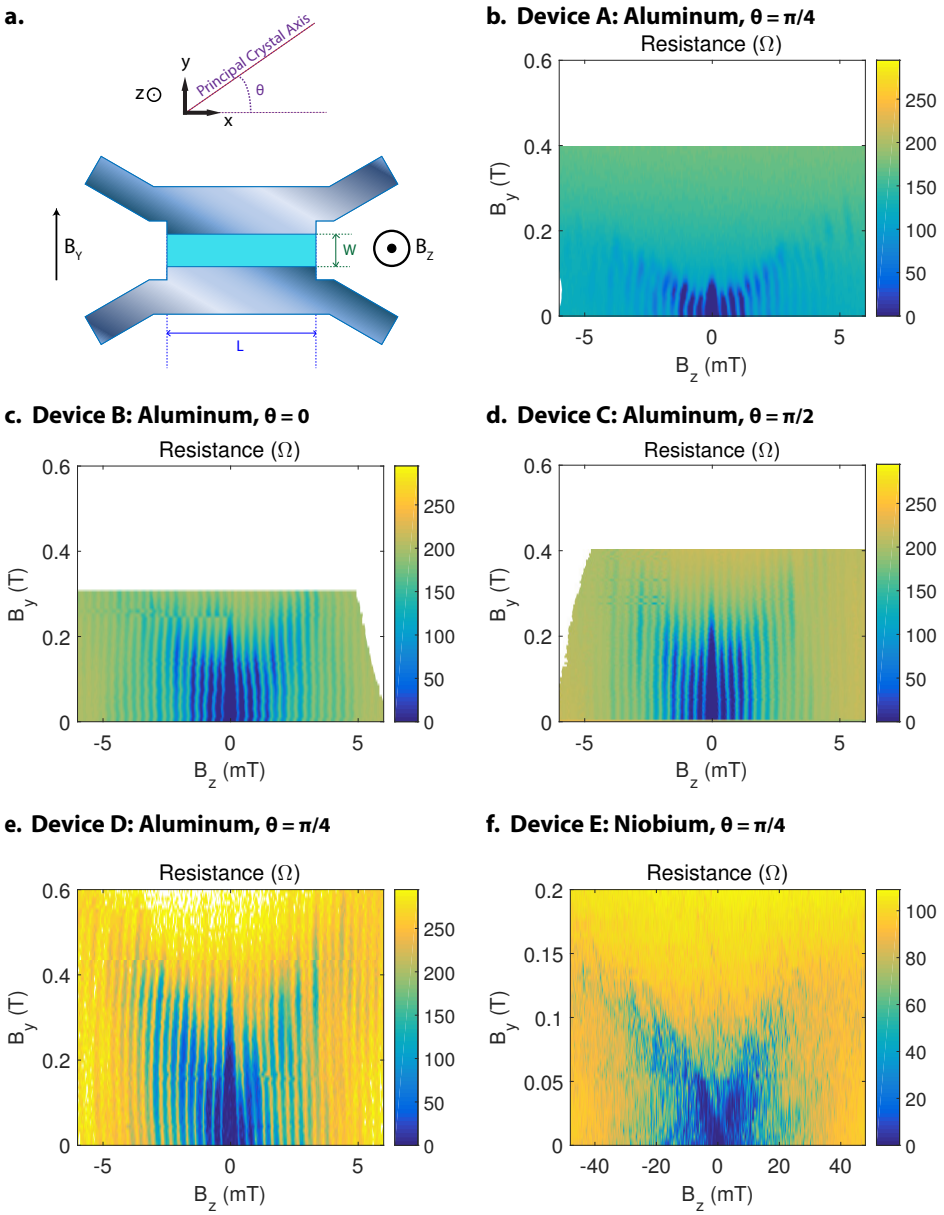

Figure 2.9: Josephson interference as the magnetic field B_y is increased. (A) Junctions were oriented at an angle θ, modulo $\pi/2$, with respect to the [100] axis of the crystal. As in Figure 2.8, devices generating data in (C-E) were concurrently fabricated with respect to the same crystal cleavage edge, and devices in (B) and (F) were separately fabricated. (B) With the junction aligned such that $\theta = \pi/4$, the differential resistance is monitored as a function of the perpendicular field B_z and the parallel field B_y. Increasing B_y rapidly causes the weight of interference fringes to shift to larger B_z values, forming a 'V' shape. The interference evolves more rapidly due to a parallel field in the y direction than in the x direction due to the fact that leads are spatially displaced in z with respect to the quantum well. (C) Orienting a junction at θ = 0 introduces no qualitative change to the behavior, as is also the case with (D) a junction oriented at $\theta = \pi/2$. Junctions with (E) aluminum and (F) niobium leads are presented, also displaying similar behavior. The enhanced scale of B_z in the niobium-based junction is due to the increased thickness of the leads.

2.7.3 Evolution of Interference Lobes as the Parallel Magnetic Field B_x Increases, in a Device with $\theta = \pi/2$

In the previous section, it was observed that at particular values of the parallel magnetic field B_x, nodes of suppressed superconductivity occur in our Josephson junctions. Additionally, this evolution of the Josephson interference with the parallel field B_x does not depend on the device orientation with respect to the crystal. The appearance of nodes with lack of θ dependence already suggests that the effect of bulk inversion asymmetry (BIA) in our devices is small, and that structural inversion asymmetry (SIA) dominates (Sections 2.8.1-2.8.4). Still, the evolution of critical currents, in particular, the maximum critical current of interference lobes occurring at nonzero perpendicular fields, can provide further evidence that BIA is weak. When $\theta = \pi/2$, in the limit of strong BIA these side lobe maximum critical currents are expected to grow as the parallel field B_x is increased from zero (Figure 2.3D). However, if SIA is strong, these critical currents are expected to monotonously decay as the parallel field increases up to the first node.

In Device C, oriented at $\theta = \pi/2$, we study the evolution of the first three sidelobes adjacent to the central lobe (Figure 2.10A). A measurement of the critical currents of these lobes indicates that all lobes are largest when $B_x = 0$ T (Figure 2.10B). We extract the maximum critical current for each side lobe, plotted in Figure 2.10C for each lobe. All critical currents are largest when $B_x = 0$ T, and all decay monotonously until becoming indistinguishable from zero. This evolution of the side lobe critical currents provides additional evidence consistent with weak BIA in our devices.

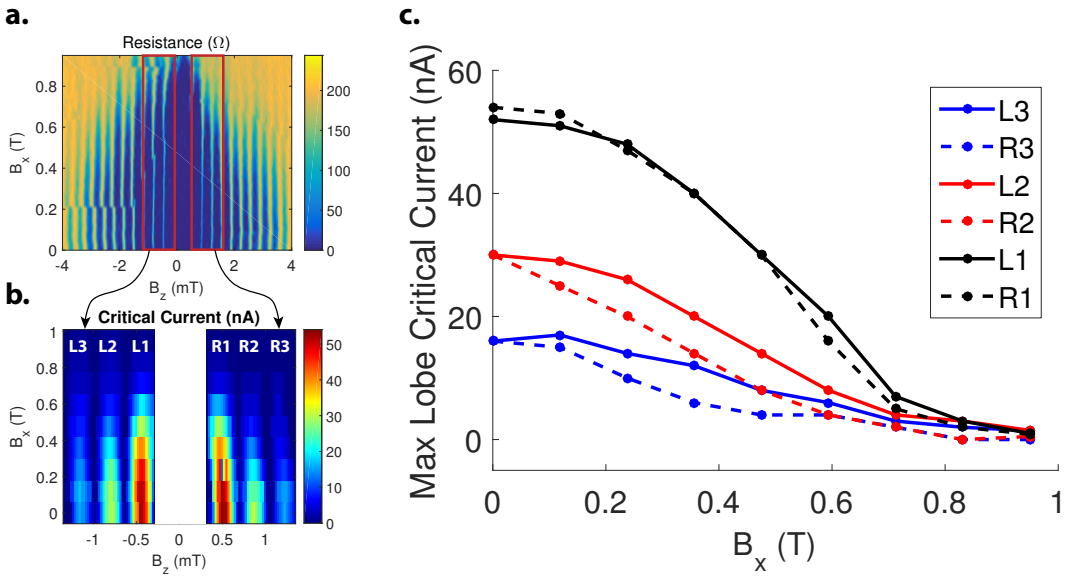

Figure 2.10: Evolution of critical currents, in Device C, oriented such that $\theta = \pi/2$. Data was taken with the top gate voltage set to 0 V. (A) The differential junction resistance, measured with no applied DC current, evolves consistently with the absence of BIA in the device. (B) The critical currents in the interference side lobes adjacent to the central lobe decay as the parallel field B_x increases from zero. The region of the critical current measurement is outlined in red in (A). Each side lobe is labeled in white. (C) The extracted maximum critical current for each side lobe. Within each lobe, the critical current decreases from its maximum value at $B_x = 0T$.

2.8 Theoretical Model of the Effects of Spin-Orbit Coupling on the Pair Propagator

2.8.1 Four-Band Model and Spin-Orbit Effects in the Quantum Well

A four-band model has been developed starting from k·p theory, and subsequently used to describe the topology of HgTe quantum wells[8]. Here we adopt an elaboration on this model, where bulk inversion asymmetry (BIA), structural inversion asymmetry (SIA), and coupling to an external magnetic field are included. The four bands originate in the *s*- and *p*-like bands of the underlying crystals, so that the basis states are written as $\left|E1, m_J = +1/2\right\rangle$, $\left|H1, m_J = +3/2\right\rangle$, $\left|E1, m_J = -1/2\right\rangle$, and $\left|H1, m_J = -3/2\right\rangle$. In this notation, $E1$ refers to electron-like states with angular momentum $1/2$, while $H1$ refers to hole-like states with angular momentum $3/2$. The Hamiltonian describing the system is then[62,70,37]:

$$\begin{aligned} H_1 = \quad & \varepsilon\left(\hat{k}^2\right) + M\left(\hat{k}^2\right) s_z + A\hat{k}_x s_x \sigma_z - A\hat{k}_y s_y + h\left(\cos(2\theta^{th})\sigma_y + \sin(2\theta^{th})\sigma_x\right) s_y \\ & + R_0 \tfrac{s_z+1}{2}\left(\hat{k}_x\sigma_y - \hat{k}_y\sigma_x\right) - \mu_B \cdot \vec{B} \cdot \vec{M} \end{aligned} \tag{2.9}$$

where

$$\varepsilon\left(\hat{k}^2\right) = C - D\left(\hat{k}_x^2 + \hat{k}_y^2\right), M\left(\hat{k}^2\right) = M - B\left(\hat{k}_x^2 + \hat{k}_y^2\right) \tag{2.10}$$

and

$$M_x = \begin{pmatrix} & g_{||} \\ g_{||} & \end{pmatrix}, M_y = \begin{pmatrix} & -ig_{||} \\ ig_{||} & \end{pmatrix}, M_z = \begin{pmatrix} g_{E\perp} & & & \\ & g_{H\perp} & & \\ & & -g_{E\perp} & \\ & & & -g_{H\perp} \end{pmatrix}. \quad (2.11)$$

The first four terms are those present in the original theory of Bernevig, Hughes, and Zhang. The fifth term describes the magnitude h of the BIA and the angle θ^{th} between the x axis and the [100] crystal direction. The sixth term includes SIA with strength $R_0/(e\mathcal{E})$, where $\mathcal{E}$ is the magnitude of an electric field oriented along the z axis. Coupling to the external magnetic field occurs anisotropically and is different for $E1$ and $H1$ states due to the inability of the magnetic field to couple $m_J = \pm 3/2$ to first order. The value of the parallel g-factor $g_{||}$ and perpendicular g-factors $g_{E\perp}$ and $g_{H\perp}$, along with all other parameter values, are listed in Table 2.1. The in-plane wavevectors are $\hat{k}_x = i\partial_x$ and $\hat{k}_y = i\partial_y$.

The bare effect of a parallel magnetic field is visualized by setting $h = 0$ and $R_0 = 0$ and calculating the conduction band spectrum, under various values of $\vec{B}$ (Figure 2.11A-C). In each plot, the bands are plotted up to the Fermi energy, which varies in order to demonstrate various limiting cases of weak or strong spin-orbit coupling. The Fermi surfaces are projected onto a plane below the bands, with the spin texture plotted at various points on the Fermi surfaces. The x and y components of the spin vectors are equal respectively to $\langle \sigma_x (1 + s_z)/2 \rangle$ and $\langle \sigma_y (1 + s_z)/2 \rangle$, the spin expectation values projected onto the $E1$ bands.

With no external magnetic field, the conduction band is doubly degenerate due to the presence

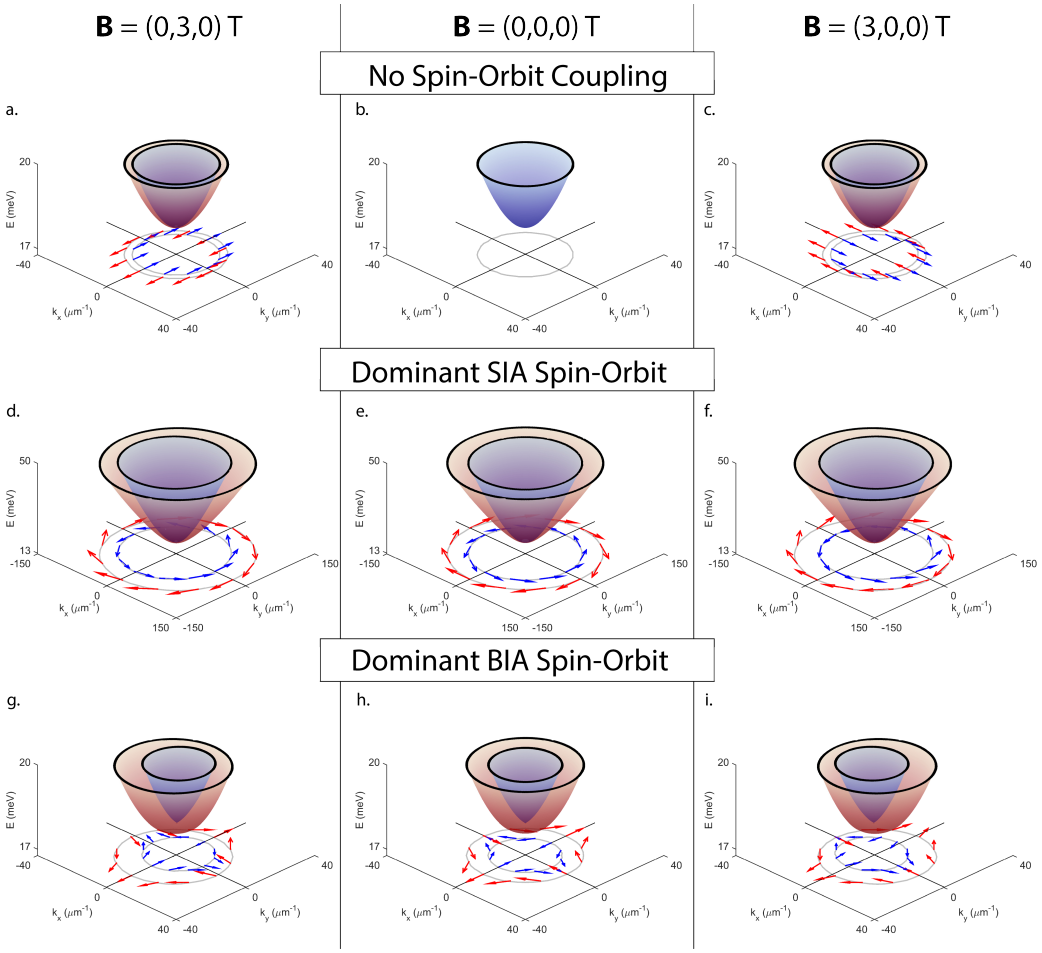

Figure 2.11: Modeling of the conduction band structure under various spin-orbit and parallel magnetic field conditions. (A-C) When the spin-orbit coupling is absent, the addition of a 3 T parallel magnetic field simply polarizes spins in a direction determined by the sign of the in-plane g-factor, $g_{||}$. With no external magnetic field, the two spin bands are degenerate (B). (D-F) Dominant structural inversion asymmetry causes axially symmetric spin-splitting to occur at finite momentum (E). This type of spin-orbit coupling causes the bands to shift orthogonally to the external magnetic field (D, F), leading to nonzero Cooper pair momentum in the shift direction. (G-I) Dominant bulk inversion asymmetry with $\theta^{th} = 0, \pi/2$ acts oppositely to structural inversion asymmetry so that external magnetic fields cause bands to shift parallel to the external magnetic field. This type of shift is not observed experimentally in our devices.

of the spin degree of freedom, modeled here up to a Fermi energy equal to 20 meV. Changing the magnetic field to 3 T in the x direction lifts this degeneracy due to the Zeeman effect, resulting in two concentric Fermi surfaces centered at $\vec{k} = 0$. Within the outer Fermi surface, spins point toward $-x$, due to the negative value of $g_{||}$. Within the inner Fermi surface, spins are oppositely oriented. Application of a 3 T magnetic field in the y direction identically splits the bands, although the spins in this case orient along $\pm y$. It can be seen that with no spin-orbit coupling and an applied in-plane magnetic field, pairs may form with nonzero wavevector in any in-plane direction.

$A(eV \cdot A)$	$B(eV \cdot A^2)$	$D(eV \cdot A^2)$	$M(eV)$	$h(eV)$	θ^{th}	$R_0/(e\mathcal{E})(\text{nm}^2)$	$\mathcal{E}$ (mV/nm)	$g_{E_\perp}$	$g_{H_\perp}$	$g_{\|\|}$
3.645	−68.6	−51.2	−0.010	0, 0.0016	0	−15.6	0, 10	22.7	−1.21	−20.5

Table 2.1: List of parameters used to model the band structure. Parameters correspond to a quantum well in the inverted regime, with a well width of 70 Å.

Including dominant SIA (equivalent to a perpendicular electric field of 10 mV/nm) with no BIA modifies the expectation for the band structure (Figure 2.11D-F). Even without any external magnetic field, in this case the bands are spin-split for all nonzero wavevectors. The axial symmetry of the spin-orbit coupling results in the spin texture shown in Figure 2.11E, modeled up to a higher Fermi energy of 50 meV to highlight the regime of strong SIA. Now coupled with an external magnetic field, these factors result in a behavior that is different from the case with no spin-orbit coupling. When a magnetic field is applied in the x (y) direction, the two Fermi surfaces shift oppositely in the y (x) direction. Consistent with our observations on aluminum-based junctions in the electron-doped regime, this shift implies that a magnetic field in the x direction introduces a pairing wavevector in the y direction. Also superficially consistent with our data, a magnetic field in the y direction leads to a

pairing wavevector in the x direction. However, the magnitude of this wavevector alone is too small to explain the experimental evolution of interference as B_y is increased. A full explanation of this effect is presented in Section 2.8.6. Finally, the lack of dependence of SIA on the angle θ^{th} is consistent with our measurements (Figures 2.8 and 2.9).

In the remaining case, the effect of dominant BIA with no SIA is investigated in Figure 2.11G-I, for an angle $\theta^{th} = 0$ and up to a Fermi energy of 20 meV. Similarly to the case of strong SIA, with no external magnetic field present, the bands are spin-split at nonzero wavevectors. However, the texture of spins at the Fermi surfaces displays tetrahedral symmetry in this case. As a result, when a parallel magnetic field is present in the x (y) direction, the two Fermi surfaces shift oppositely in the x (y) direction. This shifting is orthogonal to the shifts present with strong SIA and does not agree with our interference measurements on devices aligned with $\theta = 0$ or $\pi/2$. Furthermore, the shift direction rotates by $\pi/2$ as the angle θ^{th} becomes $\pi/4$. This prediction that the direction of induced Cooper pair momentum should depend on θ^{th} is also inconsistent with our results.

Finally, we model the evolution with density of the in-plane g-factor $\tilde{g}$, the Fermi velocity v_F, and the pair momentum shift $\Delta k \approx \tilde{g}\mu_B B_x/\hbar v_F$, under the assumption that BIA is absent and SIA is dominant (equivalent to a perpendicular electric field of 10 mV/nm). At each density, a particular value of the magnetic field satisfies the condition $\Delta k W = \pi/2$, leading to a node in the induced superconductivity in the junction. We find that the evolution with density of this nodal magnetic field value agrees with our model at high densities. In niobium and aluminum devices respectively, the value of the nodal magnetic field is consistent with values of $\tilde{g}/v_F$ that are approximately 1.9 and 1.4 times greater than those expected theoretically. Using different values for the electric field only weakly

modifies this conclusion. For example, if the SIA was instead equivalent to a perpendicular electric field of 40 mV/nm, we would find values of $\tilde{g}/v_F$ approximately 2.1 and 1.5 times greater than the theoretical expectation, only a $\sim 10\%$ difference.

2.8.2 Model of a Two-Dimensional Electron Gas Contacted by Superconducting Leads

In the following sections, we model the coupling of superconducting leads to our quantum well. We consider a geometry in which a two-dimensional electron gas (2DEG) is contacted by a pair of superconducting leads with a controlled phase difference between them, and we seek to calculate the maximum supercurrent that can be carried between the strips. The following is a more detailed derivation of the pair propagator F used earlier in this chapter to carry out this goal. We assume a Hamiltonian $H = H_0 + H_2$, where H_0 is the Hamiltonian for the 2DEG in the absence of the superconductor, and H_2 is the coupling between the superconductors and the 2DEG, described by a pairing Hamiltonian of the form

$$H_2 = -\int dxdy \left[\Delta(x,y)\Psi^\dagger(x,y) + \Delta^*(x,y)\Psi(x,y)\right]. \tag{2.12}$$

Here $\Psi(x,y) \equiv \psi_\uparrow(x,y)\psi_\downarrow(x,y)$ is an operator which annihilates a singlet pair of electrons in the 2DEG at the point (x,y), while the pair potential $\Delta(x,y)$ is a complex number that depends on the phase of the superconductor and the tunneling amplitude at that point.

We assume that the contacts between the 2DEG and the superconductors occur at the edges of the

superconductors, located at $y = 0$ and $y = W$, so that we may write

$$\Delta(x, y) = \lambda_1(x)\delta(y) + \lambda_2(x)\delta(y - W) \equiv \Delta_1(x, y) + \Delta_2(x, y), \tag{2.13}$$

with $-L/2 < x < L/2$. We assume that the magnitude of the coupling is constant along each lead, but the phase will vary if there is a perpendicular magnetic field $B_z \neq 0$. We choose a gauge where the vector potential points in the x direction, with $A_x = -B_z(y - W/2)$, so that the vector potential vanishes along the midline of the 2DEG. If the superconducting strips have identical widths W_{SC}, then the couplings λ_j will have the form

$$\lambda_j(x) = \left|\lambda_j\right| e^{2\pi i \varphi_j(x)}, \tag{2.14}$$

$$\varphi_j(x) = \varphi_j(0) + \frac{(-1)^{j-1} x B_z (W + W_{sc})}{2\Phi_0}, \tag{2.15}$$

with $j = 1, 2$. The phases in equation (2.7) are determined by the condition that there should be no net current flow along the length of the superconducting strips, so the phase gradient in each superconductor should be canceled by the vector potential along the center line of the superconductor.

We assume that B_z is sufficiently weak that the cyclotron radius $R_c = \hbar k_F / eB_z$ is large compared to W (typically in our devices $R_c \approx 10\ \mu$m, which is large compared to $W = 800$ nm). In this case, we may ignore the effect of B_z on the trajectories of electrons in the 2DEG. Moreover, since we have chosen the vector potential to vanish along the midline of the 2DEG, an electron crossing from $y = 0$

to $y = W$ will acquire no net phase due to the vector potential. We also ignore, for the moment, any orbital effects of the parallel field $B_{||}$. Thus the 2DEG Hamiltonian H_0 will include the Zeeman coupling to $B_{||}$, as well as the spin-orbit coupling, but will not include terms due to the magnetic field in the kinetic energy.

To lowest order in the pairing Hamiltonian H_2, the portion of the total energy that depends on the phase difference between the two superconducting leads can be written in the form:

$$E = -\int dx_2 \left[\lambda_2^*(x_2) \left\langle \Psi(x_2, W)\right\rangle_1 + c.c.\right], \tag{2.16}$$

where $\left\langle \Psi(x,y)\right\rangle_1$ is the order parameter at point (x,y) induced by the superconductor $j = 1$. In turn, this may be written in the form

$$\left\langle \Psi(x,y)\right\rangle_1 = \int dx_1 \lambda_1(x_1) F(x, x_1, y), \tag{2.17}$$

where F is the propagator from point $(x_1, 0)$ to point (x,y) for an induced Cooper pair. We will determine the form of F in the following section.

As a first approximation, we may ignore the fact that there are boundaries of the 2DEG at $x = \pm L/2$ and that electrons will be reflected at these boundaries (either specularly or diffusely, and possibly with a spin flip). Similarly, we ignore the possibility of single-particle reflection at $y = 0$ or $y = W$, where the superconducting leads touch the 2DEG. Furthermore, we assume that the electron density is constant in the 2DEG, and we ignore any interactions between electrons in the 2DEG. We also ignore scattering by impurities inside the 2DEG. Then the propagator F may be calculated for an

infinite, translationally invariant 2DEG, where the momentum of each electron is a good quantum number. We believe that corrections due to reflections at the boundaries will have quantitative effects but will not affect qualitatively the form of our results. Modeling of critical current including specular reflections at mesa edges will be discussed in Section 2.8.5 and 2.8.5.

2.8.3 Derivation of a General Formula for the Pair Propagator F

The four-band model Hamiltonian H_1 for our quantum wells was previously discussed. Since we presently are interested in behavior near the Fermi energy E_F, and within the conduction bands only, in the following, we adopt a simplified two-band model Hamiltonian. This Hamiltonian for an electron in the 2DEG with momentum $\vec{k}$ is given by the 2×2 matrix

$$H_{\vec{k}}^{\circ} = v_F(k - k_F) + \vec{\beta}(\hat{k}) \cdot \vec{\sigma}, \tag{2.18}$$

$$\beta_j = \tilde{g}\mu_B B_j/2 + \hat{k}_i S_{ij}, \tag{2.19}$$

where B_j are the x and y components of the in-plane magnetic field, $\tilde{g}$ is an effective g-factor, $\hat{k} \equiv \vec{k}/k$, and $\hat{k}_i S_{ij}\sigma_j$ is the spin-orbit coupling term, which we assume to be small compared to the Fermi energy. We have here assumed a single electron band and assumed that band structure is isotropic in the absence of spin-orbit coupling. We can then write

$$H_{\vec{k}}^{o} = \sum_{\eta} \varepsilon_{\vec{k}\eta} P^{\hat{k}\eta}, \tag{2.20}$$

with $\eta = \pm 1$. Here $\varepsilon_{\vec{k}\eta}$ are the two eigenvalues, and $P^{\hat{k}\eta}$ are projection matrices given by

$$\varepsilon_{\vec{k}\eta} = v_F(k - k_F) + \eta \left|\vec{\beta}\right|, P^{\hat{k}\eta} = (1 + \eta\hat{\beta}\cdot\vec{\sigma})/2, \tag{2.21}$$

with $\hat{\beta} \equiv \vec{\beta}/\left|\vec{\beta}\right|$. We next define a 2×2 matrix function

$$g(\vec{r}, \varepsilon) \equiv \frac{1}{(2\pi)^2} \sum_{\eta} \int d^2k e^{i\vec{k}\cdot\vec{r}} \delta(\varepsilon - \varepsilon_{\vec{k}\eta}) P^{\hat{k}\eta}. \tag{2.22}$$

Then, letting $\vec{r} = (x - x_1, y)$, the pair propagator $F(x, x_1, y)$ may be expressed as

$$F(\vec{r}) = \int_o^\infty d\varepsilon \int_o^\infty d\varepsilon' \frac{\mathrm{tr}\left[g(\vec{r}, \varepsilon)\sigma^y g^T(\vec{r}, \varepsilon')\sigma^y + g(\vec{r}, -\varepsilon)\sigma^y g^T(\vec{r}, -\varepsilon')\sigma^y\right]}{2(\varepsilon + \varepsilon')}, \tag{2.23}$$

where T indicates the matrix transpose.

We are interested in the situation where $k_F r \gg 1$, and $|\varepsilon| \ll E_F$. Then the integration over the direction of $\vec{k}$ is dominated by regions close to the end points where $\vec{k}$ is either parallel or antiparallel to $\vec{r}$, and the expression for $g(\vec{r}, \varepsilon)$ may be approximated by

$$g(\vec{r}, \varepsilon) \approx \frac{k_F^{1/2}}{(2\pi)^{3/2} v_F r^{1/2}} \sum_{\eta} \left[e^{ik_F r} e^{i\varepsilon r/v_F} e^{-i\pi/4} e^{-i\delta k_\eta^+ r} P^{\eta +} + e^{-ik_F r} e^{-i\varepsilon r/v_F} e^{i\pi/4} e^{i\delta k_\eta^- r} P^{\eta -}\right] \tag{2.24}$$

where $P^{\eta\pm}$ is equal to $P^{\hat{k}\eta}$, with $\hat{k} = \pm\hat{r} \equiv \pm\vec{r}/r$ and

$$\delta k_\eta^\pm = \frac{\eta \left|\vec{\beta}(\pm\hat{r})\right|}{v_F}. \tag{2.25}$$

When we substitute the expression for g in formula (2.23) for $F(\vec{r})$, we may ignore the terms proportional to $e^{\pm 2ik_F r}$, as these rapidly oscillating terms will give vanishing contribution to the energy if the width of the contacts between the 2DEG and the superconducting strips are large compared to $1/k_F$. Performing the integrals over ε and ε' in the remaining terms, one obtains the result

$$F(\vec{r}) \approx \frac{C}{r^2} \sum_{\eta\eta'} N_{\eta\eta'}(\hat{r}) e^{-i\left(\delta k_\eta^+ - \delta k_{\eta'}^-\right) r}, \tag{2.26}$$

with $C = k_F/(8\pi^2 v_F)$, and

$$N_{\eta\eta'}(\hat{r}) = N_{\eta\eta'}(-\hat{r}) = \frac{1 - \eta\eta'\hat{\beta}(\hat{r}) \cdot \hat{\beta}(-\hat{r})}{2}. \tag{2.27}$$

2.8.4 Special Cases and Limiting Forms of the Pair Propagator

Here we discuss several special cases which lead to limiting forms for the pair propagator $F(\vec{r})$. The above expressions (2.26) and (2.27) may be simplified in the limit where the Zeeman energy is small compared to the spin-orbit energy splitting. When $B_{||} = 0$, we find that $\hat{\beta}(\hat{r}) = -\hat{\beta}(-\hat{r})$, so that $N_{\eta\eta'} = \delta_{\eta\eta'}$. Furthermore, when $\eta = \eta'$, we see that the exponent in equation (2.26) is equal to zero, so F will have no oscillations as a function of r. If $B_{||}$ is nonzero but still small compared to the spin-orbit splitting, it remains a good approximation to set $N_{\eta\eta'} = \delta_{\eta\eta'}$. In the exponent, however, we

have

$$\left(\delta k_\eta^+ - \delta k_\eta^-\right) = \eta \tilde{g} \mu_B \vec{B}_{||} \cdot \vec{\beta}(\vec{r}). \tag{2.28}$$

An important example is the case of pure SIA spin-orbit coupling, where the matrix S has the Rashba form, $S \propto i\tau^y$, where τ^y is a Pauli matrix. In this case, we may write

$$\left(\delta k_\eta^+ - \delta k_\eta^-\right) r = \eta \Delta\vec{k} \cdot \vec{r} \tag{2.29}$$

with

$$\Delta\vec{k} = \hat{z} \times \vec{B}_{||} \tilde{g} \mu_B / v_F. \tag{2.30}$$

The oscillations in $F(\vec{r})$ have a simple interpretation in this case. When $B = 0$, the Fermi surface consists of two circles centered about the origin, split by the spin-orbit coupling, with spin orientations shown in Figure 2.3b. Applying a weak in-plane magnetic field will shift the two Fermi circles in opposite directions, by amounts $\pm\Delta\vec{k}/2$. The function $F(\vec{r})$ describes the propagator when a singlet pair of electrons is injected at one point and removed at a second point, separated by $\vec{r}$. For large separations, $F(\vec{r})$ is dominated by pairs of electrons that are close to the Fermi energy, with wave vectors opposite to each other and parallel or antiparallel to $\vec{r}$. Because the two electrons must have opposite spins, they must belong to the same branch of the Fermi surface. Thus, the induced pairs will have total momenta equal to $\pm\Delta\vec{k}$, depending on the branch η. The momentum shifts are manifest in the

phase factors $e^{i\eta\Delta\vec{k}\cdot\vec{r}}$, which appear in $F(\vec{r})$ in this case.

In the case of pure BIA coupling, the matrix S is $\propto \tau^z$, in our coordinate system. We may again write the phase accumulation in the form (2.29), but now the direction of $\Delta\vec{k}$ depends on the directions of $\vec{B}_{||}$ relative to the crystal axes.

The formula for $F(\vec{r})$ also becomes simple in the case where the Zeeman energy is large compared to the spin-orbit splitting. In this case, the Fermi surface consists of two concentric circles, with spins that are uniformly aligned on each circle, either parallel or antiparallel to $\vec{B}_{||}$. In order to form a spin singlet, we must choose one electron from each Fermi circle. If we also require that the momenta be parallel or antiparallel to $\vec{r}$, we see that the induced electron pair will have a total momentum equal to $\pm\hat{r}\tilde{g}\mu_B B_{||}/v_F$. Thus we should find that the phase shift is independent of the direction of $\vec{r}$.

These expectations may be confirmed using the formulas derived above. In the case where the Zeeman energy is large compared to the spin-orbit splitting, we find that $\vec{\beta}(\hat{k})$ is independent of $\hat{k}$, and thus $N_{\eta\eta'} = \delta_{\eta,-\eta'}$. Furthermore, $\delta k_\eta^+ - \delta k_{-\eta}^- = \eta\tilde{g}\mu_B B_{||}/v_F$, independent of $\vec{r}$.

2.8.5 Reflections from the Sample Edges

Taking into account the effects of electron reflections from the ends of the sample, at $x = \pm L/2$, we should rewrite the propagator F in a more general form as

$$F(x_2, x_1, W) = F_0(\vec{r}) + F_1\left[\left(x_2 + \frac{L}{2}\right), \left(x_1 + \frac{L}{2}\right), W\right] + F_2\left[\left(\frac{L}{2} - x_2\right), \left(\frac{L}{2} - x_1\right), W\right], \tag{2.31}$$

where F_0 is the function given by equation (2.26) for the infinite system, $\vec{r} = (x_2 - x_1, W)$, as before, and F_1 and F_2 describe the contributions of electrons reflected from the left boundary or right boundary respectively. We assume that the length L is long enough that we can neglect the effects of electrons that scatter multiple times from opposite boundaries. Here we will assume that the boundaries at $x = \pm L/2$ are represented by infinite potential barriers, which are perfectly smooth so that electrons are specularly reflected with no change in spin. The symmetry of our problem will then be such that F_1 and F_2 have identical functional forms, so we need only find the form of F_1. For convenience, we move the left boundary to the line $x = 0$, and we assume that the right boundary is located at $x = \infty$. Using similar reasoning to what we used in the translationally invariant case, we may write F_1 in the form

$$F_1(x_2, x_1, W) = \int_0^\infty d\varepsilon \int_0^\infty d\varepsilon' \frac{\mathrm{tr}\left[h(x_2, x_1, W, \varepsilon)\sigma^y h^T(x_2, x_1, W, \varepsilon')\sigma^y + c.c.\right]}{2(\varepsilon + \varepsilon')} \tag{2.32}$$

where

$$\begin{aligned} h(x_2, x_1, W, \varepsilon) = -\frac{k_F^{1/2}}{(2\pi)^{3/2} v_F s^{1/2}} \sum_{\eta_1, \eta_2} [& e^{ik_F s} e^{i\varepsilon s/v_F} e^{-i\pi/4} e^{-i(\delta k^+_{1,\eta_1} s_1 + \delta k^+_{2,\eta_2} s_2)} P_1^{\eta_1 +} P_2^{\eta_2 +} + \\ & + e^{-ik_F s} e^{-i\varepsilon s/v_F} e^{i\pi/4} e^{i(\delta k^-_{1,\eta_1} s_1 + \delta k^-_{2,\eta_2} s_2)} P_1^{\eta_1 -} P_2^{\eta_2 -}], \end{aligned} \tag{2.33}$$

where $s = [(x_1 + x_2)^2 + W^2]^{1/2}$, $s_1 = s x_1/(x_1 + x_2)$, $s_2 = s - s_1$, and

$$\delta k_{j,\eta}^{\pm} = \frac{\eta \left| \vec{\beta}(\pm \hat{k}_j) \right|}{v_F}, \tag{2.34}$$

for $j = 1, 2$, with

$$\hat{k}_1 = -\frac{[(x_1 + x_2), -W]}{s}, \hat{k}_2 = \frac{[(x_1 + x_2), W]}{s}. \tag{2.35}$$

s

Furthermore, we have

$$P_j^{\eta\pm} = (1 + \eta\hat{\beta}(\pm\hat{k}_j) \cdot \vec{\sigma})/2. \tag{2.36}$$

We now turn to one particular example. In order to evaluate the expression (2.32) for F_1, we must first evaluate the trace over a product of projection matrices and σ^y. In the case of strong SIA coupling and weak magnetic field, the trace simplifies, and we obtain the result

$$\mathrm{tr}\left[P_1^{\eta_1 +} P_2^{\eta_2 +} \sigma^y \left(P_1^{\eta_3 -} P_2^{\eta_4 -}\right)^T \sigma^y\right] = \delta_{\eta_1\eta_3}\delta_{\eta_2\eta_4}\left[\sin^2\theta\delta_{\eta_1\eta_2} + \cos^2\theta\delta_{\eta_1,-\eta_2}\right], \tag{2.37}$$

where $\sin\theta = W/s$. Furthermore for $B_{||}$ in the y direction, we find

$$(\delta k_{j,\eta}^{+} - \delta k_{j,\eta}^{-})s_j = (-1)^j \eta x_j \frac{\tilde{g}\mu_B B_y}{v_F}. \tag{2.38}$$

Thus, in the case of strong SIA and $B_{||}$ in the y direction, we find

$$F_1(x_2, x_1, W) = \frac{2C\left[\sin^2\theta\cos\Delta k(x_1 - x_2) + \cos^2\theta\cos\Delta k(x_1 + x_2)\right]}{(x_1 + x_2)^2 + W^2}, \tag{2.39}$$

where $\Delta k = \tilde{g}\mu_B B_y / v_F$, and the constant C is the same as in equation (2.26).

2.8.6 Modeling Josephson Interference

Using the pair propagator $F(\vec{r})$ and equation (2.16), we can calculate the Josephson energy and critical current for our junctions. In the limit of either strong BIA or strong SIA, the Cooper pair momentum shift occurs at an angle a with respect to the x axis and the pair propagator is

$$F(x_2, x_1, W) = \frac{k_F}{8\pi^2 v_F} \cdot \frac{e^{i\gamma} + e^{-i\gamma}}{(x_2 - x_1)^2 + W^2}, \gamma = \Delta k\left(\sin(a)W + \cos(a)(x_2 - x_1)\right). \tag{2.40}$$

As previously noted, in this case, pairing occurs internally to each Fermi surface. In the limit of weak spin-orbit coupling, the pair propagator instead takes the form

$$F(x_2, x_1, W) = \frac{k_F}{8\pi^2 v_F} \cdot \frac{e^{i\gamma} + e^{-i\gamma}}{(x_2 - x_1)^2 + W^2}, \gamma = \Delta k\sqrt{W^2 + (x_2 - x_1)^2}. \tag{2.41}$$

Due to the opposite spin polarization of the two Fermi surfaces, pairing in this limit is expected to occur between Fermi surfaces, in contrast to the limit of large spin-orbit coupling.

The Josephson energy E is obtained in each limit by evaluating equation (2.16). By differentiating the Josephson energy with respect to the phase difference $\varphi_1(0) - \varphi_2(0)$ we find the current-phase

relation of the junction, which is then maximized with respect to the phase difference to obtain the critical current.

Previously, we consider only a parallel field along the x direction, and we model the effect of structural imperfections in the interface between the superconducting leads and the quantum well. These would introduce random fluctuations in the direction of the in-plane magnetic field at each interface, leading to a random component of the pairing momentum in the x direction that grows linearly with the in-plane field. Hence, we introduce a random phase $\chi \propto (R_1(x_1) - R_2(x_2))\, B_x$, where the random variables $R_1(x_1)$ and $R_2(x_2)$ correspond to fluctuations in the direction of the parallel field at each interface. The modeled step size in x is 40 nm, with no correlations between adjacent positions. The random phase χ is uniformly distributed between zero and an upper bound whose absolute magnitude is equal to 15% of the maximum phase generated by the intrinsic momentum. With this randomness, the calculated critical currents diminish in magnitude as the in-plane field increases, and nodes occur over a larger range of in-plane field, in agreement with the experimental observation (shown in Figure 2.3C for the case of dominant SIA).

In general, the parallel field $\vec{B}_{||}$ can be oriented anywhere in the plane, which modifies a accordingly in the case that spin-orbit coupling is strong. Additionally, loosening the constraint that $\vec{B}_{||}$ lie parallel to x introduces an artifact wavevector $q_x \approx 2\pi B_{||} \sin(\beta) d/\Phi_o$, where d is the height difference between the centers of the quantum well and of the superconducting leads, and β is the angle between the parallel magnetic field and the x axis. This additional phase arises due to the magnetic flux penetrating the area dL formed between the leads and the quantum well due to this height difference. Importantly, no flux penetrates this area when the parallel component of the magnetic field is only in

the x direction so that in this case the pair momentum is solely determined by the Zeeman coupling and the spin-orbit coupling.

The behavior of Josephson interference in our devices essentially involves different mechanisms when the parallel magnetic field lies in the x or y direction. With the above modeling, it is clear that this difference is due to the dependence of q_x on the magnetic field angle β, so that the data for the magnetic field B_y reflects primarily the difference in height between the superconducting leads and the quantum well. Since we cannot entirely rule out either dominant Zeeman coupling or dominant SIA, we model both possibilities for this field direction. With dominant SIA and the height difference d set to either 10 nm (Figure 2.12A) or 70 nm (Figure 2.12B), the model agrees well with the experimental observation. The corresponding model without any spin-orbit coupling also agrees, however (Figure 2.12C, D).

Nevertheless, it is clear that with the parallel magnetic field in the y direction, the most prominent feature in the response of the device is driven by the parallel magnetic flux penetrating the area dL and not by effects intrinsic to the heterostructure. Assuming that only this parallel magnetic flux contributes, one can estimate the distance d for each device, accounting for the slight difference in W_{SC} for aluminum and niobium devices (1 μm and 400 nm respectively). For devices A-E, the corresponding distance $d \approx 21, 10, 9, 7$, and 70 nm, in agreement with lithographic dimensions. The similar values of d for devices B-D reflects the fact that these devices were all fabricated concurrently. Device E, in which niobium was used for the leads, has a much larger value of d due to the fact that the niobium thickness was larger than the aluminum thicknesses.

Although the parallel magnetic flux dominates the response of devices to the field B_y, with purely

SIA it is still in principle possible in this direction to extract the intrinsic nature of spin-orbit coupling. Since the wavevectors q_x and Δk add and subtract, the 'V' shape of supercurrent evolution contains two nearly identical slopes, which in our measurements are unobservable due to the concurrent decay of superconductivity. However, normalizing the theoretical critical current magnitude still reveals the possibility to determine the nature of spin-orbit coupling using this parallel field direction (Figure 2.12E).

An additional characteristic common among the data sets is an asymmetry in the interference pattern upon inversion of one component of the applied magnetic field. In Figure 2.12F we show an interference pattern measured on Device F with both positive and negative components B_y and B_z. Here the data appears invariant under inversion of both components of the magnetic field, as we expect from time-reversal symmetry. However, the lack of symmetry under inversion of a single component of the magnetic field suggests that devices lack structural symmetry under rotation by 180 degrees. We may model this asymmetry as arising from a difference in lengths of the two leads on either side of the junction. An exaggeration of this effect, where the interface to one lead is 4 microns and to the other is 4.5 microns, shows increased intensity of interference for positive perpendicular fields as compared to negative perpendicular fields (Figure 2.12G), similar to what is observed experimentally.

Finally, in all of the above modeling, we have ignored contributions due to reflections at the ends of the mesa. In Figure 2.12H, we plot the expected evolution of interference upon increasing B_y assuming dominant SIA and with $d = 0$, ignoring the possibility of reflections at mesa boundaries. We may include specular reflections at the mesa boundaries in the model, as discussed in 2.8.5. With these contributions, the interference evolution is quantitatively modified (Figure 2.12I). However, the 'V'

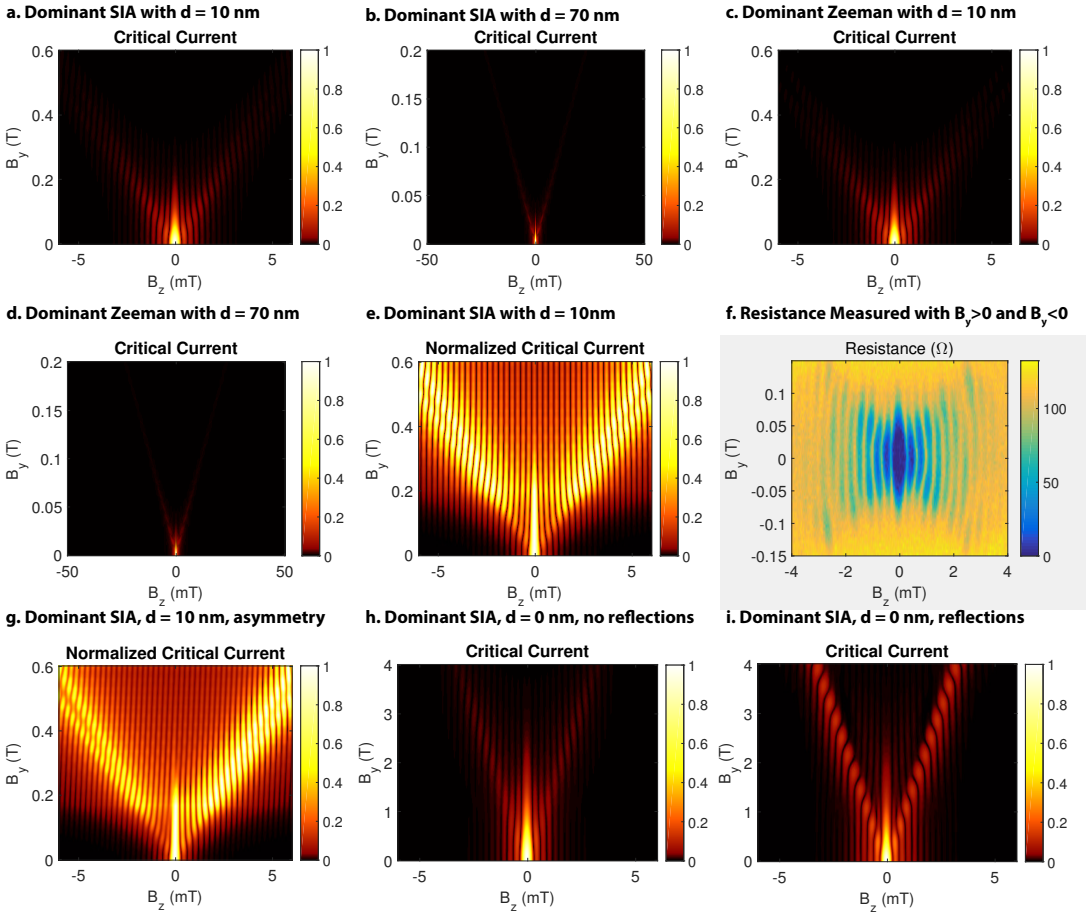

Figure 2.12: Modeling of the critical current as the perpendicular magnetic field B_z (generating flux quanta) and the parallel magnetic field B_y (generating Cooper pair momentum) are varied. (A) With dominant SIA and the height difference d between the leads and the quantum well set to 10 nm, the interference evolves consistently with measurements of differential resistance on aluminum devices (devices A-D). (B) Increasing d to 70 nm decreases the slope of each arm of the interference pattern, consistent with the measurement of a device with thicker niobium leads (device E). (C, D) Eliminating spin-orbit coupling leads to a similar picture for both values of d, highlighting the overwhelming extrinsic nature of the pairing momentum induced when the parallel field is applied in the y direction. E) Normalizing the critical current at each value of B_y reveals additional features weakly present in the interference with SIA and d = 10 nm. Since the extrinsic wavevector q_y adds and subtracts with the wavevector Δk induced due to SIA, two slopes are in principle found in each arm of the interference pattern. However, superconductivity weakens to the extent that such splitting cannot be conclusively observed in our devices. (F) The resistance of Device F, measured as both B_y and B_z are tuned to positive and negative values. The measured resistance is observed to be symmetric under inversion of both B_y and B_z, as expected from time-reversal symmetry. Under inversion of either B_y or B_z, however, the resistance is asymmetric. (G) Modeling asymmetry in the lengths of superconducting electrodes leads to asymmetry in the interference with respect to inversion of B_z. Plotted here are the expected critical currents for a device with 4 microns and 4.5 microns as the interfacial lengths. (H) The expected evolution of interference upon increasing By assuming dominant SIA and with d = 0. (I) Including specular reflections at the mesa ends, assuming the presence of a steep confining potential which does not flip spins upon reflection, quantitatively modifies the interference evolution. However, qualitatively the behavior remains unchanged.

shape of the interference evolution is still present, with each arm of the 'V' having the same slope as was obtained by ignoring edge reflections. Hence, we conclude that the contribution of specular reflections preserving the spin direction only quantitatively modifies the expected device behavior. We have not carried out calculations for other boundary conditions, such as diffuse reflection, but we expect that results in these cases would not be qualitatively different from the cases of specular reflection or no reflection at all.

2.9 Evidence for the Transition to a π-Junction

In a conventional Josephson junction with no external magnetic field, the supercurrent is related to the phase difference $\Delta\varphi$ between the leads via the Josephson relation $I_S = I_C \sin(\Delta\varphi)$. Here I_C is the critical current of the junction. When the induced order parameter oscillates in space, it is possible that this order parameter can have a different sign at the boundary of each superconducting lead. This modifies the current-phase relation by a phase shift of π, so that in such a junction $I_S = I_C \sin(\pi + \Delta\varphi)$. These junctions are referred to as π-junctions and were first explored in systems composed of a ferromagnetic layer sandwiched between two superconductors [100]. A simple experiment which provides evidence of the π phase shift consists of two junctions connected in parallel and sharing the same superconducting leads. If one of the junctions is conventional and the other is a π-junction, then if the junctions also have equal critical currents the total supercurrent must be zero in the absence of external magnetic flux B_z. This contrasts with the standard result for two conventional junctions in series, in which the maximum supercurrent is expected with $B_z = 0$.

In our junctions, applying a finite magnetic field B_x results in finite momentum pairing in the y direction. For a junction with width W, we expect that a π-junction should then be realized when $\frac{\pi}{2}\frac{\hbar v_F}{\tilde{g}\mu_B W} < B_x < \frac{3\pi}{2}\frac{\hbar v_F}{\tilde{g}\mu_B W}$, corresponding to the situation where the induced order parameter has a single node inside the junction. To carry out the experiment described above requires that we realize both a π-junction and a conventional junction. To achieve this goal, we have fabricated a device in which a junction with dimensions 800 nm $\times$ 4 μm is wired in parallel with a junction having dimensions 200 nm $\times$ 2 μm (Figure 2.13A). When the condition $\frac{\pi}{2}\frac{\hbar v_F}{\tilde{g}\mu_B W} < B_x < \frac{3\pi}{2}\frac{\hbar v_F}{\tilde{g}\mu_B W}$ is satisfied for the 800 nm junction, the 200 nm junction will still be in the conventional regime. This experiment therefore allows one to detect the π phase shift, and also to verify that the parallel field B_x necessary to achieve the shift depends on the junction width W. All data presented on this device were collected at a temperature of 10 mK in the system discussed previously (Section 2.6.1).

Due to the screening of the parallel magnetic field by the superconducting leads (described in Section 2.8.6), we have fabricated our device such that all edges of the leads which lie along the y direction are far from the active areas of the device which contain the quantum well. If this were not the case, the screened field would penetrate the quantum well inhomogeneously, leading to unwanted interference. Instead, the quantum well between the 200 nm and 800 nm junctions is etched away, forming a SQUID geometry. Any screened parallel field penetrates through this central hole, leading to SQUID-like interference between the 200 nm junction and the 800 nm junction. The critical current of this device can be simulated with varying amount of screened flux, using the formalism developed in Section 2.8.2-2.8.6. With no screened flux, the expected behavior is simulated in Figure 2.13B. In Figure 2.13C, we plot the same simulation but with experimentally relevant flux screening.

In both simulations, the perpendicular field B_z modulates the critical current. A large period of $\approx$ 1 mT corresponds to the area of the 200 nm junction, while a smaller period of $\approx$ 0.3 mT corresponds to the area of the 800 nm junction. In the simulation with no screened flux, when the parallel field Bx exceeds $\approx$ 1.2 T, the critical current develops a sharp minimum at $B_z = 0$. This critical current minimum results from the formation of a π-junction in the 800 nm section of the device. In the simulation which includes screened flux, increasing the parallel field B_x leads to oscillations in the critical current, even at $B_z = 0$. These oscillations arise because the screened flux penetrates the center of the SQUID loop formed by etching the hole between the two junctions. Here, when the parallel field B_x exceeds $\approx$ 1.2 T, the formation of a π-junction in the 800 nm junction manifests as a π phase shift in the SQUID oscillations. This is due to the fact that when one arm of the SQUID loop is a π-junction, the condition for the maximum supercurrent shifts by 1/2 flux quantum. To illustrate this effect, a line trace of the simulated critical current at $B_z = 0$ is plotted in Figure 2.13D.

To determine whether the π phase shift is present in our device, we measured the differential resistance with a small amount of DC current (20 nA) applied in order to highlight the positions of the high resistance nodes associated with critical current minima. Upon increasing the perpendicular field B_z, we observe two periods of oscillation corresponding to the areas of the 200 nm and 800 nm junctions (Figure 2.13E). With $B_z = 0$, increasing B_x reveals a series of resistance peaks, corresponding to minima of critical current brought on by the SQUID oscillations. At $B_x = 1.2$ T, only oscillations in B_z corresponding to the 200 nm area are observed, suggesting that in the 800 nm device supercurrent has been completely suppressed. Above this nodal value of Bx, we expect to observe the predicted phase shift in the SQUID oscillations which signifies the appearance of a π-junction. Plotting the dif-

ferential resistance as a function of Bx, extracted when $B_z = 0$, we find that the position of nodes does indeed shift by 1/2 flux quantum (Figure 2.13F). Therefore, we conclude that a π-junction is realized in the 800 nm junction and not in the 200 nm junction, and that the origin of this π-junction lies in oscillations of the induced order parameter brought on by the application of the parallel field B_x.

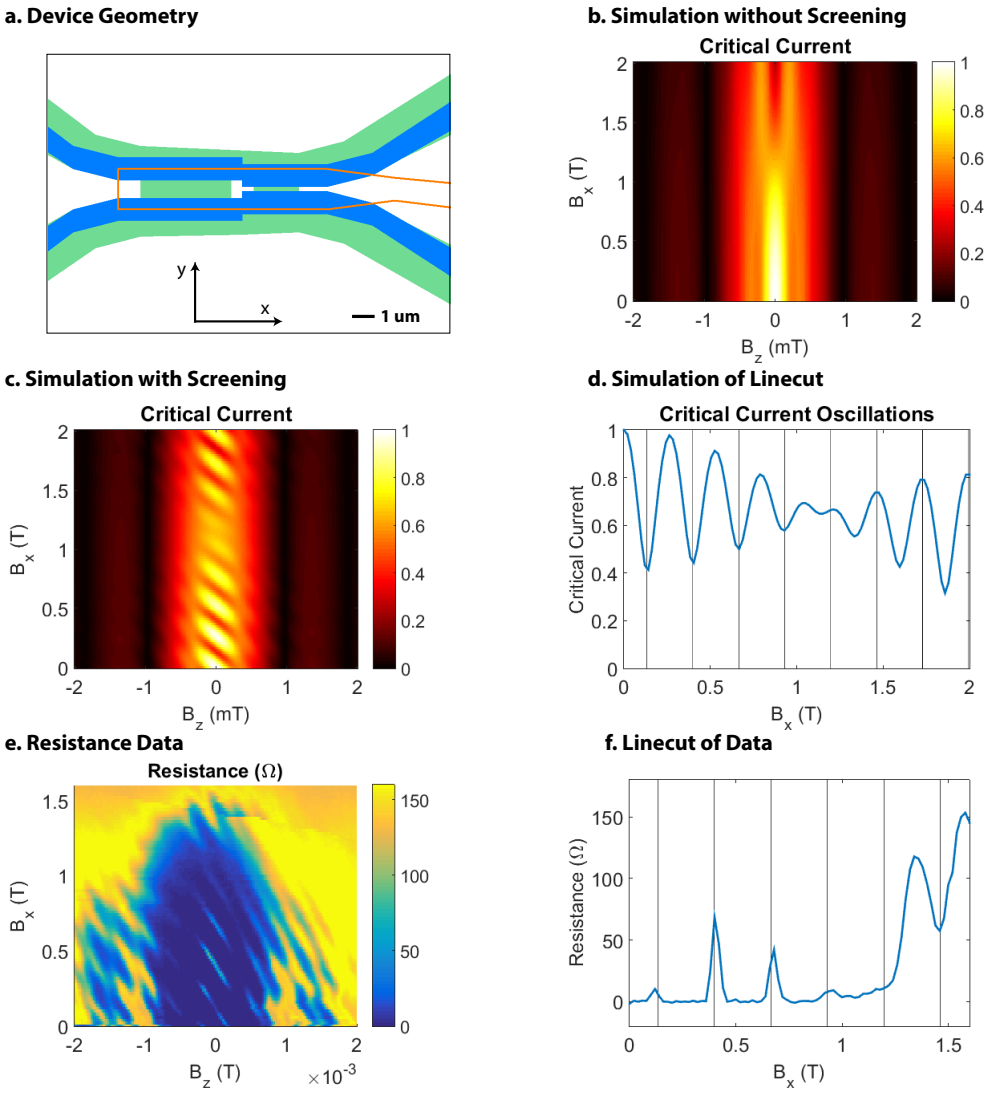

Figure 2.13: Evidence for the transition to a π-junction. (A) The device used for these measurements consists of a junction with dimensions 800 nm $\times$ 4 μm wired in parallel with a junction having dimensions 200 nm $\times$ 2 μm. A central area with no quantum well, created by etching, separates the two junctions by 1 μm. (B) An external field in both the x and z directions may be simulated, neglecting screening effects from the leads. In this case, application of the magnetic field B_x leads to a pair momentum shift in the y direction. At Bx = 1.2 T, the 800 nm junction transitions to a π-junction state. Above this nodal field, the critical current develops a minimum at B_z = o due to the presence of both a conventional and π-junction in the device. (C) Including the screening of the magnetic field B_x by the aluminum leads, the simulation shows that increasing B_x while keeping B_z = o leads to oscillations in the critical current. These are due to flux penetrating the central hole in the device and are essentially the critical current oscillations of a SQUID loop. (D) In this situation, the transition of the 800 nm junction to a π-junction is then expected to manifest as a phase shift in these SQUID oscillations. A linecut of the simulated critical current at B_z = o, as a function of B_x , displays this shift. (E) The measured differential resistance of the device, with a DC current bias of 20 nA, shows a node structure which matches the predicted interference. (F) Extracting the differential resistance at B_z = o shows a periodic dependence on B_x at low fields, with the predicted phase shift above B_x = 1.2 T.

3

Topological Superconductivity in a Phase-Controlled Josephson Junction

Topological superconductors can support localized Majorana states at their boundaries. These quasi-particle excitations have non-Abelian statistics that can be used to encode and manipulate quan-

tum information in a topologically protected manner. While signatures of Majorana bound states have been observed in one-dimensional systems, there is an ongoing effort to find alternative platforms that do not require fine-tuning of parameters and can be easily scalable to large numbers of states. Here we present a novel experimental approach towards a two-dimensional architecture, inspired by the experimental observations of the prior chapter and theoretical work that followed those observations[56]. Using a Josephson junction made of HgTe quantum well coupled to thin-film aluminum, we are able to tune between a trivial and a topological superconducting state by controlling the phase difference φ across the junction and applying an in-plane magnetic field. We determine the topological state of the induced superconductor by measuring the tunneling conductance at the edge of the junction. At low magnetic fields, we observe a minimum in the tunneling spectra near zero bias, consistent with a trivial superconductor. However, as the magnetic field increases, the tunneling conductance develops a zero-bias peak which persists over a range of φ that expands systematically with increasing magnetic fields. Our observations are consistent with theoretical predictions for this system and with full quantum mechanical numerical simulations performed on model systems with similar dimensions and parameters. Our work establishes this system as a promising platform for realizing topological superconductivity and for creating and manipulating Majorana modes and will therefore open new avenues for probing topological superconducting phases in two-dimensional systems.

3.1 Introduction

Majorana bound states (MBS) are quasiparticle excitations that are their own antiparticles and hence can serve as the basis of topological quantum computing, where quantum information can be stored and manipulated robustly[45,34,35,43,55,53,6,68,2]. Spectroscopic studies have been conducted in various one-dimensional systems such as proximitized nanowires and atomic chains, where zero-bias peaks exist in the tunneling spectroscopy in individual parts of the parameter space associated with MBS[51,61,13,14,21,1,12,17,29,74,52,42]. Despite the growing evidence, scalable networks of Majorana qubits have proven a challenge to obtain in such one-dimensional platforms, due to both the intrinsic instabilities associated with one-dimensional systems and the technological obstacles in their physical implementation[65,32]. Therefore, to understand and harvest the full power of MBS physics, two-dimensional platforms that can realize topological superconductivity are in demand for patterning large-scale networks of Majorana devices as well as integrating them with other quantum information devices and systems, in a reproducible and controlled fashion[15].

3.2 Setup of the System

3.2.1 Theoretical Setup

We design and implement a controllable two-dimensional platform for realizing topological superconductivity based on a recent theoretical proposal for a planar Josephson junction created out of a two-dimensional electron gas (2DEG) subject to a strong Rashba spin-orbit interaction, sandwiched

between two aluminum superconducting leads (Figure 3.1a)[5,6]. In this system, the phase transition between trivial and topological superconductivity can be tuned using two independent knobs - the phase difference across the junction φ, and the Zeeman energy E_Z governed by an external magnetic field applied in the plane of the junction. In a long Josephson junction which is translationally invariant along x, the direction parallel to the superconducting electrodes, supercurrent is carried by bands of Andreev bound states in the normal region, formed by successive Andreev reflections at the normal-superconductor interfaces[4,7]. The energy of each Andreev state thus depends both on φ and on the phase accumulated by the quasiparticles traversing the junction at various angles from the x-direction. Therefore, the Andreev states can have a full range of wavevectors, with the x-components of their wavenumbers k_x varying in magnitude from 0 to nearly the Fermi wavenumber k_F. Their energies hence disperse to form a continuous sub-gap spectrum. Interestingly, when normal reflection at the normal-superconductor interface is weak, these Andreev bands are relatively flat and disperse only weakly with changing k_x (Figure 3.2a). This leads to a strongly enhanced density of states near zero energy in the vicinity of the topological phase transition. When normal reflection is taken into account, the bands acquire a nonzero width (Figure 3.2b).

3.2.2 Phase Diagram of the Topological Phase Transition

A topological phase transition in a clean junction is accompanied by a zero-energy crossing at $k_x = 0$ (Figure 3.1b). When the Zeeman energy is zero, the $k_x = 0$ Andreev states are twofold degenerate and cross at $\varphi = \pi$ in the absence of normal reflections. A finite magnetic field parallel to the x-axis separates the $k_x = 0$ states by a phase difference $\Delta\varphi = 2\pi E_Z/E_T$, where E_Z is the Zeeman energy

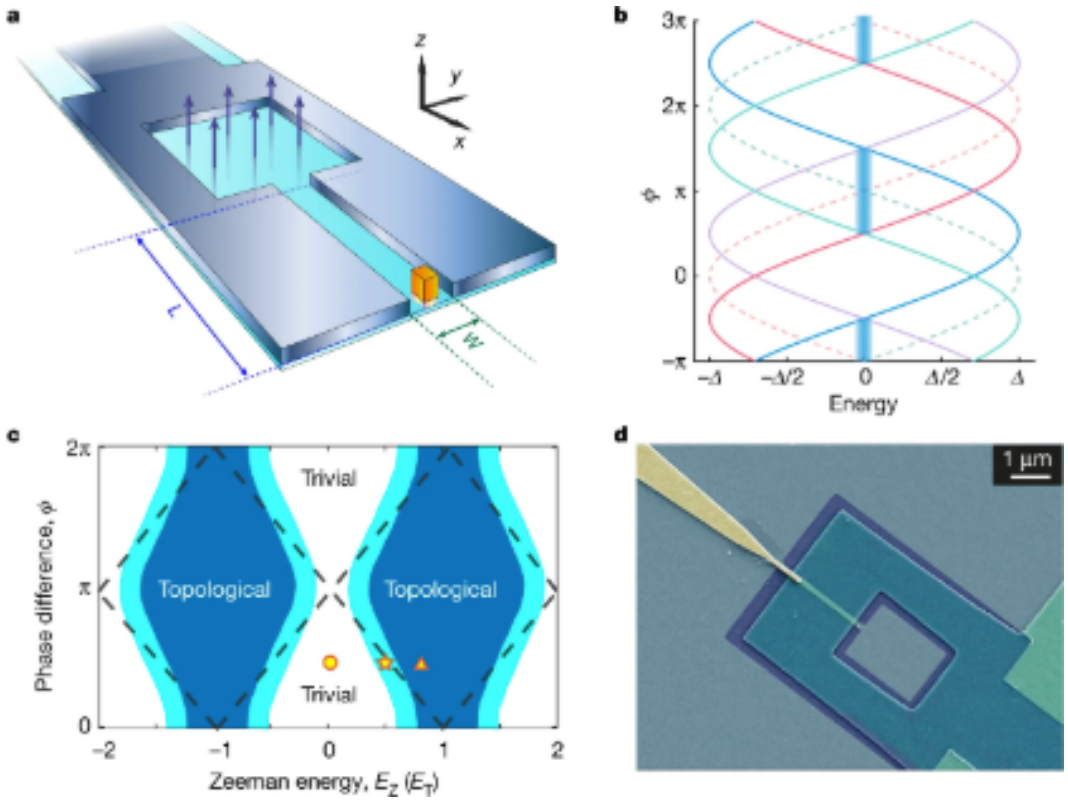

Figure 3.1: Topological transition in a phase-controlled Josephson junction. a, Device schematics for a planar Josephson junction created out of a 2DEG (shown in cyan) sandwiched between two aluminum superconducting leads, whose ends connect to form a flux loop (shown in steel blue).* The tip of the tunnel probe (shown in gold) overlaps the HgTe quantum well, separated by a region of CdHgTe (shown in pastel colors). The perpendicular component of the external magnetic field B_z is used to tune the phase difference across the junction, while its in-plane component B_x, parallel to the superconducting-normal interface, is used to tune the Zeeman energy. b, The bound-state spectrum for $k_x = 0$ for a junction that is long in the x-direction and symmetric in the y-direction. It is twofold degenerate in the absence of any external magnetic field (dashed lines), and spin-split in the presence of an external in-plane field (solid lines in rose, blue, violet, and cyan for the spin-up and spin-down electrons and holes), accommodating a topological phase to develop in the range of φ between the zero-bias crossings (shaded regions colored blue). c, Phase diagram as a function of the Zeeman energy E_Z (given in units of the Thouless energy E_T) and the phase difference φ across the junction. The dashed lines correspond to the boundary between the topological and trivial phases of superconductivity for a junction with perfect transparency, while the solid blue regions show the topological phase can deviate from the diamond shapes when considering normal reflection at the superconducting-normal interface. The cyan ribbons highlight the boundary between the two phases of superconductivity. d, False-color scanning electron micrograph of a device with a narrow junction. Green region defines the mesa area which contains the HgTe quantum well. The superconducting contact is Ti/Al (5 nm/15 nm) and colored in purple. The tunnel probe is Ti/Au (10 nm/100 nm) and colored in yellow. Data presented in the main text is taken from a device with a wider junction (600 nm) and without the hole in the mesa.

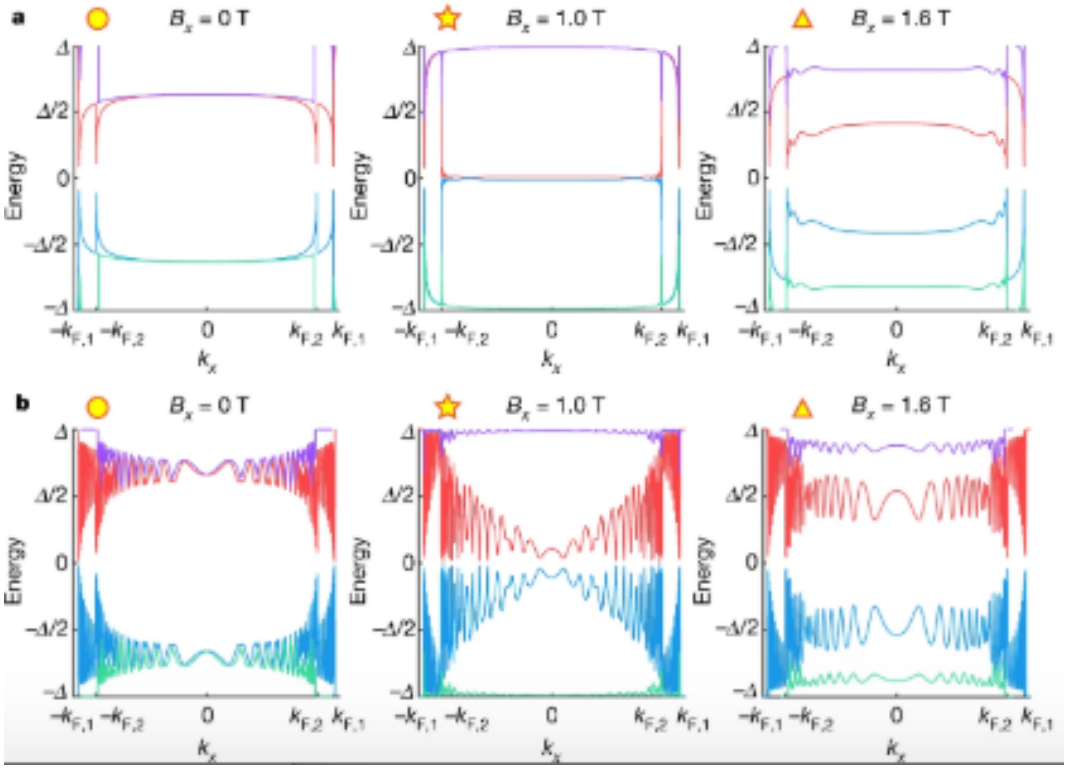

Figure 3.2: Andreev spectra in a phase-controlled Josephson junction. a, Dispersion of the Andreev band as a function of k_x, at three different values of the Zeeman energy. The circle, the star, and the triangle symbols indicate where each band diagram corresponds in the phase diagram in Figure 3.1c. The Andreev bands become relatively flat during the topological phase transition (middle panel). b, Similar Andreev spectra as calculated in d but including some normal reflection, which results in a finite width of the bands.

and $E_T = (\pi/2)(\hbar v_F/W)$ is the Thouless energy. In the range of φ between these two crossings, the occupancy of fermionic states becomes odd, and the system undergoes a phase transition into a topological superconducting phase. We can map out this phase boundary in the $\varphi - E_Z$ space (Figure 3.1c). As E_Z increases from 0 to the Thouless energy E_T, the junction becomes topological in a growing range of φ, with predicted MBS on the end of a semi-infinite junction. As E_Z further increases beyond E_T, this range in φ starts to decrease, forming overall diamond shapes (dashed lines in Figure 3.1c). In a physical system, normal reflection can occur at the interfaces, which hybridize the left- and right- moving modes in the junction and shift the phase boundary from the ideal scenario. In this case, the topological phase occupies regions deformed from the diamond shapes, but its dependence on magnetic field and phase difference are robust (solid color in Figure 3.1c) and largely insensitive to changes in geometry and electron chemical potential. Consequently, for a wide range of magnetic fields, the application of a small phase bias can easily tune the system in and out of the topological superconducting phase and is hence a powerful experimental knob that can be controlled in a rapid manner.

3.2.3 Experimental Setup

Our planar Josephson junction consists of an 8-nm-wide HgTe quantum well contacted by thermally evaporated aluminum leads about 15 nm thick, with 5 nm of titanium as a sticking layer. The junction region is 600 nm wide and about 1 micron long, with one end of each lead connected to form a flux loop. As previously established, our HgTe quantum well, grown by molecular beam epitaxy, provides a 2DEG with high mobility and dominant Rashba spin-orbit coupling, and the thin aluminum leads

can superconduct up to 1.8 T of in-plane magnetic fields[31,30]. Using our vector magnet, we apply a magnetic field B_z perpendicular to the sample plane to generate the flux that controls the phase difference across the junction, while we apply an in-plane magnetic field B_x in the x-direction to tune the Zeeman energy (Figures 3.1a and 3.1d). On the outer edge of the junction, we fabricate a weakly coupled electrode by evaporating 10 nm of titanium and 100 nm of gold, with approximately 10 nanometers of CdHgTe as a tunnel barrier, which is immediately above the HgTe layer in the MBE-grown heterostructure. The overlapping area is approximately 100 nm by 100 nm, which gives a tunneling resistance of around 300 kΩ.

By applying an AC excitation in addition to a DC voltage bias on the tunnel probe and measuring the AC current through the superconducting lead, we can obtain a two-terminal differential conductance curve as we vary the DC bias. The observed spectrum of the proximitized 2DEG typically exhibits two broad coherence peaks separated by about 120 μV in bias voltage and a valley near zero bias (3.3a). To see how the spectrum disperses with the phase difference φ, we scan B_z over a few mT near zero and record the differential conductance as a function of both the bias voltage and B_z.

3.3 Measurements and Analysis

3.3.1 Tunneling Spectra

Shown as colormaps in Figures 3.3a-3.3c, the tunneling spectrum exhibits a strong periodic modulation with B_z, where the period matches the area of the flux loop, considering the magnetic flux repelled by the superconducting lead. The in-plane field also generates an asymmetry between pos-

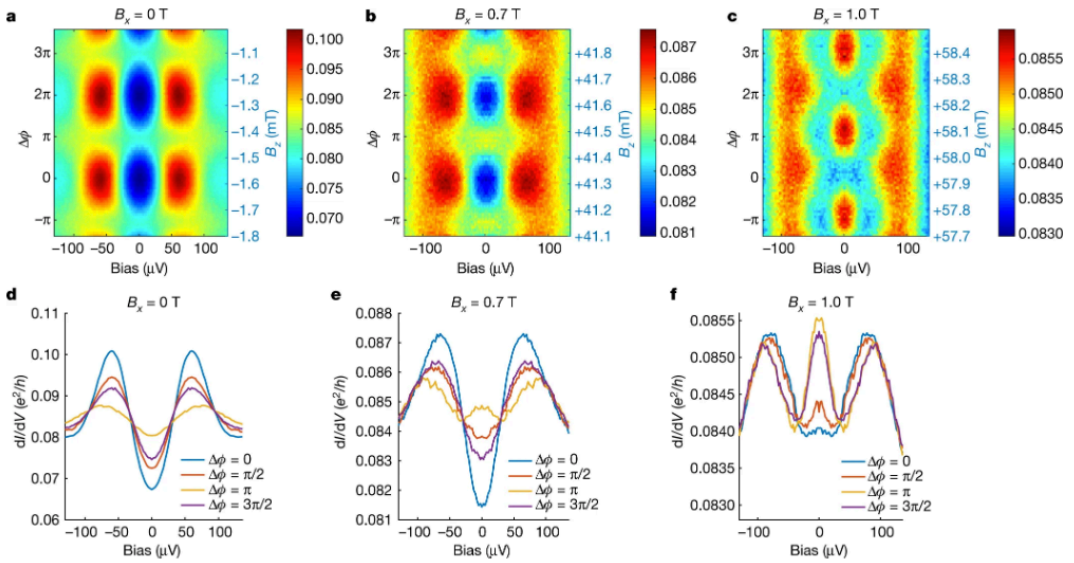

Figure 3.3: Phase modulations of the tunneling conductance at low versus high fields. a-c, Differential conductance color plots (in units of e^2/h) as a function of both the bias voltage (x-axis) and the phase difference (left y-axis) offset from the $\Delta\varphi = 0$ point, identified by the value of φ at which the coherence peaks obtain a maximum. The right y-axis records the actual B_z field supplied by the magnet. d-f, Linecuts of a-c showing the differential conductance curves as a function of the bias voltage on the tunnel probe at four representative values of phase differences, averaged over repeating lines spaced integer periods apart. a and d present data taken at $B_x = 0$ T, where no zero-bias peak exists for any phase difference. b and e present data taken at $B_x = 0.7$ T, where a zero-bias peak exists for a range of phase differences within each period. c and f present data taken at $B_x = 1.0$ T, where a zero-bias peak persists through most of the period.

itive and negative voltage biases, which we attribute to a particle-hole asymmetry. To highlight the contribution to the tunneling conductance near zero energy, we symmetrize the data at positive and negative biases (the raw data and further discussion are presented in Section 3.7).

At low in-plane fields, the tunneling spectra reveal a conductance minimum near zero bias irrespective of the applied phase difference across the junction. This behavior (Figures 3.3a and 3.3b) resembles recent measurements in a graphene Josephson junction and is interpreted as the behavior of the bulk Andreev bound states and their dependence on the phase difference across the junction[9].

We attribute the missing zero-bias conductance peak at low in-plane fields near a phase difference of π to the presence of weak normal reflections at the normal-superconducting interface. At high in-plane fields, a conductance peak develops near zero-bias over a range of φ, repeating periodically (Figures 3.3c and 3.3f). The emergence of a robust and extended zero-bias peak in φ indicates the spectrum of the sub-gap states concentrating near zero energy and persisting over a wider span in φ as the in-plane magnetic field increases (Figures 3.4a-h).

3.3.2 Extracting the Phase Diagram from the Measurements

To fully capture how the range in phase containing the zero-bias peak (ZBP) grows with magnetic field, we quantify the emergence of this conductance peak by extracting the curvature of the differential conductance curve around zero-bias, using a parabolic fit on the symmetrized data, which gives the same curvature as extracted from the raw data (Figure 3.4i). We perform this analysis at all values of phase difference φ and in-plane field B_x to produce a colormap visualizing the development of the zero-bias peak in the $\varphi - B_x$ phase space (Figure 3.4i). At low fields, most values of the phase difference give a dip (positive curvature) in the zero-bias conductance, shown in red in Figure 3.4i, indicative of a conventional superconducting phase. As B_x increases, the differential conductance becomes flatter near zero bias, and the parabolic fit yields a small absolute value, giving rise to a white region in the color plot, which expands to occupy higher fractions of each period in φ. As the magnetic field continues from 0.6 T to 1.2 T, a blue region of negative curvature emerges, marking the zero-bias peak, and expands to fill the entire period. Similar behavior of expanding ZBP region repeats for negative values of B_x, generating a phase diagram consistent with the predicted topological phase

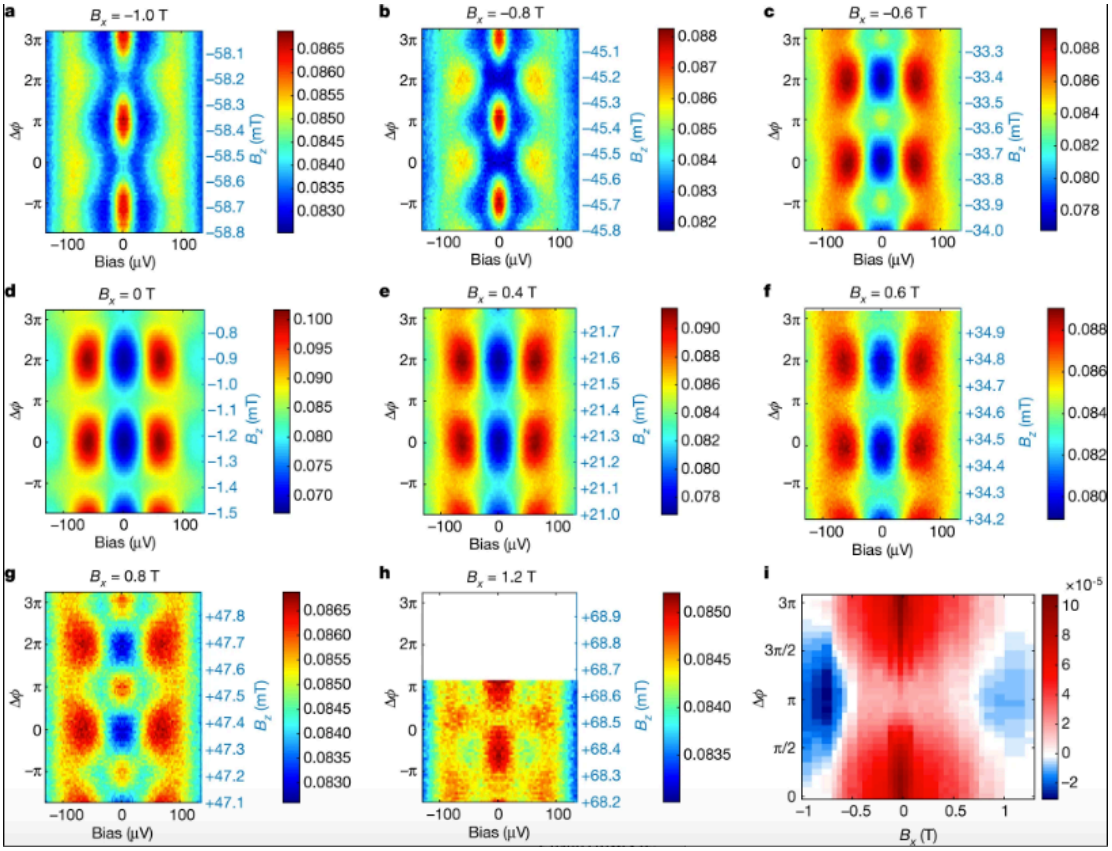

Figure 3.4: Development of zero-bias peak and the reconstructed phase diagram. a-h, Progression of tunneling conductance colorplots (in units of e^2/h) as the magnetic field B_x varies from -1.0 T to 1.2 T, skipping field values shown in Figure 2 except for $B_x = 0$ T which serves as a point of reference. All plots span over a range of 0.8 mT in B_z except $B_x = 1.2$ T. i, Colorplot showing the extracted zero-bias curvature as a function of both the in-plane magnetic field B_x and phase difference offset $\Delta\varphi$, shown in units of $e^2/h \cdot \mu\text{eV}^{-2}$. The blue region in the phase diagram shows where a well-defined zero-bias peak is present in the tunneling conductance. Its emergence and expansion with the application of both positive and negative in-plane magnetic fields agrees with the predicted phase transition (Figure 3.1c).

transition (Figure 3.1c).

3.4 Modeling the System

3.4.1 Modeling in KWANT

To simulate transport through the device, we describe the semiconductor by a tight-binding model with uniform Rashba spin-orbit coupling defined in a rectangular region. The region comprises a normal part sandwiched between two segments with proximity-induced superconductivity held at different phases (Figure 3.21, similar to Figure 3.1a). We evaluate the conductance between a metallic tunneling probe attached to the edge of the normal region and two grounded superconducting leads that contact the superconducting regions on both sides, employing a scattering matrix approach using the KWANT package[27].

Motivated by the experimental observation that the superconducting coherence peaks do not shift in energy with the in-plane magnetic field, we assume a suppressed g-factor in the proximitized parts and neglect the Zeeman field outside the normal region. Our model includes doping of the semiconductor due to the superconductor by assuming a higher density in the proximitized parts of the semiconductor. We account for the experimental resolution and nonuniform phase differences across the junction due to flux focusing by artificially broadening the theoretical data in energy and phase.

The calculated conductance, plotted as a function of bias voltage and phase in Figure 3.5A-F, reproduces key features of the experimental data. At low Zeeman fields, the heights of the coherence peaks at $V \sim \pm 70\mu$V are modulated in phase and the conductance has a dip at zero bias for all values of

the phase. At fields above $B_x = 0.5$ T, a peak at zero bias develops while the coherence peaks remain visible. In a minor deviation from the experiment, the coherence peaks shift to slightly higher energies $V \sim \pm 100\mu$V in the numerics, which can be reconciled by accounting for a small gap suppression by the Zeeman effect in the superconductor.

The emergence of the zero-bias peak at finite fields is clearly visible in Figure 3.5g, where the curvature of the zero-bias conductance with bias voltage is plotted as a function of phase difference and the magnetic field. In the experimental field range, the numerical results in Figure 3.5g are in excellent agreement with the experimental data in Figure 3.4i. For all phase differences, the curvature monotonously decreases with in-plane field and eventually transitions from a dip to a peak. At $B_x = 1$ T, a zero-bias peak exists for all values of the phase.

3.4.2 Comparison Between Measured and Theoretical Data

Comparing the theoretical curvature plot in Figure 3.5g with the phase diagram in Figure 3.1c reveals that the most pronounced zero bias peaks occur close to the topological phase boundaries. At the same time, a zero-bias dip exists deep inside the topological phase. This is consistent with our numerical findings that the Majorana wavefunction is almost completely delocalized over the junction area for the experimental sample dimensions (see Section 3.11), precluding a dominant Majorana signature in the measurement. Instead, the peak originates from a band of quasi-one-dimensional subgap states living inside the junction (Figure 3.2a). The density of states is enhanced at low energies as the band crosses zero energy in the vicinity of the topological phase transition, which manifests itself as a zero-bias conductance peak when the energy broadening is larger than the induced gap in the quasi-

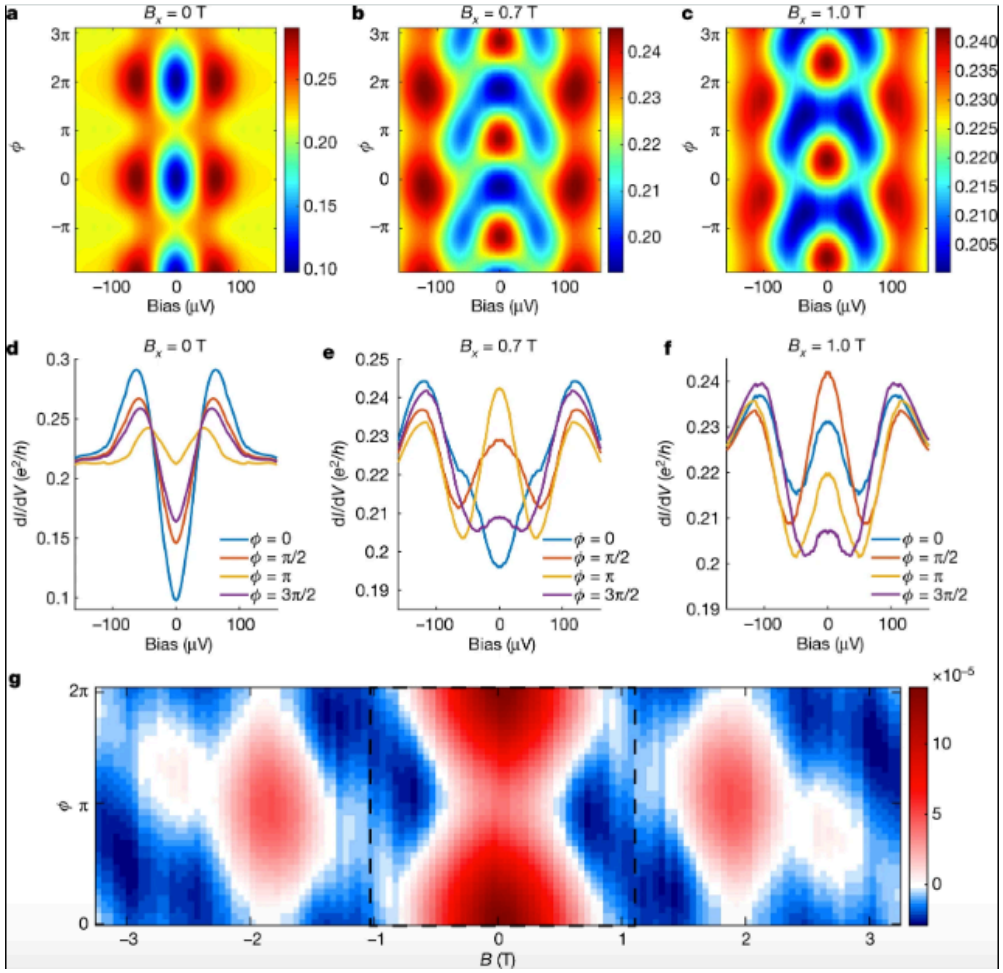

Figure 3.5: Numeric Simulation for the tunneling conductance using a tight-binding model. a-f, Calculated tunneling conductance between a metallic tunneling probe attached to the edge of the normal region and two grounded superconducting leads. d-f, Linecuts at four representative values of phase differences, taken from the conductance color plots a-c, at three B_x fields corresponding to those shown in Figure 2. The emergence of the zero-bias peak in finite fields agrees with the experimental data. g, Predicted zero-bias curvature of the tunneling conductance as a function of both the Zeeman energy E_Z and the phase difference φ, shown in units of $e^2/h \cdot \mu\text{eV}^{-2}$. Indicative of a zero-bias peak, the blue regions trace out the transition between the trivial and topological superconducting phases. Outlined in black dashed lines is the regime corresponding to the experimental data.

one-dimensional band. In the presence of normal reflection, the band acquires a finite width (Figure 3.2b), and the zero-bias conductance peak can exist in a broader parameter window around the phase transition (see Section 3.12 for a discussion of the density of states). Future directions to improve this platform include enhancing the interface quality and adopting narrower and longer junctions, which will result in a harder gap in the junction and allow robust control of the topological transition without requiring higher magnetic fields (see Section 3.14).

In conclusion, our experiment provides the first tunneling spectroscopy study of phase-controlled Josephson junction in the presence of a tunable in-plane magnetic field. The ability to phase-bias the Josephson junction offers a powerful knob with easy access and control. Our measurements of a ZBP that develops and expands with applied magnetic field provide evidence of a topological phase transition in a two-dimensional induced superconductor. Our experiment does not rely on any fine-tuning of the chemical potential or the in-plane magnetic field and can be easily generalized to other two-dimensional materials, where the interplay of phase bias, spin-orbit coupling, and Zeeman effect can create exciting opportunities to investigate topological superconductivity, making such platforms promising candidates for the detection and manipulation of Majorana bound states, and hence for realizing topologically protected quantum computation.

3.5 Device Characterization and Measurement

To characterize our two-dimensional electron gas (2DEG), we fabricate and measure a van der Pauw device on the same HgTe wafer QC0261, using the same metal deposition method described earlier in

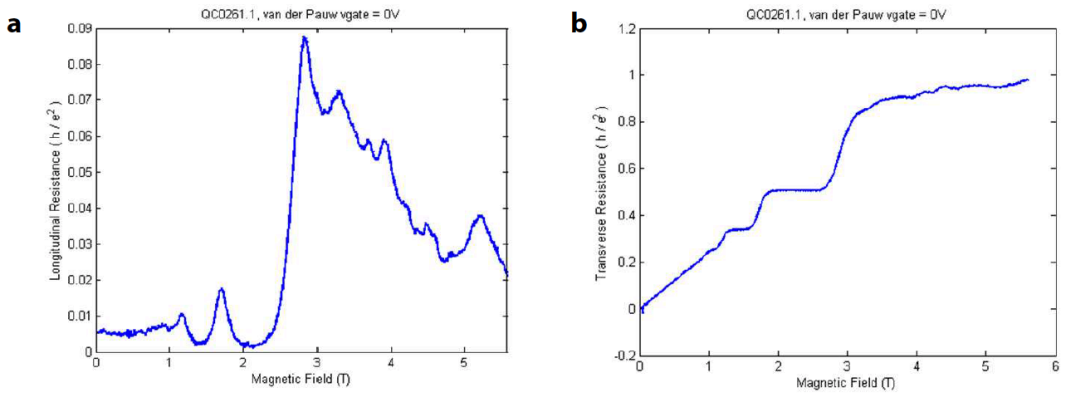

Figure 3.6: Characterization of the HgTe quantum well. Shown here are the longitudinal and Hall resistances of a van der Pauw device fabricated on wafer QC0261, as a function of the perpendicular magnetic field, at a top gate voltage of 0 V, measured at a temperature of 4 Kelvin.

the chapter except replacing the aluminum contacts with gold. By measuring the longitudinal and Hall resistances, we obtain a 2DEG mobility of around 400,000 cm^2/Vs at a density of 1.0×10^{11} cm^{-2}. The longitudinal and Hall resistances are shown respectively in Figure 3.6a and b.

We fabricate high-quality aluminum/HgTe interface using in-situ ion milling procedure described in the previous chapter as well as in Appendix A[31,30]. Here we provide a back of the envelope estimate for the transparency of our Josephson junctions using transport data. For an 800 nm wide, 4 micron long junction we made using the same fabrication procedure and with the same thickness of aluminum and sticking layer, the normal resistance $R_N = 200\Omega$. Using a formula for a Josephson junction with two equal interfaces, the resistance is given by $R = \frac{1}{M}\frac{h}{e^2}\left(1 + 2\frac{|r|^2}{|t|^2}\right)$, where M is the number of modes, and t and r are the complex transmission and reflection amplitudes. At an estimated density of 1.7×10^{11} cm^{-2} inside the junction, the Fermi wavelength is about 60 nm, which means we have 133 transport modes in a 4-micron-long junction. This places us at an interface transparency $|t|^2$ of

about 98.5%. Realistically, the doping from the aluminum leads could modify the chemical potential inside the junction, and hence the transparency is slightly lower than this number. For example, if we assumed a density of 4.0×10^{11} cm^{-2}, we would find a transparency of 78.4%. Given the uncertainty in our density estimate, we expect our interface transparency to fall inside this range of 78% to 100%.

To investigate the spectrum at the end of the Josephson junction, we perform local tunneling spectroscopy through a weakly coupled electrode, which overlaps the junction over an area of approximately 100 nm by 100 nm near its edge. We use in-situ ion milling to etch most of the CdHgTe barrier layer on top of the quantum well and stop when only a few nanometers of CdHgTe remain. We then deposit 100 nm of gold with 10 nm of titanium as a sticking layer. Both metals, especially the titanium, react chemically with CdHgTe to form alloys [11]. These semimetallic alloys facilitate the tunneling of electrons between the local electrode and the quantum well, producing low-temperature tunnel resistances ranging from 15 kΩ to 15 MΩ, depending on the thickness of the barrier layer and the overlapping area of the electrode with the quantum well.

Since the features in the tunneling conductance we study here are induced by the superconductivity in the aluminum, we expect them to only develop well below the critical temperature of the superconducting aluminum film, which can range from 1.2K to 1.6K [49]. Figure 3.7 shows the temperature dependence of the tunneling conductance curves during a cool-down process in our dilution refrigerator, for the same device discussed earlier in the chapter. As we can see, the main peaks in the conductance only start developing below 0.5 Kelvin. The separation of the two conductance peaks is typically around 120 μeV and the width of each peak is on the order of 50 μeV in energy. Above this temperature, the tunneling conductance curve is mostly flat for this energy range. Although this does

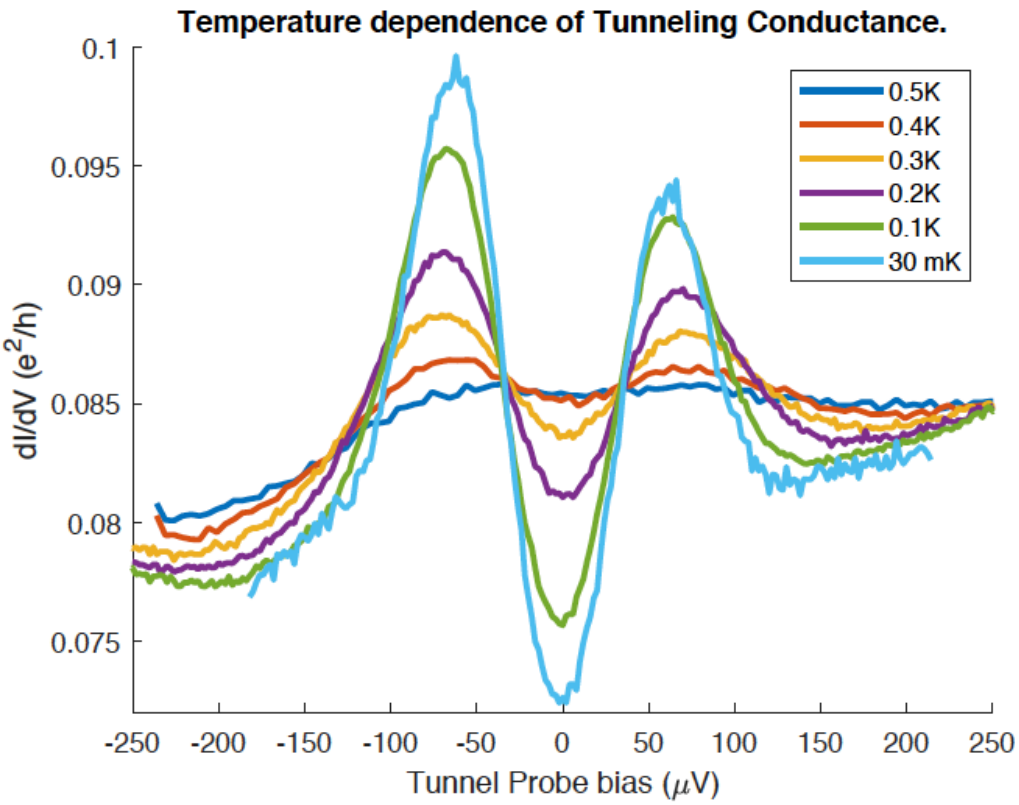

Figure 3.7: Temperature dependence of the tunneling conductance. Shown here is the temperature dependence of the tunneling conductance of device Beta, plotted against the DC bias across the tunnel probe and the superconducting lead. Different curves represent data taken at different averaged temperatures during its cool-down in our dilution refrigerator, from 0.5 Kelvin (blue curve) down to 31 millikelvins (teal curve) over a range of 0.5 mV of DC bias.

not completely rule out all possible contributions from features related to the tunnel probe that only develop at low temperatures, it does strongly suggest that these conductance peaks originate from the aluminum-induced superconducting gap in the HgTe quantum well.

During our measurements, the point in bias voltage about which the conductance curve is approximately symmetric is constant for each cool-down of the device, and we identify this point as the zero-bias point. It is worth pointing out that this true zero-bias point tends to be offset by 15-25 μeV from

zero reading on our DC voltage supply, which we attribute to a constant voltage offset that comes from the voltage source in our measurement circuitry which supplies the bias to the tunnel probe. This is a very common experimental feature, where the applied zero voltage does not translate to really zero voltage between the tunnel probe and the sample because electronic components may exert finite bias due to various circuit artifacts. To eliminate this artifact and thus avoid unnecessary confusion for the readers, we have shifted the x-axis in all of our tunneling conductance plots, so that the true zero-bias point aligns with the zero-bias reading in the plots. Therefore, the presented plots are relative to the true voltage bias rather than the instrumental reading that contains a systematic error.

3.6 Correction for Imperfect Sample-Magnet Alignment

Due to imperfect sample-magnet alignment, the in-plane field B_x will generate a small perpendicular component B_z, which offsets the B_z field corresponding to zero-flux in the phase loop. To correct for this effect and maintain our measurement in a range of phase difference near zero, we scan over a range of B_z at each B_x field and identify a range with maximal oscillation amplitude in the tunneling conductance.

Shown in Figure 3.8a is the conductance in the range of a few mT in B_z near zero, featuring periodic oscillations as the junction's phase difference is modulated, which gradually dampens as the B_z increases in both positive and negative directions. Based on this experimental observation, we maintain our measurements in the vicinity of zero phase difference by scanning over a range in B_z at each B_x field and selecting a region with maximal oscillations in the tunneling conductance (Figure 3.8a

and b). As the in-plane field B_x increases, this optimal range drifts towards higher B_z values, following a linear dependence to first order (Figures 3.8c-f).

The phase smearing effect is yet another high-field effect that is not compensated by this correction. Because of the microscopic roughness along the edge of the superconducting electrodes during the sample fabrication, the high in-plane magnetic fields can generate non-uniformity along the normal-superconducting interface, which in turn causes the phase difference along the x-direction of the junction to disperse[30]. This creates a smearing effect on the observed spectroscopy's dependence on phase, reducing the signal-to-noise ratio of the tunneling conductance. Because this effect worsens at high in-plane fields, it is necessary to adopt a junction geometry where the topological phase transition happens at low enough fields before the phase smearing effect masks the experimental signal entirely. In our experiment, the 600nm junction places us in this situation and enables us to see the emergence of the zero-bias peaks associated with the phase transition. Future development to improve the lithography and film quality of the superconducting contacts could help reduce such phase smearing effect and enhance the measurement resolution in both energy and phase at high in-plane fields.

3.7 The Electron-Hole Asymmetry with In-Plane Field

At zero in-plane field, we generally see a symmetric differential conductance between positive and negative DC voltages, endorsing the particle-hole symmetry in the local spectrum of Andreev bound states (see Figure 3.3 as an example). However, such symmetry in the LDOS is not present at high

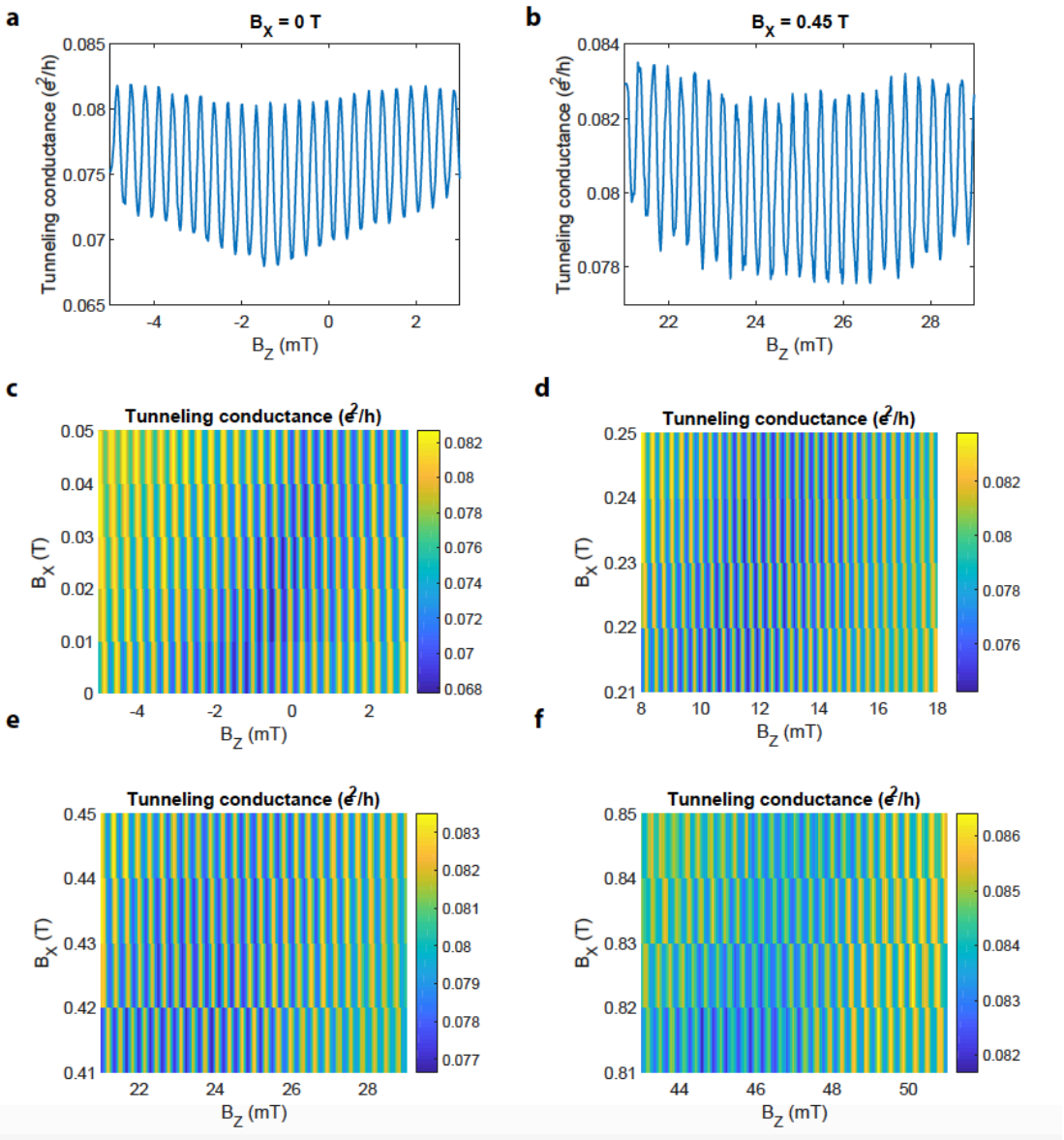

Figure 3.8: Compensation for the sample-magnet misalignment. a and b, The tunneling conductance near zero bias as a function of the out-of-plane magnetic field, B_z, at zero in-plane field $B_x = 0$ T in a) and a finite in-plane field $B_x = 0.45$ T in b). c-f, Colorplots of tunneling conductance near zero bias as a function of both the out-of-plane magnetic field B_z and the in-plane field B_x. At incremental ranges of B_z, these uncompensated plots show the linear offset of B_z growing with increasing B_x.

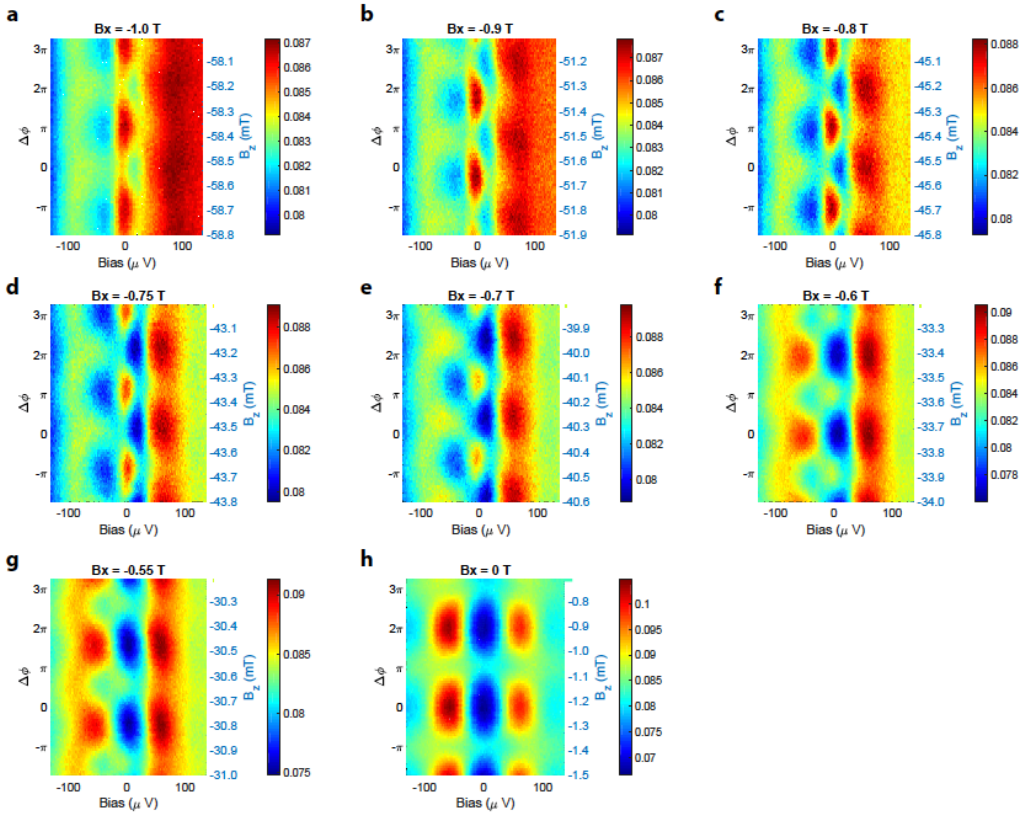

Figure 3.9: Unprocessed conductance data with in-plane magnetic fields, part 1. The raw conductance data (in units of e^2/h) at in-plane fields ranging from -1.0 T to 0 T, with an electron-hole asymmetry which grows as the magnitude of the in-plane field increase from 0 to 1.0 T. All plots show tunneling conductance in units of e^2/h as a function of both bias voltage and the span over a range of 0.8 mT in B_z.

in-plane magnetic fields. This is reflected by an asymmetry in the differential conductance about zero bias voltage[†], which grows with the in-plane magnetic field applied. Figures 3.9 and 3.10 show the raw data with this asymmetry at various magnetic fields.

To visualize this asymmetry in the tunneling conductance and see how it develops with the magnetic field, we can average the differential conductance over an entire period in the phase difference,

[†]As mentioned in Section 3.5, this true zero bias can be offset from 0 voltage reading by a constant deviation ranging from 15 to 25 μeV, due to instrumental errors.

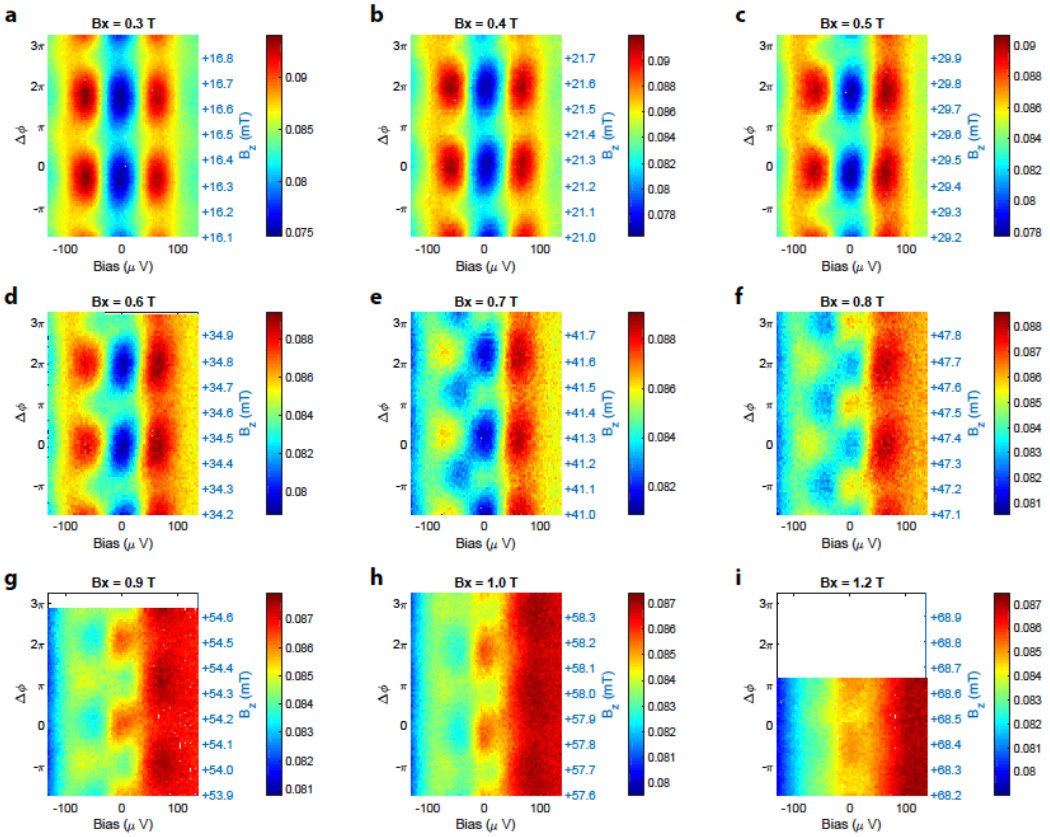

Figure 3.10: Unprocessed conductance data with in-plane magnetic fields, part 2. The raw conductance data (in units of e^2/h) with an electron-hole asymmetry which grows as the in-plane field increases from 0.3 T to 1.2 T. All plots show tunneling conductance in units of e^2/h as a function of both bias voltage and the span over a range of 0.8 mT in B_z.

at each in-plane field, as plotted in Figure 3.11. Furthermore, we can quantify it with the slope of a linear fit to the averaged conductance curve. Shown in Figure 3.12, the slope representing the asymmetry grows linearly with the magnitude of the in-plane field, and the sign of the asymmetry does not depend on the direction of the field. This is also evident from Figure 3.13, which shows a continuous evolution as the in-plane field is ramped across a broad range, as well as a broader range in the bias voltage. The out-of-plane component of the B_x field is passively compensated in linear proportion but not perfectly canceled. As a result of the minute remaining B_z field, the zero-bias conductance shows oscillations in the B_x field. We can see the same asymmetry develops from positive to negative B_x fields, although its extent does vary from device to device.

The exact mechanism for controlling this asymmetry is not well understood and hence remains an interesting topic for further studies. Meanwhile, we can correct for this asymmetry, post-measurement, by averaging the differential conductance at each positive energy with its negative counterpoint and assigning this same value for both points. We perform this symmetrization procedure for each differential conductance trace at all phases and all fields, and the corrected results were shown earlier in Figures 3.3 and 3.4.

3.8 Obtaining the Zero-Bias Curvature

To illustrate the continuous opening of the window containing the zero-energy peaks, we analyze the symmetrized data and identify whether the differential conductance curve at each particular B_z and B_x contains a zero-energy peak. To quantify this property, we extract the local curvature of the differ-

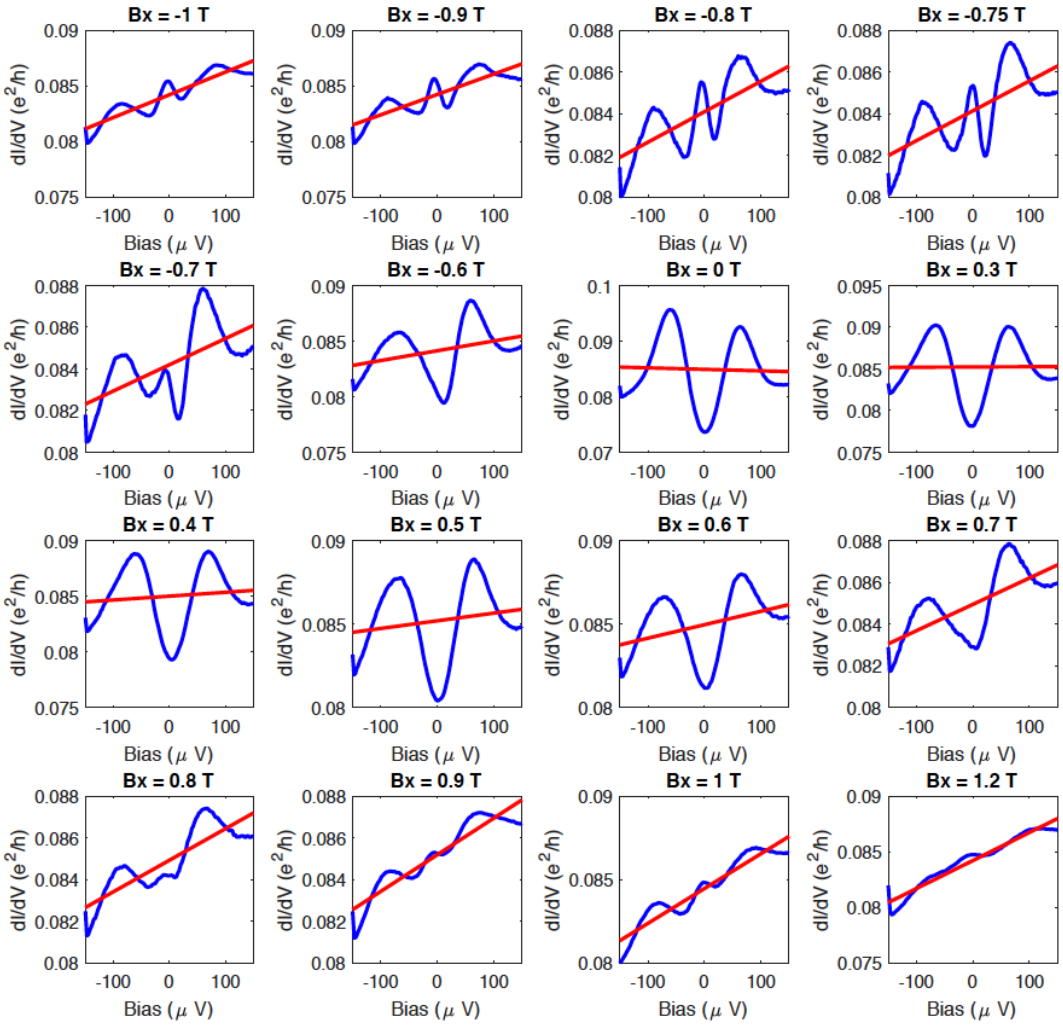

Figure 3.11: Development of the electron-hole asymmetry with the in-plane field. Each panel above shows, in a blue, solid curve, the raw measurement of the tunneling conductance, averaged over an entire period in the phase difference φ, at a given in-plane field B_x, labeled above the panel. The red line in each panel shows the linear regression of that tunneling conductance curve, from which the slope representing the asymmetry is extracted.

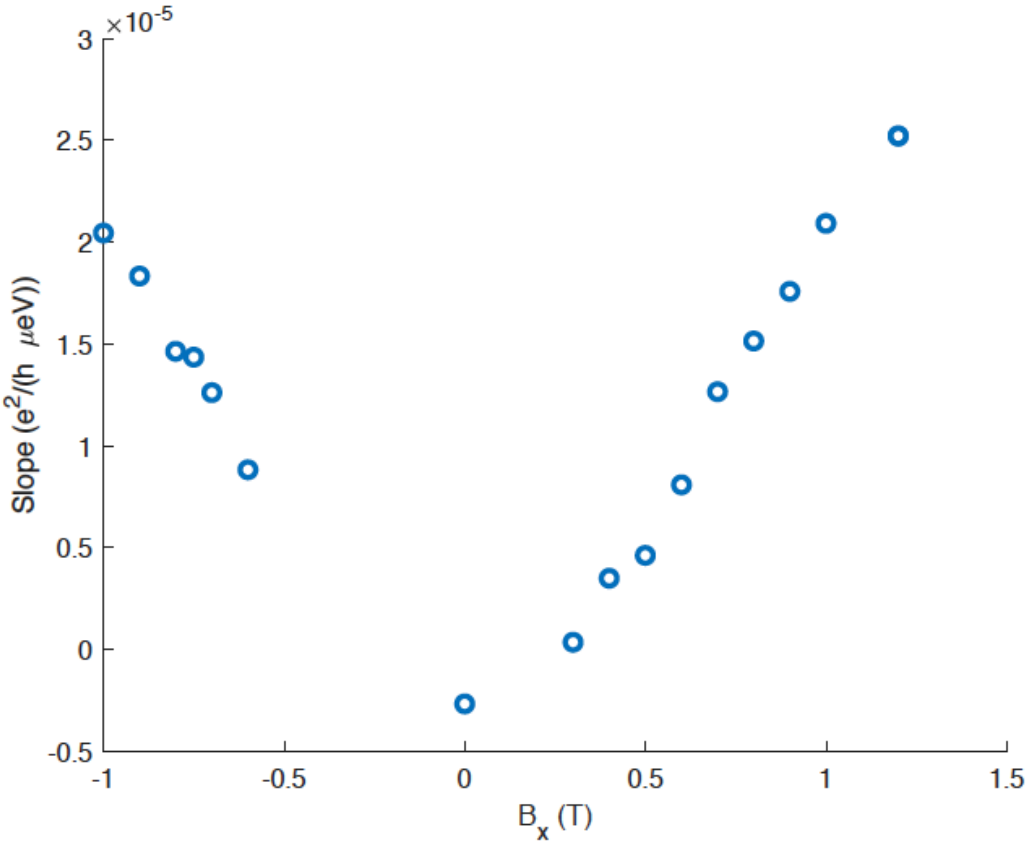

Figure 3.12: Slope of the electron-hole asymmetry versus the in-plane magnetic field. Each point in the above plot represents a slope extracted from the linear regression shown in Figure 3.11, in units of $e^2/(h \cdot \mu eV)$. Overall, the asymmetric slope increases linearly with the magnitude of the in-plane field, and it is independent of the sign of the field.

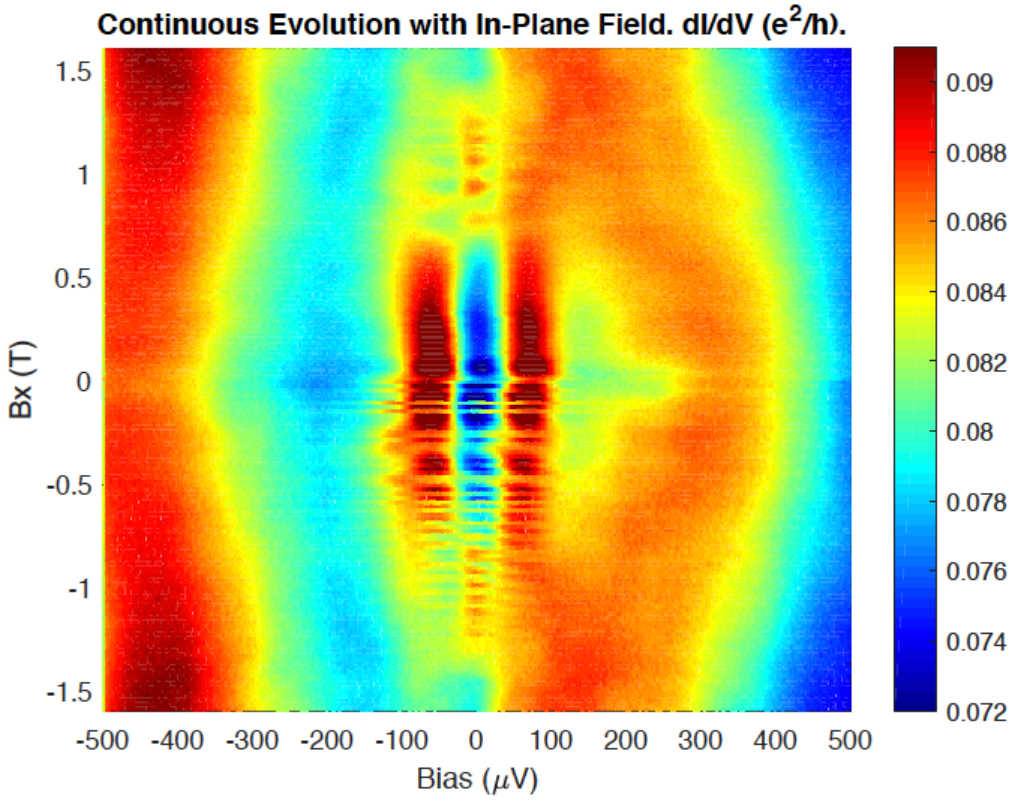

Figure 3.13: Differential conductance colormap as B_x varies continuously. Shown here is a continuous evolution of the tunneling conductance curve, over a wide range of the in-plane field B_x from -1.6 T to 1.6 T. Because our compensation of the perpendicular component of the in-plane magnetic field is not perfect, there is still a small flux which causes oscillations in the phase φ at the same time as the field grows. Data shown here is obtained from Device Beta.

ential conductance near zero-energy. For any differential conductance curve, we fit a parabola to its central segment, and hence extract the curvature from the fitting parameters. This is a good proxy for whether it contains a zero-energy peak as such peaks would make the center of the otherwise convex part of the curve concave, resulting in a negative curvature.

We obtain the curvature of the zero-energy conductance peak using parabolic fits. As seen in the fitting examples in Figure 3.14, the sign of the curvature correlates well with whether the curve contains a peak (panels e and f) or dip (panels a and c) at zero energy, and the amplitude roughly indicates its visibility. We can do this for each differential conductance curve at any particular phase difference φ and any in-plane field, B_x. The parabolic fit works the worst when the differential conductance is flat in the central region, as shown in panels b and d. In such cases, our method produces a rather small curvature, so the overall analysis is minimally affected. A color map of the extracted curvature as a function of both phase difference φ and the Zeeman field B_x is shown in Figure 3.4i earlier.

We would like to emphasize that the zero-bias curvature, which indicates the presence of a zero-bias peak in the tunneling conductance and is central to our main result, does not change during the symmetrizing process, as can be seen in the examples shown in Figure 3.15. This is because by symmetrizing the conductance as a continuous function of tunneling voltage, we preserve all even terms in its polynomial expansion and eliminate all odd terms. This results in no error in the fitting coefficient of the second-order term, which is the curvature we extract using the parabolic fit. To provide an intuitive picture, a few examples of the parabolic fits on both raw and symmetrized data are shown in Figure 3.15. The curvature extracted from symmetrized data is shown in Figure 3.16, which shows the same result as extracted from the raw data, was shown in Figure 3.4i.

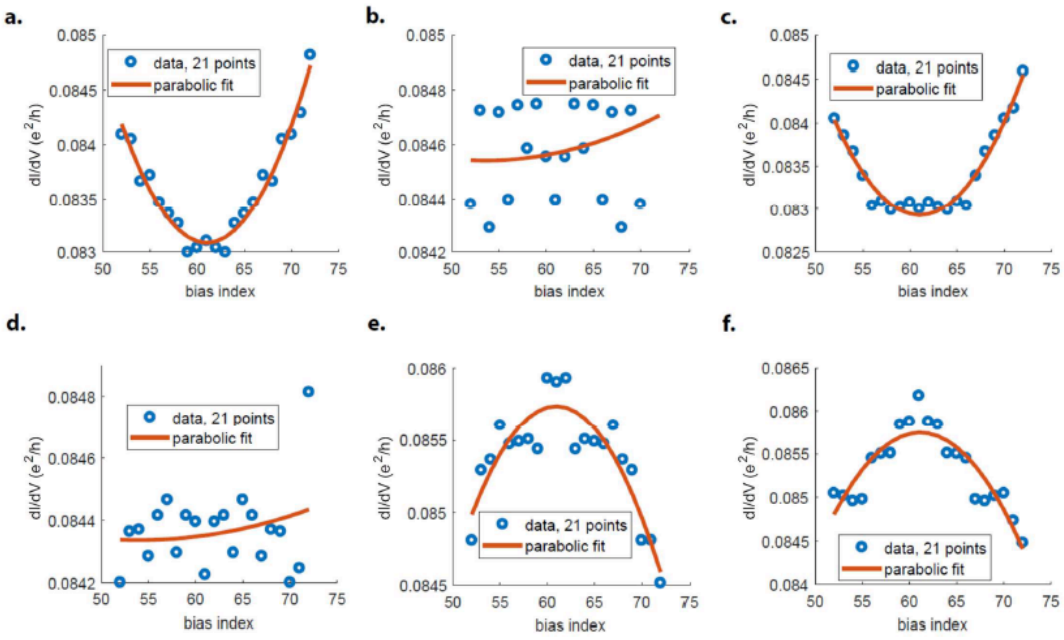

Figure 3.14: Extracting the curvature of zero-energy peaks using parabolic fits. Shown above are a few examples of extracting the curvature of zero-energy peaks using parabolic fits, at B_x =0.8 T, demonstrating the fitting procedure works nicely for a well-defined peak (dip), producing a negative (positive) curvature. Yet, the parabolic fit works not so well when the curve is flat in this region, in which case it yields a small curvature, as desired.

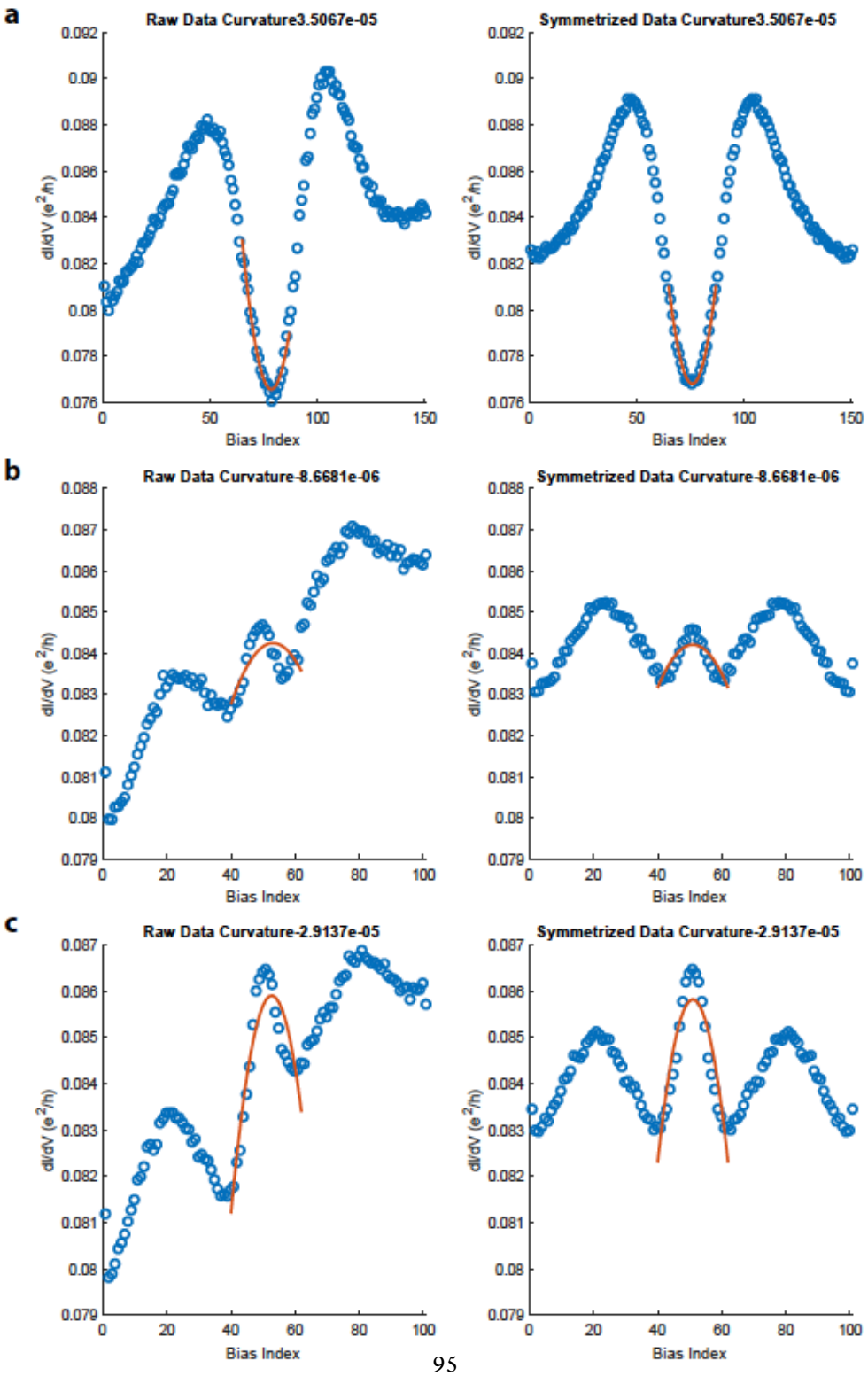

Figure 3.15: Extracted zero-energy curvatures from raw data versus symmetrized data. a-c, Shown here are three examples of extracting the curvature of zero-energy peaks using parabolic fits, from the raw conductance data on the left, and from the symmetrized conductance data on the right. They show the same results because the curvature, which is the second order coefficient, is unchanged by the symmetrizing process.

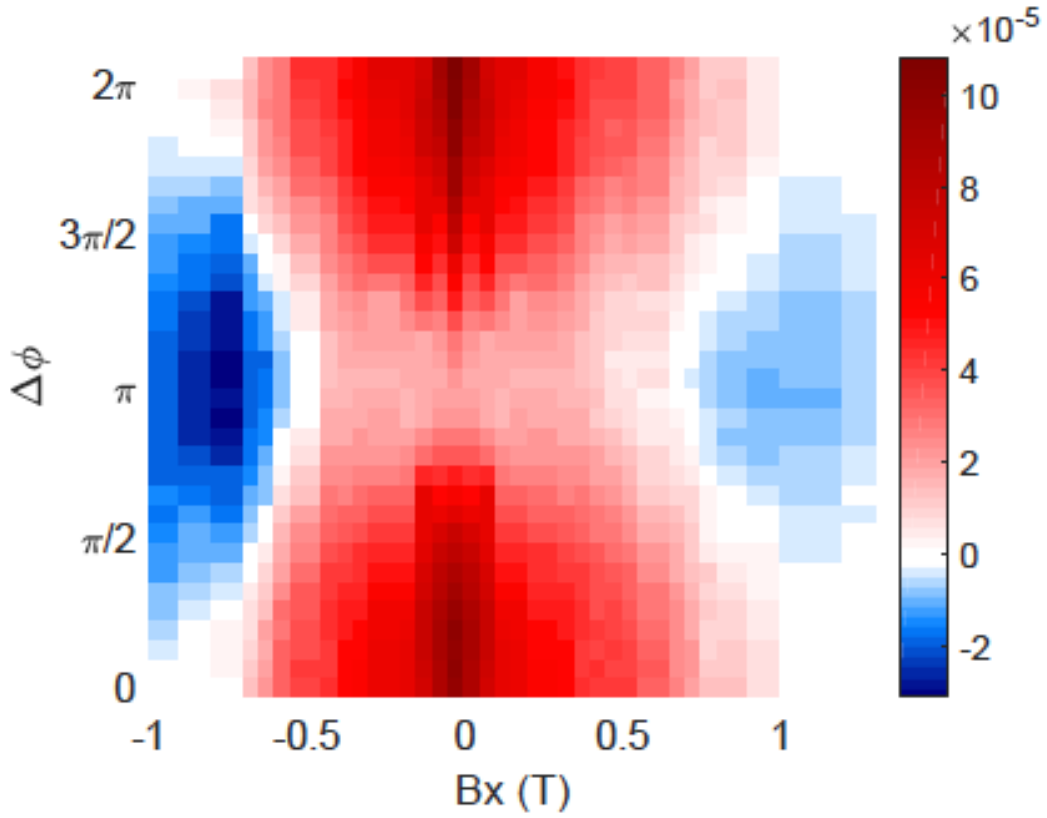

Figure 3.16: Extracted zero-energy curvatures from raw data versus symmetrized data. The zero-bias curvature extracted from the symmetrized data, as a function of both the in-plane magnetic field B_x and phase difference offset $\Delta\varphi$, shown in units of $e^2/h \cdot \mu\text{eV}^{-2}$, which produces the same graph as extracted from the raw data.

3.9 Two Additional Devices with Similar Behavior

To demonstrate reproducibility for the general trend of the zero-bias curvature, here we present two other devices with different geometries but showing similar effects as Device Beta. Device Kappa has a junction that is 400nm wide and 4 μm long, with a tunnel resistance around 12 MΩ. The raw and symmetrized conductance data of Device Kappa are shown in Figures 3.17 and 3.18 respectively. Device Zeta has a junction that is 800nm wide and 1 μm long, with a tunnel resistance around 3 MΩ. The raw and symmetrized conductance data of device Zeta are shown in Figures 3.19 and 3.20 respectively. Due to their low tunnel conductance, they give low signal-to-noise ratios, making them less immune to the phase smearing effects at high in-plane fields, as discussed in Section 3.6. Nevertheless, we see the same qualitative trend of an enhanced zero-energy conductance extending over a growing range of φ as the in-plane field increases.

We see again that the electron-hole asymmetry in the tunneling conductance is present in these two devices, and the slopes of this asymmetry in these two devices are opposite to that of Device Beta. Yet, just like in the case of the device shown earlier, the sign of this slope is independent of the sign of the field. This suggests the asymmetry may be related to device-specific effects such as local potentials or disorders.

Moving towards narrower junctions brings potential benefits to the experiment. As we will show in Section 3.14, a long junction which is 400nm wide holds the promise of showing zero-bias peaks both associated with the phase transition, in the field range we have measured, and from the Majorana bound states, at even higher fields. However, due to the phase smearing effect, the modulation of our

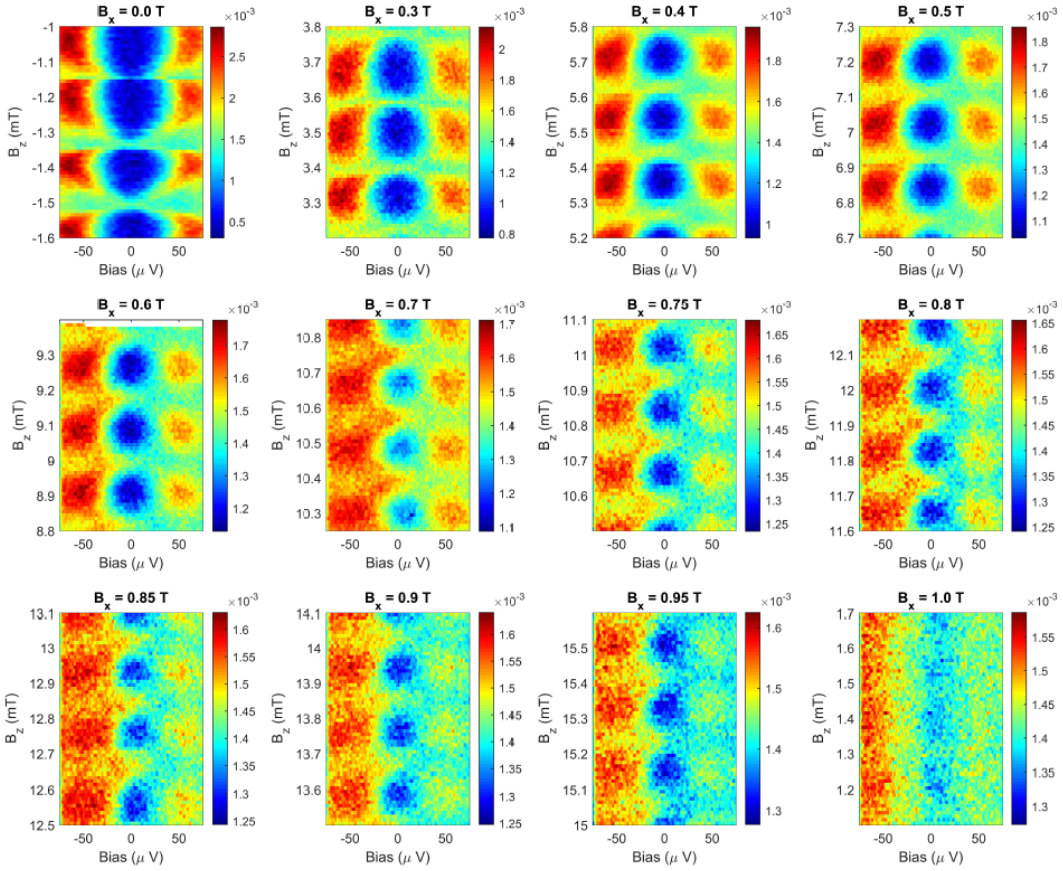

Figure 3.17: Differential conductance colormaps of device Kappa at various B_x values. Shown here is the raw data for a series of two-dimensional tunneling conductance maps as a function of the bias voltage and the perpendicular field B_z, as the in-plane field B_x increases from 0 T to 1.0 T. All plots are in units of e^2/h and span over a range of 0.6 mT in B_z.

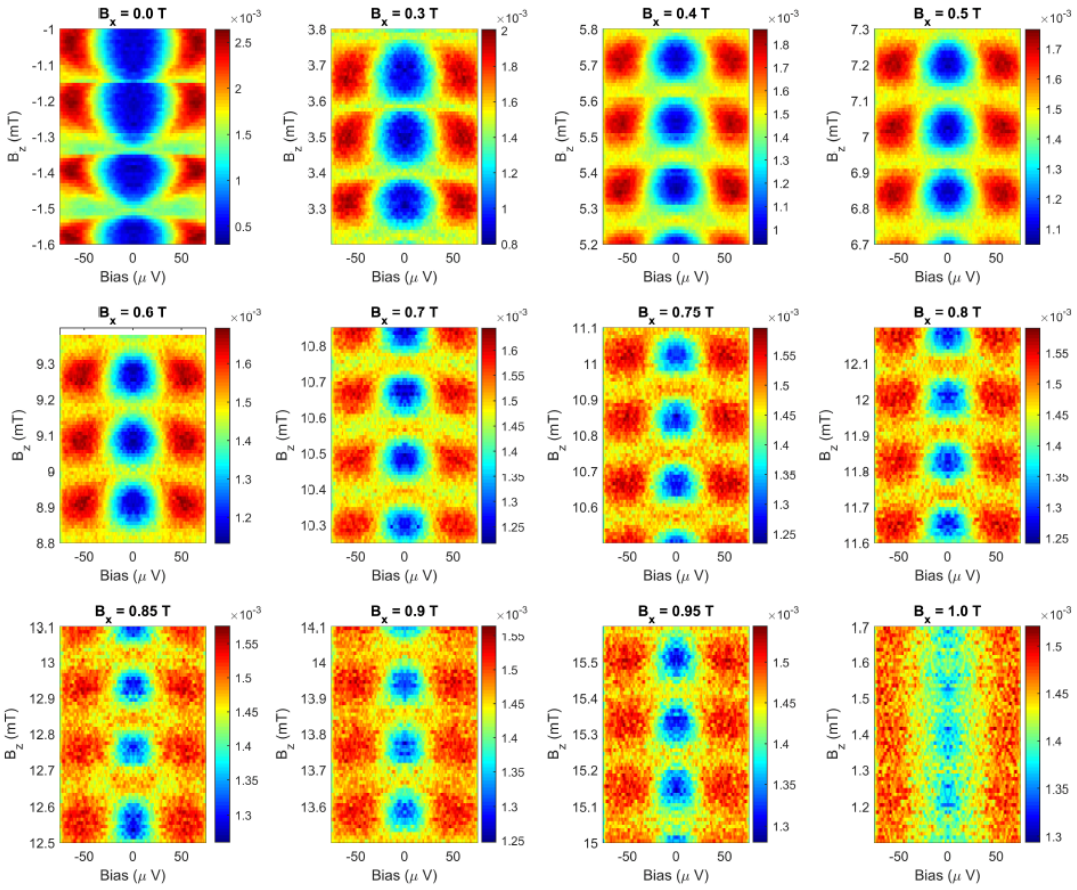

Figure 3.18: Symmetrized differential conductance colormaps of device Kappa at various B_x values. Shown here is the symmetrized data for a series of two-dimensional tunneling conductance maps as a function of the bias voltage and the perpendicular field B_z, as the in-plane field B_x increases from 0 T to 1.0 T. All plots are in units of e^2/h and span over a range of 0.6 mT in B_z.

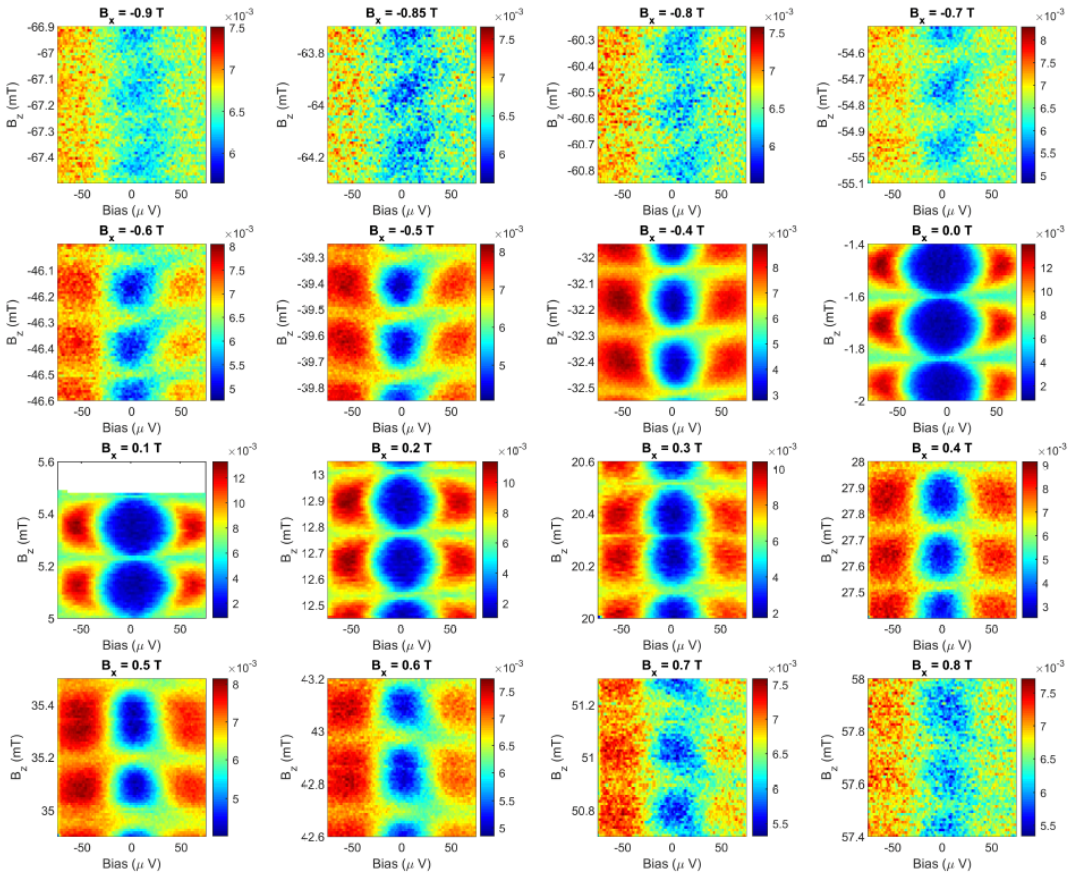

Figure 3.19: Differential conductance colormaps of device Zeta at various B_x values. Shown here is the raw data for a series of two-dimensional tunneling conductance maps, as the in-plane field B_x ranges from -0.9 T to 0.8T. All plots are in units of e^2/h and span over a range of 0.6 mT.

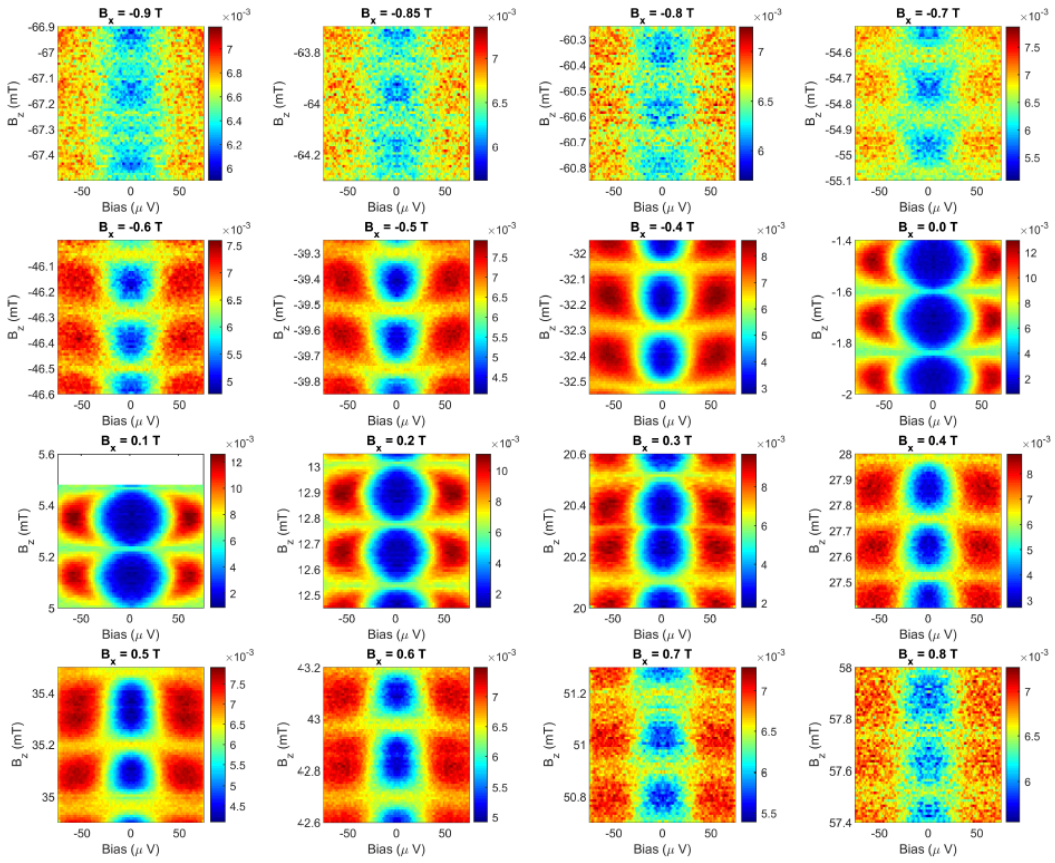

Figure 3.20: Symmetrized differential conductance colormaps of device Zeta at various B_x values. Shown here is the symmetrized data for a series of two-dimensional tunneling conductance maps, as the in-plane field B_x ranges from -0.9 T to 0.8T. All plots are in units of e^2/h and span over a range of 0.6 mT in B_z.

tunneling conductance diminishes much below the field required to see the latter ZBP in this 400-nm-wide junction, and, therefore, we only observe the former type of peak in conductance. This points out an immediate direction for fabrication development to improve the lithographic definition and interfacial quality of the superconducting film with the quantum well, so that future experiments can go up to higher in-plane fields, and, therefore, down to narrower junctions. Such improvements will allow us to explore this topological phase transition physics and the associated Majorana bound states with a more discrete spectrum, without losing the experimental signal due to the undesired phase smearing effect.

3.10 Numerical Calculation of the Tunneling Conductance

Our theoretical description of the system is based on the model used in Pientka et al. for a two-dimensional semiconductor with Rashba spin-orbit interaction defined on a rectangular region[56]. The region has length L and is divided into three segments: a normal region of width W between two superconducting regions of width W_{SC} (see rectangle with black contour in Figure 3.21). The Bogoliubov-de Gennes Hamiltonian can be written in the Nambu basis $(\psi_\uparrow, \psi_\downarrow, \psi_\downarrow^\dagger, -\psi_\uparrow^\dagger)$ as $H = \int d^2r \psi^\dagger(\mathbf{r})\mathcal{H}(\mathbf{r})\psi(\mathbf{r})$ with

$$\mathcal{H}(\mathbf{r}) = \left[\frac{p^2}{2m} - \mu(y) + \frac{ma^2}{2}\right]\tau_z + E_Z(y)\sigma_x + a(p_x\sigma_y - p_y\sigma_x)\tau_z + \Delta(y)\tau_+ + \Delta(y)\tau_-, \qquad (3.1)$$

where m is the effective mass, a the strength of the Rashba spin-orbit interaction and the σ (τ) are Pauli matrices in spin (particle-hole) space.

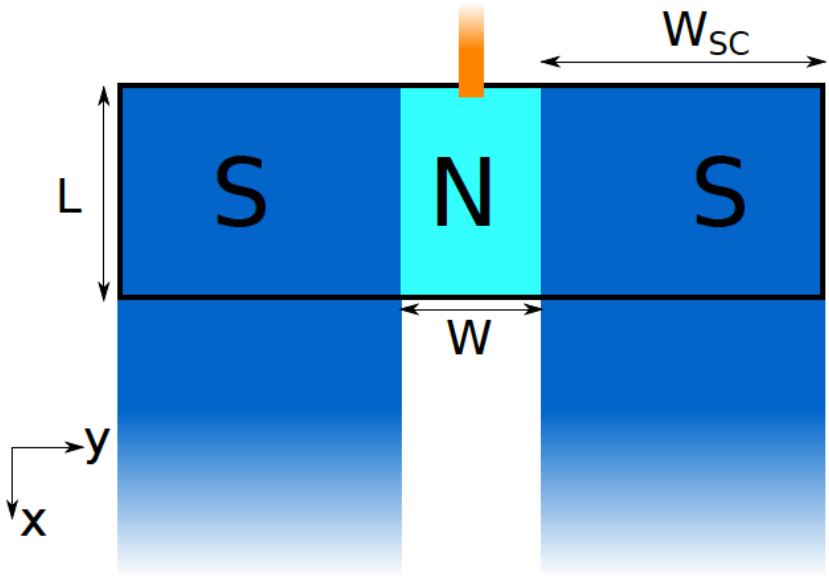

Figure 3.21: Setup modeled in the numerical calculations. The system comprises a rectangular region with a normal and two superconducting segments (black contour). To calculate the conductance, we add a semi-infinite normal lead in the junction center near the upper edge (orange) and two semi-infinite superconducting leads contacting the superconducting segments at the bottom edge.

The Zeeman energy $E_Z(y) = g(y)\mu_B B/2$, chemical potential μ and pairing strength Δ are all affected by the proximity coupling between the semiconductor and the superconductor and therefore assume different values in the junction and in the leads. We write

$$\Delta(y) = \Delta[e^{-i\varphi/2}\Theta(-y) + e^{i\varphi/2}\Theta(y-W)], \tag{3.2}$$

$$g(y) = g_N\Theta(y)\Theta(W-y) + g_{SC}[1-\Theta(y)\Theta(W-y)], \tag{3.3}$$

$$\mu(y) = \mu_N\Theta(y)\Theta(W-y) + \mu_{SC}[1-\Theta(y)\Theta(W-y)], \tag{3.4}$$

where φ is the phase difference across the junction. Because of the experimental finding that the coherence peaks remain at the same energy for the entire magnetic field range, we henceforth assume the Zeeman energy to be completely suppressed in the superconducting part, setting $g_{SC} = 0$ and denote $E_Z = g_N\mu_B B/2$.

For the numerical calculations it is convenient to consider the same model on a square lattice. The corresponding tight-binding Hamiltonian can be written in terms of the Nambu spinors $c_{i,j} = (c_{i,j,\uparrow}, c_{i,j,\downarrow}, c^\dagger_{i,j,\downarrow}, -c^\dagger_{i,j,\uparrow})^{\mathrm{T}}$ as

$$\begin{aligned} H = &-\sum_{i=1}^{L-1}\sum_{j=-W_{SC}+1}^{W+W_{SC}} [c^\dagger_{i,j}(t + ia_{\mathrm{TB}}\sigma_y)\tau_z c_{i+1,j} + \mathrm{h.c.}] \\ &-\sum_{i=1}^{L}\sum_{j=-W_{SC}+1}^{W+W_{SC}-1} [c^\dagger_{i,j}(t - ia_{\mathrm{TB}}\sigma_x)\tau_z c_{i,j+1} + \mathrm{h.c.}] \\ &+\sum_{i=1}^{L}\sum_{j=-W_{SC}+1}^{W+W_{SC}} \left[c^\dagger_{i,j}\left(4t + \frac{a^2_{\mathrm{TB}}}{t} - \mu(j) + E_Z(j)\sigma_x\right)\tau_z c_{i,j} + (\Delta(j)c_{i,j}\tau_x c_{i,j} + \mathrm{h.c.})\right] \end{aligned} \tag{3.5}$$

In the limit $t \to \infty$, the tight-binding model maps onto the continuum model in Eq. (3.1) with the replacements $c_{i,j} \to a\psi(\mathbf{r})$, $\alpha_{\mathrm{TB}} \to \alpha/2a$ and $t \to 1/2ma^2$, where a is the lattice constant.

For the numerical calculations presented earlier in Section 3.4, we use the following parameters in the continuum model of Eq. (3.1): $\alpha = 34$ meVnm, $\Delta = 64\,\mu$eV, $\mu_N = 12.5$ meV, $\mu_{SC} = 50$ meV, $g_n = 10$, and $m = 0.033m_e$, where m_e is the electron mass.

The tight-binding parameters are chosen accordingly as $t = 32$ meV, $\alpha_{\mathrm{TB}} = 0.089t$, and $a = 6$ nm.

The phase diagram and subgap spectrum shown in Figures 3.1 and 3.2 is evaluated using the continuum model with $L = \infty$ and $W_{SC} = \infty$. In this case the momentum along the x direction is conserved and can be replaced by a number k_x. The subgap spectrum can then be found by evaluating the scattering matrix $S(E)$ for states inside the junction and solving the equation

$$\det\{1 - S[E(k_x)]\} = 0 \tag{3.6}$$

(see Pientka et al. for the numerical procedure[56]). The phase boundaries correspond to zero-energy crossings at $k_x = 0$.

An evaluation of the conductance through the system requires the addition of external leads. To model the experimental setup, we attach a normal lead near the upper edge of the normal region and two superconducting leads contacting the lower edges of the superconducting segments as shown in Figure 3.21. We choose system dimensions $L = 150$, $W = 100$, and $W_{SC} = 200$ corresponding to a junction area of 900 nm $\times$ 600 nm.

The normal lead is added as a second layer, which extends infinitely in the $x \to -\infty$ direction and

is connected to the junction by vertical tunnel couplings in the area $i_1 \leq i \leq i_2$ and $j_1 \leq j \leq j_2$. The additional contribution to the Hamiltonian reads

$$\begin{aligned} H_L = & \sum_{i=-\infty}^{i_2} \sum_{j=j_1}^{j_2} (4t - \mu_L) d_{i,j}^\dagger \tau_z d_{i,j} \\ & - \Big(t \sum_{i=-\infty}^{i_2-1} \sum_{j=j_1}^{j_2} d_{i,j}^\dagger \tau_z d_{i,j+1} + t \sum_{i=-\infty}^{i_2} \sum_{j=j_1}^{j_2} d_{i-1,j}^\dagger \tau_z d_{i,j} + t_L \sum_{i=i_1}^{i_2} \sum_{j=j_1}^{j_2} d_{i,j}^\dagger \tau_z c_{ij} + \text{h.c.} \Big) \end{aligned} \tag{3.7}$$

In our simulations, we choose $\mu_L = 4t, t_L = 0.2t$. The contact area is defined by $i_1 = 1, i_2 = 6$, $j_1 = 43, j_2 = 58$, which corresponds to an area of $\sim 40\,\text{nm} \times 100\,\text{nm}$.

The superconducting leads simply continue the two superconducting segments in the $x \to \infty$ direction

$$\begin{aligned} H_{SC,L} = & - \sum_{i=L+1}^{\infty} \Big(\sum_{j=-W_{SC}+1}^{0} + \sum_{j=W+1}^{W+W_{SC}} \Big) \Big[\Big(4t + \frac{a_{\text{TB}}^2}{t} - \mu_{SC} \Big) c_{i,j}^\dagger \tau_z c_{i,j} + (\Delta(j) c_{i,j} \tau_x c_{i,j} + \text{h.c.}) \Big] \\ & - \sum_{i=L}^{\infty} \Big(\sum_{j=-W_{SC}+1}^{0} + \sum_{j=W+1}^{W+W_{SC}} \Big) [c_{i,j}^\dagger (t + i a_{\text{TB}} \sigma_y) \tau_z c_{i+1,j} + \text{h.c.}] \\ & - \sum_{i=L}^{\infty} \Big(\sum_{j=-W_{SC}+1}^{-1} + \sum_{j=W+1}^{W+W_{SC}-1} \Big) [c_{i,j}^\dagger (t - i a_{\text{TB}} \sigma_x) \tau_z c_{i,j+1} + \text{h.c.}]. \end{aligned} \tag{3.8}$$

We use the KWANT library to calculate the scattering matrix of the system with respect to the external leads. The conductance between the normal lead at a finite bias voltage eV and the two grounded superconductors can then be evaluated according to the formula

$$G(eV) = \frac{e^2}{h} [N - R_{ee}(eV) + R_{eh}(eV)], \tag{3.9}$$

where N is the number of channels in the lead and $R_{ee,eh}(\varepsilon)$ are the normal and Andreev reflection probability in the normal lead at energy ε. To account for the limited energy resolution in the experiment, we convolute the conductance as a function of energy with a Gaussian with standard deviation 24 μeV. Moreover, we include a broadening of the conductance as a function of phase difference by convolution with a Gaussian with standard deviation 0.4π. This accounts for an inhomogeneous phase difference across the junction in the experiment, caused by the flux threaded through the junction area and a spatially varying random phase due to the combination of the parallel field and the interface roughness of the superconducting leads[30].

3.11 Majorana Wavefunction

To elucidate possible Majorana signatures in the conductance, we calculate the local density of states (LDOS) associated with the lowest energy state in the junction. A bona-fide Majorana state only exists in a semi-infinite system. To consider this situation, we set $L \to \infty$ in the setup in Figure 3.21, such that both superconducting leads and the normal region are semi-infinite. We can then calculate the LDOS at zero energy as a function of position using KWANT.

The resulting spectra weight of the Majorana state is shown in Figure 3.22(a). While the state is indeed localized at the edge, its decay is nonexponential. This is consistent with the fact that the coherence length is very long for the parameters assumed in the previous section. The typical scale for the induced gap is $1/mW^2 \simeq 6\,\mu$eV which agrees with our numerical calculations of the energy spectrum. This gap translates into a coherence length of $\sim 45\mu m$.

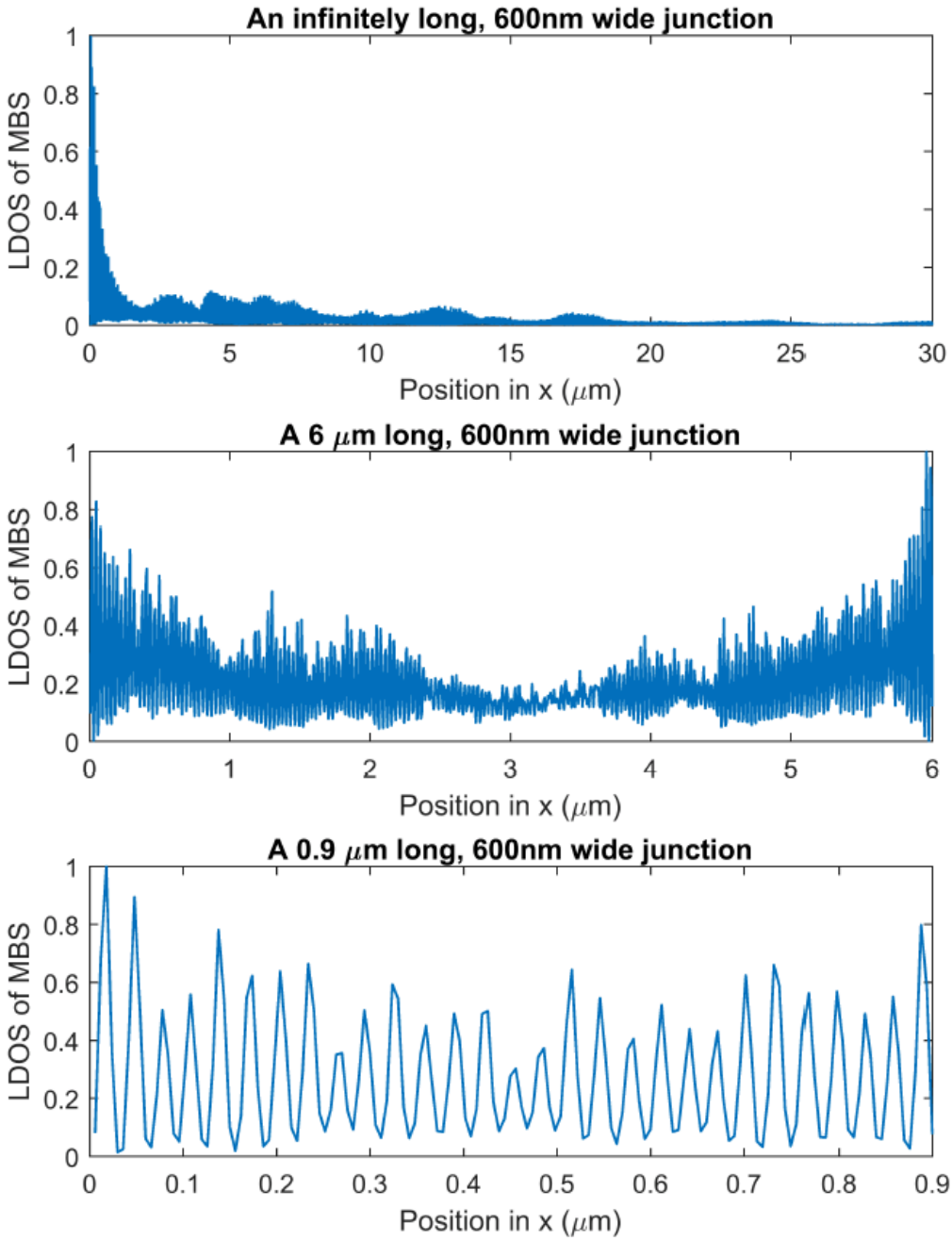

Figure 3.22: Delocalization of the Majorana bound state. Normalized local density of states of the lowest energy excitation, averaged over the width of the junction, as a function of distance from the edge in the setup of Figure 3.21 with $W = 600$ nm and (a) $L = \infty$, (b) $L = 6\,\mu$m, and (c) $L = 900$ nm.

We can also calculate the LDOS in finite-length junctions using the setup in Figure 3.21. In this case, the Majorana states at the two ends hybridize and form a finite energy excitation. In Figure 3.22(b) and (c), we show the LDOS corresponding to the lowest energy state for $L = 6\,\mu$m and $L = 900$ nm. In Figure 3.22(b), the edge localization remains visible. In contrast, the 900 nm junction in Figure 3.22(c) is too short to allow for any distinction between edge and bulk and the lowest-energy state is homogeneously distributed along the entire length of the junction.

These results suggest that, even though the system is in the topological phase, signatures of Majorana states cannot be distinguished from bulk signatures in devices with current dimensions.

3.12 Origin of the Zero-Bias Conductance Peak

The normal probe in the experiment is in the tunneling regime and the conductance is therefore expected to reflect the local density of states in the junctions. The long Majorana localization length discussed above implies a weak contribution of Majoranas to the conductance, which is washed out due to the energy broadening. Instead, the subgap conductance will be dominated by the band of Andreev states that extend along the entire length of the junction.

In this section, we derive an analytical formula for the Andreev spectrum in a certain limiting case, which can be compared with the numerical results for the full Hamiltonian (3.1) shown earlier in Figure 3.2a. We then use this estimate to calculate the density of states.

To gain analytical insight, we assume that edge effects are small and simply consider the bulk density of states in an infinitely long junction, in which the momentum component k_x is conserved. We

first focus on the case of perfect Andreev reflection and later include normal reflection. As previously, we determine the bound state energies E as a function of k_x from the scattering matrix equation (3.6) within the continuum model Eq. (3.1). It is expedient to introduce the polar angles θ_i defined by $\cos\theta_i = k_x/k_{F,i}$, where $i = 1, 2$ denotes the two Fermi surfaces and $k_{F,1/2} = \sqrt{2m\mu} \pm ma$.

We can further simplify Eq. (3.6) in the case that Andreev reflection does not mix the two Fermi surfaces. This is strictly true only at $k_x = 0$, where the spins on the two Fermi surfaces are antiparallel, while at nonzero k_x, a right moving electron can be Andreev reflected into a superposition of left moving holes from both Fermi surface sheets due to a nonzero overlap of spin states[56].

In the limit $E_Z, \Delta \ll ak_F$, however, the two spins along a particular momentum direction are antiparallel because of the Rashba-induced spin-momentum locking. In this case, the two Fermi surfaces at a fixed k_x have approximately opposite spins as long as the corresponding polar angles have similar magnitude $\theta_1(k_x) \simeq \theta_2(k_x) \equiv \theta(k_x)$.

Under these conditions, Eq. (3.6) yields[56]

$$\arccos\left[\frac{E(k_x)}{\Delta}\right] = \frac{\pi}{2}\frac{E(k_x)}{E_T(k_x)} - \frac{\pi}{2}\frac{\sin\theta E_Z}{E_T(k_x)} \pm \frac{\varphi}{2} + n\pi, \qquad n \in \mathbf{Z}, \tag{3.10}$$

where $E_T(k_x) = (\pi/2)\sin\theta v_F/W$ is the Thouless energy. The angular dependence of $E_T(k_x)$ reflects the longer distance between the superconducting leads for wavepackets with oblique incidence. The factor $\sin\theta E_Z$ accounts for the fact that spins rotate along the Fermi surface. Considering the limit $E_T(k_x) \gg \Delta$ as is appropriate in our parameter regime for states near $k_x = 0$ [$E_T(k_x = 0) =$

630 μeV], we find

$$E = \Delta \cos\Big(\frac{WE_Z}{v_F} \pm \frac{\varphi}{2} + n\pi\Big) \tag{3.11}$$

which is independent of k_x. Hence the bands are expected to be relatively flat. As k_x approaches the Fermi momentum, $E_T(k_x)$ decreases and the energy becomes momentum dependent. This is behavior is consistent with the spectrum in Figure 1e of the main text. We caution, however, that Eq. (3.10) requires $\theta_1 \simeq \theta_2$ and therefore ceases to be valid as k_x approaches the Fermi momenta.

The flatness of the dispersion should result in a strong peak in the LDOS at the corresponding energy, while the spectral weight at other energies is smaller. This implies that topological phase transitions, where the energy in Eq. (3.11) vanishes, are signaled by a conductance peak at zero bias. Importantly this is a feature of the bulk density of states and does not take into account the contribution of the Majorana states.

The spectrum changes when normal reflection is taken into account. We specifically consider normal reflection from the superconducting leads that conserves the momentum along the x direction, e.g., caused by a potential step at the N-S interface. In this case, we have to modify Eq. (3.10) by replacing

$$\varphi \to \tilde{\varphi} = \arccos[r^2 \cos(2 \sin\theta k_F W + 2\phi_N) + (1 - r^2)\cos\varphi], \tag{3.12}$$

where r is the normal reflection amplitude and ϕ_N is a phase shift associated with the normal reflec-

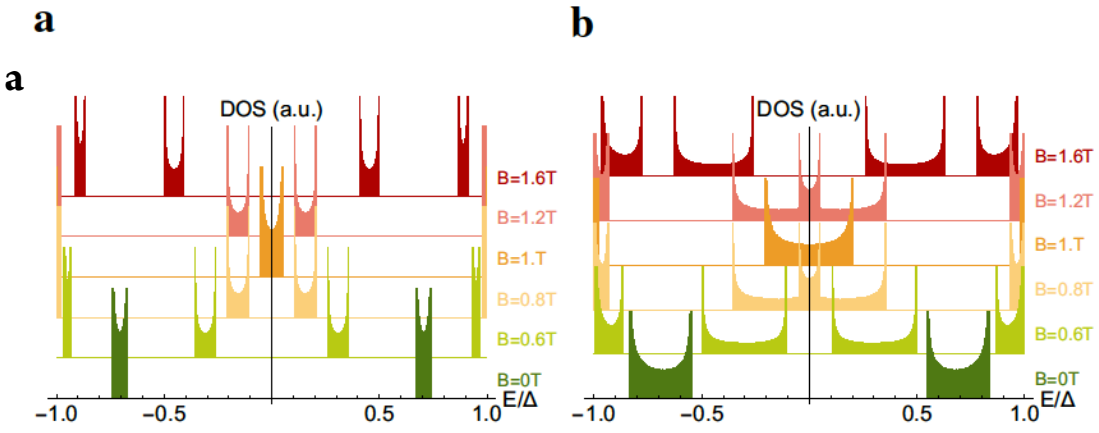

Figure 3.23: Calculated density of states of the Andreev band. Density of states of the Andreev band calculated from the approximate expression in Eqs. (3.11) and (3.12) for various values of the magnetic field. The superconducting phase difference is chosen as $\varphi = \pi/2$ and the normal reflection probability is a) $r^2 = 0.1$ and b) $r^2 = 0.4$. We assume $k_F W \gg 1$ so that the DOS is independent of ϕ_N. The other parameters are chosen as above. This choice implies that the phase transition for $\varphi = \pi/2$ and $r = 0$ occurs at $B = 1\,\mathrm{T}$ where $E_Z = E_T/2$.

tion that depends on microscopic details. Details of the derivation can be found in Pientka et al.[56] (although the prefactor $\sin\theta$ was missing in the reference). Since for our choice of parameters we have $k_F W \gg 1$, the first term in the square brackets above oscillates rapidly as a function of k_x. This results in oscillation of the Andreev energy as a function of k_x with an amplitude that scales with the reflection probability.

Indeed, these oscillations also occur in the numerical spectra shown in Figure 3.2b.

Since normal reflection broadens the band of Andreev states, the density of states calculated from Eqs. (3.11) and (3.12) exhibits significant contributions over a range of energy values. This can be seen in Figure 3.23, which shows the density of states for various values of the in-plane magnetic field calculated using Eqs. (3.11) and (3.12).

There are two van Hove singularities at the band edges because all maxima and minima of $E(k_x)$ in Eq. (3.11) occur at the same energies.

The band center and the approximate band width in Figure 3.23a is consistent with the numerical spectra shown in Figure 3.2a. Moreover, for $B = 0$ T and 1.6 T the energy minima and maxima of the spectra are roughly aligned for not too large momenta in agreement with our analytical findings. The spectrum at $B = 1$ T, by contrast, has aligned minima but not maxima.

By varying either φ or E_Z, one can tune the band center across zero energy. Once the band crosses zero energy the positive and negative energy bands overlap which leads to an enhanced density of states at zero energy. For weak normal reflection, the band widths are small and the density of states shown in Figure 3.23a is enhanced near zero energy only in a narrow window around the phase transition. This behavior is consistent with the spectra shown in Figure 3.2a.

If the normal reflection is higher, the band width increases as shown in Figure 3.23b. In this case, the density of states is enhanced near zero energy in a larger range of magnetic fields. While the density of states does not typically have a maximum at zero, an additional energy broadening applied to the data may result in a zero-bias peak. If the broadening is sufficiently large, the peak can persist between $B = 0.8$ T and $B = 1.2$ T for the parameters of Figure 3.23b. Such a behavior is quantitatively consistent with the numerical data for the conductance in Figure 3.5g, which shows a peak at zero bias over an extended region in parameter space.

We conclude that a zero-bias peak in the conductance signals the zero-energy crossing of a band of Andreev states, which corresponds to a topological phase transition. The width of the band is determined by the normal reflection probability from the superconducting leads. In the presence of a

nonzero band width and an additional broadening of the data in energy, a zero-bias peak can occur over an extended range of magnetic field strengths and phase differences in agreement with the experimental observations as well as the numerical results presented at the beginning of this chapter.

3.13 Finite-Difference Scheme and Exact Diagonalization

To show that the peak in the $\mathrm{d}I/\mathrm{d}V$ characteristics at the topological transition is a universal property for wide junctions, while for narrower junctions a competition between Andreev and Majorana bound states occurs, we perform a second type of calculation. Complementary to the previous section, we employ a finite-difference scheme to obtain the eigenspectrum and eigenstates of the finite Josephson junction shown in Figure 3.24.

These eigenstates and eigenenergies are then used to compute the local density of states (LDOS) at the edge of the normal region. For this purpose, we use the Hamiltonian (Equations 3.1-3.4) and invoke hard-wall boundary conditions in x- and y-directions to describe a Josephson junction of finite length L in the x-direction and finite width $W_{tot} = W + 2W_{SC}$ in the y-direction. Here, W is the width of the normal region and W_{SC} denotes the finite widths of the superconducting regions (see Figure 3.24). We discretize the Hamiltonian (Equations 3.1-3.4) using $\mathrm{d}\psi(x)/\mathrm{d}x \to [\psi(x_i + a) - \psi(x_i - a)]/2a$, $\mathrm{d}^2\psi(x)/\mathrm{d}x^2 \to [\psi(x_i + a) - 2\psi(x_i) + \psi(x_i - a)]/a^2$, and analogous expressions for the derivatives with respect to y, where a and $x_i = ai$ (with $i \in \mathbb{Z}$) denote the discrete step size and lattice

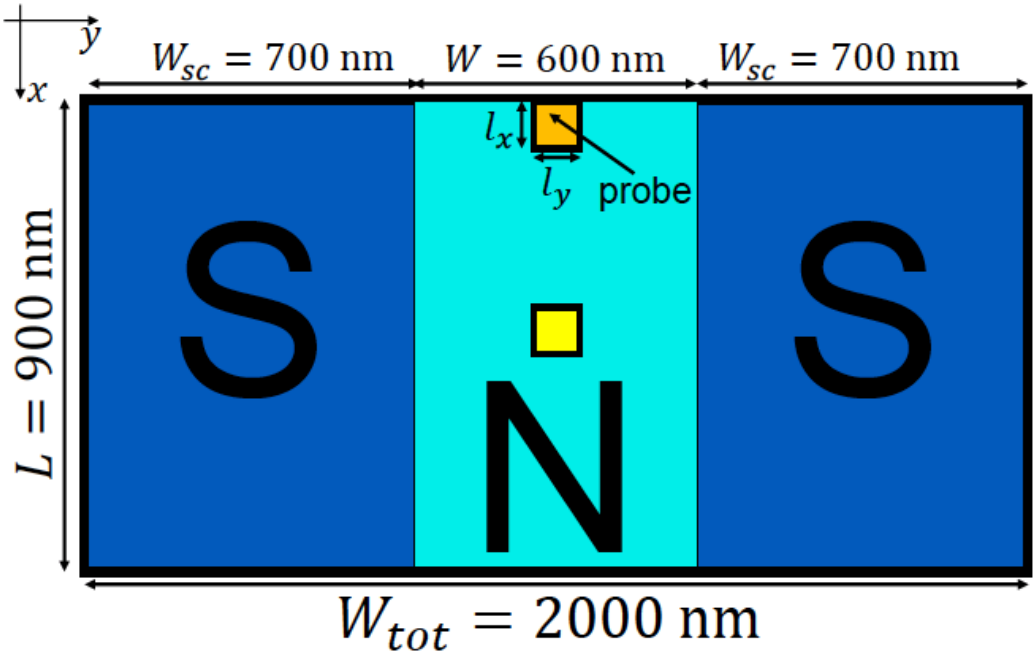

Figure 3.24: Setup considered for the complementary finite-difference eigenstate calculations. The system consists of a normal region of dimensions 900 nm $\times$600 nm and two adjacent superconducting regions of dimensions 900 nm $\times$700 nm. A phase difference of φ is applied between the two superconductors. The edge local density of states (LDOS) is calculated for an area of dimensions 100 nm $\times$100 nm at the top edge of the normal region (orange area). The LDOS in the bulk is computed from a 100 nm $\times$100 nm square in the center of the normal region (yellow area).

sites, respectively. This procedure yields Equation 3.5. If Equation 3.5 is written in the form

$$H = \sum_{i,i'=1}^{L} \sum_{j,j'=-W_{SC}+1}^{W+W_{SC}} \mathcal{H}_{i,j;i',j'}\, c^{\dagger}_{i,j} c_{i',j'}, \tag{3.13}$$

the eigenenergies $E^{(n)}$ and eigenstates $c^{(n)}_{i,j}$ of the system are found by diagonalizing the eigenvalue equation

$$\sum_{i'=1}^{L} \sum_{j'=-W_{SC}+1}^{W+W_{SC}} \mathcal{H}_{i,j;i',j'}\, c^{(n)}_{i',j'} = E^{(n)} c^{(n)}_{i,j}, \tag{3.14}$$

where n denotes the n-th eigenstate.

These eigenenergies and eigenstates are then used to compute the LDOS at the upper edge of the normal region as a function of energy E,

$$\mathrm{LDOS}(E) = \sum_{i=1}^{l_x} \sum_{j=W/2-l_y/2}^{W/2+l_y/2} \sum_{n} \left| c^{(n)}_{i,j} \right| \delta_\Gamma(E - E^{(n)}). \tag{3.15}$$

Here, $\delta_\Gamma(E - E^{(n)})$ is modeled by a Gaussian with broadening Γ. The area of summation is chosen to resemble the area covered by the tunneling probe with lengths l_x and l_y in the x- and y-directions, respectively (see Figure 3.24). In the lowest-order approximation, the $\mathrm{d}I/\mathrm{d}V$ characteristic is proportional to the LDOS. Hence, to compare with the experiment and the KWANT simulations, we first compute the LDOS for a given probe area and position and then look at the curvature $\partial^2 \mathrm{LDOS}/\partial E^2$ around $E = 0$.

3.14 Comparison of the Local Density of States for Josephson Junctions with Different Widths

In general, a zero-energy peak in the edge LDOS can originate from Majorana end states and/or low-energy bulk Andreev bound states. As discussed earlier, the most pronounced zero-energy peaks for a 600nm wide junction are expected to actually arise from the bulk Andreev bound states that describe the topological phase boundaries. Here, we study and compare the coexistence of zero-energy peaks in the edge LDOS due to Majorana end states and bulk Andreev states for samples of widths $W = 600$ nm or $W = 400$ nm.

For the calculations with a $W = 600$ nm wide normal region, we have used a=16 meVnm, Δ=65 μeV, $\mu_N = 12.5$ meV, $\mu_{SC} = 25$ meV, $g_N = 10$, $g_{SC} = 0$, and $m = 0.038 m_e$. The size of the superconducting regions is 900nm$\times$700nm and the size of the normal region 900nm$\times$600nm in the x- and y-directions, with a probe size of 100nm$\times$100nm. The discretization step is chosen as $a = 10$ nm. The lengths and widths as well as their corresponding numbers of steps are described by the same quantities, i.e. $L = 90$, $W_{tot} = 200$, $W_{SC} = 70$, $W = 60$, $l_x = 10$, and $l_y = 10$. To compute the LDOS via Eq. (3.15), a Gaussian broadening of $\Gamma = 0.25\Delta$ for $\delta_\Gamma(E - E^{(n)})$ has been used.

Figure 3.25 shows $\partial^2\text{LDOS}/\partial E^2$ at $E = 0$ for the above parameters as a function of the magnetic field B_x and the external phase difference φ between the two superconductors. Similar to the experiment and our KWANT simulations, we find that a zero-energy peak ($\partial^2\text{LDOS}/\partial E^2 < 0$) in the LDOS starts to appear at fields around $B_x = 0.4 - 0.5$ T and becomes the most pronounced around $B_x = 1.2$ T. As B_x increases further and (φ, B_x) moves away from the boundaries of the topological

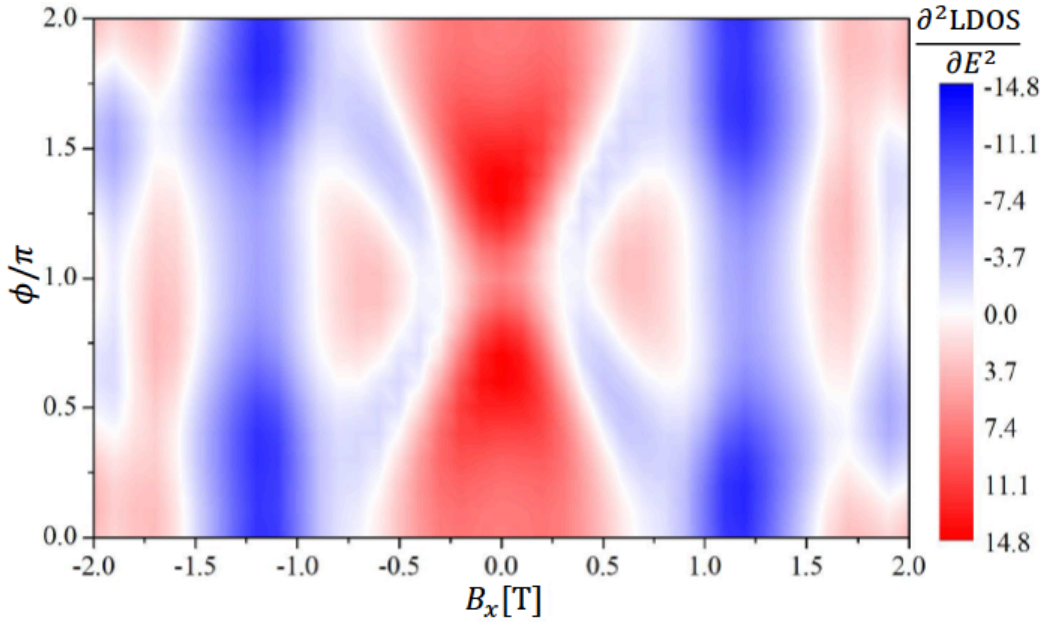

Figure 3.25: Predicted zero-bias curvature for a 600-nm junction. Calculated $\partial^2\mathrm{LDOS}/\partial E^2$ (in a.u.) at $E = 0$ as a function of magnetic field B_x and the phase difference φ between the superconducting regions for the setup illustrated in Figure 3.24. The area over which the LDOS is computed corresponds to a probe size of 100 nm $\times$100 nm at the upper edge of the normal region (orange area in Figure 3.24).

phase, the zero-bias peak disappears.

We note that we have chosen somewhat different parameters for the superconducting regions here compared to the KWANT simulations: The finite width W_{SC} of the superconducting regions is reduced to 700 nm (compared to 1200 nm), thereby increasing the amount of normal reflection due to the finite size of the superconductors. This effect is somewhat compensated for by reducing the mismatch between the chemical potentials μ_N and μ_{SC} (12.5:25 compared to 12.5:50 in the KWANT calculations), which is a second source for normal reflection at the S/N interfaces.

Likewise, the strength of Rashba SOC in the entire device is reduced by a factor of around 2 to $\alpha =$

16 meVnm to demonstrate the robust occurrence of a zero-energy peak in the LDOS/a zero-bias peak in the dI/dV-characteristic for a wide range of Rashba SOC strengths. This robustness with Rashba spin-orbit strength a of the topological phase boundaries and of zero-energy peaks at (segments of) these boundaries can also be explained within a scattering matrix approach.

The nature of the Majorana bound state is illustrated in Figure 3.26, which shows the probability amplitude $|\Psi(x, y)|^2$ of the lowest-energy state at $B_x = 1.2$ T and a phase difference $\varphi = \pi$. Due to the finite length L of the setup and the resulting hybridization of the two separate Majorana end states, this state is not situated at zero-energy. As argued above in Section 3.11, due to the small induced topological gap of the order of 6 μeV protecting the Majorana end states, these states are expected to decay only slowly away from the upper and lower edges of the normal region. This feature is exhibited in Figure 3.26, where the lowest energy state is spread over the entire normal region and only slightly localized at the boundaries of the normal region (see also Figure 3.22).

The large localization length of the Majorana end states in the sample with a 600-nm-wide normal region implies that the zero-energy peaks in the edge LDOS arise almost entirely from the bulk Andreev bound states at the topological phase boundaries. Indeed, comparing $\partial^2\text{LDOS}/\partial E^2$ around $E = 0$ computed at the edge with that computed in the center of the normal region yields qualitatively similar results.

To obtain more localized Majorana bound states, the topological gap, of the order of $\hbar^2/(mW^2)$, should be increased. Hence, a potential route is decreasing the width W and going to narrower devices. In fact, a sample with a $W = 400$ nm wide normal region is also available, Device Kappa in Section 3.9. Figure 3.27 shows $\partial^2\text{LDOS}/\partial E^2$ obtained for a junction of width $W = 400$ nm. In Figure 3.27,

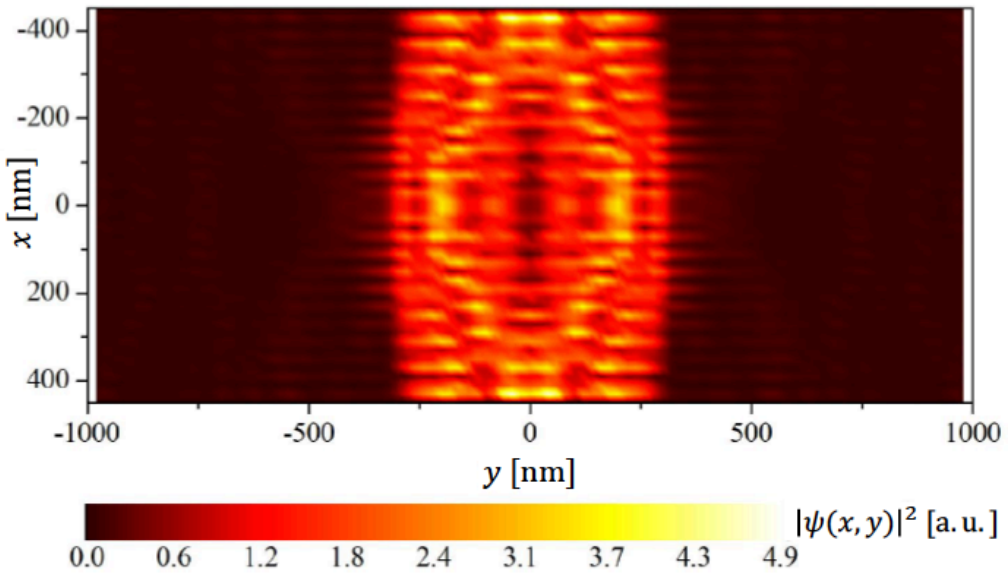

Figure 3.26: Wavefunction of the low-energy state for a 600-nm junction. Probability amplitudes $|\Psi(x,y)|^2$ of the low-energy state, calculated at $B_x = 1.2$ T and $\varphi = \pi$.

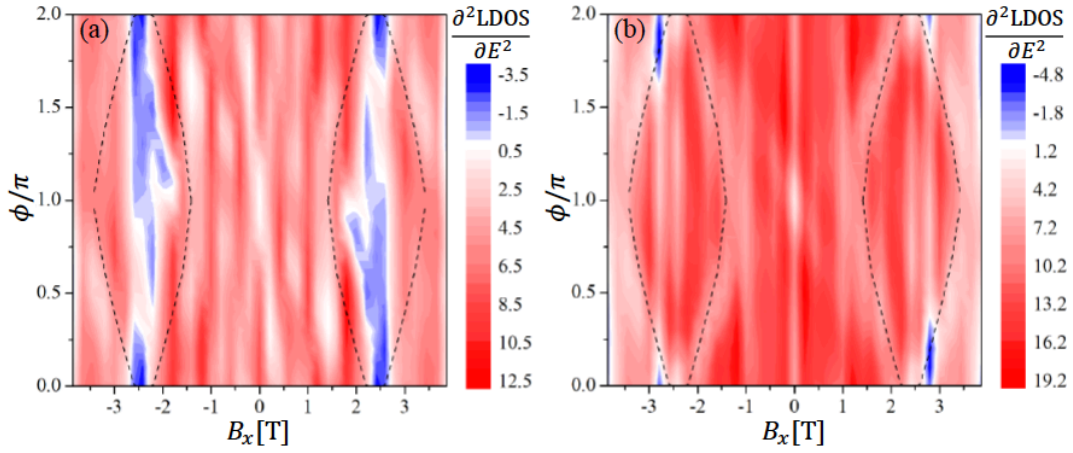

Figure 3.27: Predicted zero-bias curvature for a 400-nm junction. Calculated $\partial^2\mathrm{LDOS}/\partial E^2$ (in a.u.) at $E = 0$ for a Josephson junction of width $W = 400$ nm as a function of magnetic field B_x and the phase difference φ between the superconducting regions. Panel (a) shows the LDOS computed from a 100nm×100nm area at the upper edge of the normal region (orange area in Figure 3.24). Panel (b) shows the LDOS computed from a 100nm×100nm area in the center of the normal region (yellow area in Figure 3.24). The dashed lines indicate the boundaries of the topological phase obtained from an infinitely long junction $L \to \infty$.

the parameters are a=160 meVnm, Δ=130 μeV, $\mu_N = 10$ meV, $\mu_{SC} = 20$ meV, $g_N = 10$, $g_{SC} = 0$, and $m = 0.038 m_e$. Here, the size of the superconducting regions is 1000nm×800nm in the x- and y-directions, that of the normal region 1000nm×400 nm, and that of the probe 100nm×100nm. Using again a discretization step of $a = 10$ nm, the corresponding numbers of steps are $L = 100$, $W_{tot} = 200$, $W_{SC} = 80$, $W = 40$, $l_x = 10$, and $l_y = 10$ (again these symbols denote widths/lengths as well as the number of steps). The LDOS is computed with a Gaussian broadening of $\Gamma = 0.2\Delta$ in Eq. (3.15).

Similarly to Figure 3.25, the curvature of the LDOS at the edge of the normal region is shown in Figure 3.27(a). For these parameters, the topological phase arises only for fields above $B_x = 1$ T, as illustrated by the dashed lines denoting the boundaries of the topological phase. These boundaries have been obtained numerically for an infinitely long system ($L \to \infty$), which has other-

wise the same parameters as Figure 3.27(a). Whereas for the edge LDOS, no zero-energy peak is found outside the topological region ($\partial^2\mathrm{LDOS}/\partial E^2 > 0$; red areas in Figure 3.27), a zero-energy peak of the edge LDOS appears for a wide range of phase differences φ inside the topological region ($\partial^2\mathrm{LDOS}/\partial E^2 < 0$; blue areas in Figure 3.27). This is in contrast to the bulk LDOS measured in the center of the normal region (yellow area in Figure 3.24): As shown in Figure 3.27(b), no zero-energy peak develops for the bulk LDOS, apart from a small region in phase space slightly below $B_x = 3$ T and from $\varphi \approx 0$ to $\varphi \approx 0.4\pi$.

These regions with $\partial^2\mathrm{LDOS}/\partial E^2 < 0$ in the bulk LDOS arise from Andreev bound states at the phase boundary, providing again a fingerprint of the topological transition. We note that due to the much stronger Rashba SOC chosen here compared to Figure 3.25, the radii of the two Rashba-split Fermi circles differ considerably. Thus, the Andreev bound states arising mainly from the larger of the two Fermi circles carry significantly more weight in the LDOS than those arising from the smaller Fermi circle. As a consequence, pronounced zero-energy peaks in the bulk LDOS occur primarily at those phase boundaries that correspond to Andreev bound states formed from the larger Fermi circle.

Moreover, Figure 3.27(b) shows that the phase boundaries are usually traced by regions of nearly zero curvature (white regions), indicative of a flat LDOS at these boundaries. This is consistent with the high normal reflection that is implied by the squeezed topological regime in Figure 3.27. Indeed, large normal reflection increases the band widths of the Andreev bound states and thus the range of energies over which a flat LDOS can be expected (see Sec. 8). For the energy broadening $\Gamma = 0.2\Delta$ in Figure 3.27, the LDOS around $E = 0$ remains flat at the phase boundaries.

The above difference between the edge and bulk LDOS points to the zero-/low-energy states being

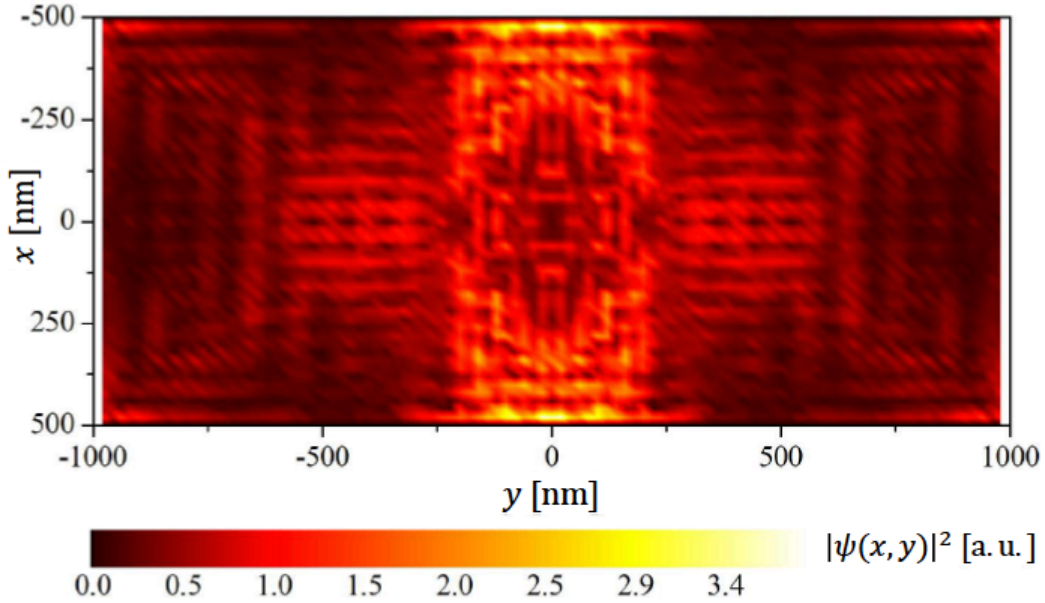

Figure 3.28: Wavefunction of the low-energy state for a 400-nm junction. Probability amplitudes $|\Psi(x,y)|^2$ of the low-energy state at $B_x = 2.4$ T and $\varphi = 1.8\pi$.

localized at the edge of the normal region. This is indeed corroborated by Figure 3.28, which, as an example, shows the wave function of the lowest-energy state at $B_x = 2.4$ T and $\varphi = 1.8\pi$: Here, the weight of the low-energy wavefunction at the edge of the normal region is significantly higher than the weight in the center of the junction.

The above results imply that for junctions with normal regions of width $W = 400$ nm, it could be possible to observe signatures of Majorana bound states by comparing the edge and bulk LDOS. Such signatures, however, are expected to occur for magnetic fields beyond the current experimental regime. Still, going to narrower devices with improved fabrication technology offers a promising route for finding fingerprints of Majorana bound states, difficult to isolate in Josephson junctions with wide

normal regions.

4

Searching for topological phase transitions in InAs quantum wells with epitaxial aluminum

An important aspect of the results of the previous two chapters is that they do not rely on the specific material HgTe that we used to conduct the aforementioned experiments, but rather should be

accessible in any system that contains the crucial ingredients of a high mobility semiconductor with strong Rashba spin-orbit coupling and induced superconductivity in the presence of in-plane magnetic fields[56]. In this chapter we discuss our attempt to reproduce these results on a system consisting of an InAs two-dimensional electron gas with an epitaxially grown aluminum superconductor. While we did not succeed in replicating the results of the prior two chapters in the InAs system for technical reasons related to the growth quality of the InAs, we present some preliminary data that suggests the potential for success in this material with higher quality substrates. We also show some preliminary data from our search for the transition of the system into a novel gapped superconducting state as predicted by certain theory work[73].

4.1 Introduction

The prior two chapters discuss fascinating experiments that show strong signatures of a topological phase transition in HgTe systems with superconductors deposited *ex situ*. The topological phase transition described in the chapters suggests the emergence of Majorana zero modes in the system, although without further experimentation we cannot conclusively confirm the presence of Majorana zero modes[56]. The topological nature of the results in the previous two chapters does not depend on the quantum well being HgTe, but rather should work with a variety of semiconductors possessing the correct ingredients of strong Rashba spin-orbit coupling and induced superconductivity in the presence of in-plane magnetic fields. We therefore decided to try to replicate the HgTe results from the previous two chapters in a different material, InAs quantum wells with epitaxial aluminum.

The decision to replicate these results on InAs was not a random choice; in fact, this specific InAs material with epitaxially grown aluminum presents a number of advantages over HgTe. In the previous chapter, we present results observed by placing metal tunneling contacts on the edges of our junctions. While metal tunneling contacts are not ideal, as deposited metal easily alloys with HgTe and HgCdTe and frequently leads to overly metallic or overly insulating contacts, it was necessary as the preferred method, gate-defined quantum point contacts, would not be feasibly in a Quantum Spin Hall system like HgTe that possesses edge states that cannot be easily gated away[31]. InAs does not have this issue, as it is not a Quantum Spin Hall material and gate-defined quantum point contacts are feasible, as we will discuss later in this chapter.

Another benefit of InAs over HgTe is the less restrictive fabrication conditions. HgTe cannot experience temperatures above 80° C without significantly degrading, while InAs can safely handle temperatures up to at least 150° C, and higher if one is feeling risky. This presents an issue with dielectric deposition on HgTe, as the dielectrics we use in our fabrication tend to be atomic layer deposited oxides, which have ideal growth temperatures above 120° C.

A third major benefit of InAs is the quality of the induced superconductor. In our HgTe systems, aluminum and niobium superconductors were deposited *ex situ*, resulting in small induced superconducting gaps in the HgTe. In our InAs systems, aluminum was deposited *in situ* in the molecular beam epitaxy chamber right after the quantum well was grown, resulting in an induced superconducting gap in the InAs quantum well that is almost as large as the standard thin-film aluminum superconducting gap[36].

4.2 InAs with epitaxial aluminum

The growth of the samples we used is discussed in papers published by the Shabani group at NYU[71 47]. Samples were grown on semi-insulating InP (100) substrates in a molecular beam epitaxy chamber. To achieve the correct lattice constant in the quantum well, a super lattice of $In_{0.53}Ga_{0.47}As$ and $In_{0.52}Al_{0.48}As$ was grown on top of the substrate, followed by an InAlAs graded buffer that gradually changed concentration from $In_{0.52}Al_{0.48}As$ to $In_{0.81}Al_{0.19}As$. The quantum well consists of a 4-6 nm layer of InAs, grown on 4-6 nm of $In_{0.81}Ga_{0.19}As$. In order to realize robust topological superconductivity, a quasiparticle should spend similar time in the superconductor as in the quantum well[68]. This is achieved by growing a 10 nm thick $In_{0.81}Ga_{0.19}As$ barrier on top of the quantum well. Finally, the substrate is cooled and 10-20 nm of epitaxial aluminum (111) is grown *in situ* on top of the InGaAs barrier. While bulk aluminum is a Type I superconductor with critical field around $\sim$ 50 mT, very thin-film aluminum can reach critical fields of over 2 T, and 10-20 nm tends to yield critical fields of around 1.5 T[65].

The interfaces of these samples tend to be very transparent, leading to induced superconducting gaps in the quantum well that are of the order of the thin-film aluminum gap, $\Delta_0 \sim 200\mu eV$[65]. The aluminum growth has one negative effect, as it tends to decrease the quantum well's electron mobility. The maximum measured mobility in these samples is around 43,000 $cm^2V^{-1}s^{-1}$, corresponding to an electron mean free path of $l_e \approx 600$ nm[22]. However, this optimal mobility is very hard to achieve* and most good growths yield mobilities of order 10,000-20,000 $cm^2V^{-1}s^{-1}$[47 65 71].

*At the time of this writing, mobilities this high have only been achieved on two growths out of hundreds, to the best of my knowledge.

The devices described in the rest of the chapter come from around 15 growths. Their mobilities are all in the range of 5,000-15,000 $cm^2V^{-1}s^{-1}$, as unfortunately we were never able to receive the top quality materials.

4.3 Experimental Setup

4.3.1 Fabrication

Here, we present the basics of fabrication on InAs samples with epitaxial aluminum.[†] The main steps of fabrication on these InAs samples are as follows: (1) alignment mark placing, (2) bondpad deposition, (3) mesa etching, (4) superconductor definition by aluminum etching, (5) dielectric deposition, and (6) gate deposition. These steps are the same for all devices we fabricated in the chapter, although the exact lithography preceding them changes depending on the type of device. Steps (2), (3), and (4) can technically occur in any order, without quality difference, but the yield rate was highest for various reasons discussed in Appendix B when we followed the order listed above. Additionally, steps (1) and (2) could be combined into one step when they followed each other. Most of the devices discussed in this chapter followed the numerical order listed above.

All fabrication steps were defined by electron beam lithography. Alignment marks and bond pads were deposited in a thermal evaporator chamber. A 10 s argon mill was run, immediately followed by the depositions of 5-10 nm of thermally evaporated titanium and 50-100 nm of thermally evaporated gold. The mesa was then etched using a mixture of water, 1M citric acid, phosphoric acid, and hydro-

[†] A much more detailed explanation of the processing occurs in Appendix B.

gen peroxide, in ratio 220:55:3:3. Because aluminum was grown epitaxially on these samples, it had to be selectively removed (instead of deposited like in the HgTe devices listed in the previous two chapters). A proprietary compound made by the Transene company, called Aluminum Etch Type D, was used for this selective etch. The aluminum etch was generally heated to temperatures 10-15°C above room temperature.

At this point, devices are able to be measured. For devices that required gating, a dielectric layer of either aluminum oxide, hafnium oxide, or a nanolaminate combination of the two was then deposited by atomic layer deposition, which was followed by gate deposition in a thermal evaporator. The gate material was generally 5-10 nm of titanium followed by an amount of gold thicker than the mesa etch. As this could sometimes reach several hundred nanometers, often the gate deposition was done in two steps, with fine features being 20-50 nm thick and coarse features that climbed the mesa etch being the necessary thickness.

4.3.2 Measurement setup

Samples were measured in three different setups. A helium dewar outfitted with a 5.6 T single-axis magnet was used for quick measurements at 4 K. Some of the QPC test data, as well as hall bar data yielding electron densities and mobilities were measured on this setup.

The low temperature data was intended to be measured in an Oxford Instruments dilution refrigerator with a base temperature of around 15 mK, which possessed a 12-3-1 T vector magnet. However, this system spent nearly two years being repaired by Oxford Instrument technicians, and so many of the low temperature measurements ended up being made on a different Oxford Instruments dilution

refrigerator with a base temperature of around 50 mK that possessed a 6-1-1 T vector magnet.

In all three systems, lockin techniques were used for measurements. AC and DC voltages and currents were applied and measured as magnetic fields were swept. The Yacoby Lab Special Measure package in Matlab was used to run these measurements and collect data.

4.4 Sample Characterization

Samples were characterized at 4 K using Hall bar techniques, for Hall bars with area of order 400-2500 μm^2. An AC current of 20-200 nA would be applied across the device, as an out of plane magnetic field was swept between -5.6 T and 5.6 T. Figures 4.1 and 4.2 respectively show the longitudinal resistance R_{xx} and Hall resistance R_{xy} of a characteristic Hall bar on one of these devices. For the device shown, the density was calculated to be 5.4×10^{11} cm^{-2} and the mobility to be 9920 $cm^2V^{-1}s^{-1}$. All of the samples measured in this chapter have densities within a factor of 10 of this device, and mobilities within a factor of 2. An important note is that mobility was not isotropic across the sample. For example, on this sample with a mobility of 9920 $cm^2V^{-1}s^{-1}$, fabricating the devices at other angles relative to the crystal axis would yield mobilities as low as 1850 $cm^2V^{-1}s^{-1}$. As a result, it is very important to fabricate devices so that electrons would travel in the optimal mobility direction. Unless mentioned otherwise, all devices in this chapter were fabricated along the optimal mobility direction.

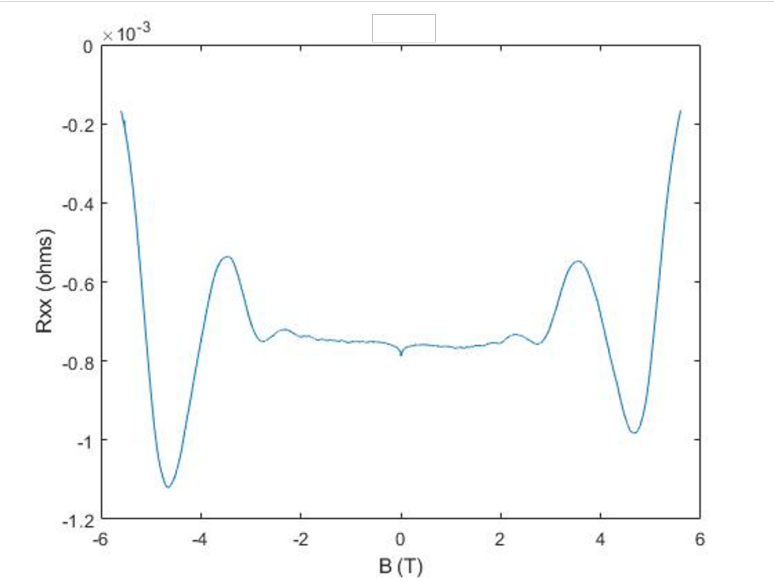

Figure 4.1: Characterization of an InAs quantum well. Shown here is the longitudinal resistance of a Hall bar device fabricated on InAs, as a function of the perpendicular magnetic field, at a top gate voltage of 0 V, measured at a temperature of 4 Kelvin.

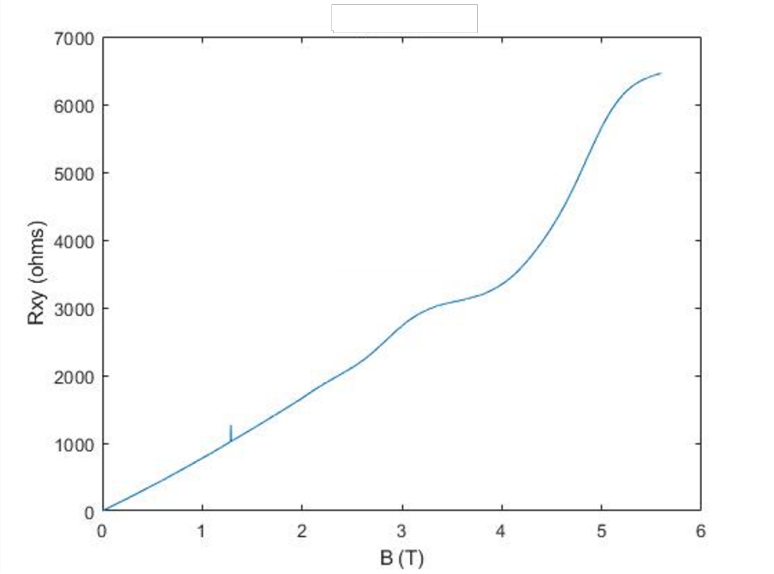

Figure 4.2: Characterization of an InAs quantum well. Shown here is the Hall resistance of a Hall bar device fabricated on InAs, as a function of the perpendicular magnetic field, at a top gate voltage of 0 V, measured at a temperature of 4 Kelvin.

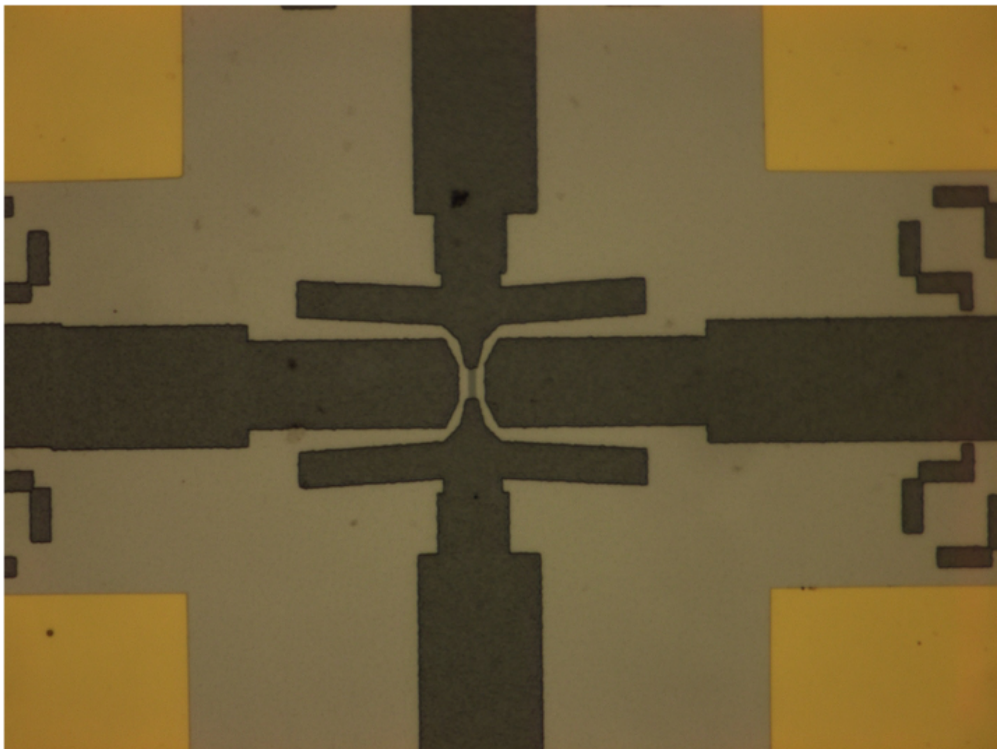

Figure 4.3: Microscope image of a Josephson junction on InAs. Shown here is an optical microscope image of a Josephson junction device. The yellow boxes in each of the four corners are bondpads. The light gray background is aluminum, and the dark gray is where the mesa is etched away. The tiny rectangle of medium gray color in the center is the weak link in the junction, where aluminum is stripped away.

4.5 Josephson junction measurements

4.5.1 Josephson junction processing

Josephson junctions were fabricated using the process described above in Section 4.3.1 and below in Appendix B. The width of the aluminum leads in the junctions was $\sim$1 μm, and the weak link dimensions varied from 2 μm to 8 μm in length and 100 nm to 800 nm in width. Example pictures of Josephson junction devices measured in this chapter are shown in Figures 4.3 and 4.4.

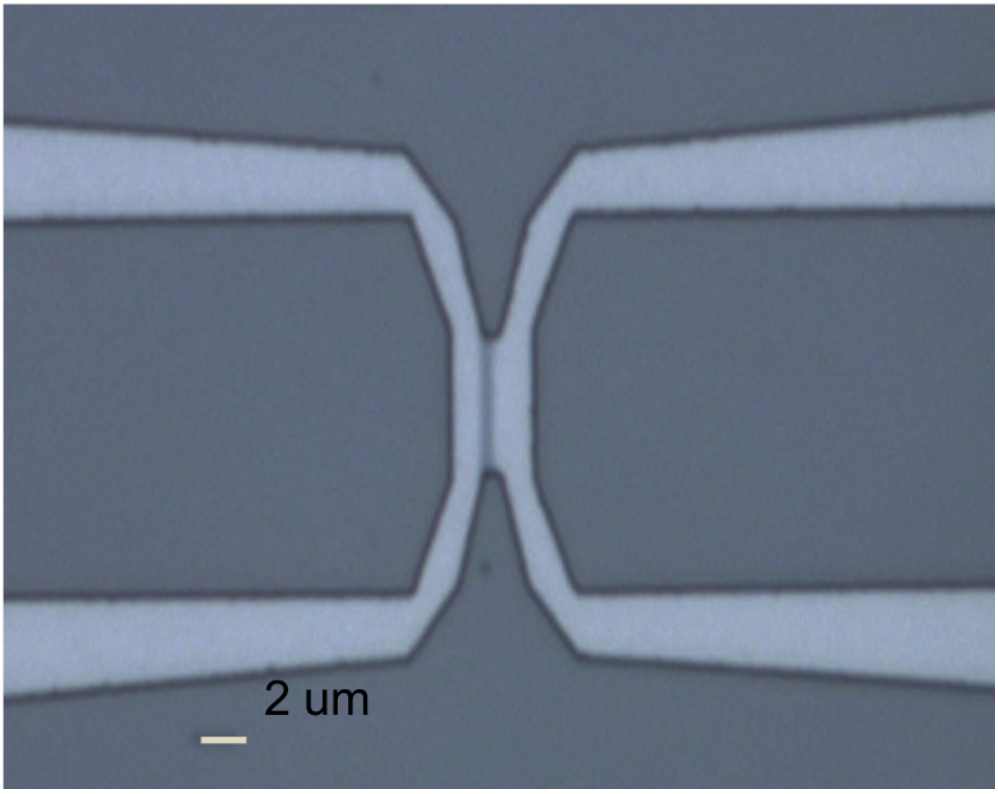

Figure 4.4: SEM image of a Josephson junction on InAs. Shown here is a scanning electron microscope image of a Josephson junction device. The dark gray background is where mesa is etched away. The light gray is the aluminum leads, and the medium gray rectangle in the middle is the weak link in the junction, where aluminum is stripped away. In this image, the aluminum etch is slightly offset from the center of the junction.

4.5.2 Fraunhofer patterns

We measured our Josephson junctions at mK temperatures to make sure they demonstrated the Josephson effect. We applied a 10 nA ac current across the junction, while sweeping out of plane magnetic field. At each value of magnetic field, we increased a dc current from 0 until past the point when the junction stopped superconducting. The resulting image gives information on the supercurrent density through the junction, and should result in a single-slit Fraunhofer interference pattern if the supercurrent is uniform through the junction, as we would expect for these samples[50]. Figure 4.5 shows the Fraunhofer pattern we measured on one of our best samples (mobility $\approx$15,000 $cm^2V^{-1}s^{-1}$). The product I_cR_n of the maximum critical current and the normal resistance of the junction is around 140 μeV, which suggests a much stronger induced superconducting gap here than we saw in HgTe. For example, the HgTe Josephson junction shown in Figure 2.1b has an I_cR_n product around 3 times smaller. We note that our junction here has one large peak, indicative of uniform supercurrent transport, although the sidelobes do not follow the single-slit interference pattern that we would expect. This is because many of our samples had a large amount of indium on their backsides, from how they were glued onto the sample holder in the molecular beam epitaxy chamber[‡]. The backside indium superconducts and screens magnetic flux for low values of out-of-plane field, causing some of the distortion that we see. If a large in-plane field is applied, the backside indium becomes normal and the distortion goes away, although the maximum critical current decreases in the

[‡]While we try to remove most of this backside indium, we are not able to remove all of it while still treating the sample gently, and so we prefer leaving some backside indium to risking the integrity of our sample and fabricated devices.

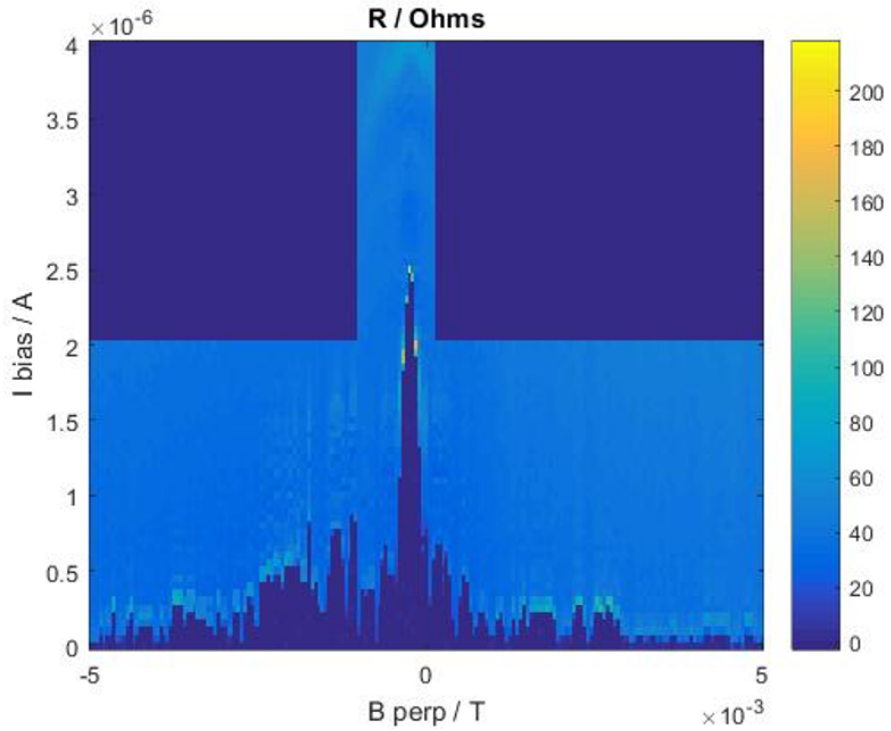

Figure 4.5: Fraunhofer pattern in an InAs Josephson junction. We plot the ac resistance due to an applied dc current at fields between −5 mT and 5 mT. The single peak much larger than the lobes is indicative of uniform supercurrent density through the junction, although the side lobes are not symmetric on either side. This is likely caused by excess indium on the backside of the sample that screens the out of plane magnetic field in a non-uniform way.

in-plane field regime. Figure 4.6 shows a Fraunhofer pattern from a much lower quality sample, but one without the backside indium. Here we see that the pattern is much more symmetric and looks like single-slit interference.

4.5.3 In-plane field measurements on InAs

After confirming that the junctions displayed Josephson effect and a strong induced superconducting gap, we attempted to repeat the measurements on HgTe from Chapter 2 that showed disappearance and re-entrance of superconductivity as a function of parallel field. Josephson junctions were

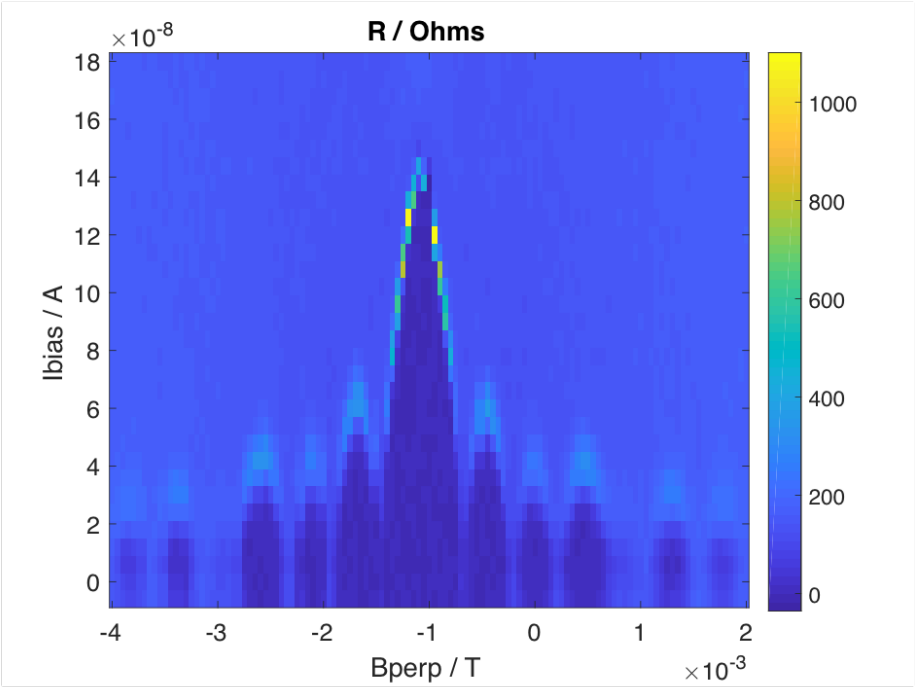

Figure 4.6: Fraunhofer pattern in an InAs Josephson junction. We plot the ac resistance due to an applied dc current as magnetic field is swept. We see a symmetric single-slit interference pattern.

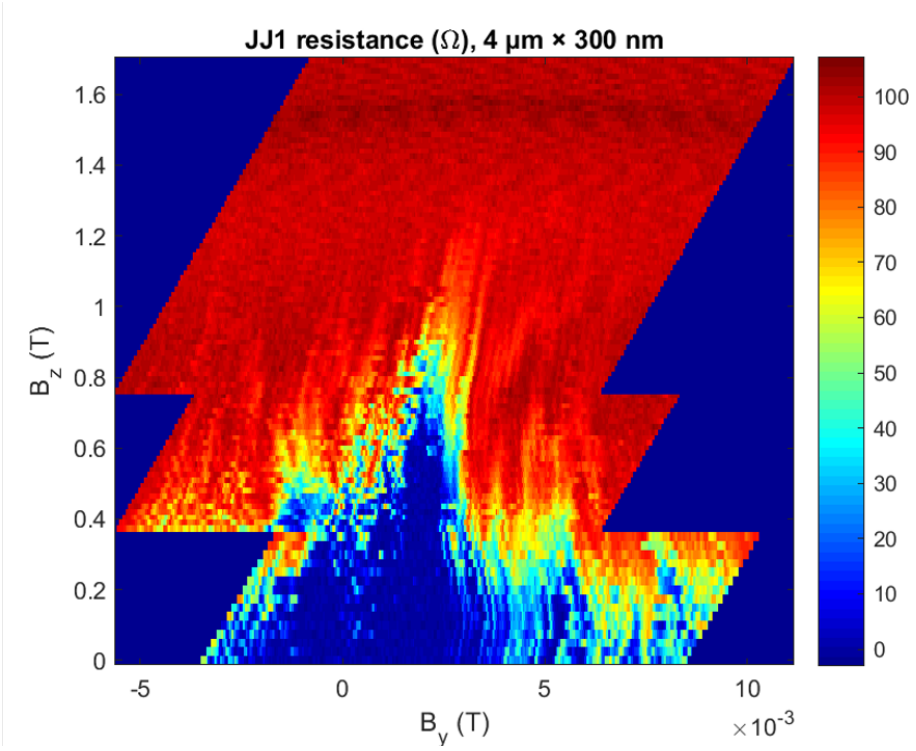

Figure 4.7: Sweeping in-plane field in an InAs Josephson junction, part 1. We plot the ac resistance as in-plane (B_z) and out-of-plane (B_y) magnetic fields are swept in a Josephson junction of dimensions 4 μm $\times$ 300 nm. The superconductivity dies off at high in-plane field but does not re-emerge at higher values.

cooled down to mK temperature, a small ac current was applied to the junction ($\sim$5 nA), and in-plane field was swept from 0 T to values between 1 T and 2 T. At each value of in-plane field, we swept out-of-plane field over a few mT. Figure 4.7 shows a characteristic example of one of our many measurements that attempted to repeat the HgTe results. In the device shown, the superconductivity died off at around 0.7 T but did not re-emerge later.

We then tried a slightly different method to test for the re-entrance of superconductivity. We swept the same in-plane and out-of-plane fields as above in Figure 4.7, but instead of keeping the current through the junction constant, we swept current from 0 nA until the junction went normal at each

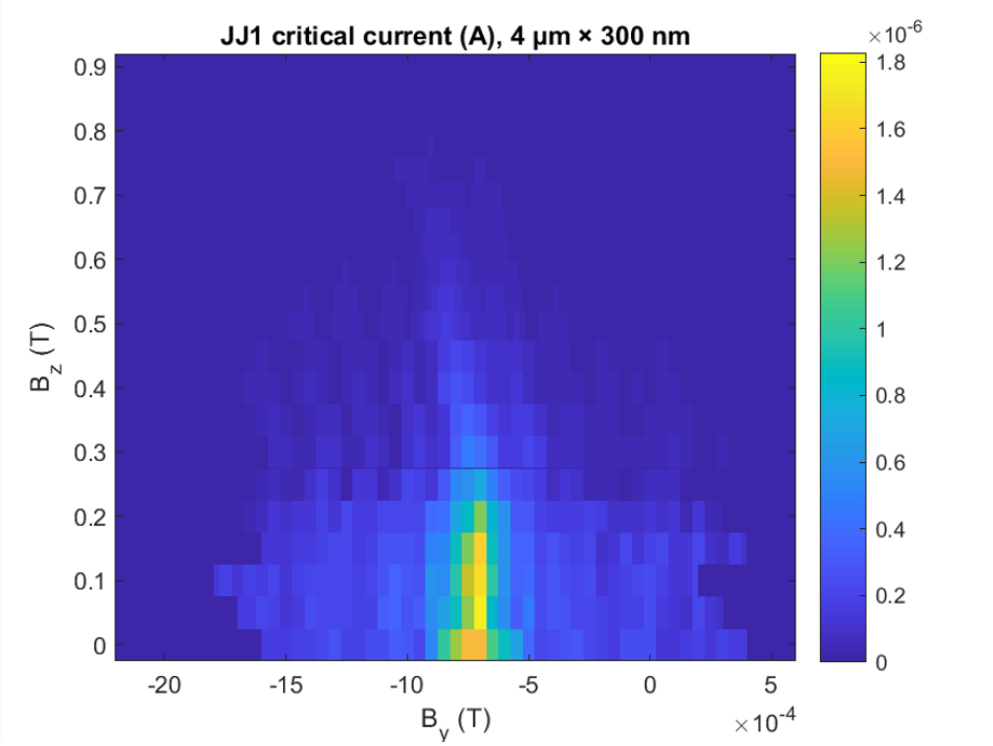

Figure 4.8: Sweeping in-plane field in an InAs Josephson junction, part 2. We plot the ac resistance as in-plane (B_z) and out-of-plane (B_y) magnetic fields are swept in a Josephson junction of dimensions 4 μm $\times$ 300 nm. The superconductivity dies off at high in-plane field but does not re-emerge at higher values.

point in field, and measured that critical current point. While this method required much more time per measurement, it also is much more sensitive. Unfortunately, as we show in Figure 4.8, we do not see any re-entrance of superconductivity in our devices even with this more careful method.

An important test was to check whether the disappearance of superconductivity in the junction at high in-plane field was due to the induced gap in the 2DEG or due to the leads themselves. If the leads themselves were unable to sustain superconductivity in the high-field regime, the lack of re-entrance would not be surprising. We checked this by measuring resistance across a single junction lead in the device shown above. We show this data in Figure 4.9, and see that the junction leads survive until

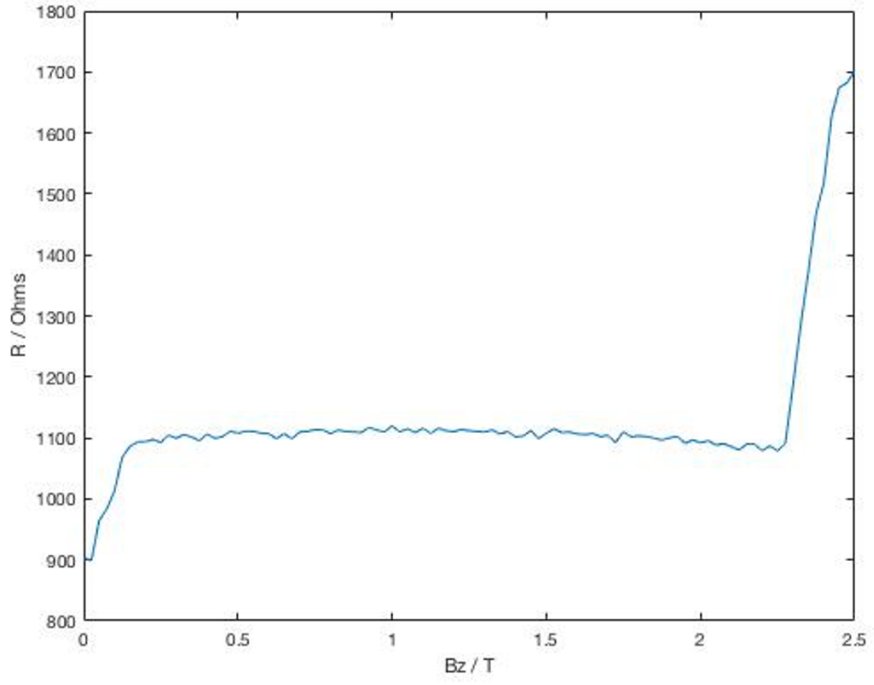

Figure 4.9: Measuring resistance across junction leads in the presence of in-plane fields. We plot the resistance of a two-terminal measurement across one of the leads of a Josephson junction. We see that the lead goes normal at around 2.3 T.

much higher values of in-plane magnetic field, around 2.3 T. This removes the possibility that the junction leads are going normal before the superconductivity would re-emerge in the junction. The likely reason for the lack of re-entrant superconductivity in these samples is their low mobility, making these junctions much more susceptible to disorder than those in HgTe with mobilities 40 times higher, as Anderson's theorem protecting singlet superconductors from the effects of low mobility is no longer valid in the high in-plane field regime, where triplet pairing comes into play as well[3]. For mobilities as low as in these samples, mean free paths are of order 150-200 nm, compared to around 7 μm in HgTe.

We attempted to find a re-entrance of superconductivity in a number of Josephson junctions of

varying dimensions on many InAs samples of varying quality, but never were able to see a re-entrance of superconductivity like in HgTe.

4.6 Quantum Point Contacts

In order to repeat the measurements of Chapter 3 on InAs, we attempted to create gate-defined quantum point contacts (QPCs) that would allow us to make tunneling measurements on our InAs devices. Although we did not have high quality InAs samples, as discussed above, we attempted to create these quantum point contacts in order to be ready for a time when we would receive high quality samples.

4.6.1 Fabrication

We followed the same procedures as described in Section 4.3.1 and Appendix B to fabricate our devices for testing quantum point contacts. We removed the aluminum from a long rectangular strip (approximately 20 μm in width and 40 μm in length) on the device, and placed three QPC devices across the rectangle in different places, so as to test several at a time[§]. Each QPC could individually be gated into the pinch-off regime or left ungated, so that each QPC could be independently measured. A picture of one of these devices is shown in Figure 4.10.

[§] Placing multiple QPCs on a single device allowed us to use the same bondpads for current and voltage measurements through the device for multiple QPCs, minimizing the number of cooldowns needed for testing.

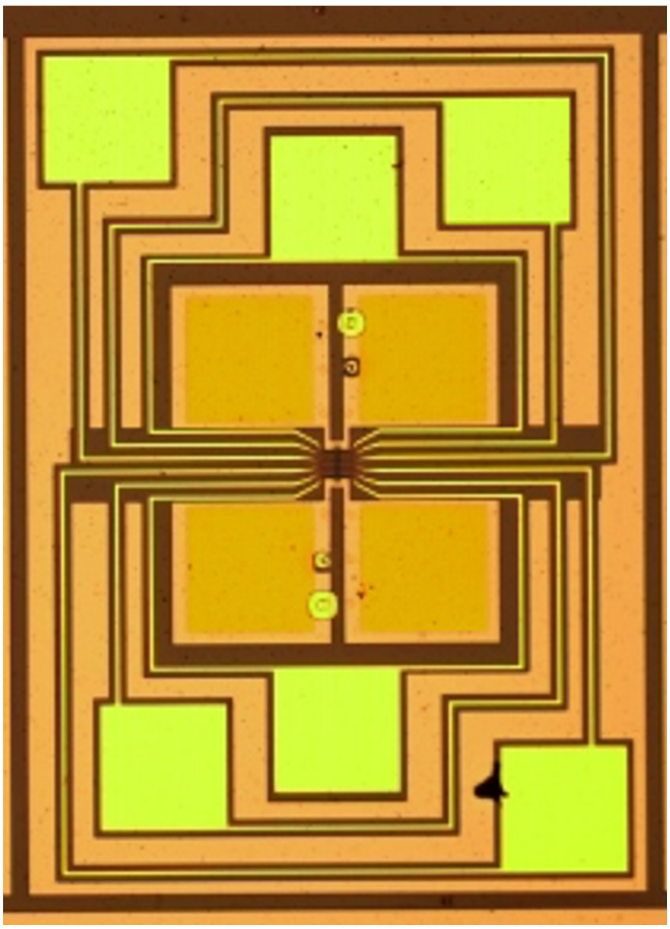

Figure 4.10: Quantum point contact test device. Shown here is an optical microscope image of a device used to test quantum point contacts. The dark brown is where the mesa is etched, separating this device from others on the chip, as well as separating bondpads from each other. The four dark gold squares in the center of the chip are gold bondpads used to make four-terminal measurements of current and voltage. The six bright gold squares are the bondpads used for gating quantum point contacts. Each of the three quantum point contacts uses two of these six bondpads. The thin gold lines attached to these six bondpads are attached to the gates, whose features are too fine to see in this image but are in the center of the chip. The orange background is where aluminum is left unetched on the chip.

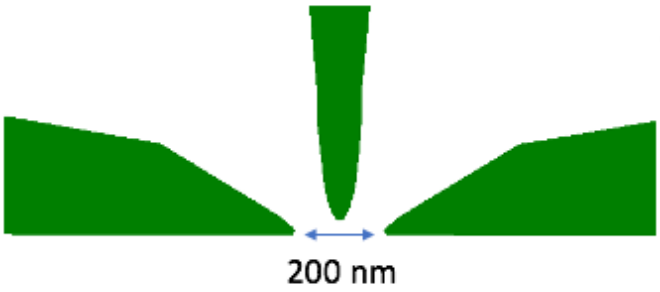

Figure 4.11: Schematic of best quantum point contact device. Shown here is a schematic of our best quantum point contact device. The three green shapes are gates. The leftmost and rightmost shape are the constriction gates, to which a large negative voltage would be applied. The middle shape would be held at a slight negative voltage to prevent the constriction gates from completely stopping any conductance. The 200 nm separation between constriction gates was ideal for our InAs quantum wells, but we expect it to scale with depth of the quantum well below the gate layer.

4.6.2 Measuring quantum point contacts

We fabricated a number of different geometries for quantum point contacts, and then measured them at 4 K temperatures. We found that it was very important for each QPC to consist of three gates, as shown in Figure 4.11, although only two are needed to create a constriction. This is because a two gate device ended up gating the region in between the two gates, depleting it too much and creating a total constriction instead of a tunneling device. The third gate was added and held at a higher gate voltage than the two constriction gates, so as to allow small amounts of current to flow through the device. An important aspect of our most successful designs was that both constriction gates were attached to the same gate bondpad. This had two significant advantage compared to devices where each constriction gate had a unique bondpad. In addition to requiring one fewer wirebond (and thus leaving more wirebonds available to test more devices per cooldown), it ensured that both gates were bonded at the same exact time and would always be at the same voltage.

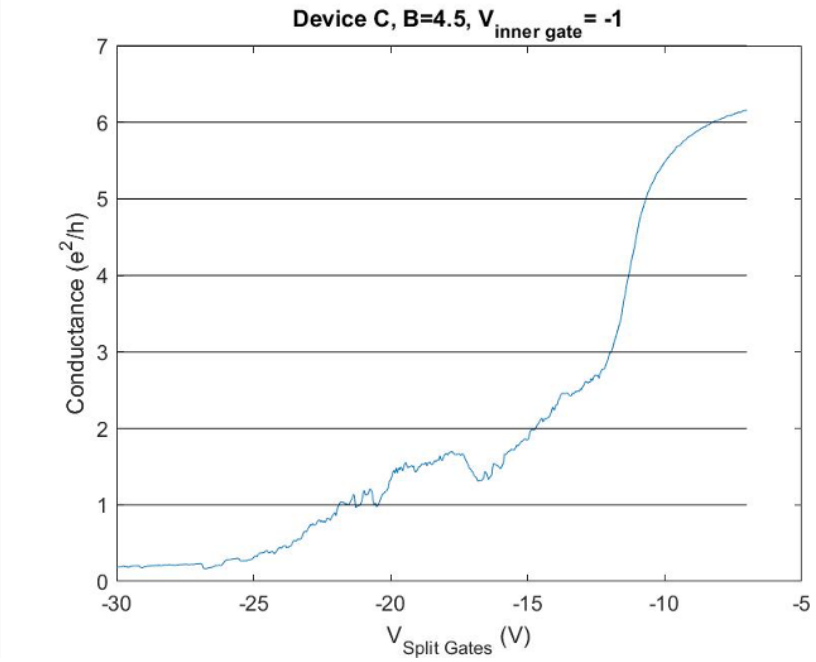

Figure 4.12: Measurement of quantum point contact device. Conductance, in units of conductance quanta $\frac{e^2}{h}$, is plotted for a QPC device as the gate voltage applied to the constriction gates is swept from -5 V to -30 V. The third gate is held at a constant -1 V, and an out of plane magnetic field of 4.5 T is applied.

An example measurement of a QPC device is shown in Figure 4.12. We see conductance drop from above six conductance quanta to zero, with stops at several plateaus. This measurement does not look like an ideal QPC, but without high mobility samples (this measurement was taken on a device with a mobility of around 10,000 $cm^2V^{-1}s^{-1}$), we do not expect to see ideal QPC behavior, especially at 4 K temperatures instead of mK.

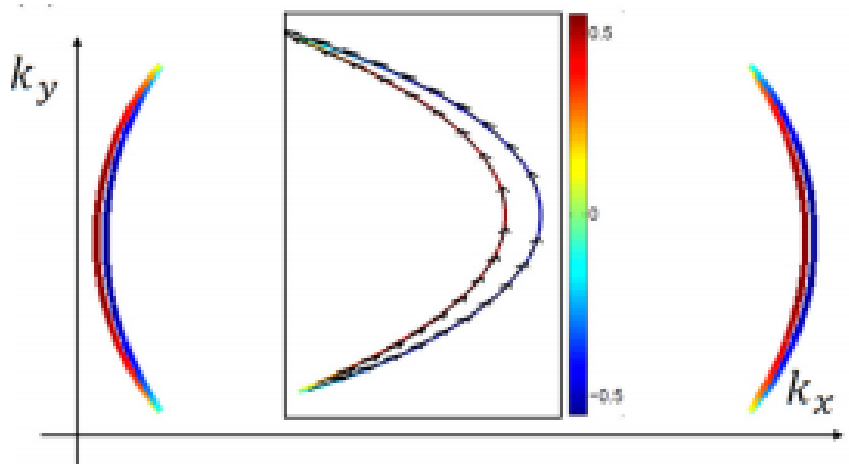

Figure 4.13: Emergence of partial Fermi surfaces. Partial Fermi surfaces in the gapless superconducting phase. Colors denote the charge distribution in units of e. Inset: The zoom-in plot of the partial Fermi surface on the $k_x > 0$ side where the arrows indicate spin polarization.

4.7 Partial Fermi surfaces

4.7.1 Yuan and Fu theory

(Note: this subsection summarizes a paper written by Noah Yuan and Liang Fu. All figures in Section 4.7.1, are from that paper.[73])

Yuan and Fu, in a 2018 paper, discuss the effects of in-plane magnetic fields on a two-dimensional system with strong Rashba spin-orbit coupling and induced superconductivity. They show that when the Zeeman energy of the in-plane field, $g\mu_B|\mathbf{B}|$, exceeds the superconducting gap, the system enters a state where a partial Fermi surface emerges as shown in Figure 4.13.

The expected density of states $N(E)$ at the surface of this system as a function of energy E at various values of Zeeman energy is plotted in Figure 4.14. We see the emergence of a gapless state as the Zeeman energy V grows larger than the superconducting pairing amplitude Δ.

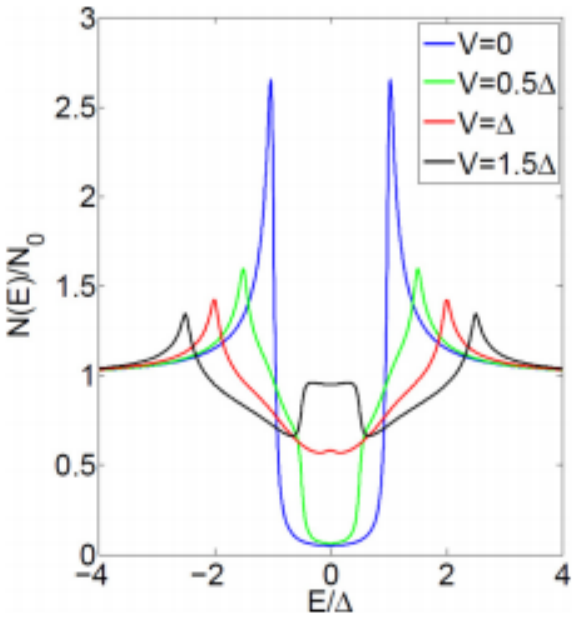

Figure 4.14: Density of states as Zeeman field is increased. Density of states $N(E)$ as functions of energy E, for different values of Zeeman energy V relative to the superconducting gap Δ. Here N_o is the normal state density of states and Δ is the superconducting pairing amplitude.

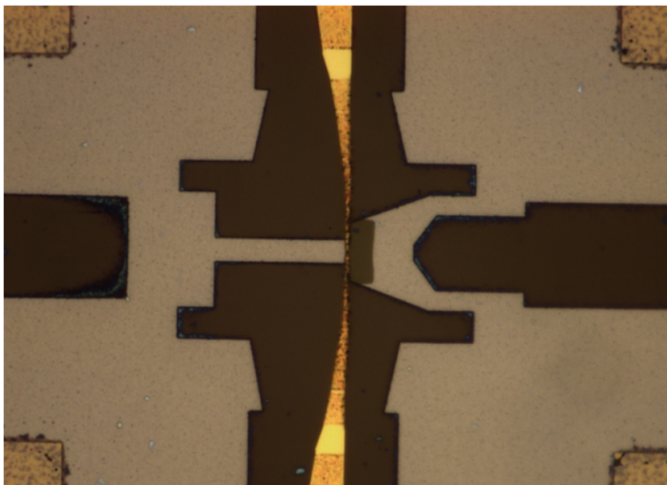

Figure 4.15: Aluminum - 2DEG interface probing device. We show an optical microscope image of a device fabricated to probe the tunneling density of states at the aluminum - 2DEG interface. The four dark gold squares in the corners are the edges of bondpads. The dark brown is where mesa was etched away. The light brown is aluminum, and the small medium brown rectangle in the center is quantum well where aluminum is etched away. The two constriction gates that form the quantum point contact are shown in bright gold, emerging from the top and bottom of the image, horizontally centered.

4.7.2 Measurements to probe partial Fermi surfaces

We expect $V > \Delta$ for an in-plane field of $\sim$ 0.5 T for Al/InAs heterostructures as is the case in our system [73]. In order to test this, we designed devices where aluminum was removed from above a small region of quantum well, and placed quantum point contact devices on at the aluminum-normal interface to measure the local density of states. A picture of these devices is shown in Figure 4.15.

We measured these devices in a dilution refrigerator at 50 mK. We depleted the constriction gates to create the quantum point contact, and measured the tunneling conductance as a function of an applied DC voltage bias (which represents the energy from Figure 4.14) at a range of in-plane fields B_z, applied in the plane of and perpendicular to the aluminum - 2DEG interface. These measurements are plotted in Figure 4.16. We see that at low magnetic fields, the system appears gapped with large

coherence peaks, similar to the blue peak in Figure 4.14. At $B_z = 600$ mT (roughly the predicted value according to Yuan and Fu[73]), we potentially see a feature resembling the red curve in Figure 4.14, which would indicate the emergence of the gapless superconducting state. However, at $B_z = 800$ mT and on, we don't see the growth of this feature and thus never are able to see the black curve from Figure 4.14. All of these measurements were repeated multiple times, with the same results, and the averaged values of these measurements are the ones shown in Figure 4.16. We expect that the lack of further gapless superconducting behavior at larger values of in-plane field is due to the same mobility problem discussed in Section 4.5.3. The mobility issues also prevent the creation of high-quality quantum point contacts, likely also affecting the quality of our measurements.

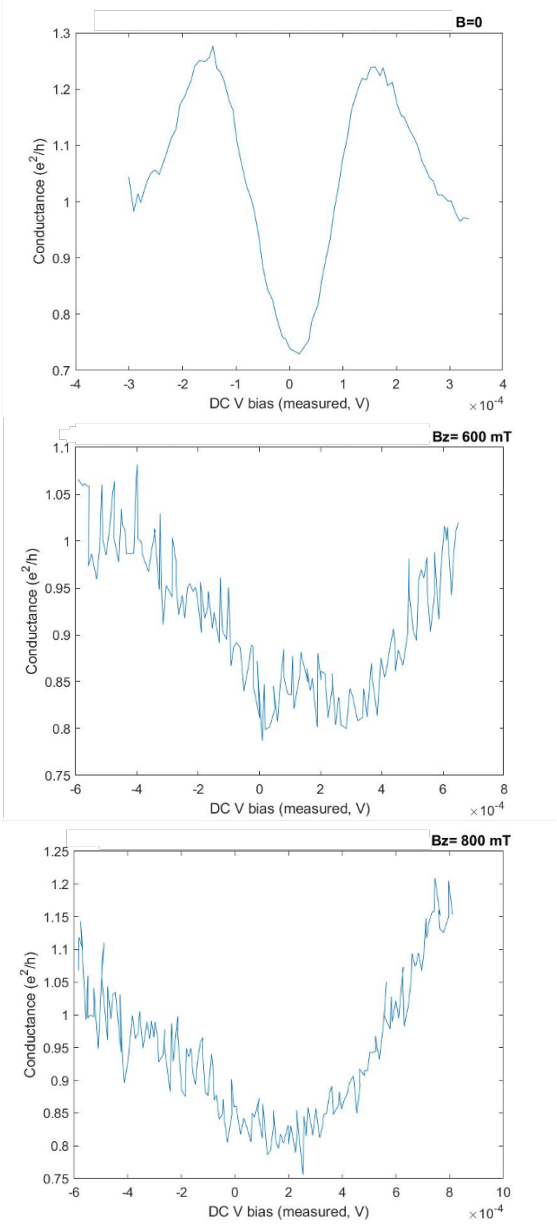

Figure 4.16: Density of states measurements at the aluminum - normal interface. Conductance in units of conductance quanta $\frac{e^2}{h}$ is plotted as a function of applied DC voltage bias for three different in-plane magnetic fields: top, $B_z = 0$, middle, $B_z = 600$ mT, and bottom, $B_z = 800$ mT. All three plots are averaged over multiple measurements, each individually showing the same behavior as the average. We see the emergence of a slight peak in the density of states at $B_z = 600$ mT, supporting the prediction of Yuan and Fu[73], which does not continue to grow at larger values of in-plane field.

5

Inducing superconductivity in buried InAs quantum wells

InAs quantum wells are able to achieve extremely high mobilities of over 1×10^6 $cm^2V^{-1}s^{-1}$ when grown tens of nanometers below the surface of a heterostructure[44]. We fabricated Josephson

junctions on these heterostructures by depositing superconductors on them *ex situ*. In doing so, we were able to drastically increase the mobility of our devices in return for sacrificing the strength of the induced superconducting gaps, compared to the InAs devices with epitaxial aluminum studied in the prior chapter. In this chapter, we discuss our success in inducing superconductivity in these high-mobility systems, the initial stages of our attempts to replicate the results of Chapter 2, and the outlook for this material to reproduce the results of Chapters 2 and 3.

5.1 Introduction

We attempted to study topological physics in InAs quantum wells for a number of reasons listed in Section 4.1. The InAs materials discussed in that chapter were heterostructures with epitaxial aluminum grown *in situ* in the molecular beam epitaxy chamber. As discussed at the end of that chapter, these materials failed to display the re-entrant superconductivity from Chapter 2, most likely due to very low mobilities in those samples. The search for higher mobility led us to experiment with a different type of InAs heterostructure, one where the quantum well is a bit deeper below the surface, but does not have aluminum deposited *in situ* with the growth. This leads to much higher mobilities (50-150 times higher than in the InAs quantum wells with epitaxial aluminum), but lower induced superconducting gaps. Because of the incredibly high mobility (which is around a factor of two higher than even that of our top quality HgTe quantum wells from Chapters 2 and 3), these buried InAs quantum wells present a promising platform to explore.

5.2 Buried InAs quantum wells

(Note: all details in this section are from the thesis of Thomas Tschirky from Werner Wegscheider's group in ETH Zurich, the group that provided these samples for us.[69])

The buried InAs quantum wells were grown in a molecular beam epitaxy chamber on GaSb substrates. The growth starts with a 600 nm GaSb layer and a ten-period superlattice, each period consisting of 2.5 nm of $Al_{0.33}Ga_{0.67}Sb$ and 2.5 nm of GaSb. This is followed by 200 nm of $Al_{0.33}Ga_{0.67}Sb$ that forms a lower barrier to the quantum well. The quantum well, consisting of 20 nm of InAs, is grown on top of the lower barrier, followed by an upper barrier of 20 nm of AlSb. A 2 nm capping layer of GaSb is grown above this barrier, as AlSb tends to oxidize if exposed to air.

This growth leads to a very high mobility. Transport measurements made by the growers of the sample used for our measurements in this chapter are shown in Figure 5.1. These measurements were taken at 1.3 K, and show strong Shubnikov-de Haas oscillations. The extracted density and mobility from the ρ_{xx} and ρ_{yy} measurements are, respectively, 7.1×10^{11} cm^{-2} and 7.7×10^5 cm^{2}V^{-1}s^{-1}.

5.3 Experimental setup

5.3.1 Fabrication

Here, we present the basics of fabrication on buried InAs quantum well samples.*

All fabrication steps were defined by electron beam lithography. Alignment marks and bond pads were deposited in a thermal evaporator chamber. A 10 s argon mill was run, immediately followed

*A much more detailed explanation of the processing occurs in Appendix C.

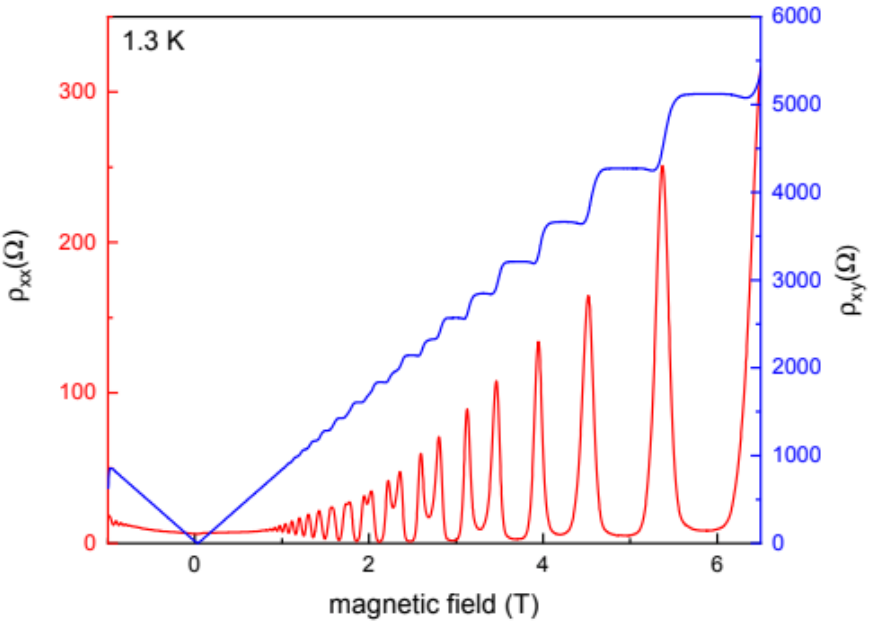

Figure 5.1: Transport measurements of our buried InAs well sample. Shown here are ρ_{xx} (in red) and ρ_{yy} (in blue) measurements on a buried InAs well sample at 1.3 K temperatures, as a magnetic field is increased to around 6.5 T. We see strong Shubnikov-de Haas oscillations in ρ_{xx} and clear plateaus in ρyy.

by the depositions of 10 nm of thermally evaporated titanium and 100 nm of thermally evaporated gold. A 90 s oxygen plasma reactive ion etch was used to clean the sample, and then the mesa was then etched using the same etch as in the previous chapter - a mixture of water, 1M citric acid, phosphoric acid, and hydrogen peroxide, in ratio 220:55:3:3. This was followed by another 90 s oxygen plasma reactive ion etch to clean the sample again before depositing superconductors. A 10 s argon mill was run, followed by the deposition of 5 nm of titanium by thermal evaporation and then either thermal evaporation of aluminum (5-15 nm) or dc sputtering of niobium ($\sim$50 nm).

5.3.2 Measurement setup

Samples were measured in two different setups. A helium dewar outfitted with a 5.6 T single-axis magnet was used for quick measurements at 4 K.

The low temperature data was measured in an Oxford Instruments dilution refrigerator with a base temperature of around 15 mK, which possessed a 12-3-1 T vector magnet.

In both systems, lockin techniques were used for measurements. AC and DC voltages and currents were applied and measured as magnetic fields were swept. The Yacoby Lab Special Measure package in Matlab was used to run these measurements and collect data.

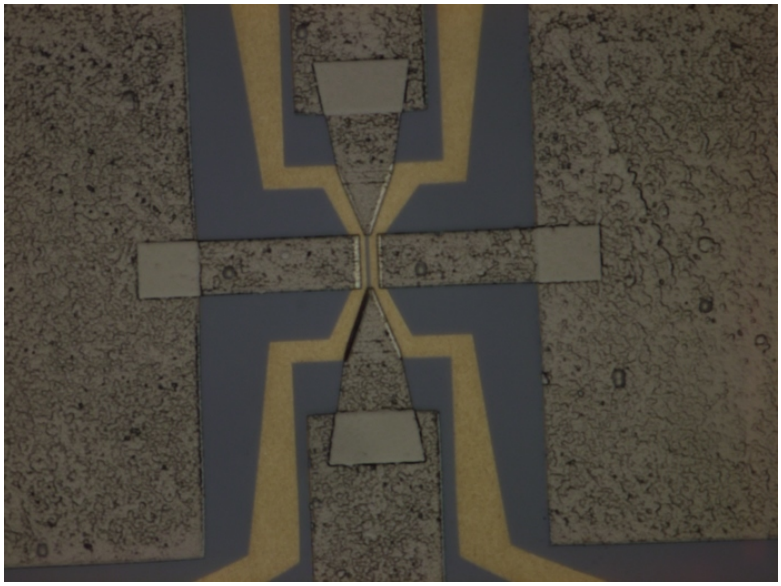

Figure 5.2: Aluminum Josephson junction on buried InAs quantum well. Shown here is a close-up optical microscope image of a Josephson junction after aluminum is deposited to define superconductors, but before a top gate was deposited. The gray background is the top of the capping layer above the quantum well barrier. The tan color on the sides is where mesa is etched away. The pattern is because the mesa did not etch uniformly on this device. The gold color is the aluminum leads.

5.4 Josephson junction measurements

5.4.1 Josephson junction fabrication

Josephson junctions were fabricated using the process described above in Section 5.3.1 and below in Appendix C. The width of the aluminum leads in the junctions was 1-1.5 μm, and the weak link dimensions varied from 4 μm to 8 μm in length and 100 nm to 800 nm in width. An example picture of a Josephson junction device measured in this chapter is shown in Figure 5.2.

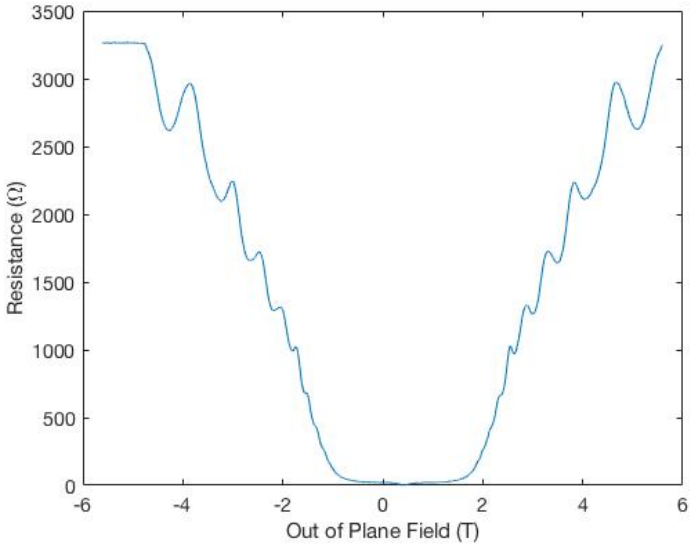

Figure 5.3: Shubnikov-de Haas oscillations in junction resistances at 4 K. The ac resistance of a Josephson junction is measured as a magnetic field is swept from -5.6 to +5.6 T. Clear Shubnikov-de Haas oscillations are observed. We observe that the field is centered around 400 mT instead of 0. The source of this offset is not clear, but seems to be caused by the magnet controller.

5.4.2 Measurements at 4 K temperatures

Junctions were measured at 4 K temperatures for characterization purposes. As aluminum's T_c is roughly 1.75 K, we could not test for superconductivity without cooling the junctions down in a dilution unit. However, we found that four terminal resistance measurements would yield resistances of 10-50 Ω at 4 K on "good" junctions.

We also ramped an out-of-plane magnetic field from -5.6 to +5.6 T at 4 K, and saw clear Shubnikov-de Haas oscillations in junction resistances as a function of field, as shown in Figure 5.3. Extracting carrier density from these measurements yielded densities between 6.5×10^{11} cm^{-2} and 8×10^{11} cm^{-2}, well in accordance with the sample's nominal density of 7.1×10^{11} cm^{-2}.

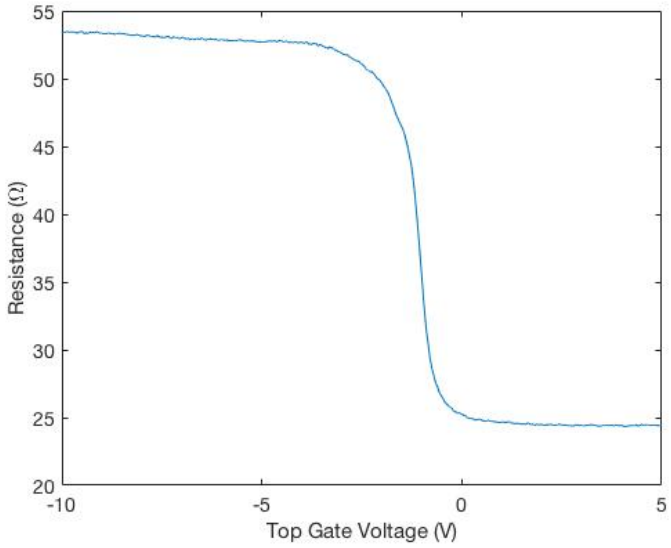

Figure 5.4: Effect of a top gate on junction resistances at 4 K. The ac resistance of a Josephson junction is measured as a top gate is swept from +5 V to −10 V. The resistance remains stable at 25 Ω until around −1 V, when it sharply increases to around 53 Ω and stays stable there until at least −10 V.

Varying a top gate over a large range of gate voltage shows a clear transition in junction resistance, as shown in Figure 5.4. We see that for positive voltages, the junction's resistance sits at around 25 Ω, and rises to around 53 Ω when the gate voltage falls below approximately −1 V. This suggests that the junction is in the two sub band regime without applied gate, and can be gated into a single sub band regime when sufficient negative voltage is applied.

5.5 Measurements on 50 nm thick aluminum Josephson junctions

5.5.1 Fraunhofer patterns

After characterizing our junctions at 4 K, we measured them at mK temperatures to make sure they demonstrated the Josephson effect. We applied a 5-10 nA ac current across the junction, while sweep-

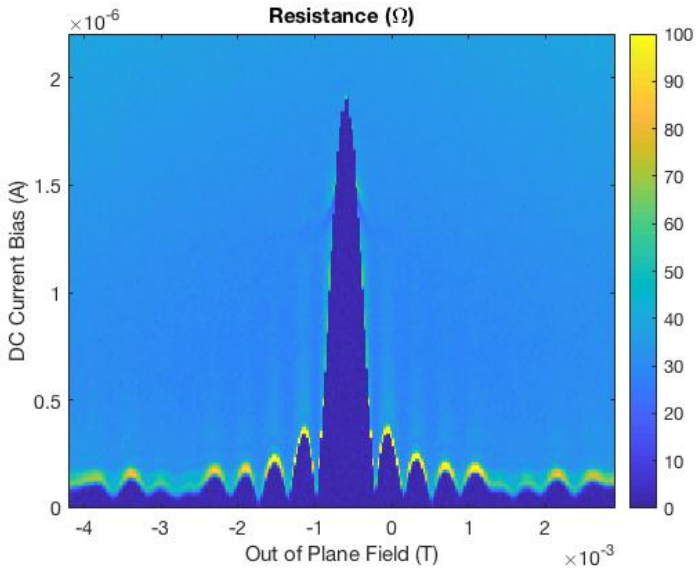

Figure 5.5: Single-slit interference pattern on a 4 μm $\times$ 800 nm aluminum junction. We plot the ac resistance due to an applied dc current as an out-of-plane magnetic field is swept in a 4 μm $\times$ 800 nm aluminum junction. We see the symmetric single-slit interference pattern that is characteristic of uniform supercurrent density throughout the junction. The critical current is approximately 1.9 μA and the normal resistance 35 Ω, leading to an I_cR_n product of $\approx$ 67 μeV.

ing out of plane magnetic field. At each value of magnetic field, we increased a dc current from 0 until past the point when the junction stopped superconducting. The resulting image gives information on the supercurrent density through the junction, and should result in a single-slit Fraunhofer interference pattern if the supercurrent is uniform through the junction, as we would expect for these samples[50]. Figures 5.5 and 5.6 show single-slit interference patterns measured on 50 nm thick aluminum junctions of respective dimensions 4 μm $\times$ 800 nm and 8 μm $\times$ 800 nm. Both junctions have I_cR_n products of around 67 μeV, suggesting an induced superconducting gap that is higher than those in our HgTe devices from Chapters 2 and 3, and roughly half of those in our epitaxial aluminum devices from Chapter 4. These measurements suggest that we have successfully induced superconductivity in our samples.

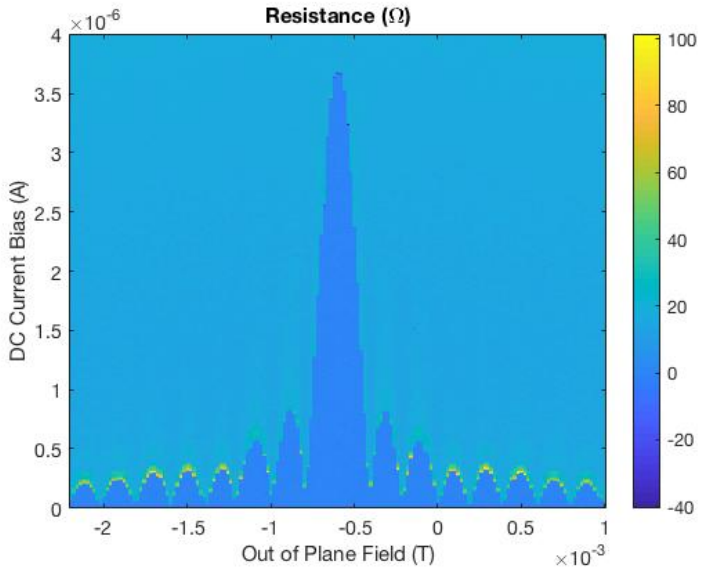

Figure 5.6: Single-slit interference pattern on an 8 μm $\times$ 800 nm aluminum junction. We plot the ac resistance due to an applied dc current as an out-of-plane magnetic field is swept in an 8 μm $\times$ 800 nm aluminum junction. We see the symmetric single-slit interference pattern that is characteristic of uniform supercurrent density throughout the junction. The critical current is approximately 3.7 μA and the normal resistance 18 Ω, leading to an $I_c R_n$ product of $\approx$ 67 μeV.

Following the procedure listed in Hart et. al, we can extract the critical current density across the junction as a function of junction length by taking the Fourier transforms of our measurements of current bias vs. out of plane field[31]. We see that the current is evenly distributed throughout the junctions, as we would expect, and plot this for the 8 μm $\times$ 800 nm junction in Figure 5.7.

5.5.2 In-plane field measurements

After confirming that the junctions displayed Josephson effect and an induced superconducting gap, we once again attempted to repeat the measurements on HgTe from Chapter 2 that showed disappearance and re-entrance of superconductivity as a function of parallel field. A small ac current of around 5 nA was applied to the junction as an in-plane field was swept. At each value of in-plane field, we swept

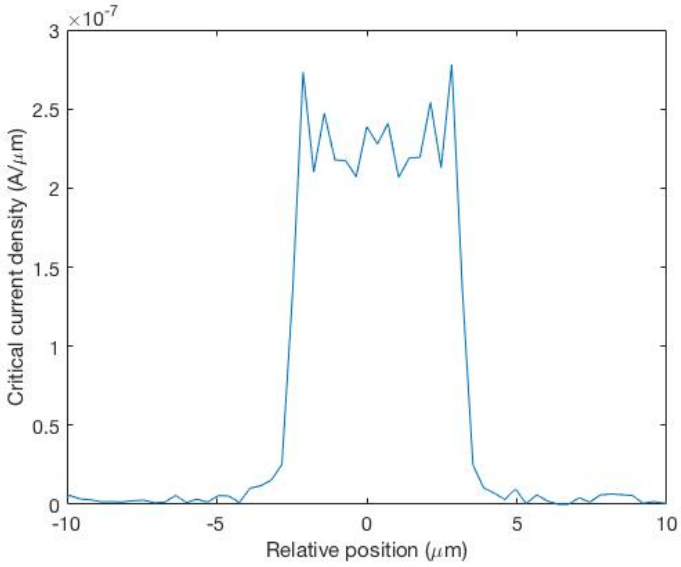

Figure 5.7: Critical current density in the 8 μm $\times$ 800 nm aluminum junction. We plot the critical current density of the 8 μm $\times$ 800 nm aluminum junction from Figure 5.6 here as a function of junction length. We see that the from -4 μm to $+4$ μm, the junction has almost constant current density, which quickly falls off to 0 outside these bounds. This suggests an 8 μm long Josephson junction in which current is uniformly flowing along the junction length.

out-of-plane field over a few mT. Figure 5.8 shows our measurements on the 4 μm $\times$ 800 nm junction discussed above in Figure 5.5. We see that the superconductivity disappears at around 0.6 T, without re-emerging later. However, this is not entirely unexpected, as this is approximately the critical field of 50 nm thick aluminum, so we would not expect the junction to superconduct after the leads went normal[57].

5.6 Measurements on 14 nm thick aluminum Josephson junctions

Once we succeeded in inducing superconductivity on these buried InAs quantum wells with 50 nm of aluminum, we tried reducing the aluminum thickness to increase the critical field in our junction leads and see if we would see re-entrant superconductivity like in HgTe.

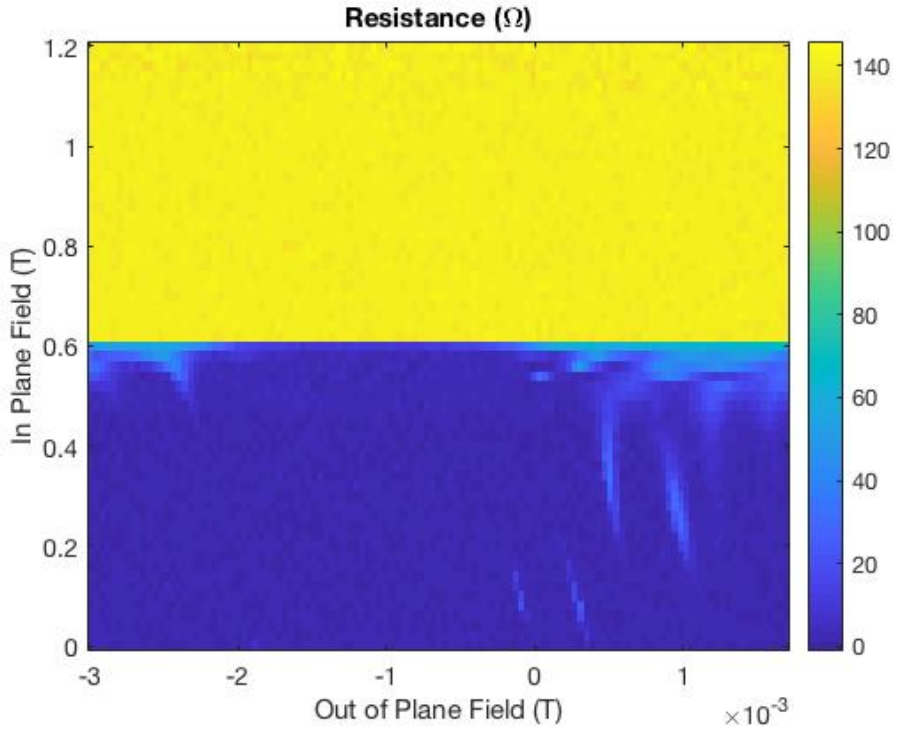

Figure 5.8: Sweeping in-plane field in a 4 μm $\times$ 800 nm Josephson junction. We plot the ac resistance as in-plane and out-of-plane magnetic fields are swept in a Josephson junction of dimensions 4 μm $\times$ 800 nm. The superconductivity dies off at 0.6 T and does not re-emerge later.

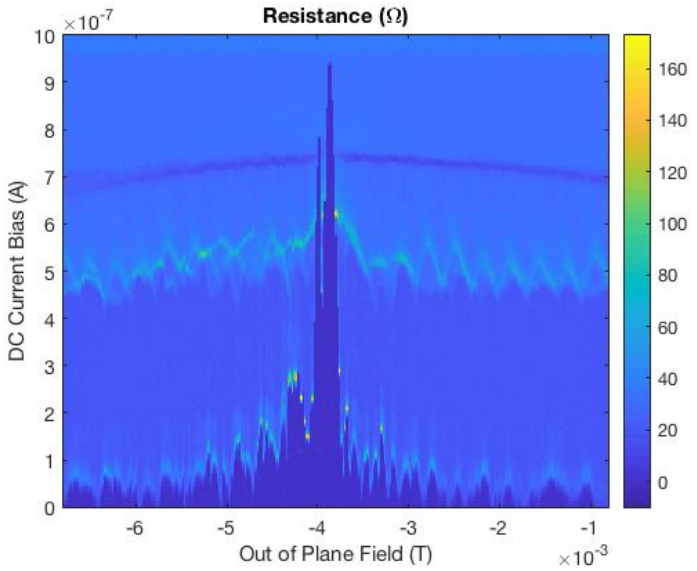

Figure 5.9: Single-slit interference pattern on an 8 μm $\times$ 800 nm thin aluminum junction. We plot the ac resistance due to an applied dc current as an out-of-plane magnetic field is swept in an 8 μm $\times$ 800 nm aluminum junction. The critical current is around 1.03 μA and the normal resistance 30 Ω, leading to an I_cR_n product of $\approx$ 31 μeV. We do see a single peak in our supercurrent, but the sidelobes do not look as much like a single-slit interference pattern as in the 50 nm thick aluminum junctions from Figures 5.5 and 5.6. We also see an oscillating feature at around 500 nA of current bias, which is not easily explained.

5.6.1 Fraunhofer patterns

We measured 14 nm thick aluminum junctions at mK temperatures the same way that we did the 50 nm thick junctions mentioned above in Section 5.5.1. Figure 5.9 shows the measurement on an 8 μ $\times$ 800 nm junction. While superconductivity is clearly observed, the I_cR_n product is around 31 μeV, around half of that for the 50 nm thick junction. More of a concern is the fact that the junction has unexplained features. There is an oscillation in the resistance pattern at around 500 nA of applied bias. Our best guest for this oscillation is that it is caused by transport outside the junction's area.

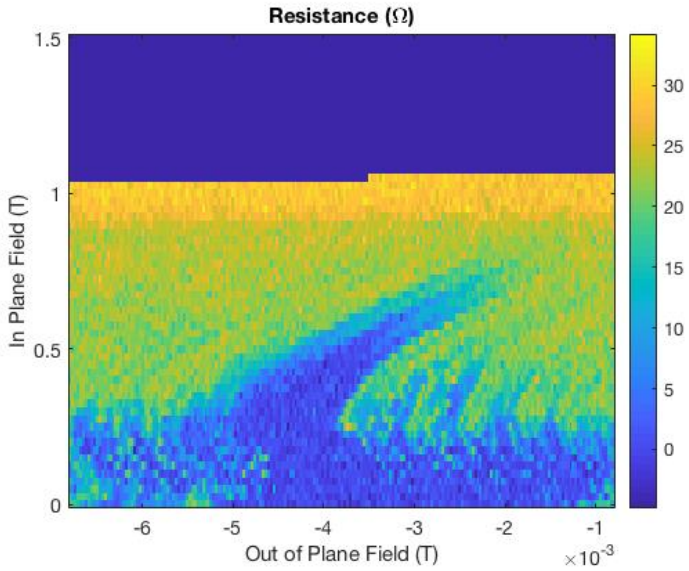

Figure 5.10: In-plane field measurement in an 8 μm $\times$ 800 nm thin aluminum junction. We plot the ac resistance as in-plane and out-of-plane magnetic fields are swept in a Josephson junction of dimensions 8 μm $\times$ 800 nm. The superconductivity dies off at around 0.7 T and does not re-emerge later. The curve of the main peak at higher in-plane fields is due to hysteresis in our vector magnet.

5.6.2 In-plane fields

We then measured our 8 μm $\times$ 800 nm junction from Figure 5.9 as a function of in-plane field, following the same procedure as in Section 5.5.2. We show this measurement in Figure 5.10. The superconductivity dies off around 0.7 T but does not re-emerge later, despite the fact that the aluminum leads in the junction still superconduct until around 1.4 T. The unexplained oscillating feature from Figure 5.9 is not apparent here when we sweep in-plane field.

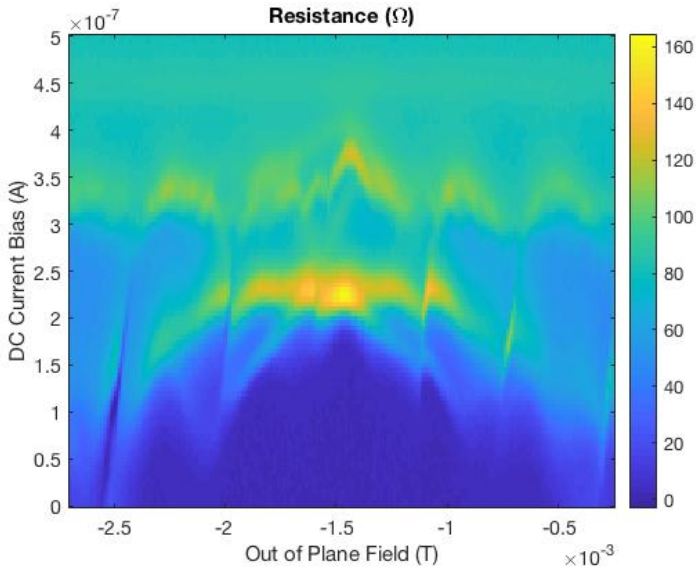

Figure 5.11: Single-slit interference pattern on a 4 μm $\times$ 500 nm aluminum junction with positive top gate voltage. We plot the ac resistance due to an applied dc current as an out-of-plane magnetic field is swept in a junction with top gate voltage set to $+5$ V. We do not see a clear interference pattern, but we do see a similar unexplained oscillation pattern to that shown in Figure 5.9.

5.6.3 Gating the 14 nm thick junction

After the failure to see re-entrant superconductivity in the 14 nm thick aluminum junctions, we put top gates on them, following the procedure laid out in Appendix C. We repeated the Fraunhofer measurements on the junctions now that they had gates. Unfortunately, the topgate for the junction in the prior section leaked through our dielectric[†], so we had to measure a lower quality junction instead. Figures 5.11 and 5.12 show this measurement with the top gate respectively set to $+5$ V and -5 V.

We then applied an in-plane magnetic field to this junction. At both positive and negative gate voltages, the resulting measurement is virtually identical, so we only present the measurement at $+5$

[†] In fact, all of our best junctions had poor top gates.

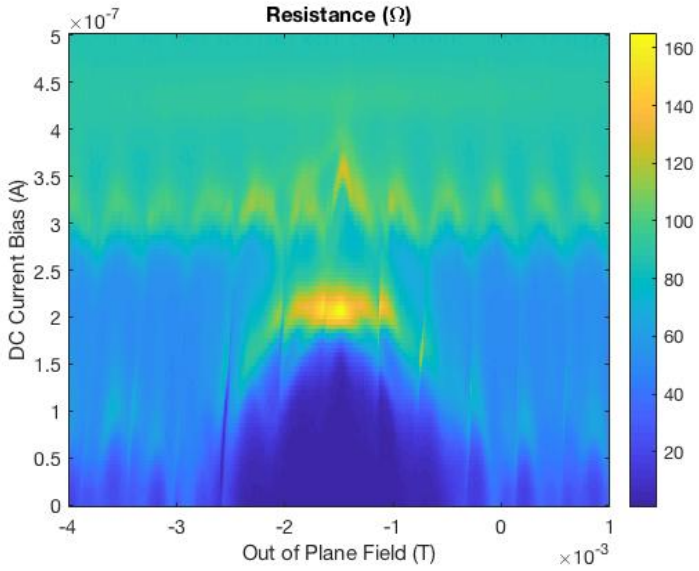

Figure 5.12: Single-slit interference pattern on a 4 μm $\times$ 500 nm aluminum junction with negative top gate voltage. We plot the ac resistance due to an applied dc current as an out-of-plane magnetic field is swept in a junction with top gate voltage set to -5 V. We don't see a clear single-slit interference pattern, but it is more single-slit-like than in the case when the top gate was set to $+5$ V in Figure 5.11. We again see the unexplained oscillation pattern shown in Figure 5.9 and in the positive top gate case.

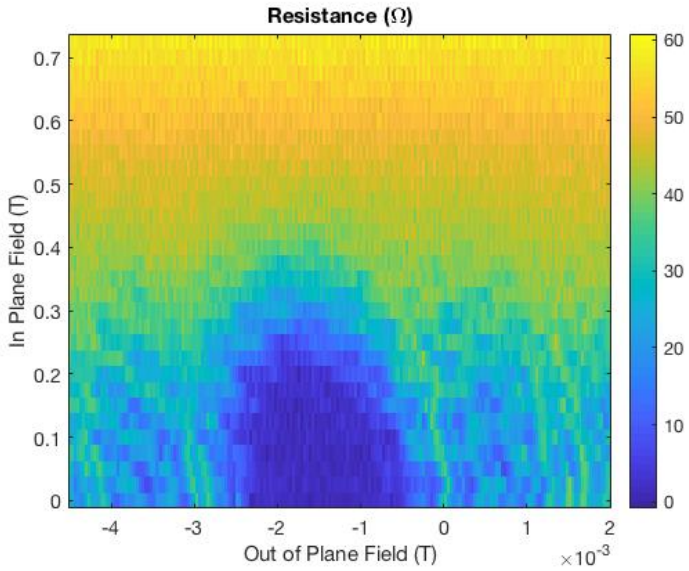

Figure 5.13: In-plane field measurement in an 4 μm $\times$ 500 nm thin aluminum junction. We plot the ac resistance as in-plane and out-of-plane magnetic fields are swept in our gated Josephson junction. The superconductivity dies off at around 0.3 T and does not re-emerge later.

V, which is shown in Figure 5.13. The superconductivity dies off around 0.3 T but does not re-emerge later, despite the fact that the aluminum leads in the junction still superconduct until around 1.4 T. The unexplained oscillating feature from Figures 5.11 and 5.12 is not apparent here when we sweep in-plane field.

5.7 Zigzag Junctions

A recent arXiv preprint by Laeven et al. discussed[40] a novel junction geometry that would increase the topological gap. As shown in Figure 5.14, a zigzag geometry prevents very long trajectories that are present in standard planar Josephson junctions. The Thouless energy, a limiting factor on the topological gap, goes as $E_{\text{th}} = \hbar/\tau_f$. By preventing long trajectories, the maximum travel time drops,

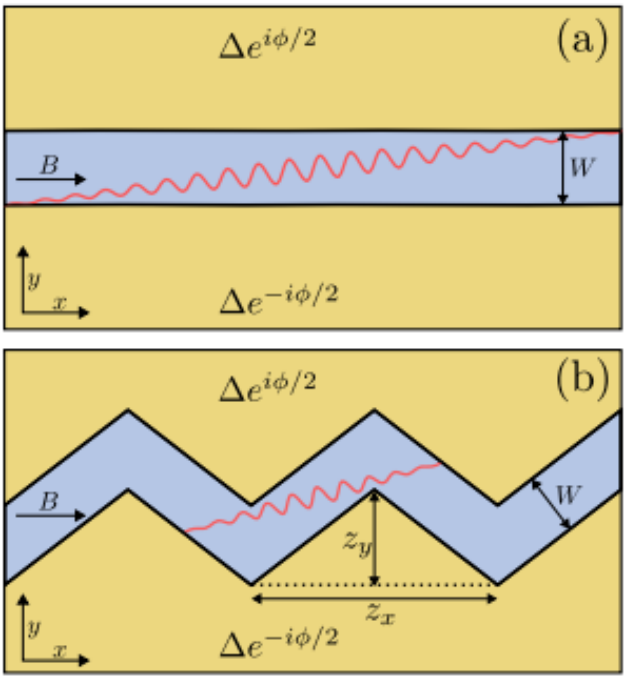

Figure 5.14: Zigzag junction schematic. (a) shows a planar junction, and (b) a zigzag junction. The yellow is superconductor, with a phase difference of φ between the leads in both cases. The middle gray region in both cases is the semiconductor with a width W. In both cases, a magnetic field B is applied in the x-direction. A trajectory traveling at a slight angle, represented by the red curve, has a much shorter flight time in the zigzag than the planar geometry, thus significantly increasing the topological gap in the former.

increasing the Thouless energy. Laeven et al. show that the topological gap should increase as well, more than an order of magnitude larger than in the planar case.

We fabricated zigzag junctions on InAs, using the same fabrication steps as for the planar junctions. Again, we used 14 nm of deposited aluminum as our superconductor. An example image of a zigzag junction is shown in Figure 5.15. The junction "zigs" and "zags" 4 times each, maintaining an 800 nm separation between the two leads the whole way. Each zig (zag) is 1.13 μm long and forms a 90° angle with the prior zag (zig).

Figure 5.16 shows the measurement of a zigzag junction in the presence of an applied out of plane

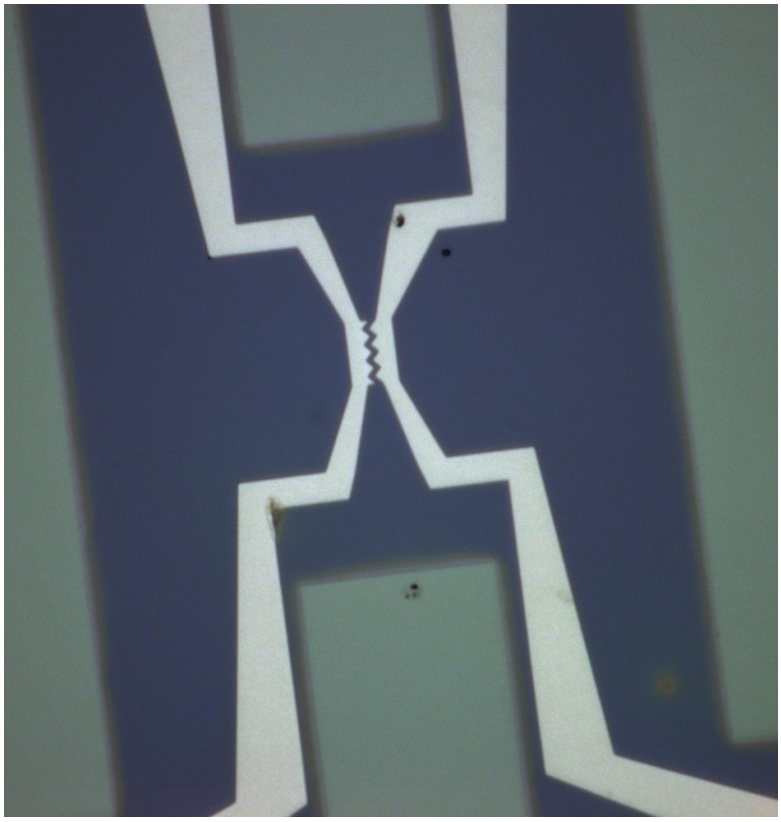

Figure 5.15: Aluminum zigzag junction on buried InAs quantum well. Shown here is a close-up optical microscope image of a zigzag junction after aluminum is deposited to define superconductors. The gray background is the top of the two-dimensional electron gas. The green-gray color on the sides is where mesa is etched away. The light white is the aluminum leads for the junction. Note that in this device, the mesa was not etched near the superconducting leads.

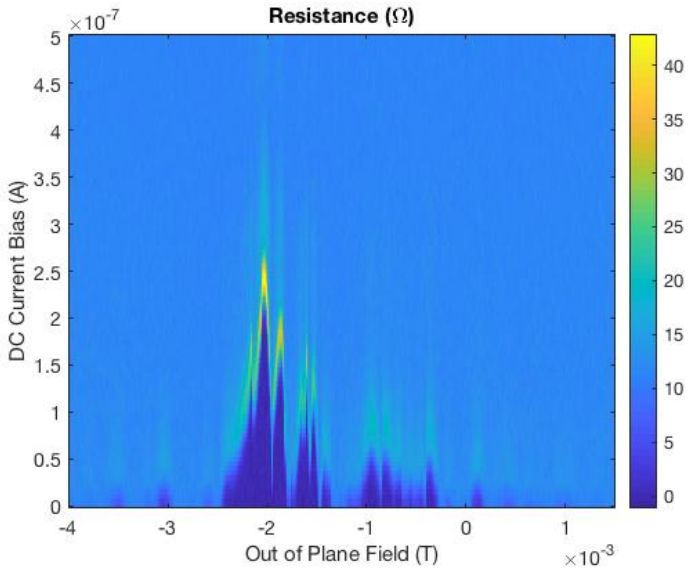

Figure 5.16: Zigzag junction in the presence of an out-of-plane magnetic field. We plot the ac resistance due to an applied dc current as an out-of-plane magnetic field is swept in a zigzag junction. We see a maximum critical current of 250 nA, and an interference pattern where the supercurrent is higher on the positive field side of the central peak. Reversing the field sweep direction reverses this pattern.

field. Figure 5.17 shows the same junction in the presence of an in-plane field. The supercurrent dies off at around 0.3 T, similar to the linear case, and does not re-emerge later, so we do not realize the theoretical benefit of a zigzag over a planar junction in this device.

5.8 Outlook

Much work remains to be done on this system of high-mobility InAs quantum wells. We successfully induced superconductivity on this system. Due to limited time working on this system, we only made a few fabrication attempts with thin aluminum superconductors, and only on one sample. The 14 nm thick aluminum devices had some unexplained features, while the 50 nm thick aluminum ones displayed textbook quality single-slit interference patterns in the presence of applied out-of-plane mag-

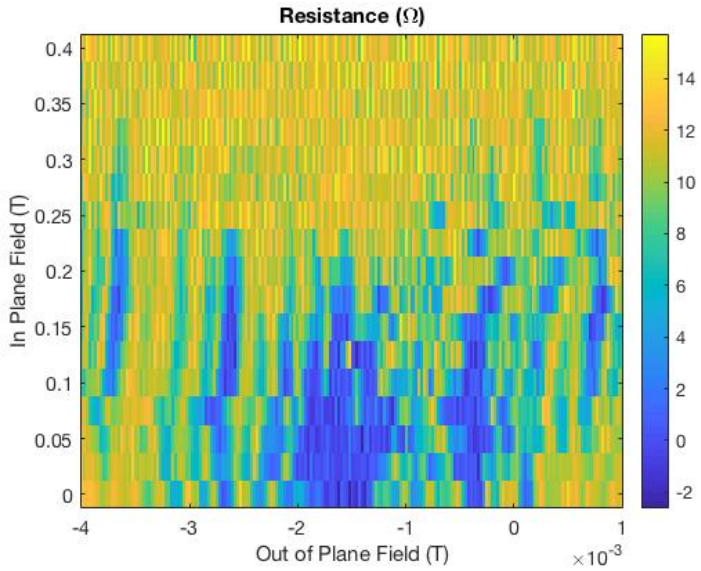

Figure 5.17: Zigzag junction in the presence of an in-plane magnetic field. We plot the ac resistance as in-plane and out-of-plane magnetic fields are swept in a zigzag junction. The superconductivity dies off at around 0.3 T and does not re-emerge later.

netic fields. Some fabrication calibration is likely needed on the 14 nm thick aluminum depositions.

We have several samples with mobility greater than 1.2×10^6 cm^{2}V^{-1}s^{-1} to measure in the future, as well as those with higher critical field niobium nitride superconductors instead of aluminum[‡]. The high mobility samples will likely support much higher quality quantum point contacts than were seen on the very low mobility InAs quantum wells from Chapter 4.

One issue of concern with these samples is their very low Rashba strength, $\alpha \approx 1.6 \times 10^{-11}$ [69]. Comparing the spin orbit energy $E_{SOC} = 0.5 m_0 \left(\frac{\alpha}{\hbar}\right)^2$ to the Zeeman energy from applied magnetic field $E_Z = g\mu B$, we see that for $g \sim 10$, the assumed g-factor in this system, the Zeeman energy exceeds the spin-orbit energy at around 90 mT. Growing these materials on a backgate-able sample

[‡]They currently sit in a desiccator as we wait for the COVID-19 outbreak to end.

may allow us to tune up the Rashba strength into a stronger Rashba regime, as is the case in our HgTe materials that showed re-entrant superconductivity.

A

Fabrication procedures for HgTe devices

A.1 Introduction

This appendix describing the processes used to fabricate the HgTe-based devices was originally compiled by Hechen Ren [59]. Small edits have been made.

A.2 Important Notes

A few general rules for fabricating HgTe/CdHgTe devices are summarized as follows.

1. HgTe/CdHgTe heterostructures are more fragile compared to most semiconductor wafers. Make sure to handle with extra care.
2. Never heat the HgTe/CdHgTe heterostructure above 80 °C, as it will rapidly degrade or damage the material.
3. The MBE-grown surface of the HgTe/CdHgTe wafers oxidizes nicely, so direct metal deposition onto the surface will likely not make ohmic contacts.
4. Most SiO_2-based films (such as e-beam evaporated SiO_2 and HSQ/Fox resists) have difficulties sticking to the MBE-grown surface of the HgTe/CdHgTe wafers, but features with dimensions over 200 microns tend to remain in place during developing. Attach small features to large features to preserve their original design.
5. The surface of CdHgTe exposed by dry etching processes oxidizes poorly, so direct metal deposition thereafter will likely make ohmic contacts.
6. Most metals react with HgTe and CdHgTe through substitution of the cadmium and mercury atoms, forming alloys at the interface.
7. Titanium reacts with HgTe or CdHgTe especially aggressively and works well as a sticking layer prior to any metal deposition.

A.3 Fabrication Procedures

A.3.1 Mesas

1. Define the etch mask using either HSQ or SiO_2/Ti.
2. (Optional) Measure the height of the etch mask before milling using a profilometer.

3. Mill using a DC argon ion source for enough time to etch through the quantum well (usually aim for 100 nm).
4. (Optional) Measure the height of the etch mask after milling using a profilometer.
5. Remove the etch mask by immersing the sample in 1:7 BOE for 7 minutes. Rinse in DI water.
6. Measure the height of the mesa using a profilometer. If you performed the optional steps you can get a sense of if the etch mask is etched at all. Typically for this process, it will not be etched.

A.3.2 Bond pads

This procedure will produce large areas of Ti/Au that make good bond pads. If the metal is deposited onto a region where the quantum well has not yet been removed, then there will also be an ohmic contact to the quantum well with typical resistances of $\approx 1\ \mathrm{k}\Omega/10,000\ \mu m^2$.

1. Define large bond pad areas in PMMA, using a low-temperature e-beam recipe.
2. After developing, load the sample into a vacuum chamber with a thermal evaporator (and optionally a DC argon source).
3. (Optional) Mill slightly using a DC argon ion source (aim for about 10 nm etch depth). This step is not strictly necessary but will improve adhesion.
4. Deposit 10 nm of titanium, followed by 50 nm of gold.
5. Lift off in acetone.

A.3.3 Contacts

This procedure will produce contacts that are suitable for inducing superconductivity.

1. Clean the sample with oxygen plasma and spin PMMA.
2. Define contact areas in PMMA, using a low-temperature e-beam recipe. These contacts should overlap the bond pads and/or contact the same continuous region of the quantum well as the bond pads.
3. After developing, load the sample into a vacuum chamber with a DC argon source and material deposition capability.
4. Mill using a DC argon ion source, aiming to expose the quantum well but not etch through.
5. Deposit the desired materials. Three options for deposition are given below:
   (a) 10 nm titanium, followed by X nm aluminum, where X is larger than the mesa height. These contacts will climb the mesa but will stop superconducting if the magnetic field applied parallel to the film exceeds 100 mT.
   (b) 5 nm titanium, followed by 15 nm aluminum. These contacts probably won't climb the mesa, but will superconduct up to 1.5-2 T applied parallel to the film.
   (c) 10 nm titanium, followed by X nm niobium. X can vary and since the niobium is sputtered, the contacts climb mesas. The contacts will superconduct up to applied fields of at least 4 T.
6. Lift off in acetone.

A.3.4 Tunnel Probes

This procedure will produce tunnel probes that give reasonable tunnel couplings to the proximitized 2DEG HgTe, based on the second approach mentioned in Chapter 3.

1. Design the tunnel probes layer for e-beam lithography. Typical dimensions of overlap are 100-150 nm by 100-150 nm. To account for misalignment and etching/re-deposition sidewalls, try to vary the overlapping areas as well as the orientation among devices on each fabrication run, so that some will fall in the optimal range.

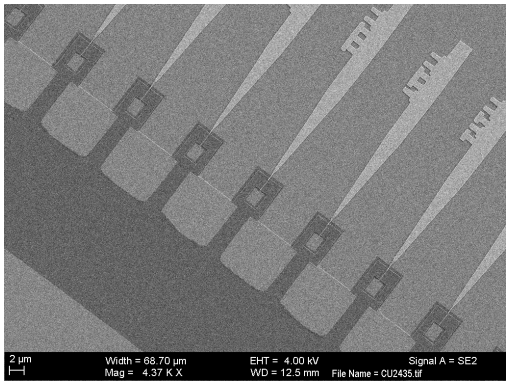

Figure A.1: An SEM of an array of tunnel probe devices with finely varying overlapping dimensions. Taking advantage of the scaling capability of HgTe fabrication, we can account for small misalignment and other effects such as the insulating sidewalls of the mesa to guarantee the production of useful devices. We use a binary code composed of a sequence of 'T's pointing up and down to label our tunnel probe devices.

1. Define tunnel probes in PMMA, using a low-temperature e-beam recipe. Pay attention to the following details.

   (a) They should overlap the bond pads and/or contact the same continuous region of the quantum well as the bond pads.

   (b) The tips of the tunnel probes should be in its separate layer and finely aligned to the nearby alignment marks contained in the mesa layer, preferably the same ones the superconducting contacts are also aligned to. Indeed, you can reused these marks and the fact they have aluminum films on top is never an issue.

   (c) For the tips of the tunnel probes, which goes down to 100 nm in width, use a dose of 5,000 $\mu C/cm^2$. For the rest of the pattern, use the usual values in A.6.3.

2. After developing, load the sample into a vacuum chamber with a DC argon source and material deposition capability.

3. Mill using a DC argon ion source, aiming to expose the quantum well but not etch through.

4. Rotate the sample stage if necessary. Deposit 10 nm titanium, followed by X nm gold, where X is greater than the mesa height. These contacts will climb the mesa but will stop superconducting if the magnetic field applied parallel to the film exceeds 100 mT.

5. Lift off in acetone. Do not be afraid to sonicate if needed as the adhesion is robust after milling.

6. Pay special attention while wire-bonding to the tunnel probe contacts. Because of their extreme pointiness, the electrostatic shocks from the wirebonder can easily blow up the tunnel probe if not carefully grounded and discharged (see Figure A.2 for a splendid example). Good practices include checking all the pins are grounded before mounting the sample, grounding yourself, and using a static eliminator such as Staticmaster 2U500 Ionizing Cartridge.

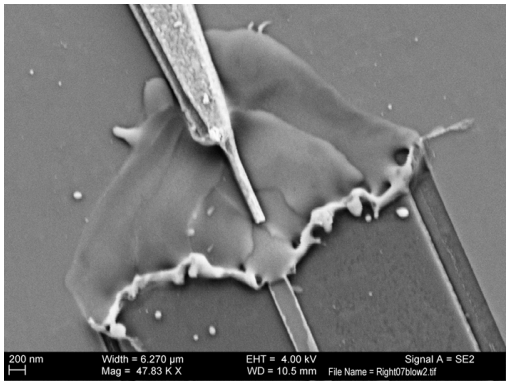

Figure A.2: An SEM of an example of tunnel probes destroyed during wirebonding. Due to their extremely thin tips, the electrostatic shocks from the wirebonder tend to destroy the tunnel probe if not carefully grounded and discharged.

A.3.5 Top Gates

Use this procedure to make top gates. It is necessary to deposit a dielectric layer between the gate metal and the substrate to prevent gate leakage.

1. Clean the sample with oxygen plasma.
2. Deposit Al_2O_3 using atomic layer deposition. The thickness of this layer was 50 nm for devices in this thesis.
3. Define the gate areas in PMMA, using a low-temperature e-beam recipe.
4. Load the sample into an evaporator and deposit 10 nm of titanium, followed by X nm of gold, where X should surpass the mesa height to ensure continuity of the gate material.
5. Lift off in acetone.

A.4 List of Procedures

A.4.1 Creating an HSQ etch mask

Use this procedure to pattern an etch mask composed of HSQ. HSQ is a negative e-beam resist, so areas exposed to the electron beam will be shielded during the etching process. This is a relatively quick method to make mesas. However, sometimes isolated small features ($<$ 10 um) do not stick to the substrate strongly enough, and can be inadvertently removed during development. We have some evidence that this problem becomes more pronounced as the resist ages, but more characterization is needed.

- Remove HSQ from refrigerator and place in a room-temperature fume hood for 30 minutes.
- Spin HSQ onto the substrate at 3000 rpm, for 45 seconds. Bake at 80°C for 4 minutes.
- Spin another layer of HSQ onto the substrate at 3000 rpm, for 45 seconds. Bake at 80°C for 4 minutes.
- Expose the pattern as soon as possible after baking. Dose: 1800 $\mu C/cm^2$.

- Develop in 25 % TMAH for 17 seconds. Take care during this step, since TMAH is extremely toxic. Dip the sample in four subsequent beakers of DI water after developing. Be as smooth and steady as possible during the developing and rinsing as turbulence tends to cause the HSQ mask to move across the surface of the wafer.
- You are now ready to etch mesas.

A.4.2 Creating a SiO_2/Ti etch mask

This is a liftoff procedure for patterning an etch mask composed of SiO_2/Ti. The titanium may not be strictly necessary, but it is etched extremely slowly by DC argon milling and is easy to deposit, so we use it.

- Define the mesa areas in PMMA, using a low-temperature e-beam recipe.
- After development, load the sample into an e-beam evaporator and deposit $\approx$ 100 nm SiO_2.
- Deposit 20 nm of titanium.
- Lift off the etch mask in acetone.
- You are now ready to etch mesas.

A.4.3 Milling the HgTe heterostructure

Use this procedure to remove material from the HgTe heterostructure. For the recipes presented here, the sample should be mounted facing a DC argon source, with the surface of the wafer oriented perpendicular to the argon flux (although angle milling is certainly also possible). We used two different

DC argon sources in this thesis, one mounted inside a thermal evaporator, and one inside a sputtering system. The following parameters characterize these two sources:

1. Veeco 3cm DC Ion Source
   - Beam voltage: 500 V
   - Beam current: 50 mA
   - Accelerator voltage: 1000 V
   - Etch rate of HgTe heterostructure: 80 nm/minute
2. Kaufman Ion Source
   - Beam voltage: 400 V
   - Beam current: 23 mA
   - Accelerator voltage: 80 V
   - Etch rate of HgTe heterostructure: 81 nm/minute

A.4.4 Oxygen plasma cleaning

This is a recipe for using an ECR-based reactive ion etcher to clean the surface of the HgTe heterostructure. We have found it essential to clean the surface prior to atomic layer deposition of Al_2O_3. Without this cleaning step there tend to be holes in the film.

For the work done in Chapter 2, we used a Nexx RIE, which got decommissioned in the Harvard cleanroom. Since then we have been using a Technics Plasma Stripper, which applies to most of the work described in Chapter 3. Below are the recipes.

A.5 Recipe for Nexx RIE

(old RIE-6)

1. Run the recipe 'burnin.rcp' for 20 minutes, to clean the chamber. If the sample is being cleaned before ALD, this time can be used to preset the ALD machine to the deposition temperature.
2. Load the sample onto the sample chuck, using a drop of Santovac5 vacuum oil on the backside of the wafer to provide a better thermal link to the stage.
3. Run the recipe 'shipblas.rcp' with the following parameters:
   (a) O2 flow (sccm): 20
   (b) Process pressure (mtorr): 15
   (c) Microwave power (watts): 400
   (d) RF power (watts): 20
   (e) Backside helium (torr): 10
   (f) Chuck temperature (C): 25.0
   (g) Tolerance delay (s): 30
   (h) Processing time (s): 300
4. Unload the sample and clean the vacuum oil off the back side using IPA.

A.6 Recipe for Technics Plasma Stripper

(RIE-5 in the CNS)

Please note the RIE-5 is an old-fashioned micro stripper which looks like a microwave oven and works like one. Everything is manual, everything is quick, and everything works (within reason, that is).

1. Do a mock run for five minutes (instead of two) before the real process to a) clean the chamber and b) make sure the metallic substrate holder does not get hot.
2. Load sample and pump chamber down to under 30 mTorr. To vent the chamber, switch 'vac' off and 'vent' on. To pump down the chamber, switch 'vent' off and then 'vac' on.
3. Turn on the switch for gas A (Oxygen). Then dial the corresponding knob to make the reading as precisely 20 sccm as this antique piece of technology allows.
4. Wait for the pressure to stabilize. Set up a timer or use the clock on the wall. Turn on the power switch and dial the corresponding knob to 100 Watts.
5. Watch the process for two minutes.
   (a) Oxygen flow (sccm): 20
   (b) Process pressure (mtorr): $\approx$ 270 mTorr
   (c) Microwave power (watts): 100
   (d) Processing time (s): 120
6. At the end of the two minutes, dial down the microwave, switch the power off, dial process gas A to zero, and turn off the gas switch.
7. Unload the sample. Refer to step 2 for how.

A.6.1 Niobium deposition

Niobium was sputtered in a commercially available AJA ATC series UHV hybrid deposition system. The base pressure of the system was in the 10^{-9} - 10^{-8} torr range. All of the niobium films in Chapters 2 and 3 were deposited using DC sputtering, with the following parameters:

- Argon flow: 50 sccm

- Power: 200 W

A.6.2 Atomic layer deposition of Al_2O_3

This a recipe for low-temperature atomic layer deposition of Al_2O_3. It was developed for a Cambridge Nanotech Savannah ALD system. It is advisable to wait until the deposition begins before walking away from the system, to make sure that pulses are firing normally. Also, the system is set up to record a screenshot when the recipe finishes.

1. Place a washer onto the center of the stage, and load the sample so that it sits in the center of the washer. This will prevent the sample from accidentally moving into the outlet of the chamber during the pump-down.
2. Pump out the chamber and run the recipe 'Al_2O_3 50C 50nm' with the following parameters:
   (a) Flow 20
   (b) Heater 9 50
   (c) Heater 8 50
   (d) Stabilize 9
   (e) Wait 60
   (f) Pulse 0 0.015
   (g) Wait 20
   (h) Pulse 3 0.015
   (i) Wait 10 10
   (j) Goto 5 500
   (k) Wait 10

3. Unload the sample.

A.6.3 Low-temperature e-beam lithography

These are instructions for a 100 kV Elionix-7000 system. We have found that exposing HgTe heterostructures to standard e-beam doses at 100 kV does not degrade their electronic properties.

1. Spin-coat the sample with PMMA. Spin each layer of PMMA at 4000 RPM for 45 seconds.
2. After spinning each layer of PMMA, bake the sample at 80°C for 10 minutes. For lift-off processes, determine how many layers of PMMA are needed based on the maximum thickness of material that will be deposited, as follows:

   - $\approx$ 30 nm: one layer of PMMA 950 A4.
   - $\approx$ 300 nm: one layer of PMMA 495 C6, followed by one layer of PMMA 950 A4.
   - For thicker films, add more layers of PMMA 495 C6.

   Note that these are just rough estimates for thicknesses when spun at 4000 RPM. Also note that PMMA will be etched slightly by argon milling, typically at a rate of $\approx$ 40 nm/minute for the parameters used in this work.
3. Expose the pattern. Dose: 2700 $\mu C/cm^2$ for small features (micron-sized); 2400 $\mu C/cm^2$ for medium features; and 1800 $\mu C/cm^2$ for large features above 100 μm.
4. Develop in chilled MIBK/IPA (1:3) for 1 minute.

B

Fabricating Devices on Surface InAs Quantum Wells with Epitaxial Aluminum

B.1 Introduction

This appendix describes the processes used to fabricate devices on the InAs surface quantum wells with epitaxial aluminum received from the Shabani group at NYU that were discussed in Chapter 4.

B.2 Important Notes

A few general rules for fabricating InAs quantum well devices are summarized below.

1. Indium has a melting point of 156.6 °C. All sorts of problems can emerge when heterostructures containing indium are heated to standard semiconductor fabrication temperatures of 180 °C, and so we do not heat these samples above 150 °C.

2. The various layers of these heterostructures tend to look very similar when using electron beam lithography machines. Furthermore, aluminum does not create a strong contrast with these materials either, and so it is strongly recommended to deposit gold alignment marks as part of the first fabrication step.

3. Etch times change from substrate to substrate - it is important to calibrate the argon mill etch time and the wet etch time before using a new sample.

4. Sonicating these materials tends to lead to the epitaxial aluminum falling off, and so should be avoided at all costs.

5. The high-indium content layers of the heterostructure tend to lead to conduction through the bulk of the material, and so deep mesa etches are needed. This is especially true for samples with ALD growth after.

6. TMAH containing compounds (such as standard photolithography developers like MF319) etch the aluminum very quickly, and so should not be used.

7. All of the following steps assume the use of the EL-4 lithography tool in the Harvard cleanroom (100 kV Elionix ELS-7000), and so there may need to be changes made to the resist, lithography, and development steps if a different tool is used.

8. Bond pads, mesa etching, and superconductor definition can occur in any order without quality differences. However, we have noticed that the order listed below gives the best yield rate, and so it is the recommended order to use. The yield rate differences for different orders was because the mesa etch tended to overetch laterally across the sample if it followed the aluminum etch to define superconductors, and the bond pads lifted off poorly if they followed mesa etching.

B.3 Fabrication Procedures

B.3.1 Ti/Au Bond pads

1. Start by coating the sample in PMMA - we use an undercut here to help liftoff.
   (a) Spin 495 PMMA A8 at 4000 RPM for 45 s.
   (b) Bake at 150 °C for 3 minutes.
   (c) Spin 950 PMMA A4 at 4000 RPM for 45 s.
   (d) Bake at 150 °C for 3 minutes.
2. Define bond pads using the Elionix. For this step, we tend to write the larger features at 20 nA and the smaller ones at 2nA.
3. Develop for 80 seconds in a beaker of MIBK:IPA (1:3) that has been chilled for more than 15 minutes, then rinse with IPA and blow dry with nitrogen.
4. Load the sample in the evaporator in the sample prep room, and pump down until it reaches below 1e−6 Torr.
5. Run the argon mill for around 10 s.
6. Deposit 10 nm of titanium.
7. Deposit 100 nm of gold.
8. Lift off in acetone.

Figure B.1 shows an example image of a Josephson junction after bond pads and alignment marks have been deposited.

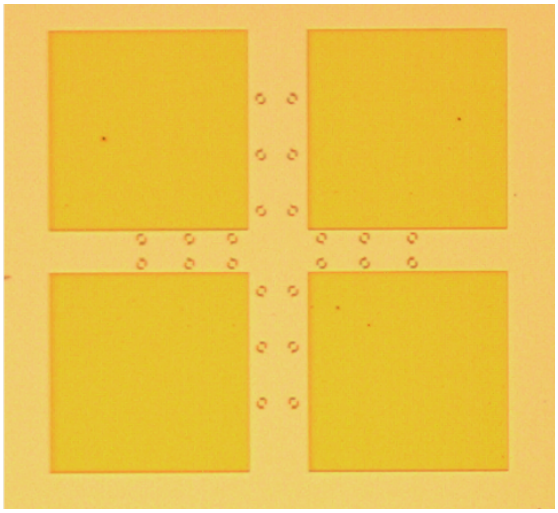

Figure B.1: Josephson junction after the bondpad deposition step. Shown here is an optical microscope image of a device with bondpads and alignment marks. The gold squares are the bondpads, and the small dark shapes are alignment marks. The lighter yellow background is aluminum.

B.3.2 Mesa etching

1. Best practice here is to run a short RIE oxygen plasma etch ($\approx 1 - 2$ minutes at a low power) to strip any PMMA that didn't wash off with acetone. However, we did not always do this here and mostly had no issues with skipping the oxygen plasma etch.

2. Spin 950 PMMA A4 at 4000 RPM for 45 s.

3. Bake at 150 °C for 3 minutes.

4. Define the mesa etch using the Elionix. For this step, we tend to write the larger features at 10 nA and the smaller ones at 2nA.

5. Develop for 80 seconds in a beaker of MIBK:IPA (1:3) that has been chilled for more than 15 minutes, then rinse with IPA and blow dry with nitrogen.

6. First, remove epitaxial aluminum using Transene Aluminum Etch Type D. Etch time is around 75 seconds, sample dependent. The Transene D should be heated for one hour prior to the etch by placing it in a water bath that is placed on a hot plate at 50 °C.

7. Rinse very briefly with water and immediately place in the citric acid compound.

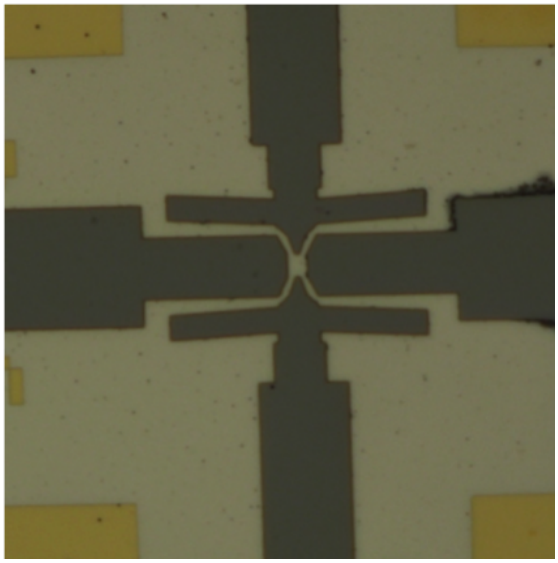

Figure B.2: Josephson junction after the mesa etch step. Shown here is an optical microscope image of a Josephson junction after the mesa is etched. The yellow boxes in each of the four corners are bondpads. The light gray background is aluminum, and the dark gray is where the mesa is etched away.

(a) Wet etch using a compound of water, 1 M citric acid, phosphoric acid and hydrogen peroxide (in proportion 220:55:3:3). 1M citric acid is made by mixing 10.56 grams of citric acid powder with 55 mL of water.

(b) The etch time for this step is around 15 minutes, in order to etch down several hundred nanometers to ensure the etch lands below the high-indium content layers of the heterostructure.

8. Rinse with water, and then immediately place back into the heated Transene D for around 5 seconds.

9. Rinse with water, blow dry with nitrogen, and then wash with acetone.

10. Measure the mesa etch depth.

Figure B.2 shows an example image of a Josephson junction after the mesa etch step.

B.3.3 Superconductor definition by aluminum etching

1. The sample has epitaxial aluminum, and so to create devices, we etch away some of the aluminum.
2. Spin 950 PMMA A4 at 4000 RPM for 45 s.
3. Bake at 150 °C for 3 minutes.
4. Define the region to etch using the Elionix. For this step, we tend to write the larger features at 10 nA and the smaller ones at 1nA.
5. Develop for 80 seconds in a beaker of MIBK:IPA (1:3) that has been chilled for more than 15 minutes, then rinse with IPA and blow dry with nitrogen.
6. Remove epitaxial aluminum using Transene Aluminum Etch Type D. Etch time is around 75 seconds, sample dependent. The Transene D should be heated for one hour prior to the etch by placing it in a water bath that is placed on a hot plate at 50 °C.
7. Rinse with water, blow dry with nitrogen, and then wash with acetone.

Figure B.3 shows an example image of a Josephson junction after the aluminum etch step that defined the superconductors.

B.3.4 Top Gate Deposition

1. First, deposit a top oxide. We use a combination of aluminum oxide and hafnium oxide. The pulse order on the ALD tools in the Harvard cleanroom is water, aluminum, water, hafnium, for 130 cycles at 150 °C. This gives a film of around 30 nm.
2. The very deep mesa etch requires a two-part gate deposition - a thin metal deposition to define the fine features of the gate, and a thick metal deposition to climb the mesa and connect the gate to its bondpad.
3. Coat the sample in PMMA - we use an undercut here to help liftoff.
   (a) Spin 495 PMMA A8 at 4000 RPM for 45 s.

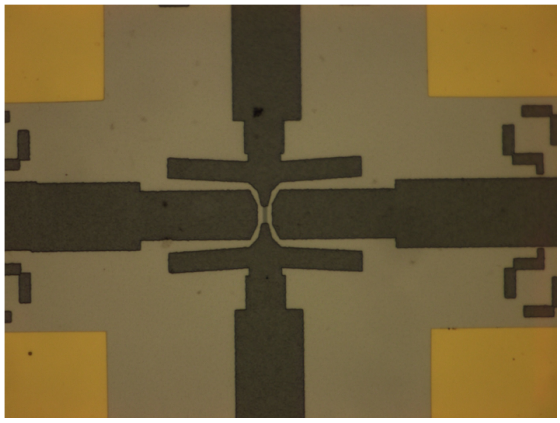

Figure B.3: Josephson junction after the aluminum etch step. Shown here is an optical microscope image of a Josephson junction after the aluminum is etched to define superconductors. The yellow boxes in each of the four corners are bondpads. The light gray background is aluminum, and the dark gray is where the mesa is etched away. The tiny rectangle of medium gray color in the center is the weak link in the junction, where aluminum is stripped away.

(b) Bake at 150 °C for 3 minutes.

(c) Spin 950 PMMA A4 at 4000 RPM for 45 s.

(d) Bake at 150 °C for 3 minutes.

4. Define the gates using the Elionix. For this step, we tend to write the larger features at 10 nA and the smaller ones at 1nA.

5. Develop for 80 seconds in a beaker of MIBK:IPA (1:3) that has been chilled for more than 15 minutes, then rinse with IPA and blow dry with nitrogen.

6. Deposit 10 nm of titanium.

7. Deposit around 20 nm of gold for the smaller gate step, and $x + 50$ nm of gold for the larger gate step, where x is the depth of the mesa etch.

8. Lift off with acetone.

Figure B.4 shows an example image of a Josephson junction after a top gate is put down.

Figure B.4: Josephson junction after the top gate deposition step. Shown here is an optical microscope image of a Josephson junction after a top gate is deposited. The upper four light yellow squares are bondpads. The light gray background is aluminum, and the dark gray is where the mesa is etched away. The darker yellow square in the bottom right corner is the bondpad for the top gate, and the dark yellow line attached to it is the arm of the topgate.

C

Fabricating Devices on the Buried InAs Quantum Wells

C.1 Introduction

This appendix describes the processes used to fabricate devices on the InAs quantum wells received from the Wegscheider group at ETH Zurich that were discussed in Chapter 5.

C.2 Important Notes

A few general rules for fabricating deep InAs quantum well devices are summarized below.

1. Indium has a melting point of 156.6 °C. All sorts of problems can emerge when heterostructures containing indium are heated to standard semiconductor fabrication temperatures of 180 °C, and so we do not heat these samples above 150 °C.

2. The various layers of these heterostructures tend to look very similar when using electron beam lithography machines. Furthermore, aluminum does not create a strong contrast with these materials either, and so it is strongly recommended to deposit gold alignment marks as part of the first fabrication step.

3. Etch times change from substrate to substrate - it is important to calibrate the argon mill etch time and the wet etch time before using a new sample.

4. All of the following steps assume the use of the EL-4 lithography tool in the Harvard cleanroom (100 kV Elionix ELS-7000), and so there may need to be changes made to the resist, lithography, and development steps if a different tool is used.

C.3 Fabrication Procedures

C.3.1 Ti/Au Bond pads

1. Start by coating the sample in PMMA - we use an undercut here to help liftoff.

   (a) Spin 495 PMMA A8 at 4000 RPM for 45 s.

   (b) Bake at 150 °C for 3 minutes.

   (c) Spin 950 PMMA A4 at 4000 RPM for 45 s.

   (d) Bake at 150 °C for 3 minutes.

2. Define bond pads using the Elionix. For this step, we tend to write the larger features at 20 nA and the smaller ones at 2nA.

3. Develop for 80 seconds in a beaker of MIBK:IPA (1:3) that has been chilled for more than 15 minutes, then rinse with IPA and blow dry with nitrogen.

4. Load the sample in the evaporator in the sample prep room, and pump down until it reaches below 1e−6 Torr.

5. Run the argon mill for around 10 s.

6. Deposit 10 nm of titanium.

7. Deposit 100 nm of gold.

8. Lift off in acetone. Sonicating may help the lift off, but do not sonicate for more than 10 seconds at a time so as to avoid lifting off desired features.

Figure C.1 shows an example image of a Josephson junction after bond pads and alignment marks have been deposited.

C.3.2 Mesa etching

1. Pre-clean the sample before etching using the RIE-9 tool at 100 W for 90 seconds, flowing 40 sccm of oxygen.

2. Spin 950 PMMA A4 at 4000 RPM for 45 s.

3. Bake at 150 °C for 3 minutes.

4. Define the mesa etch using the Elionix. For this step, we tend to write the larger features at 10 nA and the smaller ones at 2nA.

5. Develop for 80 seconds in a beaker of MIBK:IPA (1:3) that has been chilled for more than 15 minutes, then rinse with IPA and blow dry with nitrogen.

6. Wet etch using a compound of water, 1 M citric acid, phosphoric acid and hydrogen peroxide (in proportion 220:55:3:3). 1M citric acid is made by mixing 10.56 grams of citric acid powder

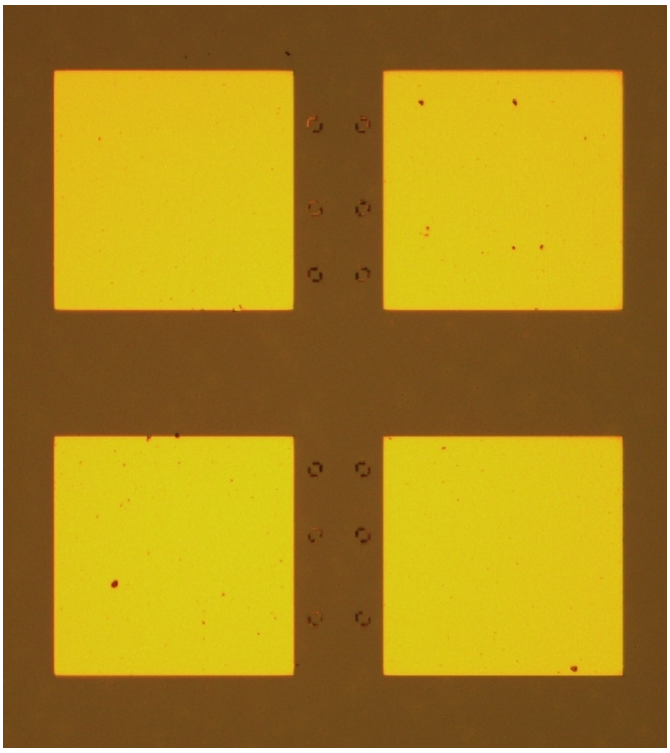

Figure C.1: Josephson junction after the bondpad deposition step. Shown here is an optical microscope image of a device with bondpads and alignment marks. The gold squares are the bondpads, and the small dark shapes are alignment marks. The brown background is the capping layer on top of the two-dimensional electron gas.

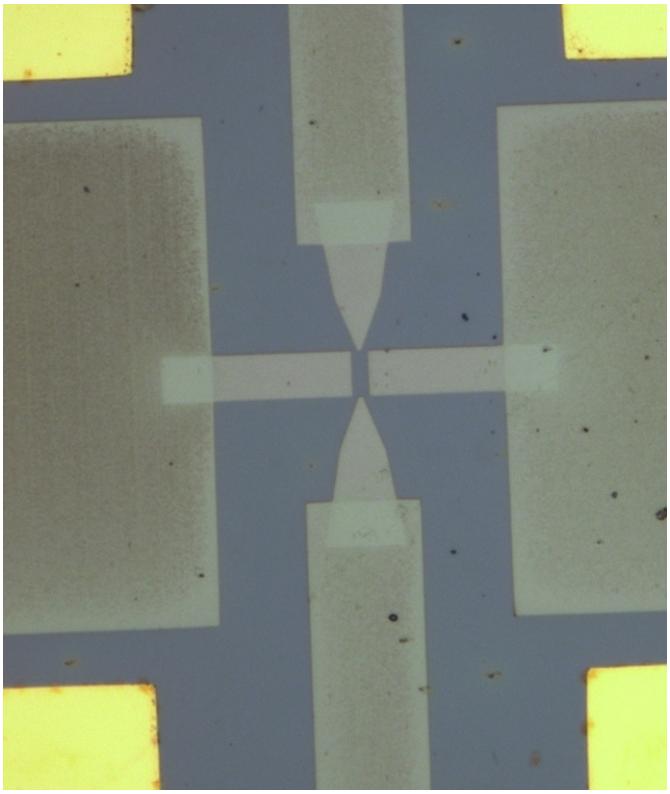

Figure C.2: Josephson junction after the mesa etch step. Shown here is an optical microscope image of a Josephson junction after the mesa is etched. The yellow boxes in each of the four corners are bondpads. The gray background is two-dimensional electron gas, and the light gray-green is where the mesa is etched away.

with 55 mL of water. The etch time for this step is around 225 seconds, although this will vary slightly depending on the exact wafer growth. The goal is to etch down several tens of nanometers below the quantum well.

7. Rinse with water, blow dry with nitrogen, and then wash off with acetone.

Figure C.2 shows an example image of a Josephson junction after the mesa etch step.

C.3.3 Superconductor Deposition

1. Pre-clean the sample before etching using the RIE-9 tool at 100 W for 90 seconds, flowing 40 sccm of oxygen.

2. Coat the sample in PMMA - we use an undercut here to help liftoff.

    (a) Spin 495 PMMA A8 at 4000 RPM for 45 s.

    (b) Bake at 150 °C for 3 minutes.

    (c) Spin 950 PMMA A4 at 4000 RPM for 45 s.

    (d) Bake at 150 °C for 3 minutes.

3. Define superconductors using the Elionix. For this step, we tend to write features at 1nA.

4. Develop for 80 seconds in a beaker of MIBK:IPA (1:3) that has been chilled for more than 15 minutes, then rinse with IPA and blow dry with nitrogen.

5. The next step is to etch down to the quantum well. We can do this either *in situ* with the superconductor deposition using an argon mill, or prior to the deposition using a wet etch.

6. We have found that in general the wet etch method tends to be very non-uniform. This is the wet etch recipe:

    (a) Wet etch using a compound of water, 1 M citric acid, phosphoric acid and hydrogen peroxide (in proportion 220:55:3:3). 1M citric acid is made by mixing 10.56 grams of citric acid powder with 55 mL of water. The etch time for this step is around 150 seconds, although this may depend based on substrate. The goal is to etch down to somewhere between the middle and bottom of the quantum well.

    (b) Wash with water, blow dry with nitrogen, and load in a deposition chamber immediately to avoid too much oxidation.

7. Deposit aluminum superconductors in the evaporator in the sample prep room, and niobium nitride superconductors in the sputterer in the sample prep room.

8. Aluminum superconductor deposition:

    (a) The first step is to use the ion mill. If a wet etch was done to etch down to the quantum well, this should just be a quick 10 s ion mill. However, if the argon mill is used to etch down to the quantum well, etch for around 225 seconds, substrate dependent, to reach the middle to bottom of the quantum well.

(b) Deposit 5 nm of titanium.

(c) Deposit 14 nm of aluminum.

9. Niobium nitride superconductor deposition:

   (a) The first step is to use the ion mill. If a wet etch was done to etch down to the quantum well, this should just be a quick 10 s ion mill. However, if the argon mill is used to etch down to the quantum well, etch for around 85 seconds, substrate dependent, to reach the middle to bottom of the quantum well.

   (b) Use the e-beam evaporator in the sputterer to deposit 5 nm of titanium.

   (c) Sputter niobium nitride for 660 seconds, this should leave deposit around 60 nm of material.

   Parameters: 50 sccm argon, 20 sccm nitrogen, power set to 200 W.

10. Lift off with acetone. Sonication may be used, although should be limited to no more than 10 seconds at a time, to avoid lifting off the superconducting leads.

Figure C.3 shows an example image of a Josephson junction after the superconductor deposition step.

C.3.4 Top Gate Deposition

1. First, deposit a top oxide. We use a combination of aluminum oxide and hafnium oxide. The pulse order on the ALD tools in the Harvard cleanroom is water, aluminum, water, hafnium, for 245 cycles at 150 °C. This gives a film of around 50 nm.

2. Coat the sample in PMMA - we use an undercut here to help liftoff.

   (a) Spin 495 PMMA A8 at 4000 RPM for 45 s.

   (b) Bake at 150 °C for 3 minutes.

   (c) Spin 950 PMMA A4 at 4000 RPM for 45 s.

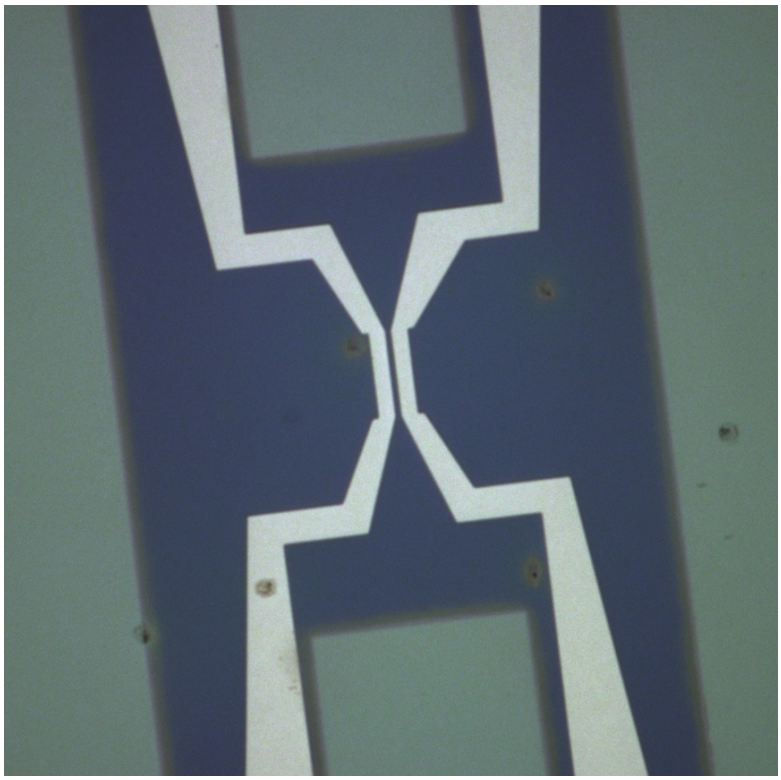

Figure C.3: Josephson junction after the superconductor deposition step. Shown here is a close-up optical microscope image of a Josephson junction after aluminum is deposited to define superconductors. The gray background is the top of the two-dimensional electron gas. The green-gray color on the sides is where mesa is etched away. The light white is the aluminum leads for the junction. Note that in this device, the mesa was not etched near the superconducting leads.

(d) Bake at 150 °C for 3 minutes.

3. Define the gates using the Elionix. For this step, we tend to write the larger features at 10 nA and the smaller ones at 1nA.
4. Develop for 80 seconds in a beaker of MIBK:IPA (1:3) that has been chilled for more than 15 minutes, then rinse with IPA and blow dry with nitrogen.
5. Deposit 10 nm of titanium.
6. Deposit around $x + 20$ nm of gold, where x is the depth of the mesa etch.
7. Lift off with acetone.

D

Operating the MX400 Cryostat with Vector Magnet

D.1 Introduction

MX400 is the pride and joy of Team Topology, an Oxford Instruments system boasting base temperatures of around 16 mK and the strongest vector magnet in the Yacoby Lab (12-3-1 T).

However, there is no existing complete documentation of fridge operation. I have written the following document to help guide future users of the system.

I would like to acknowledge Sean Hart for teaching me how to run MX400, as well as Hechen Ren who wrote some MX400 notes specific to cooldowns. I'd also like to thank Andrew Pierce for helping me run and maintain it during my time in the Yacoby Lab, and to acknowledge Shannon Harvey, whose fridge has a similar operation process and whose notes on cooling down and recovering Team Qubit's MX50 fridge I consulted repeatedly when writing up parts of this document.

If anything goes wrong with the MX400 operation, make sure to get in touch with Nick Dent from Oxford Instruments. He is the only Oxford employee with a good understanding of the system.

D.1.1 General Nomenclature Used in this Guide

I use the words fridge and insert interchangeably. Cryostat refers to the dewar that the insert goes into.

When it comes to directions (left/right), I refer to them from the perspective of the person looking at the object.

If you are standing at the entrance of the shielded room and looking into the shielded room, the left wall will be the one closest to the gas cabinet, the right wall the one closest to the 4K station, and the far wall the wall on the opposite side of the room from you.

D.1.2 Disclaimer

I tried to be as thorough as possible, and carefully proofread each step below. That being said, there is the chance that I have an error or a typo. This guide should not replace common sense - make sure to

think about each step before following blindly.

Additionally, anyone using the MX400 should first be trained multiple times before doing a solo cooldown with just this guide.

If there are no MX400 users around, an MX50 user can likely train you as well, as there are many similarities between the two fridges. The major differences are that the MX400 has a nitrogen can while the MX50 has a pulse tube and a pressurizer. The MX400 has a roots pump that the MX50 doesn't have. The MX400 also has added a manual valve right before V12a on the gas cabinet and fully replaced the gas cabinet V6 with a manual V6.

D.2 Cryogen Filling and Maintenance

There are three cryogens to fill:

1. Helium should be above 25% when running the fridge. The gauge isn't great when the helium can is low, so try to keep helium filled above 30% to be safe. When the fridge is not in use, it should be kept above 5%, unless you are planning to warm up the magnet or vacuum can for maintenance.
2. The nitrogen can should **always** be filled $> 40\%$, **even if the fridge is not operational.** A warm nitrogen can will cause a lot of damage.
3. The N2 trap should be filled above $\frac{1}{3}$ of the way when the fridge is cold. You can check this using a dipstick.

Depending on how the magnet is being run, the boiloff times for these various cryogens may be different. They should all be checked 2x/day.

D.2.1 Filling the Helium Can

1. Turn the level meter rate to fast - touch the helium fill percentage on the magnet controller, and hit the button labeled "slow". If it is on fast, it will say fast, and be highlighted in orange.
2. Turn the recovery valve from check valve to recovery.
3. Bring the helium dewar that you plan on transferring out of right next to the shielded room.
4. Optional: ground the transfer dewar to the room ground if you have a delicate sample loaded in the fridge.
5. Insert the fridge-side part of the transfer line into the helium inlet on the cryostat.
6. Insert the other part of the transfer line into the transfer dewar, connect the lines, and transfer as normal, pressurizing the dewar to around 4 PSI.
7. Once the helium level meter hits $80 - 85\%$, stop pressurizing the dewar and let the rest of the transfer finish.
8. Remove the transfer line.
9. Switch the valve back to check valve.
10. Turn the level meter rate back to slow.

D.2.2 Filling the Nitrogen Can

The nitrogen can has three inlets. Right now, one should be used for the nitrogen fill meter (the one closest to the gas cabinet side of the room), one should be closed with a rubber hose that is capped at the end (the one closest to the far wall of the shielded room), and the last is used as the exhaust port (the one closest to the door).

1. Remove the black check valve from the exhaust port. During the nitrogen transfer, gas will blow out of this port, and so ideally you should connect an open-ended rubber hose to this port and point the hose downward or otherwise pointing far from anything we care about.
2. Bring a nitrogen dewar to the shielded room entrance.
3. Remove the plugged-up rubber hose from the helium inlet that is on the far side of the room from the door, and attach the nitrogen dewar's hose to this inlet.
4. Flow nitrogen softly at first, until the hose on the inlet freezes in place. Generally you want to hold the hose in place (with cryogloves!) until it freezes.
5. Then, open up the flow fully until the nitrogen fills.
6. Be careful! When the nitrogen can fills fully, liquid nitrogen will shoot out of the exhaust. This generally happens around 98% fill level, and can damage things we care about on the top of the cryostat, or the floor. So be ready to close off the valve ASAP if you notice any nitrogen shooting out.
7. Once the transfer is complete, heat gun the dewar's hose and remove it, replacing it with the plugged-up rubber hose.
8. Heat the exhaust port inlet to remove ice, and put the black check valve back on.

D.2.3 Filling the Nitrogen trap

1. Bring a nitrogen dewar near the trap.
2. Using cryogloves, make a hook in the rubber hose from the dewar, and start slowly flowing nitrogen until the rubber freezes in a hook state.
3. Stick the hook into the nitrogen trap dewar.
4. Increase the flow of nitrogen, wait until it starts bubbling up at the top of the trap.
5. Stop the nitrogen flow, remove the dewar.

D.3 Inserting the Fridge Into the Cryostat

D.3.1 Preparing the Fridge for Insertion

1. Ideally, the helium can should be around 20% and the nitrogen can should be filled.
2. Check the fridge lines. Best way to do this is as follows:
   (a) Ground all 24 pins from the breakout box.
   (b) Using a fluke, test the resistance of the pins from the coldfinger to the breakout box by ungrounding one pin at a time. The line resistance should be roughly 500 ohms, and the resistance between the ungrounded pin and one of the grounded pins should preferably be overloaded. If not, megaohms are sufficient.
   (c) At the time of this document, pins 2 and 11 are bad, and have been bad for several years (infinite line resistance).
   (d) Remember that the pinout for MX400 pins is not exactly normal.

   The bottom of the sample holder, from left to right, has pins 3, 2, 1, 13, 14, 15.

   The numbers ascend clockwise 4, 5, ..., and counterclockwise, 16, 17, ...

   Thus, the top of the sample holder should have pins 10, 11, 12, 24, 23, 22 from left to right.
3. Mount your sample:
   (a) Put your sample into the coldfinger, press in so the pins fully go into the sockets.
   (b) Using the 4 screws, screw the guard in to the coldfinger.
   (c) Now is a good time to test your sample at room temperature to make sure all pins are still connected.
4. Attach the radiation shield:
   (a) Put on the radiation shield using the six screws.

(b) Tape up the holes at the top of the radiation shield with aluminum tape.

5. Put on the IVC:

   (a) Clean the top of the IVC (where it attaches to the insert), as well as the part of the insert where the IVC attaches with IPA. Make sure to remove any indium remnants.

   (b) Make an indium seal, using indium wire found above the MX400 desk. You can get a better seal without using vacuum grease.*

   (c) Tighten the sixteen screws until very tight. The screws are labeled in two pairs of 1 through 8, so best practice is to screw both 1s, then both 2s, etc., and proceed in this way.

   (d) Generally, you should repeat this procedure around five times, until the screws are not able to be tightened more.

   (e) Close the IVC speedivalve.

6. Pump the IVC line:

   (a) Attach the pumping manifold, to the still, IVC, and condenser valves, in order, with all valves closed.

   (b) Attach the turbopump to the manifold.

   (c) Rough out the manifold, then open the IVC speedivalve.

   (d) Turbopump the IVC until it gets to the -5s, should take several hours.

   (e) Leakcheck the IVC, making sure to spray a lot of helium around the indium seal. The leak rate should be in the -7s. Make sure to spray helium around the Fischer connector port for thermometry, as sometimes that needs to be tightened.

   (f) Disconnect the leakchecker.

   (g) Close the IVC speedivalve.

*We used to use Apiezon N vacuum grease, but do not anymore.

7. Pump the circulation lines:

    (a) Make sure the IVC speedivalve is closed, and the line from the turbopump to the manifold is pumped out!

    (b) With the roughing pump on and the turbopump off, open the still gate valve.

    (c) Wait until the pressure drops into the -1s, and then open the condenser valve.

    (d) Turn on the turbopump and pump both circulation lines into the -5s.

    (e) Leakcheck the lines, make sure they are in the low -7s.

    (f) Disconnect the leakchecker.

    (g) Close both valves and remove the turbopump.

8. Add exchange gas to the IVC:

    (a) Note: this part of the procedure is more of an art than a science.

    (b) Put a nipple on top of the IVC speedivalve.

    (c) Using a helium gas cylinder, have a very small flow of helium - about as little as you can feel against your lips.

    (d) Flush out the IVC nipple a few times, then attach the gas hose to the nipple.

    (e) Use a pliers to pinch off the hose several millimeters above the nipple.

    (f) Holding the pliers so that the hose is still pinched off, open the speedivalve to let the pinched off gas in to the IVC, then close the speedivalve all the way.

    (g) Remove the gas hose.

9. Flow gas through the 1K pot:

    (a) Attach a nipple to the 1K pot line.

    (b) Flush out this nipple with helium gas, then attach the gas hose to the nipple.

    (c) Open the 1K pot manual valve.

    (d) Open the 1K pot needle valve around 10%.

(e) Remove the filter from the bottom of the sipper.

(f) Stick a container filled with IPA at the bottom of the sipper. You should see bubbles in the IPA, where the bubbling rate should change as you open and close the needle valve.

(g) Wait a few minutes for the IPA to dry.

(h) Put the filter back at the bottom of the sipper.

(i) Keep the gas flowing through the 1K pot for the duration of the insertion process to prevent a 1K pot block!

(j) Tape down the sipper to the IVC with aluminum tape. The tape should go 360° around the IVC.

10. Put the sliding seal on the IVC. It should point such that its exhaust valve faces the far wall of the shielded room. There are lines written in sharpie on the IVC and sliding seal that should line up.

D.3.2 Inserting the Fridge

You will likely want a buddy (or two) for this procedure. The whole time, you **MUST** make sure that nothing crashes and that the helium gas line that is flowing through the 1K pot does not fall off.

1. Dump the bath pressure by turning the recovery valve from the check valve position to recovery.
2. Raise fridge all the way using the crane, and bring it close to the cryostat.
3. Unscrew and remove the baffles.
4. Quickly put the fridge over the hole and start to lower it. Proper position will have the still line facing the wall on the opposite side of the shielded room from the door - it will be right over one of the nitrogen ports.

5. Once gas cannot leak out, attach a line from the sliding seal exhaust to the recovery port on the cryostat. Turning the manual valve right after the cryostat on the recovery line will cause most of the boiloff gas to run through the sliding seal.

6. Lower the insert until it is too hard to lower anymore. If you reach a point when it is too hard to lower, wait 10 minutes or so, then heat gun and cleanroom towel dry the sliding seal, and continue.

7. You may need to unplug some cables (such as the levelmeter and the switch heater cables) as you lower the fridge, just make sure to replug them in once it is down all the way.

8. Once the insert is lowered all the way, screw it down well.

9. Attach the still, condenser, and 1K pot lines to the fridge. Clamp them well. Each line should have a plastic o-ring and clamp at some point between the insert and the wall, to avoid ground loops.

10. Turn the valve so that gas does not flow through the sliding seal.

11. Remove the sliding seal line to the exhaust, and blank it off.

12. Turn the recovery valve back to check valve.

13. Connect the thermometer cable (Fischer connector). This connects to the lower of the two possible ports that are between the still and condenser lines.

14. Connect the magnet switch heater cable (small Fischer connector, near the 1K pot line).

15. Refill the helium can to 100% as a lot will boil off during the initial cool from room to 4K, and check to see if the nitrogen can or nitrogen trap needs filling.

16. Watch the sorb temperature cool down to around 10K. This should take at least 4+ hours, and potentially overnight, depending on how much exchange gas was put in.

17. If it cools too quickly, there is too much exchange gas. You likely will need to pump it out (see below), and potentially warm up and re-do.

D.4 Condensing the Mixture

D.4.1 What to Do Before Condensing

1. Take the N2 trap out and clean as follows:
   (a) Turn the 1K pot pump exhaust to air.
   (b) Open valves V11a and V2 so you can see how much stuff comes out using the G1 gauge.
   (c) Heat gun the trap.
   (d) Pump the N2 trap using the 1K pot pump: turn on pump, turn the pump exhaust to air, open valves V5a, V2a, V7, in order.
   (e) When done pumping (wait 20 minutes or so after G1 bottoms out), close V2, V11a, V7, V2a, V5a, in order.
   (f) Open V11b to pump the cold trap that is left at room - although this is not part of the condense circuit, the valve is a little leaky so it is always good to pump out.
   (g) Put the trap back into the nitrogen dewar.
   (h) Turn the 1K pot pump exhaust back to recovery.

2. Fill the helium and nitrogen cans of the cryostat if not already filled.
3. Fill the N2 trap if not already filled.
4. Pumping the lines:
   (a) Attach the Still, Condenser, and 1K pot lines from the wall to the insert. Be careful with the condenser line!!!
   (b) Make sure that V1, V14, manual V6 are closed.
   (c) There should be a manifold that connects the Still and Condenser lines (the parts that were exposed to air) to the turbopump. Set this up and attach the turbopump. You will need to move the turbopump into the shielded room.
   (d) Rough out the turbopump lines as well as the manifold, while keeping the valves on the condenser and still lines closed. Then, open the turbopump.

(e) Once the manifold has been turbopumped down, stop the turbo (while keeping the roughing pump on). When the turbo spins down to $<$ 700 Hz, open the valve on the 4K trap, then start the turbopump again.

(f) Turbopump down (low -5s or preferably -6s), then leak check. Should see values around -7s.

(g) Close the valves between the manifold and the condenser and still lines, stop and remove the pump.

5. Optional: Removing excess exchange gas from the IVC. Do this step if you feel that there is too much exchange gas.

   (a) ***Make sure the helium bath fill level is no less than 10% and no greater than 25% for this pumping step!***

   (b) Make sure the fridge is not circulating and that all valves are closed.

   (c) Make sure the fridge temperatures (sorb, 1K pot, mixing chamber) are all below 10 K.

   (d) Attach the turbopump to the IVC valve.

   (e) Rough out the line, and turbo the line with the valve closed.

   (f) Very slowly inch open the IVC valve so as not to disrupt the turbo.

   (g) Once the IVC is fully open, turbo it out for a while (10-12 hours at least is recommended).

   (h) Close the IVC valve fully.

   (i) Stop and remove the turbo pump.

6. Collect everything from the circulation lines into the N2 trap:

   (a) Make sure the N2 trap is full.

   (b) Turn on the He3 rotary pump.

   (c) Open V1, V13a, V5.

   (d) Open manual valve V6 on the left side of the gas cabinet.

   (e) G2 should drop to around 420-440.

(f) Let sit for around 10 minutes.

(g) Close V1, V13a, V5

(h) Close manual V6

7. Insert the 4K trap:

   (a) Dump bath pressure by switching the recovery valve from check valve to recovery.

   (b) Insert the 4K trap into the helium inlet port on the side of the cryostat near the wall that is closest to the gas cabinet.

   (c) Switch the valve back to check valve.

8. Run the 1K pot:

   (a) Make sure the He4 rotary pump is on and the exhaust is on air.

   (b) Open the manual valve on the 1K pot line.

   (c) Open valve V4a.

   (d) Turn the He4 rotary pump to recovery.

   (e) Optional steps (do these steps if the 1K pot had been giving trouble before):

      i. *Close 1K pot manual valve.*

      ii. *Open V1A and close it a few times, to allow the main bath line to flush out.*

      iii. *Then close V1a and let G3 and P2 drop to 0.*

      iv. *Open the 1K pot manual valve.*

      v. *Close valve V4a so that the pot isn't being pumped.*

      vi. *Open N/V most of the way (or fully), let G3 rise to 999. Sit there for 1 minute.*

      vii. *Open V1a to equalize the bath with the pot. Leave for 1 minute.*

      viii. *Close V1a to stop the flow from the main bath.*

      ix. *Open V4a to resume pumping on the 1K pot.*

      x. *Close the needle valve fully and wait for G3, P2 to drop.*

      xi. *Wait 5 minutes after G3, P2 drop below 2, and then proceed below as normal.*

(f) Open the needle valve, generally a few percent, until P2 stabilizes between 6 and 10 mbar.

Right now, the needle valve isn't working electronically, and so it will have to be adjusted by hand. BE VERY CAREFUL when turning it.

D.4.2 Condensing the Mixture

Once you have completed all of the steps in the above section, you should be ready to condense!

Make sure the He3 rotary pump is on, the 1K pot is working as mentioned in the prior section, and the roots pump is off. The cryogens should be full[†], and both the 4K trap and the nitrogen trap should be inserted. **The still and condenser lines should have already been pumped out, and their respective vent valves closed.** When opening manual valves on the fridge, make sure these vent valves stay closed.

1. Open both manual valves on the mixture dump.
2. Open the still side of the fridge. G2 should not change as you open the valves.
   (a) Open manual V6 on the left side of the gas cabinet.
   (b) Open the gate valve on the wall in the shielded room.
   (c) Open the still line gate valve on the insert.
3. Open V13a
4. Open V5 and let the mixture sit in the nitrogen trap for around 10 minutes.

[†]At the very least, helium should be above 30% and nitrogen above 45%.

5. Close V5

6. Open the condenser side of the fridge, making sure G1 doesn't change:

   (a) Open V1.

   (b) Open the valve between the cold trap and the insert.

   (c) Open the valve from the condenser line to the insert.

7. Start condensing:

   (a) Open the manual valve between V12a and the nitrogen trap, this valve is found on the back side of the gas cabinet.

   (b) Open V9.

   (c) Slowly open V12a, a few tenths of a percent at a time, but not above 8.5%. Make sure that G1 stays below 150 mbar the whole time.

   (d) G1 and G2 should drop. Once G2 is below 200 mbar (and with G1 staying below 150 mbar the whole time), you can pump the rest of the mixture out of the dump.

   (e) Close V9.

   (f) Open V14 and watch G2, close V14 once G2 rises above 250 mbar.

   (g) Wait until G2 falls below 200 mbar. Then repeat the above step until you can leave V14 open with G2 below 250 mbar.

   (h) Open V12a all the way.

   (i) Turn on the roots pump.

   (j) (Optional:) Set still heat to 2 mW.

D.5 Pulling the Fridge

D.5.1 Recovering the Mixture

1. Zero the magnet and shut off the switch heaters.
2. Disconnect sample connections, ground your sample.
3. Make sure the manual dump valves are open.
4. Turn off the roots pump.
5. Open V3 to equalize pressure on either side of the dump.
6. Stop running the 1K pot:
   (a) Close the 1K pot needle valve, and wait for G3, P2 to fall to 0.
   (b) Close the 1K pot manual valve.
   (c) Close V4a.
7. Close V13a to stop the circulation.
8. Open V9 so mixture can flow into the dump.
9. Open V5 to short the fridge.
10. Set the still and mixing chamber heaters to 20 mW each. Note that the mixing chamber thermometer is measured as uW.
11. Set the sorb heater to 100 mW.
12. Let G2 rise.
13. When G1=0, close the manual valve on the cold trap at the back of the gas cabinet, as well as V12a.
14. Make sure the mixture is out:

(a) G2 should be a bit above 600.

(b) Mixing chamber temp should be above 5K.

(c) P1 should be <= 0.002 mbar.

15. Once the mixture is out, close everything:

(a) Close V1, V3, V5, V9, manual V6.

(b) Close both manual dump valves.

(c) Close the still gate valve on the wall and on the insert.

(d) Close the condenser line valves on the insert and towards the cold trap.

(e) Turn off all heaters.

D.5.2 Removing the Fridge

1. Make sure all valves on the gas cabinet, as well as all manual valves are closed.
2. Vent the Ts of the still line and the condenser line, **making sure that both ends on each line are closed.**
3. Remove the T and the still line.
4. Remove and clean the 4K trap:

(a) Open V1.

(b) Pull the 4K trap out of the helium inlet, close the inlet.

(c) Wait for the cold trap to fully warm (i.e. G1 stops rising), generally around 10 minutes.

(d) Make sure the 1K pot pump is on.

(e) Clean the cold trap by opening V5a, V2a, V7, V2.

(f) Once G1 falls to zero, close V1, V2, V7, V2a, V5a.

5. Vent the 1K pot by opening V1a until G3 rises to 1000, then close V1a.
6. Disconnect the 1K pot line.
7. Disconnect thermometry, needle valve, and magnet control.
8. Pressurize the bath with gas helium using the overpressure valve on the fridge exhaust.
9. Unbolt the insert.
10. Raise the fridge while overpressuring the main bath:
    (a) Lift with the crane until you see the black mark on the sliding seal that shows the insert is about to lift fully out.
    (b) Stop the helium flow.
    (c) Let the insert sit in this position for around 45 minutes.
    (d) Heat gun / blow off any condensation and frost that is on the sliding seal, then wipe it clean with cleanroom wipes.
    (e) Pull the fridge out the rest of the way, put the baffles back in, and secure them with screws.
11. Allow the insert to warm up overnight.

D.5.3 Removing Your Sample

Once the insert has fully warmed:

1. Unscrew and remove the sliding seal.
2. Remove the tape between the IVC and the sipper.

3. Remove the IVC:

    (a) Vent the IVC through the speedivalve towards the top of the insert.

    (b) Remove all but 2 IVC screws, collecting them in a container.

    (c) Break the indium seal by screwing an IVC screw into the small holes between the normal IVC screw holes.

    (d) Remove the last IVC screws, being careful to hold the IVC.

    (e) Gently remove the IVC.

4. Next, remove any tape used to tape the top of the radiation shield.

5. Unscrew the six screws holding up the radiation shield.

6. Carefully remove the radiation shield.

7. Remove the four screws on the guard that protects the sample at the bottom of the coldfinger, and then remove the guard.

8. You are now clear to remove your sample!

D.6 General Maintenance and Troubleshooting

D.6.1 Helium can maintenance

According to Nick, the helium can should be warmed up once every year or two, to prevent ice forming on the magnet leads. The best way to do this is to let the helium boil off to 0 (while keeping the nitrogen can around 40%), and then leaving the helium can in this state for a while ($\sim$ 1 week).

To recool the helium can, you want to pre-cool it with nitrogen first, and then blow out the nitrogen into the nitrogen can and fill with helium. This cooling procedure can be found in any of the Oxford manuals.

D.6.2 Sorb Maintenance

The sorb material (charcoal) should be replaced if the fridge has trouble condensing.

D.6.3 Pump Maintenance

The three pumps (He3 rotary, He4 rotary, and roots) all have slightly different maintenance.

The roots pump and He3 rotary should have their oil changed once every 18 months or so.

The He4 rotary pump should be maintained by the company every 18 months or so as well.

References

[1] Albrecht, S. M., Higginbotham, A. P., Madsen, M., Kuemmeth, F., Jespersen, T. S., Nygård, J., Krogstrup, P., & Marcus, C. M. (2016). Exponential protection of zero modes in Majorana islands. *Nature*, 531(7593), 206–209.

[2] Alicea, J. (2012). New directions in the pursuit of Majorana fermions in solid state systems. *Reports on Progress in Physics*, 75(7), 076501.

[3] Anderson, P. (1959). Theory of dirty superconductors. *Journal of Physics and Chemistry of Solids*, 11, 26–30.

[4] Andreev, A. (1964). The thermal conductivity of the intermediate state in superconductors. *Soviet Physics JETP*, 19, 1228–1231.

[5] Bardeen, J., Cooper, L. N., & Schrieffer, J. R. (1957). Theory of superconductivity. *Physical Review*, 108(5), 1175–1204.

[6] Beenakker, C. W. J. (2013). Search for Majorana fermions in superconductors. *Annu. Rev. Condens.Matter Phys.*, 4, 113–36.

[7] Beenakker, C. W. J. & Van Houten, H. (1991). Josephson current through a superconducting quantum point contact shorter than the coherence length. *Physical Review Letters*, 66(23), 3056–3059.

[8] Bernevig, B. A., Hughes, T. L., & Zhang, S.-C. (2006). Quantum spin Hall effect and topological phase transition in HgTe quantum wells. *Science*, 314(5806), 1757–61.

[9] Bretheau, L., Wang, J. I., Pisoni, R., Watanabe, K., Taniguchi, T., & Jarillo-Herrero, P. (2017). Tunnelling spectroscopy of Andreev states in graphene. *Nature Physics*, 13(8), 756–760.

[10] Buzdin, A., Bulaevskii, L., & Panyukov S.V. (1982). Critical-current oscillations as a function of the exchange field and thickness of the ferromagnetic metal (F) in an S-F-S Josephson junction. *Jetp Lett*, 35(4), 147–148.

[11] Capper, G. (2011). *Mercury Cadmium Telluride: Growth, Properties and Applications*. John Wiley & Sons.

[12] Chen, J., Yu, P., Stenger, J., Hocevar, M., Car, D., Plissard, S. R., Bakkers, E. P., Stanescu, T. D., & Frolov, S. M. (2017). Experimental phase diagram of zero-bias conductance peaks in superconductor/semiconductor nanowire devices. *Science Advances*, 3(9), 1–6.

[13] Churchill, H. O. H., Fatemi, V., Grove-Rasmussen, K., Deng, M. T., Caroff, P., Xu, H. Q., & Marcus, C. M. (2013). Superconductor-nanowire devices from tunneling to the multichannel regime: Zero-bias oscillations and magnetoconductance crossover. *Physical Review B*, 87(24).

[14] Das, A., Ronen, Y., Most, Y., Oreg, Y., Heiblum, M., & Shtrikman, H. (2012). Zero-bias peaks and splitting in an Al–InAs nanowire topological superconductor as a signature of Majorana fermions. *Nature Physics*, 8(12), 887–895.

[15] Delfanazari, K., Puddy, R. K., Ma, P., Yi, T., Cao, M., Gul, Y., Farrer, I., Ritchie, D. A., Joyce, H. J., Kelly, M. J., & Smith, C. G. (2017). On-chip andreev devices: Hard superconducting gap and quantum transport in ballistic nb–ino.75ga0.25as quantum-well–nb josephson junctions. *Advanced Mat*, 29, 1701836.

[16] Demler, E. A., Arnold, G. B., & Beasley, M. R. (1997). Superconducting proximity effects in magnetic metals. *Physical Review B*, 55(22), 15174–15182.

[17] Deng, M. T., Vaitiekenas, S., Hansen, E. B., Danon, J., Leijnse, M., Flensberg, K., Nygård, J., Krogstrup, P., & Marcus, C. M. (2016). Majorana bound state in a coupled quantum-dot hybrid-nanowire system. *Science*, 354(6319), 1557–1562.

[18] Dirac, P. (1928). The quantum theory of the electron. *Proceedings of the Royal Society of London Series A*, 117(778), 610–624.

[19] Dolcini, F., Houzet, M., & Meyer, J. (2015). Topological Josephson φ_0 -junctions. *Physical Review B*, 92, 035428.

[20] Dynes, R. C. & Fulton, T. A. (1971). Supercurrent density distribution in josephson junctions. *Physical Review B*, 3(9), 3015–3023.

[21] Finck, A. D. K., Van Harlingen, D. J., Mohseni, P. K., Jung, K., & Li, X. (2013). Anomalous modulation of a zero-bias peak in a hybrid nanowire- superconductor device. *Physical Review Letters*, 110(12), 1–5.

[22] Fornieri, A., Whiticar, A. M., Setiawan, F., Portolés, E., Drachmann, A. C. C., Keselman, A., Gronin, A., Thomas, C., Wang, C., Kallaher, R., Gardner, G. C., Berg, E., Manfra, M. J., Stern, A., Marcus, C. M., & Nichele, F. (2019). Evidence of topological superconductivity in planar josephson junctions. *Nature*, 569, 89–92.

[23] Frolov, S. M., Van Harlingen, D. J., Oboznov, V. A., Bolginov, V. V., & Ryazanov, V. V. (2004). Measurement of the current-phase relation of superconductor/ferromagnet/ superconductor π Josephson junctions. *Physical Review B*, 70(14), 1–5.

[24] Fu, L. & Kane, C. (2008). Superconducting Proximity Effect and Majorana Fermions at the Surface of a Topological Insulator. *Physical Review Letters*, 100(9), 096407.

[25] Fu, L. & Kane, C. L. (2009). Josephson current and noise at a superconductor/quantum-spin-Hall- insulator/superconductor junction. *Physical Review B*, 79(16), 1–4.

[26] Fulde, P. & Ferrell, R. A. (1964). Superconductivity in a strong spin-exchange field. *Physical Review*, 135(3A).

[27] Groth, C. W., Wimmer, M., Akhmerov, A. R., & Waintal, X. (2014). Kwant: a software package for quantum transport. *New Journal of Physics*, 16(6), 063065.

[28] Gui, Y. S., Becker, C. R., Dai, N., Liu, J., Qiu, Z. J., Novik, E. G., Schäfer, M., Shu, X. Z., Chu, J. H., Buhmann, H., & Molenkamp, L. W. (2004). Giant spin-orbit splitting in a HgTe quantum well. *Physical Review B*, 70(11), 1–5.

[29] Gül, Ö., Zhang, H., Bommer, J. D., De Moor, M. W., Car, D., Plissard, S. R., Bakkers, E. P., Geresdi, A., Watanabe, K., Taniguchi, T., & Kouwenhoven, L. P. (2018). Ballistic Majorana nanowire devices. *Nature Nanotechnology*, 13(3), 192–197.

[30] Hart, S., Ren, H., Kosowsky, M., Ben-Shach, G., Leubner, P., Brüne, C., Buhmann, H., Molenkamp, L. W., Halperin, B. I., & Yacoby, A. (2017). Controlled finite momentum pairing and spatially varying order parameter in proximitized HgTe quantum wells. *Nature Physics*, 13(1), 87–93.

[31] Hart, S., Ren, H., Wagner, T., Leubner, P., Mühlbauer, M., Brüne, C., Buhmann, H., Molenkamp, L. W., & Yacoby, A. (2014). Induced superconductivity in the quantum spin Hall edge. *Nature Physics*, 10(9), 638–643.

[32] Karzig, T., Knapp, C., Lutchyn, R. M., Bonderson, P., Hastings, M. B., Nayak, C., Alicea, J., Flensberg, K., Plugge, S., Oreg, Y., Marcus, C. M., & Freedman, M. H. (2017). Scalable designs for quasiparticle-poisoning-protected topological quantum computation with majorana zero modes. *Physical Review B*, 95(23), 235305.

[33] Kenzelmann, M., Strässle, T., Niedermayer, C., Sigrist, M., Padmanabhan, B., Zolliker, M., Bianchi, A. D., Movshovich, R., Bauer, E. D., Sarrao, J. L., & Thompson, J. D. (2008). Coupled

superconducting and magnetic order in CeCoIn$_5$. *Science*, 321(5896), 1652–4.

[34] Kitaev, A. (2001). Unpaired Majorana fermions in quantum wires. *Phys.-Usp*, 44, 1–16.

[35] Kitaev, A. Y. (2003). Fault-Tolerant Quantum Computation by Anyons. *Ann. Phys.*, 303, 2–30.

[36] Kjaergaard, M., Suominen, H. J., Nowak, M., Akhmerov, A. R., Shabani, J., Palmstrom, C. J., Nichele, F., & Marcus, C. M. (2017). Transparent semiconductor-superconductor interface and induced gap in an epitaxial heterostructure josephson junction. *Physical Review Applied*, 7, 034029.

[37] Koenig, M., Buhmann, H., Molenkamp, L. W., Hughes, T. L., Liu, C.-X., Qi, X.-L., & Zhang, S.-C. (2008). The Quantum Spin Hall Effect: Theory and Experiment. *J. Phys. Soc. Jap.*, 77, 031007.

[38] König, M., Wiedmann, S., Brüne, C., Roth, A., Buhmann, H., Molenkamp, L. W., Qi, X.-l., & Zhang, S.-c. (2007). Quantum Spin Hall Insulator State in HgTe Quantum Wells. *Science*, 318(November), 766–771.

[39] Kontos, T., Aprili, M., Lesueur, J., Genêt, F., Stephanidis, B., & Boursier, R. (2002). Josephson Junction through a Thin Ferromagnetic Layer: Negative Coupling. *Physical Review Letters*, 89(13), 137007.

[40] Laeven, T., Nijholt, B., Wimmer, M., & Akhmerov, A. R. (2019). Enhanced proximity effect in zigzag-shaped Majorana Josephson junctions. *arXiv e-prints*, (pp. arXiv:1903.06168).

[41] Larkin, A. I. & Ovchinnikov, Y. N. (1965). Inhomogenous State of Superconductors. *Soviet Physics JETP*, 20(3), 762.

[42] Li, J., Neupert, T., Bernevig, B. A., & Yazdani, A. (2016). Manipulating Majorana zero modes on atomic rings with an external magnetic field. *Nature Communications*, 7, 1–6.

[43] Lutchyn, R. M., Sau, J. D., & Das Sarma, S. (2010). Majorana fermions and a topological phase transition in semiconductor-superconductor heterostructures. *Physical Review Letters*, 105(7).

[44] Ma, M. K., Hossain, M. S., Villegas Rosales, K. A., Deng, H., Tschirky, T., Wegscheider, W., & Shayegan, M. (2017). Observation of fractional quantum hall effect in an inas quantum well. *Physical Review B*, 96, 241301.

[45] Majorana, E. & Maiani, L. (1937). A symmetric theory of electrons and positrons. *Nuovo Cimento*, 5(171), 201–233.

[46] Mayaffre, H., Krämer, S., Horvatić, M., Berthier, C., Miyagawa, K., Kanoda, K., & Mitrović, V. F. (2014). Evidence of Andreev bound states as a hallmark of the FFLO phase in κ -(BEDT-TTF)2CuNCS)2. *Nature Physics*, 10(12), 928–932.

[47] Mayer, W., Yuan, J., Wickramasinghe, K. S., Nguyen, T., Dartiailh, M. C., & Shabani, J. (2019). Superconducting proximity effect in epitaxial al-inas heterostructures. *Applied Physics Letters*, 114, 103104.

[48] Meissner, W. & Ochsenfeld, R. (1933). Einneuer Effektbeieintritt der Supraleitfahigkeit. *Die Naturwissenschaften*, 21(44), 787–788.

[49] Meservey, R. & Tedrow, P. M. (1971). Properties of very thin aluminum films. *Journal of Applied Physics*, 42(1), 51–53.

[50] Michael Tinkham (1996). *Introduction to Superconductivity*. Courier Corporation.

[51] Mourik, V., Zuo, K., Frolov, S. M., Plissard, S. R., Bakkers, E. P. A. M., & Kouwenhoven, L. P. (2012). Signatures of Majorana Fermions in Hybrid Superconductor-Semiconductor Nanowire Devices. *Science*, 336(6084), 1003–1007.

[52] Nadj-Perge, S., Drozdov, I. K., Li, J., Chen, H., Jeon, S., Seo, J., MacDonald, A. H., Bernevig, B. A., & Yazdani, A. (2014). Observation of Majorana fermions in ferromagnetic atomic chains on a superconductor. *Science*, 346(6209), 602–607.

[53] Nayak, C., Simon, S. H., Stern, A., Freedman, M., & Das Sarma, S. (2008). Non-Abelian anyons and topological quantum computation. *Reviews of Modern Physics*, 80(3), 1083–1159.

[54] Oostinga, J. B., Maier, L., Schüffelgen, P., Knott, D., Ames, C., Brüne, C., Tkachov, G., Buhmann, H., & Molenkamp, L. W. (2013). Josephson supercurrent through the topological surface states of strained bulk HgTe. *Physical Review X*, 3(2), 1–7.

[55] Oreg, Y., Refael, G., & Von Oppen, F. (2010). Helical liquids and Majorana bound states in quantum wires. *Physical Review Letters*, 105(17), 1–4.

[56] Pientka, F., Keselman, A., Berg, E., Yacoby, A., Stern, A., & Halperin, B. I. (2017). Topological superconductivity in a planar Josephson junction. *Physical Review X*, 7(2), 1–17.

[57] Reale, C. (1974). Thickness and temperature dependence of the critical magnetic field of thin superconducting films of the aluminium group metals. *Acta Physica Academiae Scientiarum Hungaricae*, 37, 53–60.

[58] Reeg, C. R. & Maslov, D. L. (2015). Proximity-induced triplet superconductivity in Rashba materials. *Physical Review B*, 92(13), 1–12.

[59] Ren, H. (2018). *Topological Superconductivity in Two-Dimensional Electronic Systems*. PhD thesis, Harvard University.

[60] Ren, H., Pientka, F., Hart, S., Pierce, A., Kosowsky, M., Lunczer, L., Schlereth, R., Scharf, B., Hankiewicz, E. M., Molenkamp, L., Halperin, B. I., & Yacoby, A. (2019). Topological superconductivity in a phase-controlled josephson junction. *Nature*, 569, 93–98.

[61] Rokhinson, L. P., Liu, X., & Furdyna, J. K. (2012). The fractional a.c. Josephson effect in a semiconductor-superconductor nanowire as a signature of Majorana particles. *Nature Physics*, 8(11), 795–799.

[62] Rothe, D. G., Reinthaler, R. W., Liu, C. X., Molenkamp, L. W., Zhang, S. C., & Hankiewicz, E. M. (2010). Fingerprint of different spin-orbit terms for spin transport in HgTe quantum wells. *New Journal of Physics*, 12, 0–22.

[63] Sau, J. D., Lutchyn, R. M., Tewari, S., & Das Sarma, S. (2010). Generic new platform for topological quantum computation using semiconductor heterostructures. *Physical Review Letters*, 104(4), 1–4.

[64] Sellier, H., Baraduc, C., Lefloch, F., & Calemczuk, R. (2003). Temperature-induced crossover between 0 and π states in S/F/S junctions. *Physical Review B*, 68(5), 54531.

[65] Shabani, J., Kjaergaard, M., Suominen, H. J., Kim, Y., Nichele, F., Pakrouski, K., Stankevic, T., Lutchyn, R. M., Krogstrup, P., Feidenhans'L, R., Kraemer, S., Nayak, C., Troyer, M., Marcus, C. M., & Palmstrøm, C. J. (2016). Two-dimensional epitaxial superconductor-semiconductor heterostructures: A platform for topological superconducting networks. *Physical Review B*, 93(15), 1–6.

[66] Shor, P. (1994). Algorithms for quantum computation: Discrete logarithms and factoring. In *Proceedings of the 35th Annual Symposium on Foundations of Computer Science* (pp. 124–134).

[67] Shor, P. (1996). Fault-tolerant quantum computation. *arXiv e-prints*, (pp. quant–ph/9605011).

[68] Stanescu, T. D., Lutchyn, R., & Das Sarma, S. (2011). Majorana fermions in semiconductor nanowires. *Physical Review B*, 84(14), 144522.

[69] Tschirky, T. (2018). *MBE Growth of 6.1 Å Family Semiconductor Heterostructures*. PhD thesis, ETH Zurich.

[70] Weithofer, L. & Recher, P. (2013). Chiral Majorana edge states in HgTe quantum wells. *New Journal of Physics*, 15.

[71] Wickramasinghe, K. S., Mayer, W., Yuan, J., Nguyen, T., Jiao, L., Manucharyan, V., & Sha (2018). Transport properties of near surface inas two-dimensional heterostructures. *Applied Physics Letters*, 113, 262104.

[72] Yokoyama, T., Eto, M., & Nazarov, Y. V. (2014). Anomalous Josephson effect induced by spin-orbit interaction and Zeeman effect in semiconductor nanowires. *Physical Review B*, 89(19), 195407.

[73] Yuan, N. & Fu, L. (2018). Zeeman-induced gapless superconductivity with a partial fermi surface. *Physical Review B*, 97, 115139.

[74] Zhang, H., Liu, C.-X., Gazibegovic, S., Xu, D., Logan, J. A., Wang, G., van Loo, N., Bommer, J. D. S., de Moor, M. W. A., Car, D., het Veld, R. L. M. O., van Veldhoven, P. J., Koelling, S., Verheijen, M. A., Pendharkar, M., Pennachio, D. J., Shojaei, B., Lee, J. S., Palmstrom, C. J., Bakkers, E. P. A. M., Sarma, S. D., & Kouwenhoven, L. P. (2018). Quantized Majorana conductance. *Nature*, 556(556), 74–79.

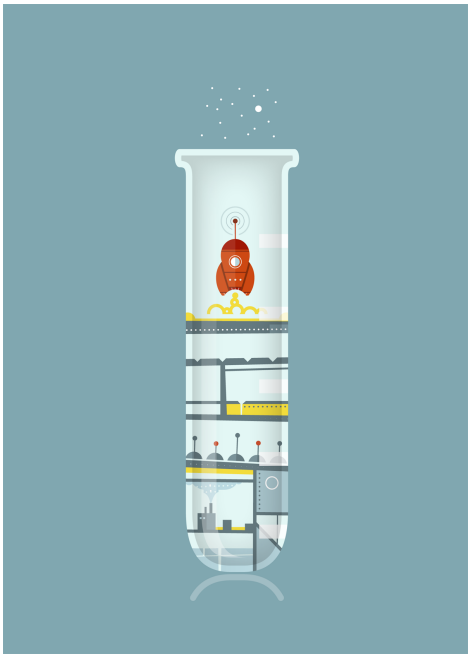

This thesis was typeset using LaTeX, originally developed by Leslie Lamport and based on Donald Knuth's TeX. The body text is set in 11 point Egenolff-Berner Garamond, a revival of Claude Garamont's humanist typeface. The above illustration, *Science Experiment 02*, was created by Ben Schlitter and released under CC BY-NC-ND 3.0. A template that can be used to format a PhD dissertation with this look & feel has been released under the permissive AGPL license, and can be found online at github.com/suchow/Dissertate or from its lead author, Jordan Suchow, at suchow@post.harvard.edu.